

**STRUCTURES OF BARE AND SOLVATED METAL ION – URACIL
COMPLEXES THROUGH INFRARED MULTIPLE PHOTON
DISSOCIATION SPECTROSCOPY AND COMPUTATIONAL METHODS**

by

© Barry Peter Frederick Power

A Thesis submitted to the

School of Graduate Studies

in partial fulfillment of the requirements of the degree of

Doctor of Philosophy

Department of Chemistry

Memorial University of Newfoundland

May, 2017

St. John's

Newfoundland and Labrador

ABSTRACT

Metal ions are essential to nucleic acid stability and activity, however at increased levels, unwanted conformational changes are observed in nucleobases as a result of a direct interaction with the ions. These changes can give rise to improper base pairing, and subsequently lead to genetic mutations. Consequently, examination of the structure of metal ion – nucleobase complexes has been of particular interest. These structures are studied using gas phase techniques as a means of replicating the cellular environment, as condensed phase analysis is hindered by bulk solvent effects. In order to observe the impact that solvent molecules have on the isomerization of such complexes, microsolvation is employed in gas phase experiments. Infrared multiple photon dissociation (IRMPD) is a technique commonly used in the determination of these structures.

IRMPD spectra of alkaline earth metal complexes with uracil, both monomeric and dimeric at varying degrees of hydration, are compared to those computed using electronic structure calculations to determine the structures of these complexes. The spectra of the structures calculated as lowest in energy offer good agreement with the experimental spectra. In these lowest energy isomers, deprotonation of uracil is found to occur at the N3 position. In the dimeric complexes, the second uracil exists as a keto-enol tautomer, with an intramolecular hydrogen bond formed between uracil moieties. In the case of hydrated complexes, water coordination is always directly to the metal center.

Monomeric and dimeric uracil complexes with divalent d-block ions are also examined, both hydrated and ammoniated. For the most part, good agreement is again obtained between the calculated spectra of lowest energy isomers and the experimental

spectra. These complexes also generally exhibit uracil deprotonation at the N3 position, with the exception of copper complexes, where a distinct solvent effect is observed. As the degree of hydration increases, the deprotonation site in uracil changes from the N1 to the N3 position. The lowest energy singly hydrated Zn complex experiences proton transfer from the water molecule to the uracil, resulting in a complex of the form $[\text{Zn}(\text{Ura})(\text{OH})]^+$ where the uracil is a keto-enol tautomer. The ammoniated dimeric complexes adopt a similar structure as that of the alkaline earth hydrated dimers, again with the exception of the copper complex, where Jahn-Teller distortions result in a square planar structure with ammonia coordination to the metal and a tridentate interaction with the neighbouring uracil molecules.

ACKNOWLEDGEMENTS

There are so many people who had a hand in helping me craft this thesis, in one way or another. First of all, my supervisor, Dr. Travis Fridgen, provided the guidance, support, feedback and criticism that allowed me to successfully complete my program, when there were countless times that the task seemed too daunting. Not only as a supervisor, but as the Head of Department, Dr. Fridgen also allowed me the flexibility to continue in my non-academic pursuits, specifically with the Canadian Forces and the Army Cadet Program, which has been a large part of my life for the past 17 years – an organization that I owe my current skills in teaching and leadership, among many others. Most importantly, my relationship with Dr. Fridgen was more than just academic. With both of us being avid hockey fans, almost all of our conversations either started or ended with that – and I have to point out, that at the time this thesis is published, the Senators still have never beaten the Maple Leafs in the playoffs. You're welcome, Travis.

All our group members, past and present, were an invaluable resource for myself through the collaboration of ideas, sharing of experiences, and critiquing of my work and presentations. The efforts of my supervisory committee, Dr. Christina Bottaro and Dr. Bob Davis, helped transform my thesis into one that was comprehensive and well-written. My co-workers in the Chemistry Department, the Instructional Assistants and Laboratory Instructors, were especially accommodating when I needed to adjust my schedule in order to travel for research. During those travels, the collaboration with Jean-Yves Salpin and Violette Haldys provided me with my first experience in collaborating with other research

groups. I am particularly indebted to Dr. Salpin, who provided helpful feedback on three of my manuscripts as they were being drafted. While at the CLIO facility in Orsay, France, the support from Vincent Steinmetz and Dr. Philippe Maître allowed us to keep our experiments going around the clock, which gave me plenty to write about.

Finally, my family and friends would provide the constant motivation it takes to actually do research and draft a thesis. Without that support, there's no knowing how long it would have taken me to get through this, if at all. There's no way to describe how much the support from everyone in my life has meant to me. Thank you all.

TABLE OF CONTENTS

ABSTRACT.....	ii
ACKNOWLEDGEMENTS.....	iv
TABLE OF CONTENTS.....	vi
LIST OF FIGURES	x
LIST OF TABLES	xvi
LIST OF SCHEMES.....	xvii
LIST OF ABBREVIATIONS AND SYMBOLS	xviii
LIST OF APPENDICES.....	xxi
CO-AUTHORSHIP STATEMENT.....	xxii
 CHAPTER 1 – Introduction and Overview	 1
1.1 General Introduction	1
1.2 Nucleobases.....	2
1.2.1 Properties of Uracil.....	4
1.2.2 Previous Studies of Metal Ion – Uracil Complexes.....	6
1.2.2.1 Alkali Metal – Uracil Complexes	6
1.2.2.2 Metal Dication – Uracil Complexes	8
1.2.2.3 $[M(\text{Ura-H})(\text{Ura})]^+$ and $[M(\text{Ura-H})(\text{H}_2\text{O})_n]^+$ (M = Sr, Ba; n = 1, 2) Complexes.....	15
1.2.2.4 Structures and Fragmentation of $[\text{Cu}(\text{Ura-H})(\text{Ura})]^+$ Complexes.....	18
1.2.2.5 Structures of Electrosprayed $\text{Pb}(\text{Uracil-H})^+$ Complexes	20
1.3 Experimental Methods	21
1.3.1 Fourier Transform Ion Cyclotron Resonance Mass Spectrometry (FTICR-MS)	21
1.3.2 Electrospray Ionization.....	24
1.3.3 Sustained Off-Resonance Irradiation Collision Induced Dissociation (SORI- CID).....	26
1.3.4 Infrared Multiple Photon Dissociation (IRMPD) Spectroscopy	27

1.3.4.1 Free Electron Laser	31
1.3.4.2 Optical Parametric Oscillator	33
1.4 Theoretical Methods	35
1.4.1 Density Functional Theory	36
1.4.2 Basis Sets	37
1.4.3 Collecting and Processing Data	39
1.4.4 Atoms in Molecules Theory	42
1.5 References	43
 CHAPTER 2 – Structures of Bare and Singly Hydrated [M(Ura-H)(Ura)]⁺ (M = Mg, Ca, Sr, Ba) Complexes in the Gas Phase by IRMPD Spectroscopy in the Fingerprint Region	 50
2.1 Introduction	51
2.2 Methods	53
2.2.1 Experimental	53
2.2.2 Computational	54
2.3 Results and Discussion	56
2.3.1 Examination of the IRMPD Spectra	56
2.3.2 Computed Structures for [M(Ura-H)(Ura)] ⁺	58
2.3.2.1 Comparison of Computed and Experimental Spectra	62
2.3.3 Computed Structures for [M(Ura-H)(Ura)(H ₂ O)] ⁺	64
2.3.3.1 Comparison of Computed and Experimental Spectra	67
2.3.4 Comparison of Computational Methods	69
2.4 Summary	70
2.5 Acknowledgements	71
2.6 References	71
 CHAPTER 3 – Structures of [M(Ura-H)(H₂O)_n]⁺ (M = Mg, Ca, Sr, Ba; n = 1–3) Complexes in the Gas Phase by IRMPD Spectroscopy and Theoretical Studies	 76
3.1 Introduction	77

3.2 Methods.....	79
3.2.1 Experimental.....	79
3.2.2 Computational.....	80
3.3 Results and Discussion.....	81
3.3.1 Examination of the IRMPD Spectra.....	81
3.3.2 Computed Structures for $[M(\text{Ura-H})(\text{H}_2\text{O})]^+$	86
3.3.2.1 Comparison of Computed and Experimental Spectra.....	89
3.3.3 Computed Structures for $[M(\text{Ura-H})(\text{H}_2\text{O})_2]^+$	91
3.3.3.1 Comparison of Computed and Experimental Spectra.....	94
3.3.4 Computed Structures for $[Mg(\text{Ura-H})(\text{H}_2\text{O})_3]^+$	96
3.3.4.1 Comparison of Computed and Experimental Spectra.....	98
3.4 Summary	100
3.5 Acknowledgements	101
3.6 References	102

CHAPTER 4 – Structures of $[M(\text{Ura-H})(\text{Ura})]^+$ and $[M(\text{Ura-H})(\text{H}_2\text{O})_n]^+$ ($M = \text{Cu, Zn, Pb}$; $n = 1 - 3$) Complexes in the Gas Phase by IRMPD Spectroscopy in the Fingerprint Region and Theoretical Studies

4.1 Introduction	106
4.2 Methods.....	108
4.2.1 Experimental.....	108
4.2.2 Computational.....	108
4.3 Results and Discussion.....	110
4.3.1 Examination of the IRMPD Spectra.....	110
4.3.2 Computed Structures for $[M(\text{Ura-H})(\text{Ura})]^+$	114
4.3.2.1 Comparison of Computed and Experimental Spectra.....	117
4.3.3 Computed Structures for $[M(\text{Ura-H})(\text{H}_2\text{O})]^+$	119
4.3.3.1 Comparison of Computed and Experimental Spectra for $[\text{Zn}(\text{Ura-H})(\text{H}_2\text{O})]^+$ and $[\text{Pb}(\text{Ura-H})(\text{H}_2\text{O})]^+$	122
4.3.3.2 Spectra for $[\text{Cu}(\text{Ura-H})(\text{H}_2\text{O})]^+$	124

4.3.4 Computed Structures for $[M(\text{Ura-H})(\text{H}_2\text{O})_2]^+$	125
4.3.4.1 Comparison of Computed and Experimental Spectra.....	127
4.3.5 Computed Structures for $[\text{Zn}(\text{Ura-H})(\text{H}_2\text{O})_3]^+$	129
4.3.5.1 Comparison of Computed and Experimental Spectra.....	130
4.4 Summary	131
4.5 Acknowledgements	132
4.6 References	132
 CHAPTER 5 – Ammoniated Complexes of Uracil and Transition Metal Ions: Structures of $[M(\text{Ura-H})(\text{Ura})(\text{NH}_3)]^+$ by IRMPD Spectroscopy and Computational Methods (M = Fe, Co, Ni, Cu, Zn, Cd).....	 136
5.1 Introduction	137
5.2 Methods.....	139
5.2.1 Experimental.....	139
5.2.2 Computational.....	140
5.3 Results and Discussion.....	141
5.3.1 IRMPD Spectroscopy	141
5.3.2 Computed Structures for $[M(\text{Ura-H})(\text{Ura})(\text{NH}_3)]^+$	143
5.3.3 Comparison of the Computed and Experimental Spectra	151
5.4 Summary	153
5.5 Acknowledgements	154
5.6 References	154
 CHAPTER 6 – Conclusions and Future Work	 158
6.1 Summary	158
6.2 Potential Future Work	163
 APPENDICES	 165

LIST OF FIGURES

Chapter 1

Figure 1.1. Nucleobases found in DNA and RNA	3
Figure 1.2. Hydrogen bond interaction in DNA Watson-Crick pairings	4
Figure 1.3. Six tautomeric forms of uracil	5
Figure 1.4. The stable isomers of Na ⁺ -thymine and Na ⁺ -adenine (left) and a comparison of the experimental and theoretical bond dissociation energies at 0 K in the M-L complexes. L = uracil (▼,▽), thymine (▲,△), adenine (●,○), and imidazole (■). Figure adapted from <i>J. Am. Chem. Soc.</i> , 2000 , 122, 8548, with permission. Closed shape results from <i>J. Am. Chem. Soc.</i> , 2000 , 122, 8548, open shape results from <i>J. Am. Chem. Soc.</i> , 1996 , 118, 11884	7
Figure 1.5. Potential energy profile corresponding to the Coulomb explosions yielding [CaOH] ⁺ . Relative energies are in kJ mol ⁻¹ . Figure reproduced from <i>Int. J. Mass Spectrom.</i> , 2011 , 306, 27, with permission	10
Figure 1.6. Lowest energy structures for uracil and thiouracil derivatives complexed with Cu ⁺ and Cu ²⁺ . Figures adapted from <i>ChemPhysChem</i> , 2003 , 4, 1011 (top) and <i>ChemPhysChem</i> , 2004 , 5, 1871 (bottom), both with permission	12
Figure 1.7. Energy profile for the isomerization of the [Cu(Ura) ₂] ²⁺ global minimum, <i>a</i> , to yield the di-enolic forms <i>a(e2)</i> and <i>a(e1)</i> as precursors of the (U-H)UCu(O2O4) deprotonated species. Relative energies are in kJ mol ⁻¹ . Figure reproduced from <i>Org. Biomol. Chem.</i> , 2013 , 11, 3862, with permission	13
Figure 1.8. Lowest energy structures for the thiouracil derivatives complexed with Pb ²⁺ . Figure adapted from <i>J. Am. Soc. Mass Spectrom.</i> , 2009 , 20, 359, with permission..	14
Figure 1.9. Experimental spectrum of [Sr(Ura-H)(Ura)] ⁺ in the O-H/N-H stretching region compared to the two lowest energy structures. Relative enthalpies and Gibbs energies (in parenthesis) are given at 298 K. Figure adapted from <i>Int. J. Mass Spectrom.</i> , 2012 , 330-332, 233, with permission	16
Figure 1.10. Experimental spectra of [Sr(Ura-H)(H ₂ O)] ⁺ (top) and [Sr(Ura-H)(H ₂ O) ₂] ⁺ (bottom) in the O-H/N-H stretching region compared to the two lowest energy structures. Relative enthalpies and Gibbs energies (in parenthesis) are given at 298 K. Figure adapted from <i>Int. J. Mass Spectrom.</i> , 2012 , 330-332, 233, with permission	18

Figure 1.11. Structures of the three lowest energy isomers of $[\text{Cu}(\text{Ura-H})(\text{Ura})]^+$. The relative enthalpies and Gibbs energies (in parenthesis) are given at 298 K. Figure adapted from <i>ChemPhysChem</i> , 2012 , 13, 588, with permission	19
Figure 1.12. Ion cyclotron motion in a magnetic field. Figure reproduced from <i>Mass Spectrom. Rev.</i> , 1998 , 17, 1, with permission	22
Figure 1.13. Excitation and detection of ions in FTICR-MS to yield a mass spectrum.....	24
Figure 1.14. Electrospray ionization process. A solution (a) is flowed through a capillary with a potential applied across a narrow opening. This produces charged droplets (b) that shrink as solvent evaporates (c). Gas-phase ions are then produced by either the charged-residue (d) or ion evaporation (e) models. Figure reproduced from <i>Anal. Chem.</i> , 1993 , 65, 972, with permission	25
Figure 1.15. Schematic of a Bruker Apex Qe 7.0 T FTICR-MS	26
Figure 1.16. Illustration of the IRMPD process. Figure recreated with permission from Dr. Travis Fridgen	29
Figure 1.17. Fragmentation during an IRMPD scan of $[\text{Ca}(\text{Pro-H})(\text{Pro})]^+$ about the free N-H stretching mode at 3400 cm^{-1}	30
Figure 1.18. Schematic of a Free Electron Laser (FEL). Figure recreated with permission from the Ph.D. thesis of Khadijeh Rajabi	32
Figure 1.19. Schematic of the Nd:YAG laser with KTP/OPO. Figure recreated with permission from the Ph.D. thesis of Michael B. Burt	34
Figure 1.20. Energy of the idler beam produced by KTP/OPO as a function of wavelength. Figure used with permission from Dr. André Peremans	34
Figure 1.21. (a) Electron density contour map of pyridine, showing bond critical points denoted by green dots. (b) Contour map of the Laplacian of the electron density of pyridine, with red representing a negative Laplacian and blue a positive Laplacian. Figure adapted from <i>CrystEngComm</i> , 2013 , 15, 3536, with permission	42

Chapter 2

Figure 2.1. Comparison of IRMPD spectra for $[\text{M}(\text{Ura-H})(\text{Ura})]^+$ and $[\text{M}(\text{Ura-H})(\text{Ura})(\text{H}_2\text{O})]^+$ complexes, M = Ba, Sr, Ca, Mg, in the $1000 - 1900\text{ cm}^{-1}$ region	58
--	----

Figure 2.2. Comparison of the energies and structures for the three lowest energy $[M(\text{Ura-H})(\text{Ura})]^+$ complexes, $M = \text{Ba}, \text{Sr}, \text{Ca}, \text{Mg}$. The thermochemistry reported here are those from method 259

Figure 2.3. Experimental IRMPD spectrum (bottom) for $[M(\text{Ura-H})(\text{Ura})]^+$ compared with the B3LYP computed spectra using computational method 2 for the three lowest energy structures. Lowest energy structures represent the (i) $\text{N3O4/N3O2}(\text{O4-O2})$, (ii) $\text{N3O4/N3O4}(\text{O2-O2})$ and (iii) $\text{N3O2/N3O2}(\text{O4-O4})$ tautomers. The calculated relative enthalpies and 298 K Gibbs energies (*italics*) are also shown62

Figure 2.4. Comparison of the energies and structures for the three lowest energy $[M(\text{Ura-H})(\text{Ura})(\text{H}_2\text{O})]^+$ complexes, $M = \text{Ba}, \text{Sr}, \text{Ca}, \text{Mg}$. The thermochemistry reported here are those from method 2. For complexes of Mg, all/wO4b or/wO2b labels are replaced simply by/w65

Figure 2.5. Experimental IRMPD spectrum (bottom) for $[M(\text{Ura-H})(\text{Ura})(\text{H}_2\text{O})]^+$ compared with the B3LYP computed spectra using computational method 2 for the three lowest energy structures. Lowest energy structures represent the (i-w) $\text{N3O4/N3O2}(\text{O4-O2})/\text{wO4b}$, (ii-w) $\text{N3O4/N3O4}(\text{O2-O2})/\text{wO4b}$ and (iii-w) $\text{N3O2/N3O2}(\text{O4-O4})/\text{wO2b}$ tautomers. The calculated relative enthalpies and Gibbs energies (*italics*) are also shown68

Chapter 3

Figure 3.1. Infrared multiple photon dissociation spectra for $[\text{Ba}(\text{Ura-H})(\text{H}_2\text{O})]^+$, $[\text{Sr}(\text{Ura-H})(\text{H}_2\text{O})]^+$, $[\text{Ca}(\text{Ura-H})(\text{H}_2\text{O})]^+$ and $[\text{Mg}(\text{Ura-H})(\text{H}_2\text{O})]^+$ in the 1000 – 1900 cm^{-1} region82

Figure 3.2. Infrared multiple photon dissociation spectra for $[\text{Ba}(\text{Ura-H})(\text{H}_2\text{O})_2]^+$, $[\text{Sr}(\text{Ura-H})(\text{H}_2\text{O})_2]^+$, $[\text{Ca}(\text{Ura-H})(\text{H}_2\text{O})_2]^+$ and $[\text{Mg}(\text{Ura-H})(\text{H}_2\text{O})_2]^+$ in the 1000 – 1900 cm^{-1} region84

Figure 3.3. Infrared multiple photon dissociation spectra for $[\text{Ca}(\text{Ura-H})(\text{H}_2\text{O})_2]^+$, $[\text{Ca}(\text{Ura-H})(\text{H}_2\text{O})]^+$, $[\text{Mg}(\text{Ura-H})(\text{H}_2\text{O})_3]^+$, $[\text{Mg}(\text{Ura-H})(\text{H}_2\text{O})_2]^+$ and $[\text{Mg}(\text{Ura-H})(\text{H}_2\text{O})]^+$ in the 2700 – 3800 cm^{-1} region86

Figure 3.4. Comparison of the energies and structures for the three lowest energy $[M(\text{Ura-H})(\text{H}_2\text{O})]^+$ complexes, $M = \text{Ba}, \text{Sr}, \text{Ca}, \text{Mg}$. The thermochemistry reported here are those from method 2. Energies are expressed in kJ mol^{-1} and distances in Angströms.....87

Figure 3.5. Experimental infrared multiple photon dissociation spectrum (bottom) for $[M(\text{Ura-H})(\text{H}_2\text{O})]^+$ compared with the B3LYP computed spectra using computational method 2 for the three lowest energy structures. Lowest energy structures represent the (i) N3O4/wbO2, (ii) N3O2/wbO4 and (iii) N3O4/wbO4 tautomers. The relative enthalpies and Gibbs energies (italics) calculated at 298 K are also shown in kJ mol^{-1}90

Figure 3.6. Comparison of the energies and structures for the three lowest energy $[M(\text{Ura-H})(\text{H}_2\text{O})_2]^+$ complexes, $M = \text{Ba}, \text{Sr}, \text{Ca}, \text{Mg}$. The thermochemistry reported here are those from method 2. Energies are expressed in kJ mol^{-1} and distances in Angströms92

Figure 3.7. Experimental infrared multiple photon dissociation spectrum (bottom) for $[M(\text{Ura-H})(\text{H}_2\text{O})_2]^+$ compared with the B3LYP computed spectra using computational method 2 for the three lowest energy structures. Lowest energy structures represent the (i) N3O4/wbO2/w(bO4), (ii) N3O2/wbO4/w(bO2) and (iii) N3O2/wbO4/w tautomers. The relative enthalpies and Gibbs energies (italics) calculated at 298 K are also shown in kJ mol^{-1} 95

Figure 3.8. Comparison of the energies and structures for the three lowest energy $[\text{Mg}(\text{Ura-H})(\text{Ura})(\text{H}_2\text{O})_3]^+$ complexes. The thermochemistry reported here are those from method 2. Energies are expressed in kJ mol^{-1} and distances in Angströms97

Figure 3.9. Experimental infrared multiple photon dissociation spectrum (bottom) for $[\text{Mg}(\text{Ura-H})(\text{H}_2\text{O})_3]^+$ compared with the B3LYP computed spectra using computational method 2 for the three lowest energy structures. Lowest energy structures represent the (i) N3O4/2wbO4/wbO2, (ii) N3O2/wbO4/2wbO2 and (iii) N3O4/wbO2/wbwbO4 tautomers. The relative enthalpies and Gibbs free energies (italics) calculated at 298 K are also shown in kJ mol^{-1} 99

Chapter 4

Figure 4.1. Infrared multiple photon dissociation spectra for $[M(\text{Ura-H})(\text{Ura})]^+$ ($M = \text{Cu}, \text{Zn}, \text{Pb}$) in the $1000 - 1900 \text{ cm}^{-1}$ region111

Figure 4.2. Infrared multiple photon dissociation spectra for $[M(\text{Ura-H})(\text{H}_2\text{O})]^+$ ($M = \text{Cu}, \text{Zn}, \text{Pb}$) in the $1000 - 1900 \text{ cm}^{-1}$ region113

Figure 4.3. Infrared multiple photon dissociation spectra for $[\text{Zn}(\text{Ura-H})(\text{H}_2\text{O})_2]^+$, $[\text{Cu}(\text{Ura-H})(\text{H}_2\text{O})_2]^+$ and $[\text{Zn}(\text{Ura-H})(\text{H}_2\text{O})_3]^+$ in the $1000 - 1900 \text{ cm}^{-1}$ region114

Figure 4.4. Comparison of the energies and structures for the lowest energy $[M(\text{Ura-H})(\text{Ura})]^+$ complexes, $M = \text{Cu}, \text{Zn}, \text{Pb}$. The thermochemistry reported here are those from method 2115

Figure 4.5. Experimental IRMPD spectrum (bottom) for $[M(\text{Ura-H})(\text{Ura})]^+$ compared with the B3LYP computed spectra using computational method 2 for the lowest energy structures. The calculated relative enthalpies and 298 K Gibbs energies (italics) are also shown118

Figure 4.6. Comparison of the energies and structures for the lowest energy $[M(\text{Ura-H})(\text{H}_2\text{O})]^+$ complexes, $M = \text{Cu, Zn, Pb}$. The thermochemistry reported here are those from method 2120

Figure 4.7. Experimental IRMPD spectrum (bottom) for $[M(\text{Ura-H})(\text{H}_2\text{O})]^+$ compared with the B3LYP computed spectra using computational method 2 for the lowest energy structures. The calculated relative enthalpies and 298 K Gibbs energies (italics) are also shown123

Figure 4.8. Experimental IRMPD spectrum (bottom) for $[M(\text{Ura-H})(\text{H}_2\text{O})_2]^+$, $M = \text{Cu}$ (left) and Zn (right), compared with the B3LYP computed spectra using computational method 2 for the three lowest energy structures. The calculated relative enthalpies and Gibbs energies (italics) are also shown126

Figure 4.9. Experimental IRMPD spectrum (bottom) for $[\text{Zn}(\text{Ura-H})(\text{H}_2\text{O})_3]^+$, compared with the B3LYP computed spectra using computational method 2 for the four lowest energy structures. Isomer 3-i is also shown rotated 90° clockwise about a vertical axis. The calculated relative enthalpies and Gibbs energies (italics) are also shown129

Chapter 5

Figure 5.1. IRMPD Spectra for $[M(\text{Ura-H})(\text{Ura})(\text{NH}_3)]^+$ ($M = \text{Fe, Co, Ni, Cu, Zn, Cd}$) in the $1000 - 1900 \text{ cm}^{-1}$ region142

Figure 5.2. Comparison of the structures for the lowest energy $[M(\text{Ura-H})(\text{Ura})(\text{NH}_3)]^+$ isomers, $M = \text{Fe, Co, Ni, Zn, Cd}$. The unsolvated structures are representative of the parent dimers used as a starting point for calculations to determine the lowest energy $[M(\text{Ura-H})(\text{Ura})(\text{NH}_3)]^+$ structures144

Figure 5.3. Comparison of the ammonia coordination in the lowest energy $[M(\text{Ura-H})(\text{Ura})(\text{NH}_3)]^+$ complexes, $M = \text{Fe, Co, Ni, Cu, Zn, Cd}$. Rotation is 90° clockwise about the vertical axis146

Figure 5.4. Comparison of the structures for the lowest energy $[\text{Cu}(\text{Ura-H})(\text{Ura})(\text{NH}_3)]^+$ complexes147

Figure 5.5. Experimental IRMPD spectrum (bottom) for $[\text{M}(\text{Ura-H})(\text{Ura})(\text{NH}_3)]^+$ compared with the B3LYP computed spectra using computational method 2 for the lowest energy structures. The relative enthalpies and Gibbs free energies (*italics*) calculated at 298 K are also shown in kJ mol^{-1} 152

LIST OF TABLES

Chapter 5

Table 5.1. Thermochemistry and bond distances for the lowest energy $[\text{M}(\text{Ura-H})(\text{Ura})(\text{NH}_3)]^+$ complexes, $\text{M} = \text{Fe}, \text{Co}, \text{Ni}, \text{Zn}, \text{Cd}$. The thermochemistry reported here are those from method 2. Energies are expressed in kJ mol^{-1} and distances in Angströms..... 148

Table 5.2. Thermochemistry and bond distances for the lowest energy $[\text{Cu}(\text{Ura-H})(\text{Ura})(\text{NH}_3)]^+$ complexes. The thermochemistry reported here are those from method 2. Energies are expressed in kJ mol^{-1} and distances in Angströms148

LIST OF SCHEMES

Chapter 2

Scheme 2.1. Numbering scheme for uracil	52
--	----

LIST OF ABBREVIATIONS AND SYMBOLS

$\nabla^2\rho$	Laplacian of electron density
$\Delta E(0K)$	zero point energy
ΔE_{el}	electronic energy
$\Delta_{rel}G$	relative Gibbs energy
$\Delta_{rel}H$	relative enthalpy
Å	Angströms
ACEnet	Atlantic Computational Excellence network
Ade	Adenine
AIM	Atoms in Molecules
B	magnetic field strength
B3LYP	Becke, 3-parameter, Lee-Yang-Parr
BCP	bond critical point
CFI	Canada Foundation for Innovation
CID	collision induced dissociation
CLIO	Centre Laser Infrarouge d'Orsay
cm^{-1}	wavenumbers; inverse centimetres
Cyt	Cytosine
D_0	0 K dissociation energy
DFT	density functional theory
DNA	deoxyribonucleic acid
e Å^{-3}	electrons per cubic angstrom
e Å^{-5}	electrons per quintic angstrom

ε	ellipticity
E_{rot}	rotational energy
E_{trans}	translational energy
E_{vib}	vibrational energy
ESI	electrospray ionization
f_c	cyclotron frequency
FEL	free electron laser
FTICR-MS	Fourier-transform ion cyclotron resonance mass spectrometry
FWHM	full width at half maximum
Gua	Guanine
h	Planck's constant
I	intensity
ICR	ion cyclotron resonance
IR	infrared
IRMPD	infrared multiple photon dissociation
K	temperature; Kelvin
k_B	Boltzmann constant
kJ mol^{-1}	kilojoules per mole
KTP	potassium titanyl phosphate, KTiOPO_4
LANL2DZ	Los Alamos National Laboratory 2 double zeta
m	mass
M	molarity; moles per litre
$\mu\text{L h}^{-1}$	microlitres per hour
mmol L^{-1}	millimoles per litre

m/z	mass-to-charge ratio
MP2	Møller–Plesset second order perturbation theory
MΩ-cm	megohm centimetres
Nd:YAG	neodymium-doped yttrium aluminum garnet, Nd:Y ₃ Al ₅ O ₁₂
NSERC	Natural Sciences and Engineering Research Council of Canada
OPO	optical parametric oscillator
ω_c	angular velocity
ρ	electron density
RF	radio frequency
RNA	ribonucleic acid
s	seconds
SORI-CID	sustained off-resonance irradiation collision induced dissociation
T	tesla
Thy	Thymine
Ura	Uracil

LIST OF APPENDICES

APPENDIX A – Chapter 2 Supplemental Information.....	165
APPENDIX B – Chapter 3 Supplemental Information.....	205
APPENDIX C – Chapter 4 Supplemental Information.....	236
APPENDIX D – Chapter 5 Supplemental Information.....	267

CO-AUTHORSHIP STATEMENT

The experiments described in Chapters 2 – 5 were designed by the principal author in collaboration with Dr. Travis Fridgen, and are an extension of the research presented in the Ph.D. thesis of Osama Ali. All experiments described herein were conducted by the principal author. For experiments conducted at the CLIO facility, Dr. Fridgen also contributed to data collection. In Chapters 2, 3 and 4, Dr. Jean-Yves Salpin and Violette Haldys also collaborated in the collection of experimental data at the CLIO facility. The principal author conducted all data analysis and prepared all research for publication. Dr. Fridgen contributed to the final versions of each chapter, while Dr. Salpin contributed to the final versions of Chapters 2, 3 and 4. In Chapter 5, Dr. Paul Mayer assisted in the collection of experimental data, while some of the computational chemistry was performed by Steven Rowe.

CHAPTER 1 – Introduction and Overview

1.1 General Introduction

Many biological processes are heavily dependent on ion-molecule complexes, in which they play a critical role. In particular, the ion-molecule complexes formed as the result of non-covalent interactions between metal ions and DNA or RNA nucleobases have garnered great interest given their key role in both the synthesis and stabilization of DNA and RNA strands. Observing these interactions in the gas phase is often employed as a means to explore the structure and properties of such ions, providing a greater understanding into the behaviour of these molecules. By removing the bulk solvent effects present in aqueous media, the weak interactions that give these molecules their structure can be thoroughly investigated. To understand what impact, if any, that solvent molecules play on the structure of biologically relevant molecules, microsolvation – the addition of one or a few water molecules – can be employed in the gas phase.

The major focus of this thesis are the interactions between metal dications and the RNA nucleobase, uracil. The experimental method of choice is ion-trapping mass spectrometry to select the ions of interest, through the use of Fourier-Transform Ion Cyclotron Resonance mass spectrometry (FTICR-MS), in combination with structural characterization through Infrared Multiple Photon Dissociation (IRMPD) spectroscopy. Experimental results are then compared to those obtained through electronic structure calculations, employing density functional theory and a variety of different basis sets for geometry optimization and frequency calculations.

This work contained herein is divided into four sections. The first offers an exploration into the structures of dimeric uracil complexes with group 2 metals, both bare

and singly hydrated. The following section expands even further on the examination of group 2 metal complexes; this time, the focus is on monomeric uracil complexes at varying degrees of hydration, from 1 to 3 water molecules. The next chapter is an examination of bare dimers and hydrated monomers of copper, zinc and lead uracil complexes. And finally, a return to dimeric uracil complexes in combination with various transition metal dications, solvated instead by ammonia.

This chapter will outline the properties of DNA and RNA nucleobases, specifically uracil, including a review of previous studies of similar metal ion – uracil complexes. Following that, further background will be given into the experimental and theoretical methods employed within this research.

1.2 Nucleobases

Nucleobase molecules are the building blocks of DNA and RNA strands. Watson and Crick [1] used X-ray diffraction to determine that strings of these bases form a two-strand double-helix structure, where the two strands have a different structure, and specific bases from opposite strands are paired together within the double-helix through hydrogen bonding. Nucleobases are nitrogen-containing cyclic structures, and can be classified as being either purine or pyrimidine [2–4]. Purine structures contain two bicyclic rings, while the pyrimidines have a single 6-member ring structure. The purine nucleobases are adenine (Ade) and guanine (Gua), and the pyrimidines are thymine (Thy), cytosine (Cyt) and uracil (Ura). These 5 nucleobases are shown in Figure 1.1; they all contain amine groups, and many of them also have imine and carbonyl groups, resulting in a number of acceptor or donor hydrogen bonding sites. However, there are also many possible tautomers of these

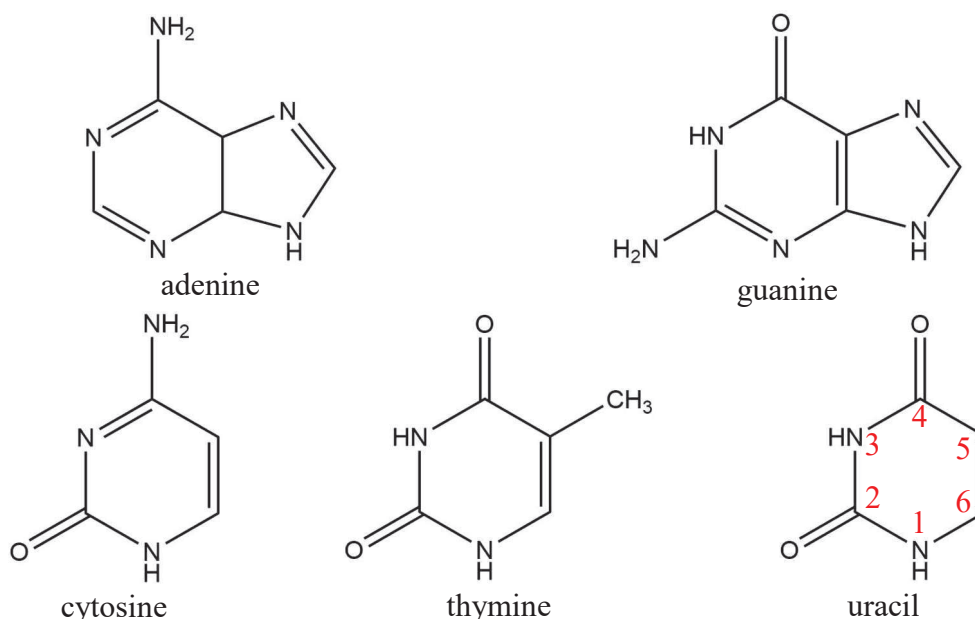


Figure 1.1. Nucleobases found in DNA and RNA.

nucleobases, which can alter the functionality of the molecule and vary the location of the hydrogen bonding sites.

Not only is hydrogen bonding between nucleobases mainly responsible for giving DNA and RNA its double-helix structure, there are also very specific purine-pyrimidine pairs that interact together in these hydrogen bonds. In DNA in particular, Ade will hydrogen bond with Thy, while Gua will hydrogen bond with Cyt. In RNA, Thy is substituted by Ura. These specific pairs are referred to as Watson-Crick pairings, and the hydrogen bonding interactions between pairs are highlighted in Figure 1.2. The proper pairing of nucleobases in DNA and RNA is critical for the transfer of genetic information. Messenger RNA will copy information from a DNA strand in a process known as transcription, by matching the nucleobases in the DNA strand with the corresponding pair [5]. The messenger RNA then transports this information to ribosomes in cells, where it

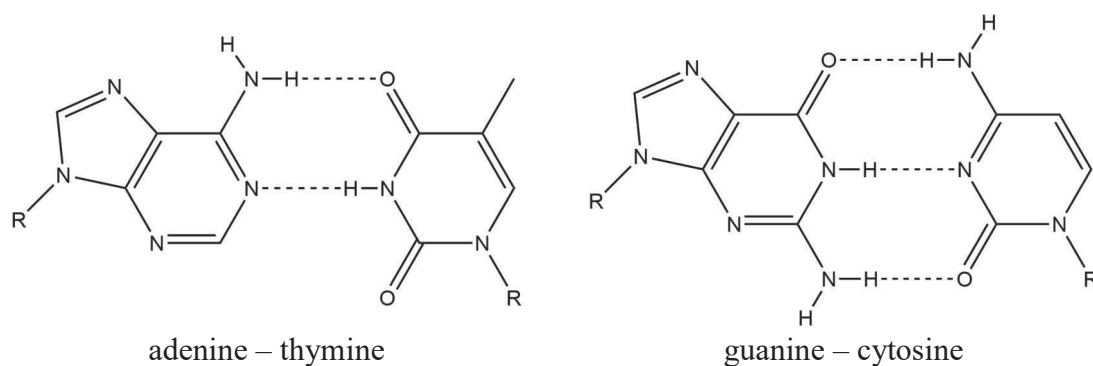


Figure 1.2. Hydrogen bond interaction in DNA Watson-Crick pairings.

is then translated into the amino acid sequence required for the proteins responsible for gene expression. As previously mentioned, tautomerization of the nucleobases can affect the hydrogen bonding sites which may also result in mismatch of the base pairings. This can lead to genetic mutations, and has been the focus of several theoretical studies [6–9]. In this research, uracil is the nucleobase of interest.

1.2.1 Properties of Uracil

Uracil is a nucleobase found only in RNA, and is also formed through deamination of Cyt. In replacing Thy in Fig 1.2, it forms hydrogen bonds with Ade, acting as both a hydrogen bond donor (at its N-H site) and acceptor (at the carbonyl) to form two hydrogen bond interactions. There are derivatives of uracil which have been employed for medicinal purposes, namely 5-bromouracil, which is biologically active [10] and 5-fluorouracil, also biologically active and has also been used as an anticancer drug [11].

As uracil has such a critical role in a vital biological system, it has been the subject of a wide range of research, which includes both its acidity [12–16] and basicity [15–17], as well as reactivity and hydrogen-bonding with DNA species [16]. Metalation also plays

a critical role in the stabilization of nucleic acids as well as the structural organization of proteins. A number of studies have focused on the interaction between metal ions and uracil [18–39], which are reviewed in the next section, and is also the focus of this research.

The two N-H sites in uracil make it a weak acid with pK_a of 9.38. The acidities of both sites have been explored thoroughly [40–43] and are found to be comparable in the aqueous phase. However, in the gas phase, the N-H site surrounded by both carbonyls (N3 in Fig 1.1) is much less acidic than the other N-H site (N1), by a difference in ΔH_{acid} of 42 kJ mol^{-1} [13]. This discrepancy in the gas phase could be the result of the less acidic site being the preferred site for glycosylation.

There are six possible isomers (or tautomers) of uracil, which are shown in Figure 1.3. Of these six tautomers, (1) is in the di-keto form, (6) in the di-enol form, and the remainder are keto-enol tautomers. A tautomer is an isomer that differs in the position of a hydrogen atom and a π bond. Different tautomers have different hydrogen bonding sites, which can impact the base pairings in DNA and RNA, potentially leading to genetic mutations [44]. It had been determined by Tsuchiya *et al.* [45] that the di-keto structure, structure (1), is the most stable structure. In the gas phase, structure (1) is preferred over structure (2), which is next in terms of lowest relative energy, by 81.8 kJ mol^{-1} [46]. The effect that metal binding has on the tautomerization of the most stable form of uracil has

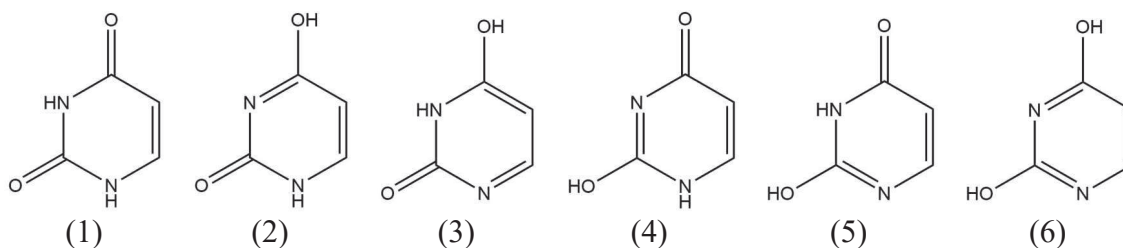


Figure 1.3. Six tautomeric forms of uracil.

been explored through experimental and theoretical methods, determining the preferred binding site in the metal-base complexes and the properties of these complexes. Some of those studies are reviewed in the following section.

1.2.2 Previous Studies of Metal Ion – Uracil Complexes

Metal ion – uracil complexes, as well as derivatives of uracil, have been widely examined, both experimentally and theoretically. The following sections present a review of the previous experiments involving complexes similar to those in this thesis.

1.2.2.1 Alkali Metal – Uracil Complexes

Main group metals complexed together with uracil provided some of the initial insights to the interaction between metals and uracil. Rogers and Armentrout [18] used collision induced dissociation (CID) to examine the interactions of Li^+ , K^+ and Na^+ with uracil, as well as thymine and adenine. The only products of CID are the metal ion and an intact uracil fragment. Strong binding of an electrostatic nature was observed for each metal which increased with decreasing metal size, which is to be expected as the charge density would be increased. Bond dissociation energies of K^+ , Na^+ and Li^+ ions were found to be approximately 100, 140 and 200 kJ mol^{-1} respectively, for all nucleobases, confirmed with relatively good agreement from calculations and comparative to previous work [47]. The preferred binding site for the alkali metals to both uracil and thymine is to the O4 position, as determined through *ab initio* electronic structure calculations, with a second stable structure found where the metal is bound to O2. In the lowest energy O4-binding configuration, the metal is shifted slightly away from the neighbouring N3 amine group,

attributed to steric interactions. The alkali metal ion binding has a stabilizing effect on nucleic acids strands, through reduction of the charge on the nucleic acid in a zwitterion effect, as well as through additional electrostatic interactions between the alkali metal ion and the nucleobases. Figure 1.4 offers the isomers of the stable metal ion – adenine and thymine (and, by extension, uracil) complexes, along with the binding energies comparing experimental to theoretical.

In subsequent experiments, the impact of these interactions were examined in derivatives of uracil using CID and *ab initio* calculations; namely, the impact of halogenation [19], methylation [20] and thio-keto substitution [21] on these interactions, all conducted by Yang and Rodgers. In halogenated species, substitutions were made at the 5 and 6 positions of uracil. In instances where the 5 position is halogenated, metal ion coordination now becomes bidentate, to the O4 carbonyl and 5 position halogen. Even

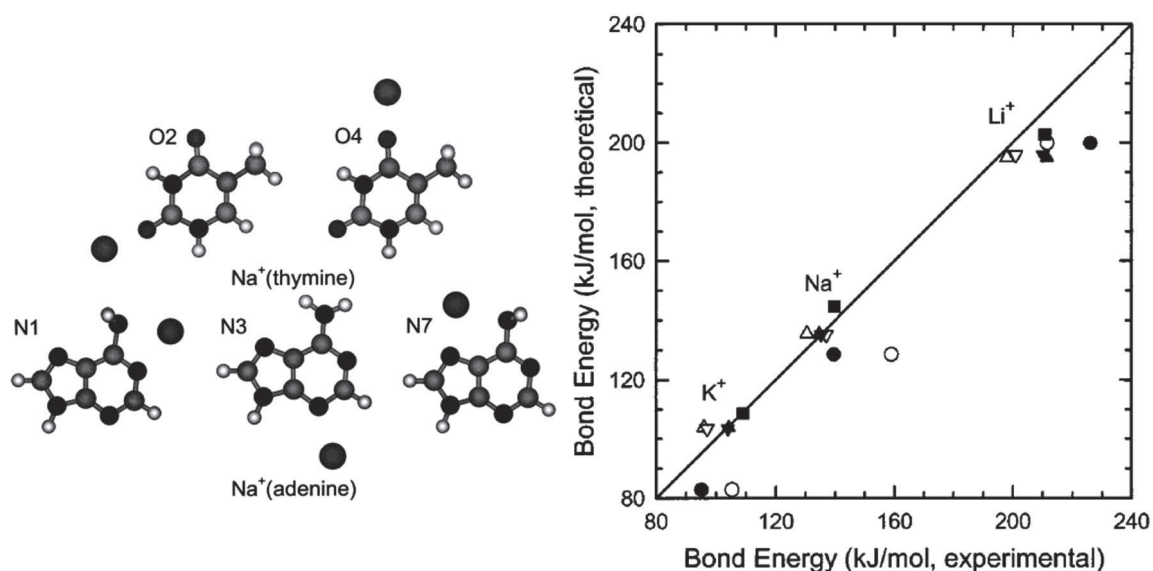


Figure 1.4. The stable isomers of Na⁺-thymine and Na⁺-adenine (left) and a comparison of the experimental and theoretical bond dissociation energies at 0 K in the M-L complexes. L = uracil (▼, ▽), thymine (▲, △), adenine (●, ○), and imidazole (■). Figure adapted from Ref 18 with permission. Closed shape results from Ref 18, open shape results from Ref 47.

though halogenation decreases the dipole moment, the bond dissociation energies between the metal and uracil ligand have increased, as the alkali metal is now in alignment with that dipole moment. Halogenation is also found to further influence the stability of nucleic acids through decreasing the proton affinity of uracil. Halogenation also adds to the stability of the adenine-uracil base pair. Methylation, however, was found to have a negligible impact on nucleic acid stability [20]. Thio-keto substitution leads to an increase in both the proton affinity and the acidity of uracil [21]. 2-thiouracil with metal binding directly to O4 is the preferred isomer as determined theoretically. 2-thio substitution generally results in an increase in the alkali metal ion binding affinities but has almost no effect on the stability of the adenine-thiouracil base pair. In contrast, 4-thio substitution results in a decrease in the alkali metal ion binding affinities as well as a significant decrease in the stability of the adenine-thiouracil base pair. However, the stabilizing effect on nucleic acids gained through alkali metal binding is consistent throughout, regardless of substituted groups. In more recent work, Nei *et al.* [22] examined both sodiated uracil and thiouracil complexes using IRMPD, experimentally confirming the structures found theoretically [18,20] with sodium bound directly to O4 in both uracil and 2-thiouracil as the experimentally observed structures.

1.2.2.2 Metal Dication – Uracil Complexes

In terms of group 2 cations, Trujillo *et al.* [23] examined the structure of Ca^{2+} ions with uracil and thiouracil derivatives, using density functional theory (DFT) calculations. As was the case with the alkali metals, the preferred structures for the uracil and 2,4-thiouracil complexes was Ca binding directly to the heteroatom in the 4 position. However,

in both 2-thiouracil and 4-thiouracil, a bidentate interaction is preferred, where proton transfer occurs between the N3 position to the 4 position, forming an enol or thioenol tautomer, and Ca is bidentate to N3 and the 2 position. These enol and enethiol tautomers should not be observed normally in the gas phase, however complexation with Ca makes them the preferred tautomer.

After determining the preferred isomers of $[\text{Ca}(\text{Ura})]^{2+}$ as well as the thio derivatives, Trujillo *et al.* [24] used nanoelectrospray ionization / mass spectrometry with DFT calculations to predict the unimolecular reactivity of the $[\text{Ca}(\text{Ura})]^{2+}$ ion. In contrast to the alkali metal complexes previously discussed, the lowest energy structure has Ca coordination directly to the O2 carbonyl. Experimentally, the $[\text{CaOH}]^+$ and $[\text{C}_4\text{N}_2\text{OH}_3]^+$ ions are the most intense fragment ions in the mass spectrum, which suggests charge separation through Coulombic explosion as the primary reaction mechanism. The Coulombic explosion fragmentation pathways for a number of global minima $[\text{Ca}(\text{Ura})]^{2+}$ structures is given in Figure 1.5. Each mechanism involves proton transfer to the carbonyl participating in the Ca coordination, with the source of this proton depending on the starting isomer of $[\text{Ca}(\text{Ura})]^{2+}$. Alternative fragmentation pathways involving loss of neutral fragments HNCO and H_2O were also observed, where HNCO is lost from the C2 and N3 positions, as confirmed by labelling experiments with both ^{13}C and ^{15}N in CID. Multiple fragmentation pathways are observed, a stark contrast to the alkali metal complexes previously discussed. In comparison to complexes of Cu and Pb, to be discussed in more detail later, loss of HNCO is the only common fragmentation pathway. Both the Cu and Pb complexes do not form dications, instead uracil is deprotonated forming a singly charged cation.

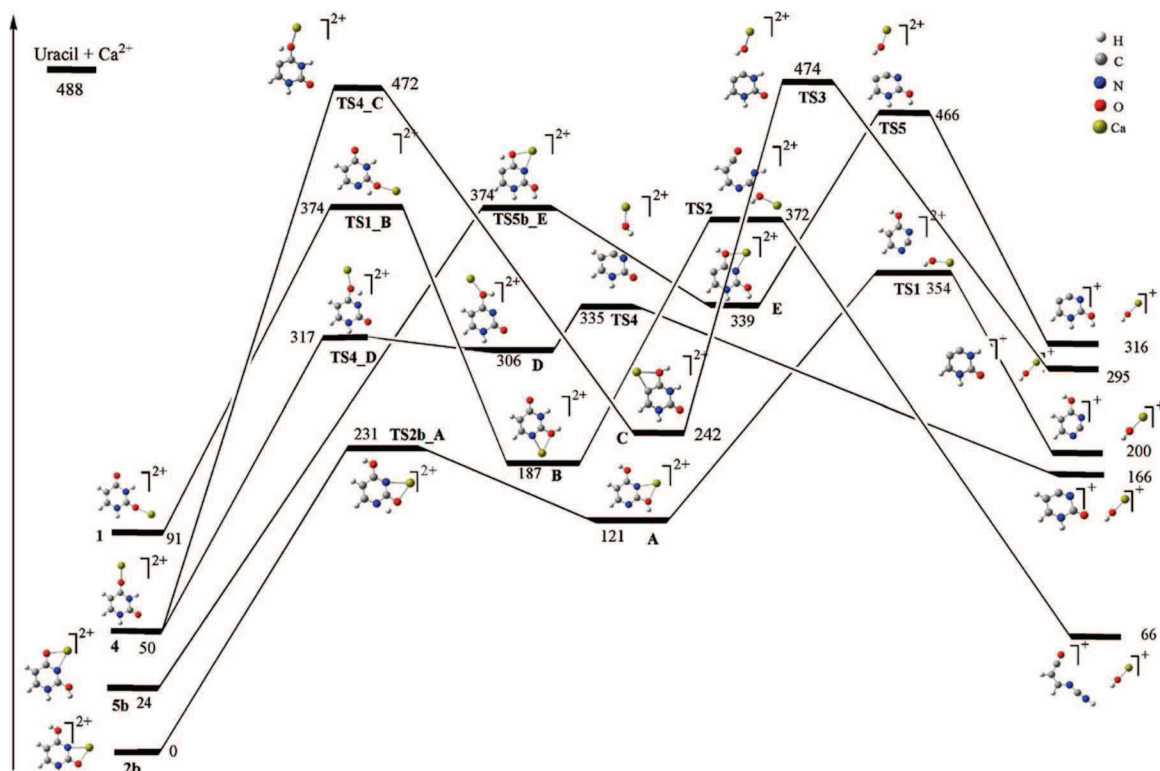


Figure 1.5. Potential energy profile corresponding to the Coulomb explosions yielding $[\text{CaOH}]^+$. Relative energies are in kJ mol^{-1} . Figure reproduced from Ref 24 with permission.

Fragmentation of dimeric complexes $[\text{M}(\text{Ura-H})(\text{Ura})]^+$ has also been examined by Ali *et al.* [25] through SORI-CID and IRMPD for a wide variety of dications, including all group 2 metals as well as the transition metals Mn through Zn, Cd, Pd and Pb. Larger metal centers, Ba, Sr and Pb, show fragmentation exclusively through the loss of uracil in both SORI-CID and IRMPD experiments. The remainder, with the exception of Ca, exhibit loss of HNCO as the primary fragmentation pathway by both methods. The binding energy of the metal to uracil has been shown to be inversely related to the metal ion size, with the smaller ions more tightly bound to the uracil moieties, and as a result, fragmentation of uracil occurs rather than the loss of uracil seen for the larger metal dications. Calcium, being intermediate in size, produced an intriguing result, losing uracil by SORI-CID and

HNCO by the softer IRMPD. As IRMPD has small energy jumps, the fragmentation pathway with lowest activation energy is favoured – which in the case of the Ca complex, is loss of HNCO. On the other hand, SORI-CID is able to access higher internal energies of the complex, and so loss of uracil, which has a large pre-exponential factor and greater activation energy, now prevails.

Of all metal ions, the association of Cu with uracil has been most widely explored. Lamsabhi *et al.* [26] explored the association of Cu^{2+} to uracil and thiouracil using theoretical methods. It was observed that in the case of uracil and 2-thiouracil, Cu^{2+} association occurs at the O4 carbonyl. For 4-thiouracil, Cu^{2+} is bound to the O2 carbonyl, and when both groups are thio-substituted, Cu^{2+} is bound to the thiocarbonyl at the 2 position. This is in contrast to previous findings for the Cu^+ ion [27], which would bind to the sulfur atom in 2-thiouracil as well as 4-thiouracil as opposed to the oxygen, and preferred the thiocarbonyl in the 4 position when binding to 2,4-thiouracil. The binding energies for Cu^{2+} were found to be 4 times larger than Cu^+ , with proton affinities in the Cu^{2+} complex 1.2 times larger than those of the Cu^+ complex. A comparison of Cu^+ and Cu^{2+} binding to uracil and its thio derivatives is given in Figure 1.6.

Although the $[\text{Cu}(\text{Ura})]^{2+}$ complex has been explored theoretically, it has never been experimentally detected. Deprotonated monomeric and dimeric complexes $[\text{Cu}(\text{Ura-H})]^+$ and $[\text{Cu}(\text{Ura-H})(\text{Ura})]^+$ are quite common however. Lamsabhi *et al.* [28] explored the deprotonation pathway of $[\text{Cu}(\text{Ura})]^{2+}$, as well as the thio derivatives, by DFT theoretical methods. For uracil, deprotonation was found to occur at the N1 position, with Cu^{2+} bridged to N1 and O2. In 2-thiouracil, the same general structure exists, with proton transfer occurring from N3 to the carbonyl at O4 resulting in a tautomer. Both 4-thiouracil

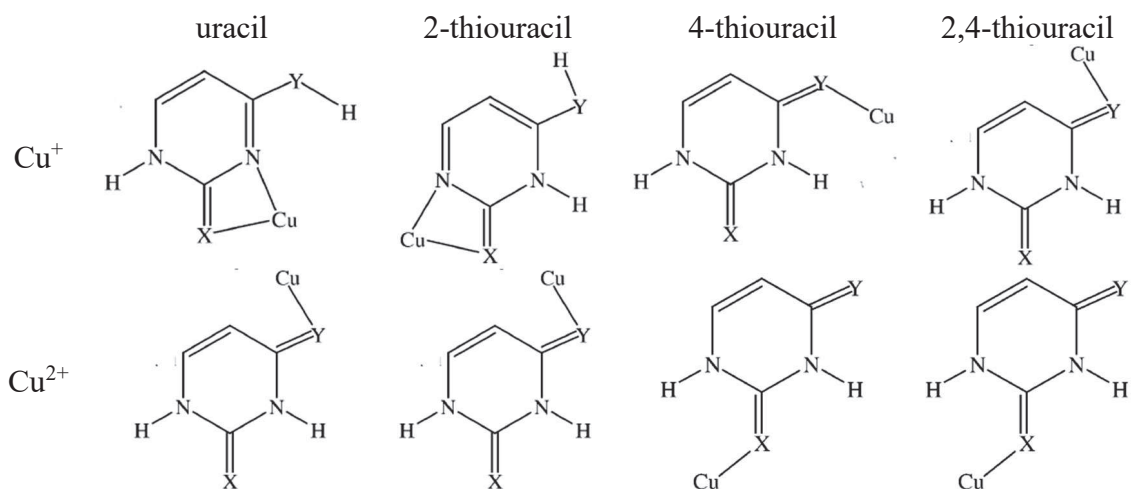


Figure 1.6. Lowest energy structures for uracil and thiouracil derivatives complexed with Cu^+ and Cu^{2+} . Figure adapted from Ref 27 (top) and 26 (bottom), both with permission.

and 2,4-thiouracil adopt a similar configuration, where deprotonation instead occurs at the N3 position, and the Cu is bridged between N3 and the thiocarbonyl at the 4 position. Deprotonation results in a preference for Cu to bind to sulfur, rather than oxygen as was noted in the $[\text{Cu}(\text{Ura})]^{2+}$ complexes. In all cases, the metal-ligand binding is found to be largely covalent in character. Formation of dimeric complexes, and the associated deprotonation pathways, were examined theoretically by Brea *et al.* [29]. Formation of the dimer requires enolization of the system, and the energy profile for the lowest energy dimeric species is given in Figure 1.7. Originating with the $[\text{Cu}(\text{Ura})_2]^{2+}$ complex at global minima **a**, the uracil moieties consecutively undergo proton transfer from N3 positions to the O2 carbonyls, forming enols. These are structures **a(e2)** followed by **a(e1)**. Proton transfer to a third uracil moiety then occurs, resulting in the lowest energy dimeric structure, labelled as **(U-H)UCu(O2O4)** in Fig 1.7. Brea *et al.* [30] then examined this mechanism in more detail to explore why enolization, a process which should have a high activation barrier, is now occurring spontaneously following deprotonation. Using reaction-force,

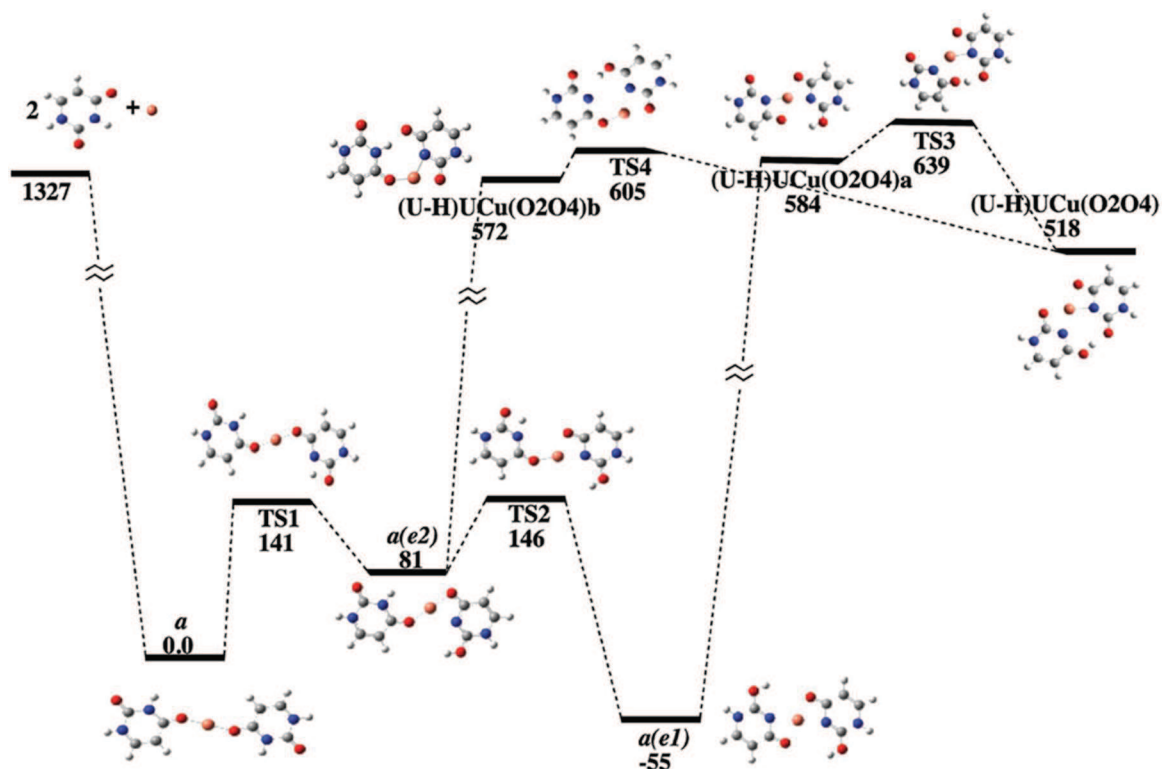


Figure 1.7. Energy profile for the isomerization of the $[\text{Cu}(\text{Ura})_2]^{2+}$ global minimum, *a*, to yield the di-enolic forms *a(e2)* and *a(e1)* as precursors of the $(\text{U-H})\text{UCu}(\text{O}_2\text{O}_4)$ deprotonated species. Relative energies are in kJ mol^{-1} . Figure reproduced from Ref 29 with permission.

chemical-potential and electronic-flux models, the mechanism in Fig 1.7 is found to be more complex than shown, where the enolization following deprotonation actually occurs through a three-step process, with each step having a relatively small activation barrier. Starting with $(\text{U-H})\text{UCu}(\text{O}_2\text{O}_4)\text{b}$ in Fig 1.7, a proton transfer occurs from the N-H group of one uracil moiety to the carbonyl of the other, followed by a translation of one uracil moiety with respect to the other to enable the formation of a new, strong O-H---O hydrogen bond, and concludes with a second proton transfer along this hydrogen bond, back to the uracil which originally lost the proton, leading to the product.

Lead – uracil complexes, as well as the thio derivatives, have been examined by Salpin *et al.* [31]. Lead structures again show a preference towards a bidentate interaction, with deprotonation occurring exclusively at the N3 position. A stronger affinity to sulfur as opposed to oxygen is observed in the Pb ions, leading to N3 and sulfur coordination, regardless of the placement of sulfur, in 2-thiouracil and 4-thiouracil. The lowest energy structures of these Pb-thiouracil complexes are shown in Figure 1.8. It was found that 2-thiouracil and 4-thiouracil could be distinguished based on their distinct fragmentation pathways when complexed with Pb. In 2-thiouracil, the $[\text{PbNCS}]^+$ fragment is produced, whereas 4-thiouracil will produce $[\text{PbNCO}]^+$.

Of the studies that have been previously conducted, there are three which form an important and immediate foundation for the current work, both of which use the same experimental techniques utilized herein. Power *et al.* [32] examined both hydrated monomeric and bare dimeric complexes of uracil with Sr and Ba ions, which forms the basis of the work in chapters 2 and 3. Ali and Fridgen [33] studied the structures and fragmentation of the $[\text{Cu}(\text{Ura-H})(\text{Ura})]^+$ complex in the gas phase, leading to the more expanded examination of this same complex in the fingerprint region in chapter 4, along

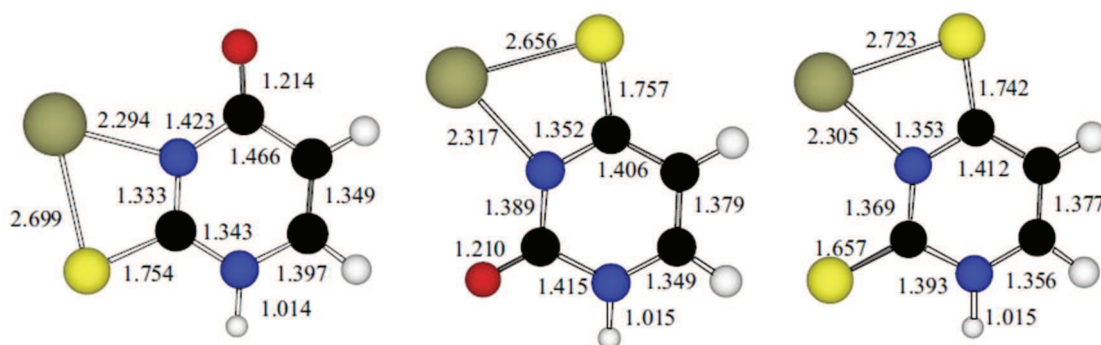


Figure 1.8. Lowest energy structures for the thiouracil derivatives complexed with Pb^{2+} . Figure adapted from Ref 31 with permission.

with their hydrated monomers. This study also serves as a basis for the examination of ammoniated dimers of uracil metalated by various transition metal dications, including copper, in chapter 5. The bare dimer and hydrated monomer complexes of Zn and Pb are also discussed in chapter 4, providing additional insight into the previously examined structures of Pb-uracil complexes in the O-H/N-H stretching region, also conducted by Ali and Fridgen [34].

1.2.2.3 $[M(\text{Ura-H})(\text{Ura})]^+$ and $[M(\text{Ura-H})(\text{H}_2\text{O})_n]^+$ ($M = \text{Sr}, \text{Ba}; n = 1, 2$) Complexes

Structures of $[M(\text{Ura-H})(\text{Ura})]^+$ and $[M(\text{Ura-H})(\text{H}_2\text{O})_n]^+$ where $M = \text{Sr}$ or Ba and $n = 1$ or 2 were explored in the O-H/N-H stretching region, from $3200 - 3900 \text{ cm}^{-1}$ [32]. For the dimeric complexes, the lowest energy structure obtained from the calculations is a planar structure where one uracil is deprotonated at the N3 position, the metal ion is tetracoordinate between the N3 and O4 positions of the deprotonated uracil, and the N3 and O2 positions of the neutral uracil. Proton transfer occurs in the neutral uracil from the N3 to O4 position, forming a new tautomer, and this proton then participates in an intramolecular hydrogen bond with the O2 carbonyl of the deprotonated uracil. A second structure, only slightly higher in energy, is again deprotonated at the N3 position, with metal coordination to N3 and O4. However, in the neutral uracil, proton transfer now occurs from N3 to O2 to form a different tautomer, and the enol now at the O2 position forms the intramolecular hydrogen bond to the O2 of deprotonated uracil. All other calculated structures were found to be significantly higher in energy ($> 40 \text{ kJ mol}^{-1}$). The experimental IRMPD spectrum is compared to those of the two lowest energy structures of

the Sr complex in Figure 1.9. The only band evident in the experimental spectrum is the free N-H stretch, centered about 3490 cm^{-1} . The calculated spectra for both structures match the experimental spectrum well. However, no differentiating features are observed and so no definitive conclusion can be drawn on the correct structure of the complex. For the monomeric species, although the bare structures were not experimentally observed, calculations reveal that the lowest energy structure is the isomer in which deprotonation occurs at the N3 position, and the metal is bidentate to N3 and O4. The isomer deprotonated at N3 and metal chelation to N3 and O2 is slightly higher in energy, at 8 and 10 kJ mol^{-1} for the Ba and Sr complexes respectively. By microsolvating, solvent molecules can be added one by one to the complex to examine the effect these solvent molecules have on the overall structure and thermodynamics of the complex, where they attach, or at what degree of solvation structural changes are observed, if any. Both singly and doubly hydrated complexes display the same general configuration, with deprotonation occurring at the N3 position of uracil, metal coordination to N3 and O4, and water molecules bound directly to

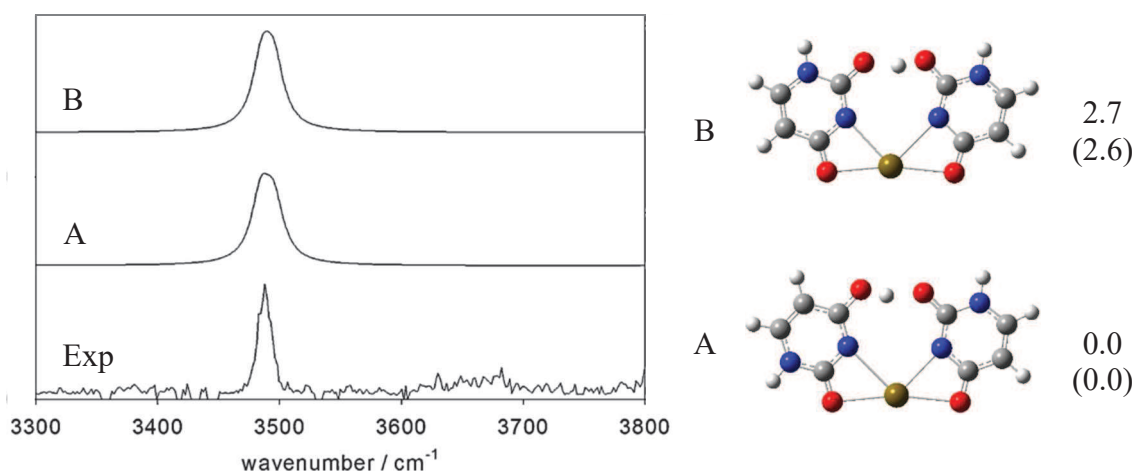


Figure 1.9. Experimental spectrum of $[\text{Sr}(\text{Ura-H})(\text{Ura})]^+$ in the O-H/N-H stretching region compared to the two lowest energy structures. Relative enthalpies and Gibbs energies (in parenthesis) are given at 298 K. Figure adapted from Ref 32 with permission.

the metal ion. For singly hydrated species, the water molecule participates in an intramolecular hydrogen bond to the O2 position in the lowest energy structure. The next isomer in terms of energy also exhibits N3 deprotonation, metal binding to N3 and O2, with water coordination to the metal and hydrogen bonded to the O4 carbonyl. For doubly hydrated structures, both water molecules are bound to the metal ion, with both the O2 and O4 carbonyls each participating in hydrogen bonding with one of the water molecules. Deprotonation occurs at the N3 position once again, with the lowest energy structure having metal coordination between N3 and O4, and a structure slightly higher in energy with the metal located between N3 and O2. The structures and energetics of the two lowest energy $[\text{Sr}(\text{Ura-H})(\text{H}_2\text{O})]^+$ and $[\text{Sr}(\text{Ura-H})(\text{H}_2\text{O})_2]^+$ complexes along with a comparison to the experimental spectra is given in Figure 1.10. The $[\text{Ba}(\text{Ura-H})(\text{H}_2\text{O})_2]^+$ complex was not experimentally observed. The high energy free O-H stretch of water and the lower energy N-H stretch of uracil correspond well with calculated spectra for the two complexes once again, and no evidence exists to discriminate between calculated structures.

In chapter 2 of this thesis, the aim is to identify the predominant isomer in the dimeric species, which could not be accomplished in the O-H/N-H region, by using IRMPD in the fingerprint region. In addition to this, chapter 2 expands upon the metals to include both Ca and Mg in addition to Sr and Ba, and also incorporates microsolvation on the dimeric complexes. Chapter 3 turns its focus to the monomeric species, again with the intent of pinpointing the principal isomer by using IRMPD in the fingerprint region. Once again, Ca and Mg are included to complete the set of group 2 cations, while also expanding the degree of solvation up to 3 water molecules.

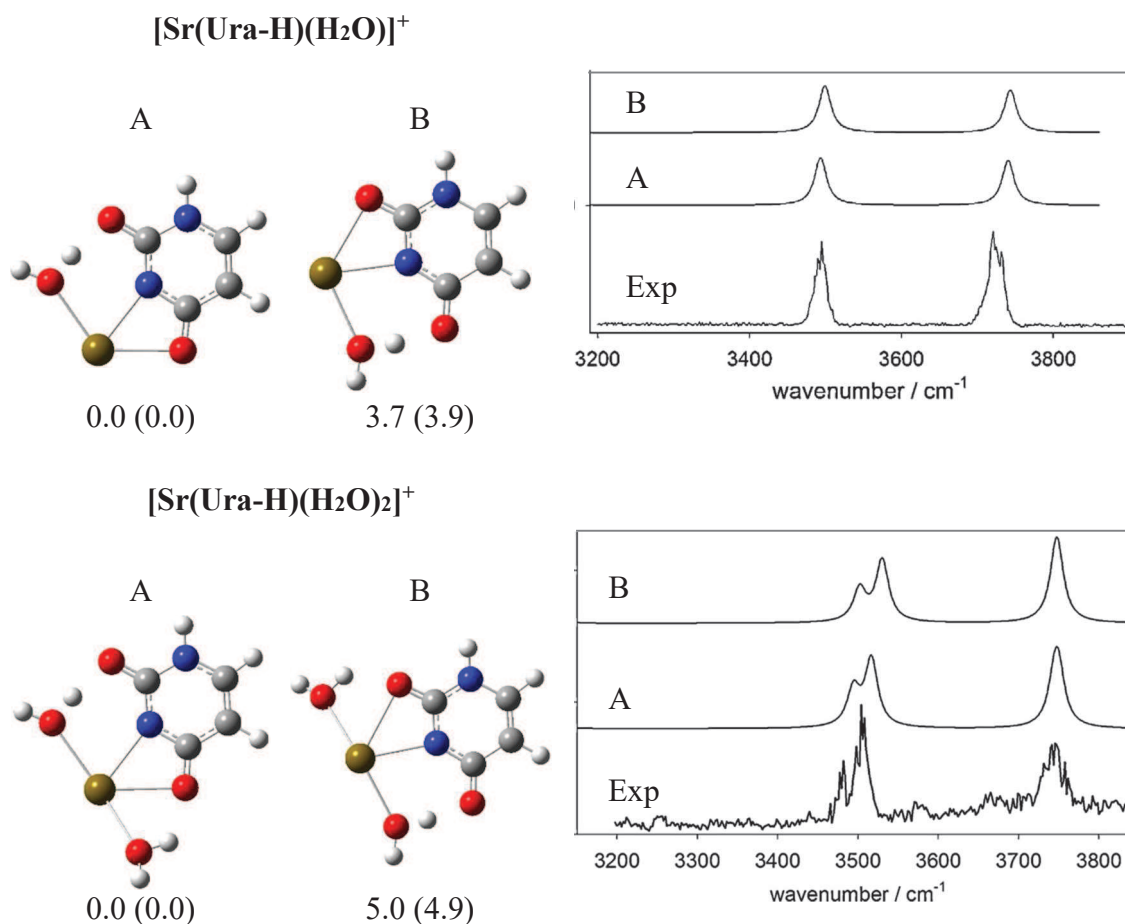


Figure 1.10. Experimental spectra of [Sr(Ura-H)(H₂O)]⁺ (top) and [Sr(Ura-H)(H₂O)₂]⁺ (bottom) in the O-H/N-H stretching region compared to the two lowest energy structures. Relative enthalpies and Gibbs energies (in parenthesis) are given at 298 K. Figure adapted from Ref 32 with permission.

1.2.2.4 Structures and Fragmentation of [Cu(Ura-H)(Ura)]⁺ Complexes

While this thesis does not examine fragmentation pathways or mechanisms in great depth, the study by Ali and Fridgen [33] does offer important structural insights to the [Cu(Ura-H)(Ura)]⁺ complex, albeit without the use of IRMPD spectroscopy. Initially, the structure of [Cu(Ura-H)]⁺ is determined computationally. In a contrast to the [Sr(Ura-H)]⁺ and [Ba(Ura-H)]⁺ structures previously examined, deprotonation in the lowest energy structure of [Cu(Ura-H)]⁺ occurs at the N1 position in the gas phase, with metal

coordination between the N1 and O2 positions. The structure which is deprotonated at the N3 position and the metal is chelated to N3 and O4 is calculated to be $> 30 \text{ kJ mol}^{-1}$ higher in energy in the gas phase, although the two structures are comparable in the aqueous phase. This adds intrigue to the effect of microsolvation in these Cu-uracil complexes.

The three lowest energy $[\text{Cu}(\text{Ura-H})(\text{Ura})]^+$ structures are presented in Figure 1.11. Even though deprotonation in the monomer occurs at the N1 position in the gas phase, the preferred structure for the dimer follows the same configuration as the analogous complexes of Ba and Sr. In the lowest energy structure, deprotonation is at the N3, metal coordination to N3 and O4, while in the neutral uracil, proton transfer occurs from N3 to O4 with the resulting enol forming an intramolecular hydrogen bond with the O2 carbonyl of the deprotonated uracil moiety. There are two other configurations just slightly higher in energy that have the same basic form, but with variations in metal binding sites and proton transfer in the neutral uracil. The consistent features, however, are deprotonation at the N3 position, tetracoordinate metal interactions, and an intramolecular hydrogen bond.

In chapter 4, bare dimers and hydrated monomers of uracil metalated by Cu, along with Zn and Pb, are explored in the IR fingerprint region. Chapter 5 also draws upon this work, as the dimeric complexes are explored expanding the transition metals beyond Cu to include Fe, Co, Ni, Zn and Cd. Microsolvation is also considered, this time with the inclusion of a single ammonia solvent molecule.

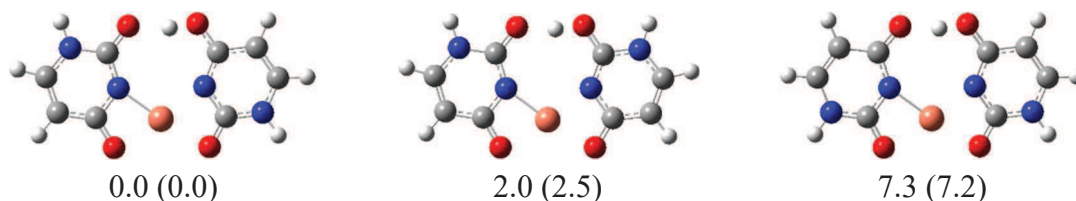


Figure 1.11. Structures of the three lowest energy isomers of $[\text{Cu}(\text{Ura-H})(\text{Ura})]^+$. The relative enthalpies and Gibbs energies (in parenthesis) are given at 298 K. Figure adapted from Ref 33 with permission.

1.2.2.5 Structures of Electrosprayed Pb(Uracil-H)⁺ Complexes

Similar to the work involving Ba and Sr complexes [32], the O-H/N-H stretching region in the infrared displays good agreement between experimental and theoretical results for the $[\text{Pb}(\text{Ura-H})(\text{Ura})]^+$, $[\text{Pb}(\text{Ura-H})(\text{H}_2\text{O})]^+$ and $[\text{Pb}(\text{Ura-H})(\text{H}_2\text{O})_2]^+$ complexes, but once again cannot discriminate between the two lowest energy structures for all [34]. In each instance, however, the deprotonation of uracil occurs at the N3 position and the lowest energy structure of each complex is the one by which Pb is coordinated at N3 and O4 of this deprotonated uracil. In the case of the bare dimer, the same pattern of hydrogen transfer from N3 to O4 of the neutral uracil is observed, which results in the formation of an intramolecular hydrogen bond. For the hydrated monomers, solvent coordination once again occurs directly to the metal center, with hydrogen bonding taking place between water and a neighbouring carbonyl group from uracil, namely the O2 carbonyl in the lowest energy structures. When doubly hydrated, the second water molecule does not hydrogen bond to the uracil. Although a spectrum for the bare monomer could not be experimentally obtained, likely the result of the high dissociation energy that is unattainable using the soft IRMPD fragmentation method, the results from the calculations show that deprotonation still occurs at the N3 position, and metal coordination is to N3 and O4. This result is consistent with the behaviour observed in the dimeric and solvated complexes, and so it would appear that Cu [33] is an exception in this regard, and not the rule.

Chapter 4 makes use of the fingerprint region of the infrared with the intent of determining the principal structure for each of the $[\text{Pb}(\text{Ura-H})(\text{Ura})]^+$, $[\text{Pb}(\text{Ura-H})(\text{H}_2\text{O})]^+$ and $[\text{Pb}(\text{Ura-H})(\text{H}_2\text{O})_2]^+$ complexes, as well as both Zn and Cu analogues.

1.3 Experimental Methods

Studies of these small biological molecules is typically carried out using mass spectrometry. The molecules are ionized into the gas phase where they can then be separated based on mass-to-charge ratio, m/z . While there are a wide variety of ion sources, mass analyzers and detectors, electrospray ionization (ESI) into a Fourier transform ion cyclotron resonance mass spectrometer (FTICR-MS) is the experimental technique of choice for this research. FTICR-MS is advantageous due to its ion trapping and storage capabilities, where further experiments can be conducted. Blackbody infrared radiative dissociation (BIRD), collision induced dissociation (CID) and sustained off-resonance irradiation collision induced dissociation (SORI/CID) experiments are commonly applied to small biological molecules trapped in an FTICR-MS, however it is infrared multiple photon dissociation (IRMPD) spectroscopy that is the technique of choice for this research. In the following subsections, FTICR-MS, ESI, SORI-CID and IRMPD spectroscopy will be explained in further detail.

1.3.1 Fourier Transform Ion Cyclotron Resonance Mass Spectrometry (FTICR-MS)

Fourier transform ion cyclotron resonance mass spectrometry is a technique by which ions orbit within a magnetic field, and the cyclotron frequency of this orbit is then measured to obtain the mass-to-charge ratio of the ion [48]. The ion cyclotron motion in a magnetic field is shown in Figure 1.12. FTICR-MS is considered to be a very high resolution technique, attributable to the strong magnetic fields used, providing very accurate mass measurements [49]. In this work, a magnetic field of 7.0 T is used to trap ions radially under high vacuum conditions of approximately 10^{-10} mbar.

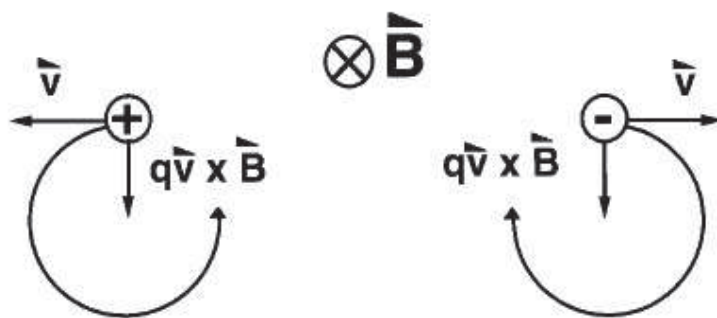


Figure 1.12. Ion cyclotron motion in a magnetic field. Figure reproduced from Ref 48 with permission.

A variety of cell geometries are used in FTICR, however the most commonly employed is the cylindrical cell. In a cylindrical cell, there are two end cap trapping plates, two excitation plates and two detection plates, with each pair of plates directly opposing each other. A small potential voltage is applied to the trapping plates at the ends of the cell, keeping the ions constrained axially within the cell. This trapping voltage is in the opposite direction of the Lorentz force experienced by the ion, which is perpendicular to the magnetic field, thus keeping the ion from falling out of the magnetic field. By trapping the ions within the cell, it allows for experiments to be conducted within the cell, such as kinetic experiments, ion-molecule reactions and spectroscopy, the latter of which is used extensively within this thesis. Once the ions are trapped, the excitation plates and detection plates allow for their observation.

The cyclotron frequency of the ion, f_c , and the angular velocity, ω_c , are dependent upon the mass to charge ratio [48–51], defined as m/q below, but independent of the kinetic energy of the ion:

$$f_c = \frac{\omega_c}{2\pi} \quad \text{Eq 1.1}$$

$$\omega_c = \frac{qB}{m} \quad \text{Eq 1.2}$$

$$\frac{m}{q} = \frac{B}{2\pi f_c} \quad \text{Eq 1.3}$$

where Eq 1.1 and 1.2 are combined and rearranged to result in Eq 1.3, an expression for the mass to charge ratio of an ion based on the magnetic field (B) and cyclotron frequency. To isolate an ion of particular m/z within the ICR cell, all frequencies, aside from the frequency corresponding to the m/z of interest, are scanned. In doing so, the unwanted ions are excited to a cyclotron radius larger than the dimensions within the ICR cell, and are subsequently neutralized.

Ions within the cell must be excited into larger orbits to allow for their detection. In order to achieve this, a sinusoidal voltage is applied to the excitation plates. As the ions are excited, they move within a ‘packet’ or collection of ions, which are grouped together based upon their mass to charge ratio. As energy is absorbed by these ions, the radii of their cyclotron orbit increases, as the cyclotron frequency remains the same. The radii of the cyclotron orbit reaches a point where the ion packet will pass near a detection plate, and the electrons in the ion are attracted towards the plate. As cyclotron motion continues and the ions reach the second detection plate, the electrons are now attracted to this plate, and are drawn away from the first detection plate. The ions passing by each detection plate produce an image current, and as this image current oscillates from plate to plate, the cyclotron frequency of the ions can be measured. Applying a Fourier transform, the time domain signal is converted to frequency domain, and subsequently converted to a mass spectrum through the use of Eq 1.3. Figure 1.13 depicts the process of excitation, detection, and production of a mass spectrum.

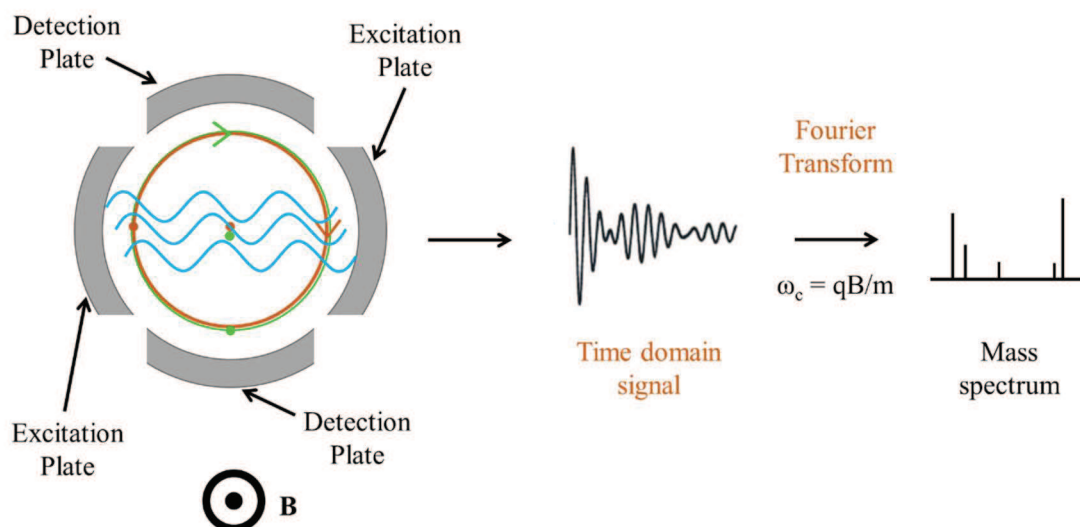


Figure 1.13. Excitation and detection of ions in FTICR-MS to yield a mass spectrum.

1.3.2 Electrospray Ionization

Of course, the ions need to be introduced into the cell and converted from solution to gas phase. This introduction of ions is accomplished through electrospray ionization (ESI), a soft, non-destructive method of ionization [52–56]. A solution containing the molecule of interest is prepared, typically in a polar solvent system, and introduced into a narrow steel capillary. A high voltage electric field is applied to the capillary, which, in positive ion mode as is used throughout, draws positive ions to the surface while pushing away negative ions. Due to this accumulation of positive charge at the surface, the resulting Coulombic repulsion causes the solution to eventually break away into highly charged droplets. The limiting charge Q at which a spherical droplet with a radius r and surface tension λ will hold together is governed by the Rayleigh equation [53]:

$$Q = 64\pi^2 \epsilon_0 \lambda r^3 \quad \text{Eq 1.4}$$

where ϵ_0 is the permittivity of the vacuum. The solvent evaporates from the droplet, resulting in a reduction in size. Using volatile organic solvents in combination with heating

the ion source accelerates this process. As the droplet shrinks, this leads to greater electrostatic repulsion, as the charge becomes more concentrated, and eventually fission will occur. The division of droplets will continue until eventually droplets containing just a single ion remain. Through this process, positively charged gas phase ions are being formed from the solution of the sample. The final step in the formation of gas phase ions is the result of one of two theories – either the charge-residue model, by which solvent evaporation occurs to a point where a single desolvated ion remains, or the ion evaporation model, whereby the ions themselves evaporate from larger droplets [53]. The ion evaporation model is the theory most closely linked to smaller ions such as the ones studied in this research, whereas the charge-residue model is the predominant mechanism for larger ions such as proteins [57]. The overall schematic of ESI is depicted in Figure 1.14. As ESI takes place at atmospheric pressure, and the ICR cell is under near vacuum at 10^{-10} mbar, differential pumping is needed in order to adequately reduce the pressure. A gate valve separates high and low pressure regions within the instrument, with a general schematic of a FTICR-MS shown in Figure 1.15.

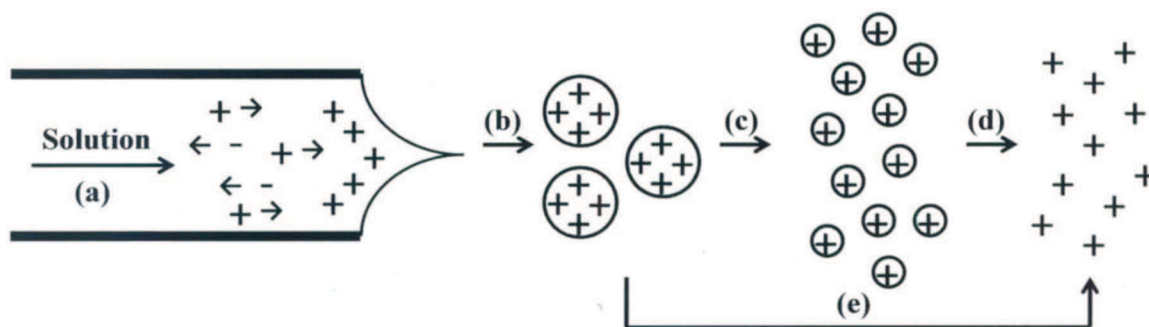


Figure 1.14. Electrospray ionization process. A solution (a) is flowed through a capillary with a potential applied across a narrow opening. This produces charged droplets (b) that shrink as solvent evaporates (c). Gas-phase ions are then produced by either the charged-residue (d) or ion evaporation (e) models. Figure reproduced from Ref 53 with permission.

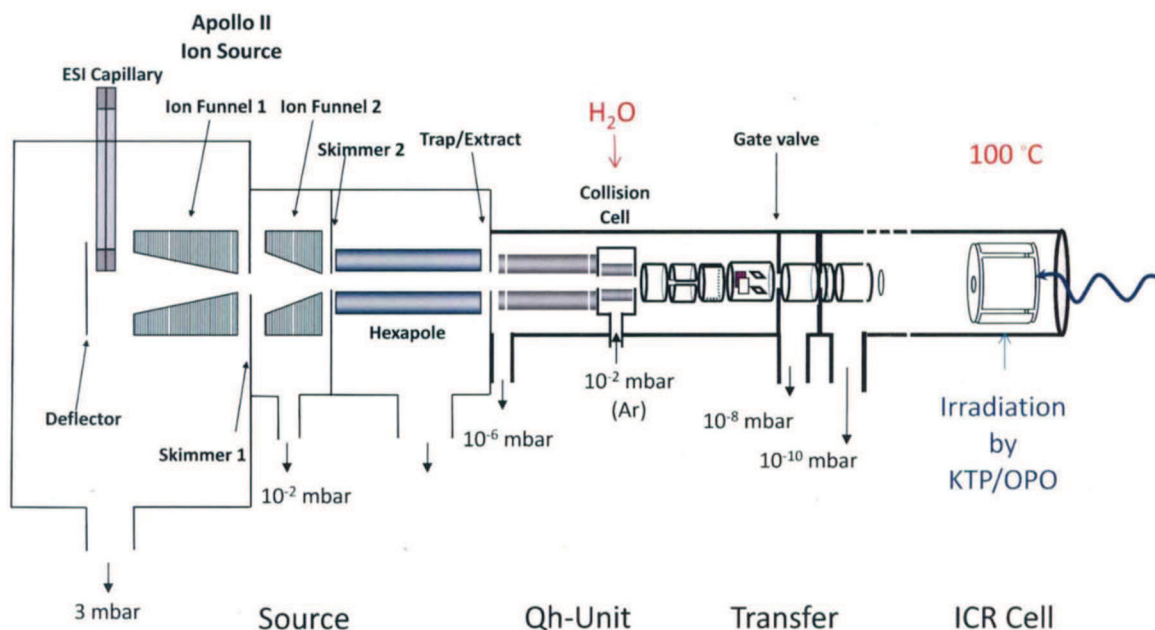


Figure 1.15. Schematic of a Bruker Apex Qe 7.0 T FTICR-MS.

1.3.3 Sustained Off-Resonance Irradiation Collision Induced Dissociation (SORI-CID)

Though not used extensively within this work, it is important to provide a brief overview of sustained off-resonance irradiation collision induced dissociation (SORI-CID), which is a similar process to IRMPD. In SORI-CID, ions that have been trapped in the ICR cell are excited by an RF frequency which is slightly higher than the natural cyclotron frequency of the ion. This creates alternating periods of acceleration and deceleration of the ion [58]. A neutral collision gas, typically Ar or N₂, is introduced to the ICR cell through a pulse valve at pressures of approximately 10⁻⁸ mbar. Collisions between the ion and the gas convert kinetic energy to internal energy. The maximum kinetic energy, or laboratory frame energy, is given by:

$$E_{lab} = \frac{\beta^2 q^2 V_{p-p}}{32\pi^2 m d^2 \Delta\nu^2} \quad \text{Eq 1.5}$$

where β is the geometrical factor of the ICR cell, d is the diameter of the ICR cell, m and q represent the ion mass and charge, V_{p-p} is the peak-to-peak excitation voltage and $\Delta\nu$ is the difference the natural cyclotron frequency and the applied RF frequency.

The ion kinetic energy in SORI-CID is relatively low, which means that the activation process is long, on the order of tenths of a second. Within this timeframe, the ion can experience hundreds of collisions, which can result in attaining the threshold dissociation energy, and thus dissociation of the ion. As a result, low energy fragmentation or rearrangement reactions may be observed in a SORI-CID mass spectrum, making it a very useful tool for structural characterization.

1.3.4 Infrared Multiple Photon Dissociation (IRMPD) Spectroscopy

Infrared spectroscopy is a commonly used technique for the determination of structural features within molecules. Molecules will absorb infrared radiation that is resonant with a vibrational mode contained within the molecule. Detecting the amount of infrared light transmitted or absorbed across a range of frequencies can be used to determine the functional groups contained within a molecule, as specific functional groups have unique vibrational frequencies. Infrared spectroscopy is used for neutrals in all phases, but cannot be effectively employed for gas phase ions, as the low ion density does not allow for adequate detection of a change in radiation intensity. However, an alternative to traditional infrared spectroscopy has emerged in which trapping mass spectrometers, such as the FTICR-MS, are paired with high intensity infrared light sources, known as infrared multiple photon dissociation (IRMPD) spectroscopy. This is a form of consequence spectroscopy where molecules absorb multiple photons of light at a frequency resonant

with a vibrational mode contained within the molecule. The absorption of this energy leads to dissociation of the molecule, and changes in the mass spectrum are monitored in order to produce an infrared spectrum [59–62]. Plotting the fragmentation efficiency, given by Eq 1.6, against the wavenumber of the infrared radiation produces the infrared spectrum:

$$IRMPD_{eff} = -\log \left(\frac{I_{parent}}{I_{parent} + \sum_i I_{fragment(i)}} \right) \quad \text{Eq 1.6}$$

where I represents the signal intensity in the mass spectrum of the parent and fragment ions.

The process of IRMPD begins with the absorption of a single photon of infrared light in resonance with a ground state $v = 0 \rightarrow 1$ vibrational transition. As the ion absorbs this energy and becomes vibrationally excited, that energy is redistributed across the other internal energy states of the molecule via intramolecular vibrational redistribution and relaxation of the absorbing vibrational mode subsequently occurs. This allows for the absorption of another photon of light at the same frequency, where excitation and redistribution of energy occurs yet again. As long as the light source has sufficient intensity, this process will continue until the minimum dissociation threshold D_0 is reached, and the molecule fragments. The overall process of IRMPD is illustrated in Figure 1.16.

The growth of a band in an IRMPD spectrum is illustrated in Figure 1.17 using the $[\text{Ca}(\text{Pro-H})(\text{Pro})]^+$ complex, which has m/z of 269, as a representative example [63]. This complex has a resonant mode at 3360 cm^{-1} , corresponding to the free N-H stretch in proline. As the laser scans, beginning with 3400 cm^{-1} , some minimal fragmentation is observed, visible by the new band at 154 m/z in the mass spectrum, which represents a loss of proline (m/z 115) from the parent ion. The first signs of a band in the IR spectrum are noted. By 3800 cm^{-1} , the fragment at 154 m/z has grown in intensity, along with the appearance of

another fragment with m/z of 251, corresponding to loss of water (m/z 18). The band in the IRMPD spectrum continues to gain intensity. At 3600 cm^{-1} , the vibrational frequency of the free N-H, the intensity of both fragment ions is at a maximum in the mass spectrum, matching the maximum noted for this stretching mode in the IRMPD spectrum. Beyond this point, both the fragment intensity and IRMPD intensity decay until fragmentation is no longer observed at 3300 cm^{-1} .

There are two light sources in particular that have been used in the experiments described by this thesis – a Free Electron Laser, at the Centre Laser Infrarouge D’Orsay (CLIO) in Orsay, France [64], and an Optical Parametric Oscillator laser [65,66], at the

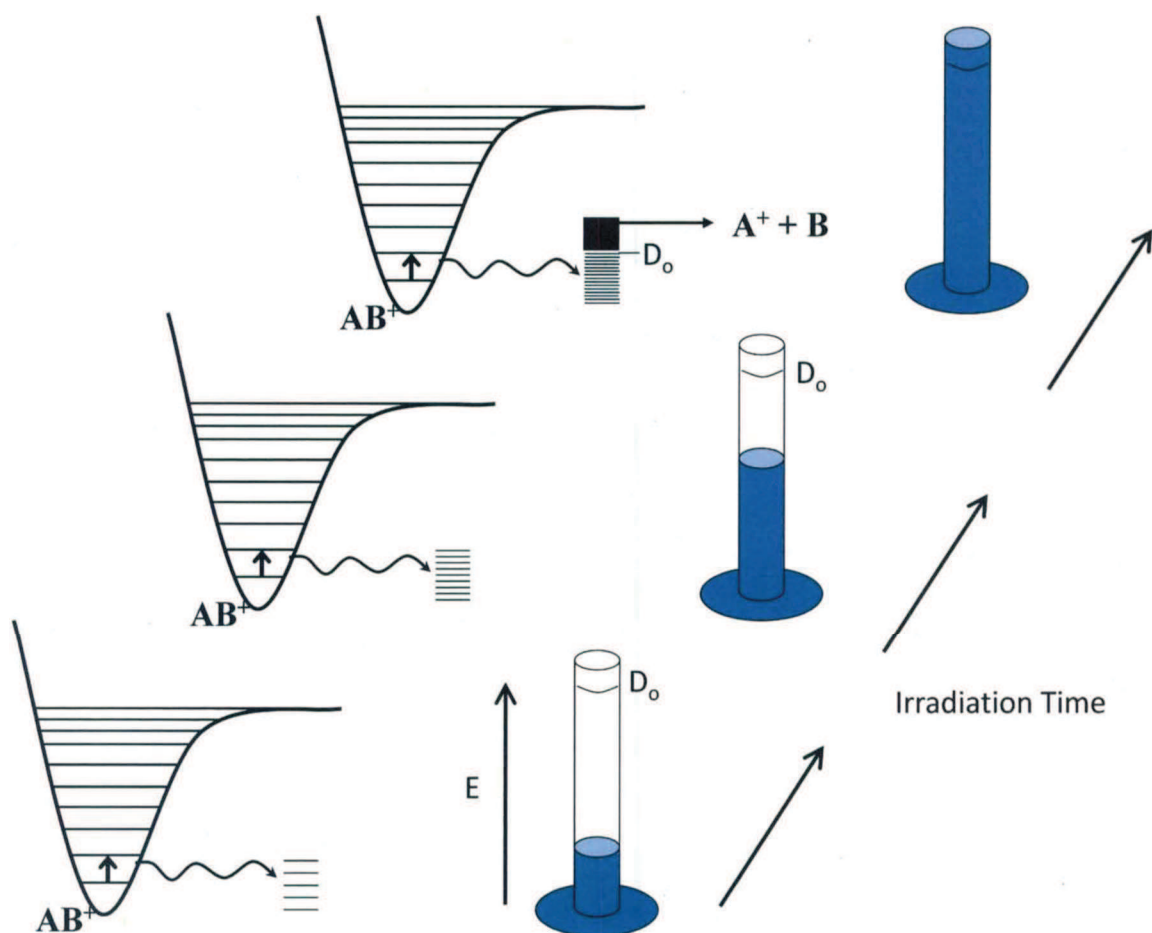


Figure 1.16. Illustration of the IRMPD process. Figure recreated with permission from Dr. Travis Fridgen.

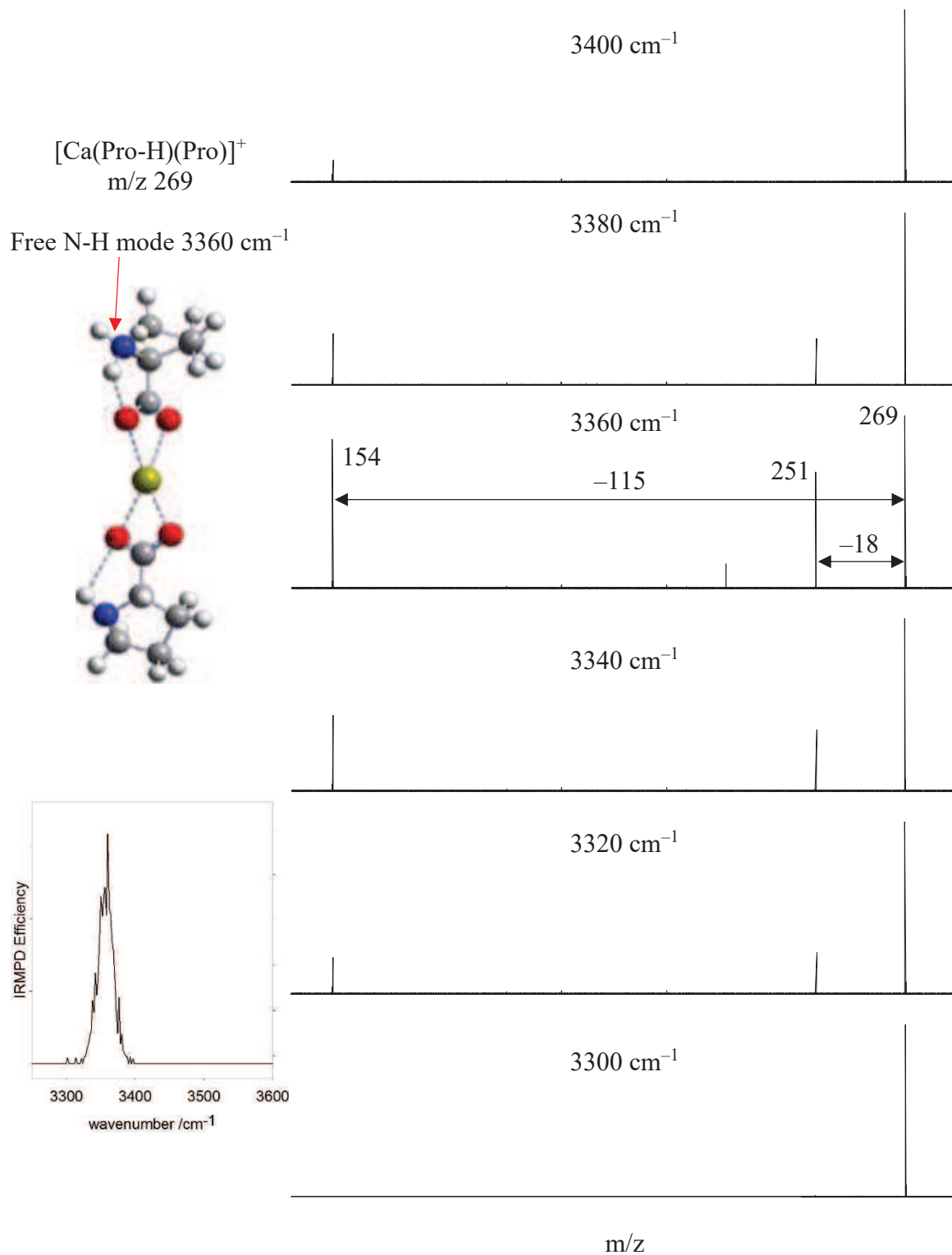


Figure 1.17. Fragmentation during an IRMPD scan of $[\text{Ca}(\text{Pro-H})(\text{Pro})]^+$ about the free N-H stretching mode at 3400 cm^{-1} .

Laboratory for the Study of Structures, Energetics and Reactions of Gas-Phase Ions at Memorial University of Newfoundland. Both are described in the following subsections.

1.3.4.1 Free Electron Laser

In a free electron laser (FEL), a beam of high-energy electrons is employed to amplify light [67,68], with the Bremsstrahlung radiation produced by the accelerated relativistic electrons forming the basis of operation within these lasers [69]. Groups of electrons, on the order of gigaamperes, are ejected from an electron gun and subsequently accelerated to mega electron volts by a radio frequency linear accelerator. This beam of electrons is then directed through an undulator, a set of transverse magnetics, which will create a sinusoidal motion among the electrons as the results of the Lorentz force. These electrons then emit radiation in a continuous frequency band as the direction of the magnetic field in the undulator changes. This radiation is emitted in a straight line, while the beam of electrons continues to move in its sinusoidal wave pattern. This, in combination with the fact that the electron beams travel at a speed slower than light, causes a lag between the radiation and the electron beam, resulting in the radiation being incoherent. To circumvent this, the undulator is set in such a way that the lag is $n\lambda$, where n is any integer and λ is the wavelength. A schematic of an FEL is shown in Figure 1.18.

The radiation emitted is typically weak, as the electrons typically emit radiation which is out of phase. To amplify this radiation, two spherical mirrors are placed near the undulator on opposite ends, forming an optical cavity, resulting in coherent and more intense radiation. The placement of these mirrors is such that the cavity length will result in resonance between the electron packets and emitted light.

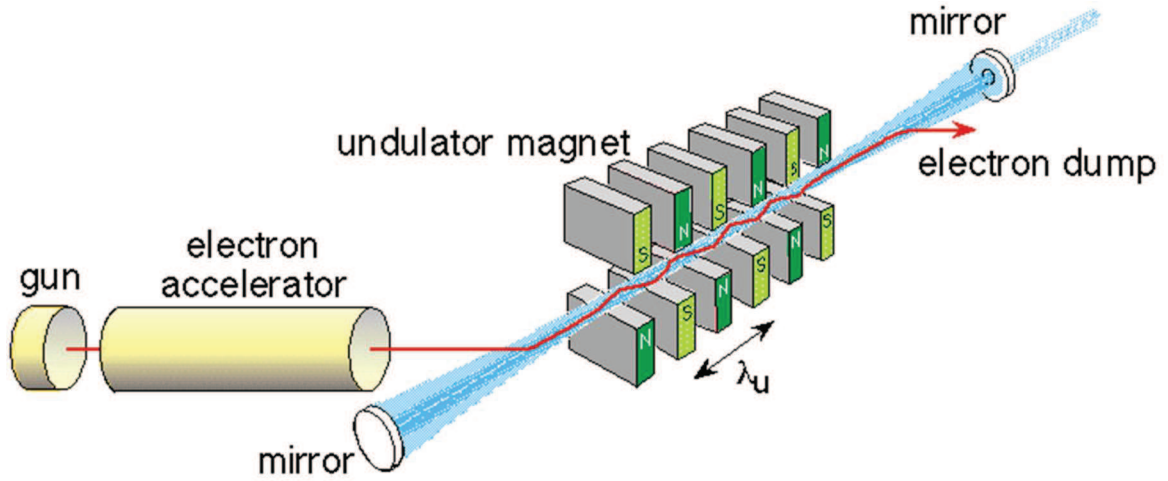


Figure 1.18. Schematic of a Free Electron Laser (FEL). Figure recreated with permission from the Ph.D. Thesis of Khadijeh Rajabi.

The wavelength, defined as the lag between the electron beam and the radiated light, is a function of the magnetic field strength in the undulator. As a result, it becomes possible to tune the wavelength of the laser as shown by the following equation:

$$\lambda_n = \frac{\lambda_U (1 + K_{rms}^2)}{2n\gamma^2} \quad \text{Eq 1.7}$$

As illustrated in Eq 1.7, the FEL radiation wavelength, λ_n , is dependent upon the electron energy γ , the undulator parameter K_{rms} , the undulator period λ_U and the radiation harmonic number n . The magnetic field strength dependence is incorporated in the undulator parameter as follows:

$$K_{rms} = \frac{eB_U\lambda_U}{2\pi m_e c} \quad \text{Eq 1.8}$$

where e and m_e are electron speed and mass respectively, c is the speed of light and B_U is the rms amplitude of the magnetic field on the undulator axis. Therefore, wavelength can be altered by manipulating with the magnetic field of the undulator or the energy of the electrons. Changing the magnetic field of the undulator is accomplished through varying

the gap between magnet arrangements. The FEL at the Centre Laser Infrarouge d'Orsay (CLIO) [63], which is used for the majority of the work contained herein, has the ability to generate electrons between 8 and 50 MeV. With this wide range of attainable electron energy, this is a high intensity laser source which can be tuned efficiently between 500 and 2500 cm^{-1} , revealing useful structural information regarding active functional groups contained within the complexes examined.

1.3.4.2 Optical Parametric Oscillator

An Optical Parametric Oscillator (OPO) is a non-linear crystal that converts high energy photons, such as coherent light from a laser, into two lower energy waves [70]. The frequency of the two resultant waves, known as the signal and idler waves, are dependent upon the angle at which the photons strike the crystal. Rotating the crystal changes the frequency of these waves, allowing for tuning, however the sum of the frequencies of the signal and idler waves will be the initial pumping frequency:

$$\omega_s + \omega_i = \omega_p \quad \text{Eq 1.9}$$

The FTICR-MS at the Laboratory for the Study of Structures, Energetics and Reactions of Gas-Phase Ions at Memorial University of Newfoundland is coupled with a Brilliant B Nd:YAG laser (neodymium-doped $\text{Y}_3\text{Al}_5\text{O}_{12}$) which pumps a fundamental line of 1064 nm [64,65]. The OPO is an 8 x 12 x 25 mm KTP crystal (KTiOPO_4), cut in the ZX plane at an angle of 47.2° relative to the z axis. Rotation of the OPO by $\pm 8^\circ$ gives signal waves between 1.5 and 2.1 μm , and idler waves between 2.1 and 3.5 μm . The OPO is placed in an optical cavity of 35 mm, containing two dichroic mirrors, which have

varying reflection and transmission properties at different wavelengths. The input mirror has maximum reflectivity, whereas the output mirror reflects only approximately 30% of the signal wave and is transparent to the Nd:YAG pump wave as well as the idler wave. The result are two perpendicular waves, with the idler wave directed towards the ICR cell to be used for IRMPD. The signal wave is detected, and the frequency of the idler wave determined from Eq 1.9. The Nd:YAG KTP/OPO setup is depicted in Figure 1.19.

The energy of the idler wave used for IRMPD is dependent on the wavelength. The maximum energy of the idler wave occurs at 2.6 μm , decreasing in energy until 3.4 μm , where it becomes non-existent. A plot of the energy of the idler beam as a function of

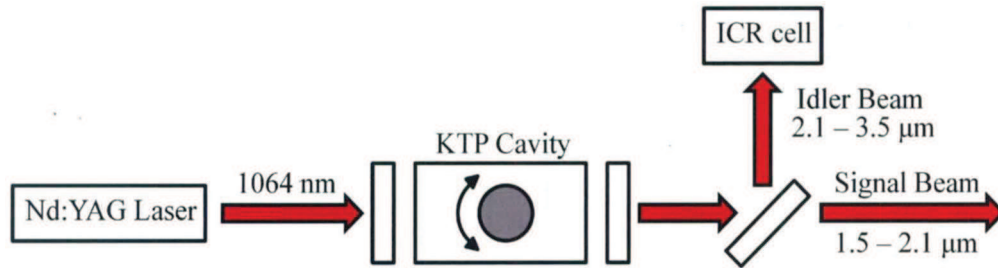


Figure 1.19. Schematic of the Nd:YAG laser with KTP/OPO. Figure recreated with permission from the Ph.D. thesis of Michael B. Burt.

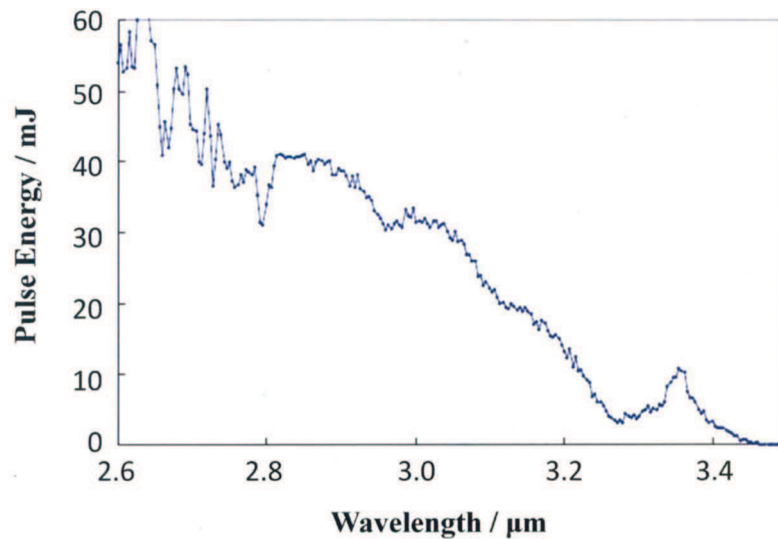


Figure 1.20. Energy of the idler beam produced by KTP/OPO as a function of wavelength. Figure used with permission from Dr. André Peremans.

wavelength is given in Figure 1.20. This places the useable range of idler wavelengths between 2.5 and 3.13 μm , corresponding to frequencies of 4000 to 3200 cm^{-1} . The stretching frequencies of O-H and N-H functional groups occur within this range, making the OPO suitable for structural determination of compounds containing these features.

1.4 Theoretical Methods

While the experimental results on their own can identify functional groups contained (or not contained) in a molecule, and may also be able to provide some further insights based on the red or blue shifting of vibrational frequencies in the IR, those results alone are not sufficient to concretely identify the structure of a molecule. Theoretical methods are often used to complement the experimental results through the determination of molecular geometry, energetics and vibrational spectra, which can be compared to the experimental results in order to characterize the molecule. Computational chemistry can also be used as a standalone method for the determination of molecular structures, if experimental methods are not available.

There are a number of different approaches or methods used in computational chemistry, combining different levels of theory with basis sets in order to describe the molecular orbitals. Certain combinations of level of theory and basis set have varying applications and degrees of accuracy based on the molecules to be examined. The level of theory used strictly throughout this work is Density Functional Theory (DFT), which is described in detail in section 1.4.1, while different basis sets are used, outlined in sections 1.4.2, and their effectiveness compared throughout the experimental chapters 2 – 5.

1.4.1 Density Functional Theory

Whereas *ab initio* methods of calculation are based upon wavefunctions, Density Functional Theory depends upon the electron density of the molecule, $\rho(r)$. This particular method, introduced by Hohenberg and Kohn [71], strikes a good balance between the level of accuracy obtained and the computational cost required, while also producing results with greater correlation to experimental data in comparison to Hartree-Fock theory. The density functional integrates the electron density across all space, returning the number of electrons [72–74]:

$$N[\rho(r)] = \int \rho(r) dr = n \quad \text{Eq 1.10}$$

The electron density is a function of three variables, x, y and z, and can be measured through X-ray diffraction. A method for determining these ground state densities, ρ_o , and ground state energies, E_o , based upon non-interacting electrons and their orbitals was developed by Kohn and Sham [75]. The energy density functional is given by:

$$E[\rho(r)] = T_s[\rho(r)] + V_{ne}[\rho(r)] + V_{ee}[\rho(r)] + \Delta T[\rho(r)] + \Delta V_{ee}[\rho(r)] \quad \text{Eq 1.11}$$

In this equation, T_s is the kinetic energy for the system of non-interacting electrons, V_{ne} is the classical potential energy related to nuclear-electron interaction, V_{ee} is the electrostatic electron-electron repulsion functional, ΔT is the correction to kinetic energy from the interacting system of electrons and ΔV_{ee} is the non-classical correction to electron-electron repulsion.

There are different classes of DFT calculations, with one of those being a hybrid method in which functionals from other methods are combined, leading to more accurate results. A hybrid DFT method is used exclusively in this work, namely the B3LYP level

of theory. In B3LYP, the Becke 3 parameter exchange functional (B3) [76,77] is combined with the Lee-Yang-Parr correlation functional (LYP) [78]. This is the most popular of the hybrid DFT methods, and leads to good accuracy in the determination of structures and energetics of molecules, and is particularly useful for small biological molecules such as those examined in this thesis. In particular, this theory takes into consideration the charge donation and backdonation in metal-ligand complexes, making it an excellent choice for the geometry optimization of these molecules. In terms of comparison to experimental IRMPD technique, the B3LYP level of theory has proven to be a reliable predictor of band position and intensity [79–92], despite the incoherent, multiphoton character of IRMPD. However, both scaling and broadening of the line spectrum is required, as anharmonic coupling between modes results in a red shift and broadening of the bands observed experimentally. These specific adjustments are noted in the experimental sections of chapters 2 – 5.

1.4.2 Basis Sets

Along with the choice of level of theory, the choice of a good basis set is also an important consideration in computational chemistry. A basis set is a linear combination of atomic orbitals used to build the molecular orbitals; the larger the basis set, the more complex the calculations become. A number of basis sets are used throughout this research, the most simple of which is the 6-31+G(d,p) basis set, alternatively written as 6-31+G**. This basis set is a split valence double-zeta basis set. In this notation, the numbers 6 and 31 are used to approximate the Gaussian function describing the atomic orbitals for the core and valence orbitals, respectively; six primitive Gaussian functions are linearly combined

to describe the core electrons while for the valence electrons, there are two basis functions, one constructed through the combination of three primitive Gaussian functions, and a second which is just a single Gaussian function [93]. The addition of (d,p) or ** to the basis set incorporates a polarization function, allowing more flexibility for the wavefunction to change its shape and for atomic orbitals to behave asymmetrically leading to more accurate geometries and vibrational frequencies. When atoms form molecules, the distribution of charge is distorted as the result of polarization. By including (d,p) in the basis set, a set of five *d* orbitals are added to atoms Li through Ca, and a set of three *p* orbitals are added to H and He atoms. Although group 2 metals, the focus of chapters 2 and 3, contain only *s*-type functions in their ground state, including higher level functions is advisable. This is because these metals are both strong σ electron donors to more electronegative atoms, while also accepting π electrons. Weaker bond strengths are predicted when *p* orbital functions are omitted, evident through longer bond lengths and larger dipole moments. Inclusion of *d* orbital functions are also critical to properly describing equilibrium geometries.

Another basis set used in this research, 6-311+G(3df,3pd), is a more expansive triple-zeta basis set where the numbers 311 indicate three basis functions are used to represent the valence shell atomic orbitals. The polarization function incorporates 3 sets of *d* orbitals and 1 set of *f* orbitals on heavier atoms, and 3 sets of *p* orbitals and 1 set of *d* orbitals on hydrogen and helium.

Both basis sets include the notation +, known as the diffuse function. The diffuse function accounts for electron density at distances far from the nuclei, making them particularly important for anionic species, ions containing lone pairs, or hydrogen bonded

species, which are contained throughout this research. The diffuse function incorporates an additional set of highly diffuse s , p_x , p_y and p_z functions to each non-hydrogen atom.

Larger atoms, particularly the Ba, Sr and Cd atoms examined in this research, are too large to be accommodated by the 6-31+G(d,p) basis set, which is applicable only for elements up to Kr. In this case, the 6-31+G(d,p) and 6-311+G(3df,3pd) basis sets are substituted on these metals for the LANL2DZ basis set (Los Alamos National Laboratories 2-Double-Zeta) [94]. In this particular basis set, the inner shell atomic orbitals are replaced by a relativistic core potential, and two basis functions are applied to the valence electrons.

A fourth basis set used is the def2-TZVPP basis set, which is applied to all metal atoms in secondary calculations and then used to compare the effectiveness and accuracy across basis sets. The def2-TZVPP basis set is shown to be more accurate than the LANL2DZ basis set for metal-amino acid cationic complexes [95,96]. This is a triple-zeta basis set which is balanced for all atoms, and includes both polarization and diffuse functions [97].

1.4.3 Collecting and Processing Data

All structure calculations were performed with Gaussian (G09) [98]. Initial guesses of multiple conformers for each complex were optimized for geometry, and the vibrational frequencies and intensities calculated, at the B3LYP level of theory using the 6-31G+(d,p) basis set, with the exception of Sr, Ba and Cd atoms, to which the LANL2DZ effective core potential is applied. Once optimized, these structures were then submitted to single point energy calculations at the 6-311+G(3df,3pd) basis set. Using the electronic energy from these single point calculations, along with the corrections to thermal (H_{corr}) and Gibbs

energy (G_{corr}) from the initial calculations, theoretical enthalpy and Gibbs energy are determined:

$$\Delta_{\text{theo}}H = E_e + H_{\text{corr}} \quad \text{Eq 1.12}$$

$$\Delta_{\text{theo}}G = E_e + G_{\text{corr}} \quad \text{Eq 1.13}$$

where the energy corrections are defined as:

$$H_{\text{corr}} = E_{\text{tot}} + k_B T \quad \text{Eq 1.14}$$

$$G_{\text{corr}} = H_{\text{corr}} - TS_{\text{tot}} \quad \text{Eq 1.15}$$

In the determination of these corrections, k_B is the Boltzmann constant and E_{tot} is the sum of translational, vibrational, rotational and electronic energies.

Once $\Delta_{\text{theo}}H$ and $\Delta_{\text{theo}}G$ are determined for a given complex, relative enthalpy ($\Delta_{\text{rel}}H$) and relative Gibbs energy ($\Delta_{\text{rel}}G$) are obtained by subtracting all values of $\Delta_{\text{theo}}H$ and $\Delta_{\text{theo}}G$ by the lowest. As all values obtained are in Hartrees, conversion to kJ mol^{-1} is accomplished by multiplying by a conversion factor of $2625.5 \text{ kJ mol}^{-1} \text{ Hartree}^{-1}$.

To determine if any dependency on basis set exists, the calculations were repeated on several the lowest energy structures determined from the first collection of calculation results. In chapters 2 – 4, geometry optimization was obtained and vibrational frequencies were calculated applying the 6-31+G(d,p) basis set to only C, H, N and O atoms, with the def2-TZVPP basis set applied to all metals. An effective core potential is also included in the def2-TZVPP basis set for Ba, Sr and Cd atoms. From the results of these calculations, single point energy calculations were then carried out using the 6-311+G(3df,3pd) on C, H, N and O atoms and def2-TZVPP once again on all metals. Relative enthalpy and Gibbs energy were obtained following the same procedure as previously described. In chapter 5, from the lowest energy conformers obtained in the first collection of calculations, only one

follow up calculation was conducted where the def2-TZVPP basis set was applied to all atoms. This one calculation was used to determine geometry, vibrational frequencies, relative enthalpy and relative Gibbs energy.

When comparing the calculated vibrational stretching frequencies to the experimental spectra obtained through IRMPD, a blue shift typically occurs due to the harmonic approximation used in the calculations, where anharmonic effects are not considered. Therefore, a scaling factor is employed which is closer to 1 in the lower energy fingerprint region where there is less of an anharmonic effect when compared to the higher energy modes, where the scaling factor is further from 1. Throughout this research, scaling factors of 0.97 and 0.96 were used in the fingerprint and O-H/N-H stretching regions, respectively. Bands in the experimental spectra are also broadened as a result of anharmonicity, and so the computed spectra are convoluted using a Lorentzian profile, which broadens the bands to 15 cm⁻¹ FWHM.

When an isomer of a complex is optimized using computational chemistry, the result is a local energy minimum. The possibility exists that a structure could be a transition state between two other conformers, which would be found at a saddle point on the potential energy surface between two isomers. A transition state can be easily detected by the presence of imaginary, or “negative,” vibrational frequencies. These transition states are then submitted to calculations once again with tighter convergence criteria in order to return a proper isomer.

1.4.4 Atoms in Molecules Theory

In the quantum theory of atoms in molecules, atoms and bonds are expressed using the electron density distribution function [99]. Topology of the electron density can allow for the location of nuclei within a molecule, as well as to define the locations of bonds. When examining a contour map reflective of the electron density, maxima will occur at the locations of the atomic nuclei. Moving away from the nuclei, electron density decays. When the first derivative of the electron density is 0 in all dimensions, a saddle point occurs. Saddle points in the electron density contour represent the bond critical points, with the bond path being defined as the trajectory running between two electron density maxima, the atoms, through the bond critical point. A sample electron density contour is given in Figure 1.21 for pyridine [100], which outlines the positions of atoms at the maxima and bond critical points at the saddle points.

The atoms in molecules topological analysis can confirm whether any interactions exist between metal ions and uracil, or intramolecular hydrogen bonds, as well as where these linkages occur. It also reveals useful information regarding these bonds through the

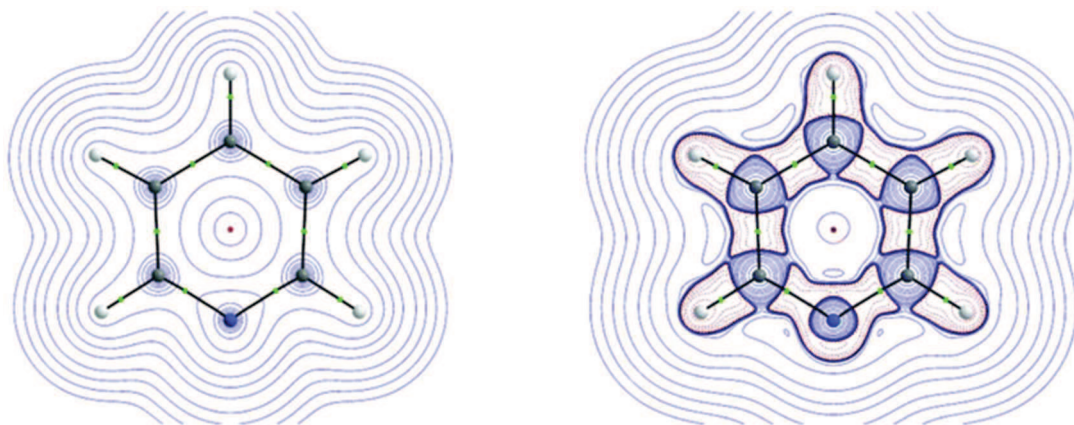


Figure 1.21. (a) Electron density contour map of pyridine, showing bond critical points denoted by green dots. (b) Contour map of the Laplacian of the electron density of pyridine, with red representing a negative Laplacian and blue a positive Laplacian. Figure adapted from Ref 100 with permission.

Laplacian of the electron density at the bond critical points, $\nabla^2\rho$, which is the scalar derivative of the gradient vector field of electron density. In instances where $\nabla^2\rho$ is positive, electronic charge is depleted, meaning that the interaction between the two atoms linked by this bond critical point is electrostatic in nature. On the other hand, if $\nabla^2\rho$ of a bond critical point is negative, then electronic charge is locally concentrated, meaning the bond is covalent in nature. The topological analysis in this thesis is conducted using the AIMAll software [101].

1.5 References

1. J.D. Watson, F.H. Crick, *Nature*, **1953**, 171, 737.
2. T.L.V. Ulbricht, *Purines Pyrimidines and Nucleotides and the Chemistry of Nucleic Acids*, Pergamon Press, New York, NY, **1964**.
3. G.M. Blackburn, M.J. Gait, *Nucleic Acids in Chemistry and Biology*, Oxford University Press Inc., New York, NY, **1996**.
4. S. Neidle, *Oxford Hand Book of Nucleic Acid Structure*, Oxford University Press Inc., New York, NY, **1999**.
5. J. Francois, S. Brenner, *Compt. Rend.*, **1963**, 256, 298.
6. S. Scheiner, C.W. Kern, *J. Am. Chem. Soc.*, **1979**, 101, 4081.
7. V. Hroudá, J. Florian, P. Hobla, *J. Phys. Chem.*, **1993**, 97, 1542.
8. J. Florian, V. Hroudá, P. Hobza, *J. Am. Chem. Soc.*, **1994**, 116, 1457.
9. J. Florian, J. Leszczynski, *J. Am. Chem. Soc.*, **1996**, 118, 3010.
10. A.J.F. Griffiths, S.R. Wessler, S.B. Carroll, J. Doebley, *Introduction to Genetic Analysis*, 10th Ed., W.H. Freeman, New York, NY, **2010**.

11. Drugs of Choice for Cancer, *Treat Guidel. Med Lett.*, **2003**, 7, 41.
12. J.K. Lee, *Int. J. Mass Spectrom.*, **2005**, 240, 261.
13. M.A. Kurinovich, J.K. Lee, *J. Am. Chem. Soc.*, **2000**, 122, 6258.
14. M.A. Kurinovich, J.K. Lee, *J. Am. Soc. Mass Spectrom.*, **2002**, 13, 985.
15. T.M. Miller, S.T. Arnold, A.A. Viggiano, A.E.S. Miller, *J. Phys. Chem. A*, **2004**, 108, 3439.
16. A.K. Chandra, M.T. Nguyen, T. Uchimaru, T. Zecgers-Huyskens, *J. Phys Chem. A*, **1999**, 103, 8853.
17. M.A. Kurinovich, L.M. Phillips, S. Sharma, J.K. Lee, *Chem. Commun.*, **2002**, 20, 2354.
18. M.T. Rodgers, P.B. Armentrout, *J. Am. Chem. Soc.*, **2000**, 122, 8548.
19. Z. Yang, M.T. Rodgers, *J. Am. Chem. Soc.*, **2004**, 126, 16217.
20. Z. Yang, M.T. Rodgers, *Int. J. Mass Spectrom.*, **2005**, 241, 225.
21. Z. Yang, M.T. Rodgers, *J. Phys. Chem. A*, **2006**, 110, 1455.
22. Y.-w. Nei, T.E. Akinyemi, C.M. Kaczan, J.D. Steill, G. Berden, J. Oomens, M.T. Rodgers, *Int. J. Mass Spectrom.*, **2011**, 308, 191.
23. C. Trujillo, A.M. Lamsabhi, O. Mó, M. Yáñez, J.-Y. Salpin, *Org. Biomol. Chem.*, **2008**, 6, 3695.
24. C. Trujillo, A.M. Lamsabhi, O. Mó, M. Yáñez, J.-Y. Salpin, *Int. J. Mass Spectrom.*, **2011**, 306, 27.
25. O.Y. Ali, N.M. Randell, T.D. Fridgen, *ChemPhysChem*, **2012**, 13, 1507.
26. A.M. Lamsabhi, M. Alcamí, O. Mó, M. Yáñez, J. Tortajada, *ChemPhysChem*, **2004**, 5, 1871.
27. A.M. Lamsabhi, M. Alcamí, O. Mó, M. Yáñez, *ChemPhysChem*, **2003**, 4, 1011.

28. A.M. Lamsabhi, M. Alcamí, O. Mó, M. Yáñez, J. Tortajada, *J. Phys. Chem. A*, **2006**, *110*, 1943.
29. O. Brea, M. Yáñez, O. Mó, A.M. Lamsabhi, *Org. Biomol. Chem.*, **2013**, *11*, 3862.
30. O. Brea, M. Yáñez, O. Mó, *ChemPhysChem*, **2015**, *16*, 2375.
31. J.-Y. Salpin, S. Guillaumont, J. Tortajada, A.M. Lamsabhi, *J. Am. Soc. Mass Spectrom.*, **2009**, *20*, 359.
32. A.A. Power, O.Y. Ali, M.B. Burt, T.D. Fridgen, *Int. J. Mass Spectrom.*, **2012**, 330-332, 233.
33. O.Y. Ali, T.D. Fridgen, *ChemPhysChem*, **2012**, *13*, 588.
34. O.Y. Ali, T.D. Fridgen, *Int. J. Mass Spectrom.*, **2011**, *308*, 167.
35. E.A.L. Gillis, M. Demireva, K. Nanda, G.J.O. Beran, E. Williams, T.D. Fridgen, *Phys. Chem. Chem. Phys.*, **2012**, *14*, 3304.
36. E.A.L. Gillis, K. Rajabi, T.D. Fridgen, *J. Phys. Chem. A*, **2009**, *113*, 824.
37. J.V. Burda, J. Šponer, J. Leszczynski, P. Hobza, *J. Phys. Chem. B*, **1997**, *101*, 9670.
38. M.A.S. Prado, E. Garcia, J.B.L. Martins, *Chem. Phys. Lett.*, **2006**, *418*, 264.
39. J. Šponer, J.V. Burda, M. Sabat, J. Leszczynski, P. Hobza, *J. Phys. Chem. A*, **1998**, *102*, 5951.
40. M. Meot-Ner, *J. Am. Chem. Soc.*, **1979**, *101*, 2396.
41. F. Greco, A. Liguori, G. Sindona, N. Uccella, *J. Am. Chem. Soc.*, **1990**, *112*, 9092.
42. M.T. Nguyen, A.K. Chandra, T. Zeegers-Huyskens, *J. Chem. Soc. Faraday Trans.*, **1998**, *94*, 1277.
43. K.B. Green-Church, P.A. Limbach, *J. Am. Soc. Mass Spectrom.*, **2000**, *11*, 24.
44. P.O. Lowdin, *Rev. Mod. Phys.*, **1963**, *35*, 724.

45. Y. Tsuchiya, T. Tamura, M. Fujii, M. Ito, *J. Phys. Chem.*, **1988**, 92, 1760.
46. M.J. Scanlan, I.H. Hillier, *J. Am. Chem. Soc.*, **1984**, 106, 3737.
47. B.A. Cerda, C. Wesdemiotis, *J. Am. Chem. Soc.*, **1996**, 118, 11884.
48. A.G. Marshall, C.L. Hendrickson, G.S. Jackson, *Mass Spectrom. Rev.*, **1998**, 17, 1.
49. M.B. Comisarow, A.G. Marshall, *Chem. Phys. Lett.*, **1974**, 15, 282.
50. A.G. Marshall, P.B. Grosshans, *Anal. Chem.*, **1991**, 63, 215A.
51. A.G. Marshall, C.L. Hendrickson, *Int. J. Mass Spectrom.*, **2002**, 215, 59.
52. R.D. Smith, J.A. Loo, C.G. Edmonds, C.J. Barinaga, H.R. Udseth, *Anal. Chem.*, **1990**, 62, 882.
53. P. Kebarle, L. Tang, *Anal. Chem.*, **1993**, 65, 972.
54. M.W. Senko, C.L. Hendrickson, L. Paša-Tolić, J.A. Marto, F.M. White, S. Guan, A.G. Marshall, *Rapid Commun. Mass Spectrom.*, **1996**, 10, 1824.
55. J.A. Loo, *Mass Spectrom. Rev.*, **1997**, 16, 1.
56. S.J. Gaskell, *J. Mass Spectrom.*, **1997**, 32, 677.
57. R.B. Cole, *J. Mass Spectrom.*, **2000**, 35, 763.
58. K.A. Herrmann, A. Somogyi, V.H. Wysocki, L. Drahos, K. Vekey, *Anal. Chem.*, **2005**, 77, 7626.
59. T.D. Fridgen, *Mass Spectrom. Rev.*, **2009**, 28, 586.
60. N.C. Polfer, J. Oomens, *Mass Spectrom. Rev.*, **2009**, 28, 468.
61. N.C. Polfer, *Chem. Soc. Rev.*, **2011**, 40, 2211.
62. J.R. Eyler, *Mass Spectrom. Rev.*, **2009**, 28, 448.

63. Y. Jami-Alahmadi, T.D. Fridgen, *Phys. Chem. Chem. Phys.*, **2016**, *18*, 2023.
64. J.M. Ortega, J.M. Berset, R. Chaput, F. Glotin, G. Humbert, D. Jaroszynski, P. Joly, B. Kergosien, J. Lesrel, *Nucl. Instrum. Methods Phys. Res., Sect. A*, **1996**, *375*, 618.
65. K. Kato, *IEEE J. Quantum Electron.*, **1991**, *27*, 1137.
66. S.T. Yang, R.C. Eckardt, R.L. Byer, *Opt. Lett.*, **1993**, *18*, 971.
67. L. MacAleese, P. Maître, *Mass Spectrom. Rev.*, **2007**, *26*, 583.
68. K.D. Henry, E.R. Williams, B.H. Wang, F.W. McLafferty, J. Shabanowitz, D.F. Hunt, *Proc. Natl. Acad. Sci. USA*, **1989**, *86*, 9075.
69. H. Mehdian, S. Jafari, A. Hasanbeigi, F. Ebrahimi, *Nucl. Instrum. Methods Phys. Res., Sect. A*, **2009**, *604*, 471.
70. J.A. Armstrong, N. Bloembergen, J. Ducuing, P.S. Pershan, *Phys. Rev.*, **1962**, *127*, 1918.
71. P. Hohenberg, W. Kohn, *Phys. Rev.*, **1964**, *136*, 864.
72. Y. Sahni, *Quantal Density Functional Theory*, Springer, Berlin, Germany, **2004**.
73. E.K.U. Gross, R.M. Dreizler, *Density Functional Theory*, Plenum Press, New York, NY, **1995**.
74. M.C. Holthausen, W. Koch, *A Chemist's Guide to Density Functional Theory*, 2nd ed., Wiley-VCH, Weinheim, Germany, **2001**.
75. W. Kohn, L.J. Sham, *Phys. Rev.*, **1965**, *140*, 1133.
76. A.D. Becke, *J. Chem. Phys.*, **1993**, *98*, 5648.
77. A.D. Becke, *J. Chem. Phys.*, **1996**, *104*, 1040.
78. C. Lee, W. Yang, R.G. Parr, *Phys. Rev. B*, **1988**, *37*, 785.
79. M. Okumura, L.I. Yeh, Y.T. Lee, *J. Chem. Phys.*, **1985**, *83*, 3705.

80. J. Lemaire, P. Boissel, M. Heninger, G. Mauclaire, G. Bellec, H. Mestdagh, A. Simon, S. Le Caer, J.M. Ortega, F. Glotin, P. Maître, *Phys. Rev. Lett.*, **2002**, 89, 273002.
81. M.F. Bush, J. Oomens, E.R. Williams, *J. Phys. Chem. A*, **2009**, 113, 431.
82. A.L. Heaton, V.N. Bowman, J. Oomens, J.D. Steill, P.B. Armentrout, *J. Phys. Chem. A*, **2009**, 113, 5519.
83. R.M. Moision, P.B. Armentrout, *J. Phys. Chem. A*, **2002**, 106, 10350.
84. R.M. Moision, P.B. Armentrout, *Phys. Chem. Chem. Phys.*, **2004**, 6, 2588.
85. J.T. O'Brien, J.S. Prell, J.D. Steill, J. Oomens, E.R. Williams, *J. Am. Chem. Soc.*, **2009**, 131, 3905.
86. M.T. Rodgers, P.B. Armentrout, *Int. J. Mass Spectrom.*, **2007**, 267, 167.
87. C.W. Bauschlicher, S.R. Langhoff, *Spectrochimica Acta A*, **1997**, 53, 1225.
88. S. Hoyau, K. Norrman, T.B. McMahon, G. Ohanessian, *J. Am. Chem. Soc.*, **1999**, 121, 8875.
89. P. Maître, S. Le Caer, A. Simon, W. Jones, J. Lemaire, H.N. Mestdagh, M. Heninger, G. Mauclaire, P. Boisset, R. Prazeres, F. Glotin, J.M. Ortega, *Nucl. Instrum. Methods. Phys. Res. Sect. A*, **2003**, 507, 541.
90. N.C. Polfer, B. Paizs, L.C. Snoek, I. Compagnon, S. Suhai, G. Meijer, G. von Heiden, J. Oomens, *J. Am. Chem. Soc.*, **2005**, 127, 8571.
91. N.C. Polfer, J. Oomens, D.T. Moore, G. von Heiden, G. Meijer, R.C. Dunbar, *J. Am. Chem. Soc.*, **2006**, 128, 517.
92. J.A. Stearns, O.V. Boyarkin, T.R. Rizzo, *J. Am. Chem. Soc.*, **2007**, 129, 13821.
93. N.I. Levine, *Quantum Chemistry*, 5th ed., Prentice Hall, Englewood Cliffs, NJ, **2000**.
94. W.R. Wadt, J.H. Hay, *J. Chem. Phys.*, **1985**, 82, 284.
95. P.B. Armentrout, M. Citir, Y. Chen, M.T. Rodgers, *J. Phys. Chem. A*, **2012**, 116, 11823.

96. P.B. Armentrout, Y. Chen, M.T. Rodgers, *J. Phys. Chem. A*, **2012**, *116*, 3989.
97. F. Weigend, R. Ahlrichs, *Phys. Chem. Chem. Phys.*, **2005**, *7*, 3297.
98. M.J. Frisch, G.W. Trucks, H.B. Schlegel, G.E. Scuseria, M.A. Robb, J.R. Cheeseman, G. Scalmani, V. Barone, B. Mennucci, G.A. Petersson, H. Nakatsuji, M. Caricato, X. Li, H.P. Hratchian, A.F. Izmaylov, J. Bloino, G. Zheng, J.L. Sonnenberg, M. Hada, M. Ehara, K. Toyota, R. Fukuda, J. Hasegawa, M. Ishida, T. Nakajima, Y. Honda, O. Kitao, H. Nakai, T. Vreven, J.A. Montgomery, J.E. Peralta J., F. Ogliaro, M. Bearpark, J.J. Heyd, E. Brothers, K.N. Kudin, V.N. Staroverov, T. Keith, R. Kobayashi, J. Normand, K. Raghavachari, A. Rendell, J.C. Burant, S.S. Iyengar, J. Tomasi, M. Cossi, N. Rega, J.M. Millam, M. Klene, J.E. Knox, J.B. Cross, V. Bakken, C. Adamo, J. Jaramillo, R. Gomperts, R.E. Stratmann, O. Yazyev, A.J. Austin, R. Cammi, C. Pomelli, J.W. Ochterski, R.L. Martin, K. Morokuma, V.G. Zakrzewski, G.A. Voth, P. Salvador, J.J. Dannenberg, S. Dapprich, A.D. Daniels, O. Farkas, J.B. Foresman, J.V. Ortiz, J. Cioslowski, D.J. Fox, *Gaussian 09*, Revision D.01, Gaussian Inc., Wallingford, CT, **2013**.
99. R.F.W. Bader, *Atoms in Molecules: A Quantum Theory*, Clarendon Press, Oxford University Press, New York, NY, **1990**.
100. H.-G. Stammler, Y.V. Vishnevskiy, C. Sicking, N.W. Mitzel, *CrystEngComm*, **2013**, *15*, 3536.
101. T.A. Keith, *AIMAll*, Version 14.10.27, TK Gristmill Software, Overland Park, KS, **2014**, aim.tkgristmill.com.

CHAPTER 2 – Structures of Bare and Singly Hydrated $[M(\text{Ura-H})(\text{Ura})]^+$ ($M = \text{Mg}, \text{Ca}, \text{Sr}, \text{Ba}$) Complexes in the Gas Phase by IRMPD Spectroscopy in the Fingerprint Region

The structures of deprotonated group 2 metal dication bound uracil dimers as well as the singly hydrated dimers were explored in the gas phase using infrared multiple photon dissociation (IRMPD) spectroscopy ($1000 - 1900 \text{ cm}^{-1}$) in a Fourier transform ion cyclotron resonance mass spectrometer (FTICR-MS). The IRMPD spectra were then compared to computed IR spectra for various isomers. Calculations were performed using B3LYP with the 6-31+G(d,p) basis set for all atoms except Ba^{2+} and Sr^{2+} , for which the LANL2DZ or the def2-TZVPP basis sets with relativistic core potentials were used. The lowest energy structures are those in which the one uracil is deprotonated at the N3 position while the neutral uracil is a tautomer where the N3 hydrogen is at the O4 or O2 carbonyl oxygen and the metal is tetracoordinate interacting with N3 and O4 of deprotonated uracil and either N3 and O2 or N3 and O4 of neutral uracil. In the solvated complexes, the water molecule is also coordinated to the metal ion.

A version of this chapter has been published:

B. Power, V. Haldys, J.-Y. Salpin and T.D. Fridgen, *Int. J. Mass Spectrom.*, **2015**, 378, 328.

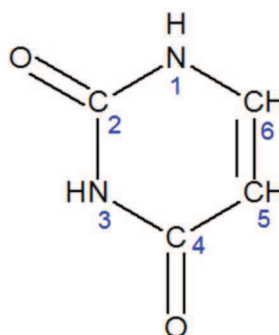
2.1 Introduction

Metal cations are known to play a central role in many biological systems. In particular, divalent cations have been shown to be crucial in the stability and activity of nucleic acids, as well as the folding of RNA structures [1–4]. These ions provide their stabilizing effect to the structure of DNA [5,6] and RNA [1], through both charge neutralization and noncovalent interactions with the phosphate backbone of the nucleic acids. Even in trace amounts, the interaction of metal cations with nucleic acids has a vital role in setting the course for the functionality of various biological molecules [7,8], however, striking a balance is critical. Even though these metal ions play essential roles, the influence they hold over the behaviour of nucleic acids can often be detrimental. Unwanted conformational changes can result from an excess of metal dications, and through interaction of the ions with nucleobases themselves [2,6,9–13]. In particular, if nucleobases deviate from their canonical tautomer, improper base pairings and mutations are likely to result [14–17]. The interaction of metal ions with nucleobases has been the subject of many studies through a variety of techniques [18–32]. A major obstacle is the difficulty to replicate a cellular environment in condensed phase analysis. Rather, gas phase conditions are desired to allow for direct structural examination without the hindrance of bulk solvents, which may otherwise alter the complex structure. To accomplish this, action or consequence spectroscopy has been employed recently. In particular, infrared multiple photon dissociation (IRMPD) is a technique that has been successfully applied in many of these studies, and is the method of choice for this research.

The conventional numbering scheme for uracil is presented in Scheme 2.1. The most stable form of neutral uracil is the canonical, 2–4 diketo tautomer, in both the solid

and gas phases [33–51]. However, metal ions have the ability to stabilize the keto-enol tautomer. Even though alkaline earth dications do not have as strong an affinity towards nucleobases as transition metal dications [52], similar effects are observed. Trujillo and coworkers determined that in $[\text{Ca}(\text{Ura})]^{2+}$, uracil tautomerizes to the 4-enol form, and the calcium ion bridges the O2 and dehydrogenated N3 atoms [53]. While such complexes having the form $[\text{M}(\text{Ura})]^{2+}$ are stable in the case of alkaline-earth metals like Ca, the Pb^{2+} ion or transition metal dications such as Ni^{2+} and Cu^{2+} , will lead to deprotonation of the uracil moiety. For example, the lead(II)–uracil complex, $[\text{Pb}(\text{Ura-H})]^+$, shows a preference towards the canonical, 2,4-diketo conformation of uracil [18] but it is deprotonated at N3. Although the monomeric complexes formed may differ based upon the interaction between the ion and uracil (electrostatic vs. covalent), the dimeric complexes $[\text{M}(\text{Ura-H})(\text{Ura})]^+$ all behave similarly in the fact that one uracil is deprotonated, and the other remains neutral. The $[\text{M}(\text{Ura})_2]^{2+}$ complex is generally not observed in the gas phase.

Previous works have determined that in these dimeric complexes the dication is tetracoordinate regardless of whether it is a transition metal [22,27] or alkaline earth metal [31]. The neutral uracil in the lowest energy complex is an enol, which participates in a hydrogen bond with a carbonyl of the neighbouring deprotonated uracil. Although good



Scheme 2.1. Numbering scheme for uracil.

agreement was obtained between the computed lowest energy structures and the experimental spectra in each case, spectroscopically the exact placement of metal ion coordination could not be determined. In the N-H/O-H stretching region which was used to examine these complexes, no distinction could be made between those where the neutral uracil was the O2 or O4 enol resulting in the metal binding to N3 and O4 or N3 and O2, respectively. Even though the general structures of these dimeric complexes are expected to be similar for all dications, the pathway of fragmentation differs. Within the alkaline earth group, Ba^{2+} and Sr^{2+} complexes fragment by loss of uracil, while Ca^{2+} and Mg^{2+} complexes lose an HNCO unit upon IRMPD or CID activation [30].

The current work aims to provide further insight into the previously examined [31] alkaline earth metal dimeric complexes, $[\text{M}(\text{Ura-H})(\text{Ura})]^+$, using IRMPD spectroscopy in the mid-infrared region, $1000 - 1900 \text{ cm}^{-1}$. In this fingerprint region, carbonyl stretching frequencies are obtained and distinguishing features between the N3O4 and N3O2 coordinated complexes are exposed. Along with the bare dimeric complexes, $[\text{M}(\text{Ura-H})(\text{Ura})]^+$, we also probe the singly hydrated complexes, $[\text{M}(\text{Ura-H})(\text{Ura})(\text{H}_2\text{O})]^+$. The experimental spectra are compared to those computed using electronic structure calculations. A comparison of spectra and energies computed through different methods is also offered.

2.2 Methods

2.2.1 Experimental

All experiments were performed using a Fourier-transform ion cyclotron resonance mass spectrometer (FT-ICR-MS) coupled to a mid-infrared free electron laser (FEL) at the

Centre Laser Infrarouge d'Orsay (CLIO) [54,55]. 0.01 M solutions of the chloride salts of each of the metal ions were prepared in 18 MΩ water (Millipore). Uracil solutions were prepared to 1mM in 18MΩ water (Millipore). Mixtures were then prepared in a 1 to 10 ratio of metal solution to uracil solution, and introduced via syringe injection to the electrospray ion source at a flow rate of 75 μL h⁻¹. The ions were mass selected with a quadrupole mass filter and irradiated with the free electron laser following introduction and isolation into the ICR cell. Hydrated ions were prepared by first mass selecting the bare [M(Ura)(Ura-H)]⁺ ion in the quadrupole filter and storing them in the hexapole storage cell into which water vapour had been leaked [56]. Irradiation times varied from 0.1 to 3 s, with the more weakly bound and, therefore, faster dissociating hydrated ions being irradiated for the shortest time. Certain areas of the IRMPD spectra which were saturated were scanned after attenuation of the FEL. The laser was scanned at 5 cm⁻¹ intervals from ~1000 to 1900 cm⁻¹. The IRMPD efficiency is the negative of the natural logarithm of parent ion intensity divided by the sum of parent and fragment ion signals.

2.2.2 Computational

Calculations for all structures were conducted using the Gaussian 09 suite of programs [57]. Each structure was optimized and infrared spectra computed using B3LYP density functional theory. In the cases of [M(Ura-H)(Ura)]⁺ and [M(Ura-H)(Ura)(H₂O)]⁺, where M = Ca²⁺ or Mg²⁺, the 6-31+G(d,p) basis set was used for all atoms. For the [M(Ura-H)(Ura)]⁺ and [M(Ura-H)(Ura)(H₂O)]⁺ complexes, where M = Ba²⁺ and Sr²⁺, the LANL2DZ basis set with relativistic core potential was used for strontium and barium atoms and the 6-31+G(d,p) basis was used for all other atoms. Single point energy

calculations were then carried out using B3LYP with the 6-311+G(3df,3pd) basis set on all atoms except Sr and Ba for which the LANL2DZ basis set with relativistic core potential was used. This computational method will be referred to as method 1.

All calculations were then repeated, for the five lowest energy structures, with the def2-TZVPP basis set which has been found to work better for metal-cation amino acid complexes than the LANL2DZ [58,59] for all metals during both the optimization and single point energy calculations. The def2-TZVPP basis set contains polarization functions, which are not included in the LANL2DZ basis set. The 6-31+G(d,p) basis set was again used for all other atoms (C, H, N and O) during optimization, followed by the 6-311+G(3df,3pd) basis set for single point energy calculations. This computational method will be referred to as method 2.

These single-point electronic energies, using methods 1 and 2 were used to compute the enthalpies and Gibbs energies of isomeric species at 298 K, using the unscaled harmonic vibrational frequencies calculated at the optimized geometry.

The bonding within the individual equilibrium structures was also analyzed by locating the bond critical points (BCPs) using atoms-in-molecules (AIM) theory [60], which is based on a topological analysis of the electronic density at the BCPs, and is a good descriptor of the bond strength or weakness. This analysis was conducted using optimized structures from method 2. Data from the topological analysis are given collectively in Appendix A as Figure A26.

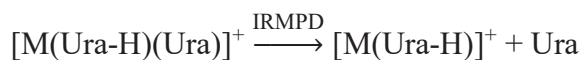
For comparison with the experimental spectra, the computed infrared spectra were all scaled by a factor of 0.97 and convoluted with a Lorentzian profile with a width (FWHM) of 15 cm^{-1} .

2.3 Results and Discussion

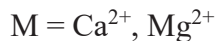
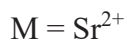
2.3.1 Examination of the IRMPD Spectra

When complexes were irradiated with the FEL, the following dissociation pathways were observed:

All M except Mg



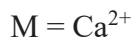
Following the loss of neutral Ura:



All M



Following the loss of H_2O :



The observed dissociation pathways are in agreement with previous studies which determined the fragmentation for Ba^{2+} and Sr^{2+} uracil dimers occurs initially through loss of uracil, whereas Ca^{2+} and Mg^{2+} dimers undergo more complicated fragmentation beginning with the loss of HNCO [30].

Figure 2.1A shows the IRMPD spectra for $[M(\text{Ura-H})(\text{Ura})]^+$ in the 1000 – 1900 cm^{-1} region. All $[M(\text{Ura-H})(\text{Ura})]^+$ spectra display an intense band centred between 1614 and 1627 cm^{-1} , in the C=O stretching region of carbonyl groups. This band is red-shifted in comparison to the free carbonyl stretch of uracil, centred about 1750 cm^{-1} in the gas phase [61], presumably due to hydrogen bonding and carbonyls that are ligated to the metal cation which have the effect of lengthening and weakening the carbonyl bond. This band is even red-shifted in comparison with sodiated uracil, where the stretch is observed to be between 1630 and 1675 cm^{-1} [28]. The dicationic nature of the metal ions leads to further weakening of the metal coordinated C=O bond compared to sodium, results in a lower stretching frequency. Complexes of Ba^{2+} , Sr^{2+} , Ca^{2+} and Mg^{2+} each exhibit a second band centred between 1530 – 1548 cm^{-1} , attributed to the enolic C–OH stretch expected in these dimers (*vide infra*).

Along with some weak features at lower energy, the $[M(\text{Ura-H})(\text{Ura})(\text{H}_2\text{O})]^+$ spectra (Figure 2.1B) also contain two prominent carbonyl stretching bands. The most intense band is significantly blue-shifted by between 10 and 30 cm^{-1} compared to the same band for bare $[M(\text{Ura-H})(\text{Ura})]^+$. The enol C–OH stretching bands are also blue-shifted by about 10–20 cm^{-1} upon hydration. These blue-shifts observed upon hydration are most likely the result of water binding to the metal and donation of electron density back to the remainder of the complex, particularly the carbonyl bonds; an inductive effect that results in a mild strengthening of the C=O bond.

Another interesting observation is that as the metal gets lighter over the Ba, Sr, and Ca series, the intense carbonyl stretching bands shift slightly from 1621 to 1617 to 1612 cm^{-1} , but for Mg, the band is observed at 1629 cm^{-1} . A similar pattern of shifting in position

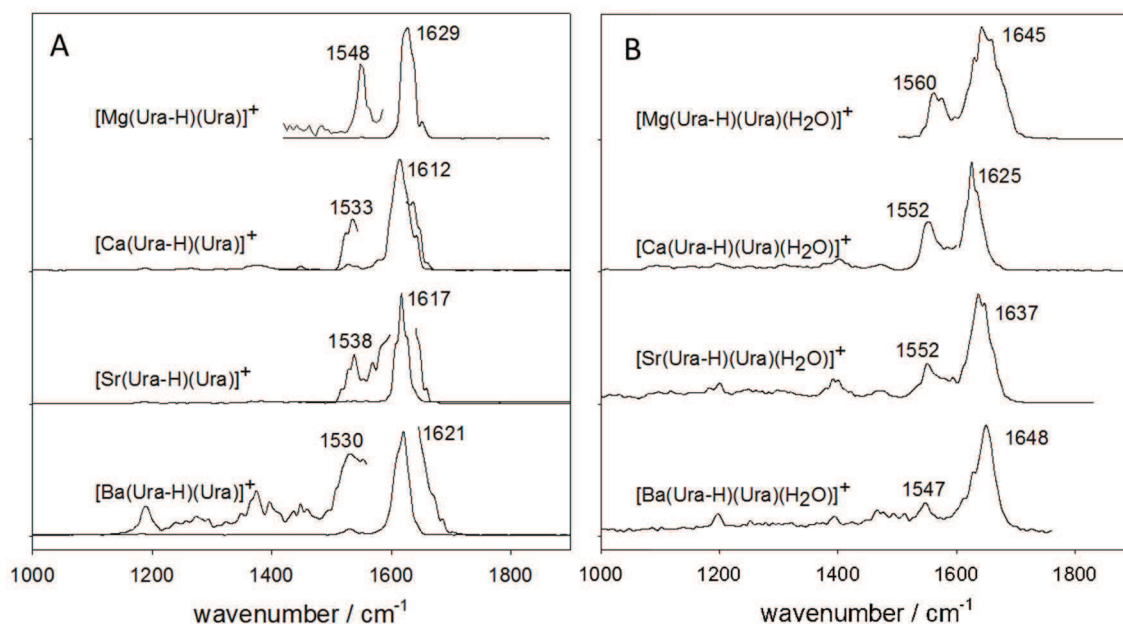


Figure 2.1. Comparison of IRMPD spectra for $[M(\text{Ura-H})(\text{Ura})]^+$ and $[M(\text{Ura-H})(\text{Ura})(\text{H}_2\text{O})]^+$ complexes, $M = \text{Ba}, \text{Sr}, \text{Ca}, \text{Mg}$, in the $1000 - 1900 \text{ cm}^{-1}$ region.

of that band for the hydrated complexes are observed although more pronounced – 1648 , 1637 , 1625 cm^{-1} for the hydrated Ba, Sr, and Ca complexes, but 1645 cm^{-1} for the Mg complex. While the shifts for Ba, Sr, and Ca can be rationalized as being due to stronger metal-uracil binding for the smaller, more densely charged ions, we are unsure of why the bands in the Mg complexes are blue-shifted relative to the other C=O stretching bands.

2.3.2 Computed Structures for $[M(\text{Ura-H})(\text{Ura})]^+$

A total of 26 isomers were found for the Ba^{2+} and Ca^{2+} complexes, and 25 isomers were obtained for Sr^{2+} and Mg^{2+} . In Figure 2.2, the geometries and energetics for the three lowest energy structures are presented. In Figures A1 to A4 (Appendix A), all structures and energies are presented for the Method 1 calculations and in Table A1 (Appendix A), the energetics of five lowest energy structures are compared. The N3O4/N3O2(O4–O2)

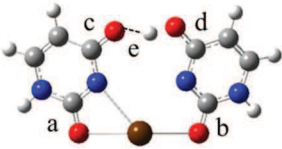
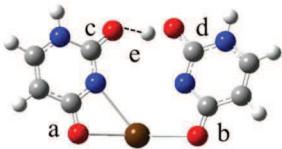
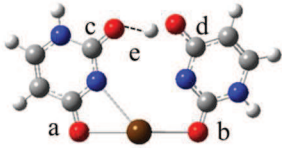
iii		M	$\Delta_{\text{rel}}H/\Delta_{\text{rel}}G$	a	b	c	d	e
		Ba	4.1/4.1	1.270	1.260	1.255	1.291	1.444
		Sr	4.1/4.1	1.272	1.262	1.254	1.287	1.424
		Ca	4.7/5.3	1.275	1.266	1.254	1.285	1.412
		Mg	9.3/9.1	1.279	1.272	1.253	1.283	1.420
ii		M	$\Delta_{\text{rel}}H/\Delta_{\text{rel}}G$	a	b	c	d	e
		Ba	4.7/4.8	1.272	1.263	1.258	1.291	1.406
		Sr	3.8/3.9	1.273	1.264	1.257	1.288	1.392
		Ca	2.6/2.3	1.276	1.268	1.256	1.285	1.380
		Mg	0/0	1.281	1.274	1.255	1.283	1.388
i		M	$\Delta_{\text{rel}}H/\Delta_{\text{rel}}G$	a	b	c	d	e
		Ba	0/0	1.274	1.259	1.252	1.295	1.493
		Sr	0/0	1.276	1.261	1.251	1.292	1.478
		Ca	0/0	1.279	1.264	1.250	1.290	1.473
		Mg	0.8/0.6	1.283	1.270	1.248	1.288	1.487

Figure 2.2. Comparison of the energies and structures for the three lowest energy $[M(\text{Ura-H})(\text{Ura})]^+$ complexes, $M = \text{Ba}, \text{Sr}, \text{Ca}, \text{Mg}$. The thermochemistry reported here are those from method 2.

structure is the lowest energy structure in the case of the Ba^{2+} , Sr^{2+} and Ca^{2+} complexes and is second by a negligible amount for Mg^{2+} . This is in agreement with previous results for Sr^{2+} and Ba^{2+} [31], and is consistent with results previously obtained for other dications, notably Pb^{2+} [22] and Cu^{2+} [27]. In this structure, one uracil is deprotonated at N3, with metal coordination to N3 and O4. The neutral uracil is a tautomer where hydrogen has been transferred from N3 to O4, and the metal is coordinated to N3 and O2. Tetradentate interactions are confirmed by the Bader topological analysis, since four bond critical points (BCPs) connecting the metal to the two uracil units, are systematically found. Furthermore, positive values of the Laplacian of the electron density $\nabla^2\rho$ indicates the electrostatic nature of these interactions (Appendix A Figure A26). An intramolecular hydrogen bond is found

between O4H of the neutral uracil and O2 of the deprotonated uracil, and is fairly strong, predicted to be only ~ 1.48 Å for all metals. This hydrogen bonding is confirmed by the topological analysis (low electron density, positive $\nabla^2\rho$). The enolic C–OH bond length is significantly longer, ~ 1.29 Å, than the other carbonyl bonds, all ~ 1.2 Å or less. The hydrogen bond established also induces a slight decrease in the electron density of the C2=O2 BCP. The weakening of the carbonyl groups interacting with the metallic centre is also evidenced by the topological analysis. Concerning the deprotonated uracil moiety, a decrease of $0.022\text{--}0.026$ e Å⁻³ of the electron density at the C4=O4 BCP is observed with respect to deprotonated uracil (dU, Figure A26). The effect is even more pronounced ($0.034\text{--}0.040$ e Å⁻³) for the C2=O2 carbonyl group with the neutral U2 tautomer, where proton transfer has occurred from N3 to O4 (the carbonyl denoted C2'=O2' in Figure A26 for the sake of clarity). Furthermore, as would be expected, the two metal coordinated carbonyl bond lengths decrease slightly with increasing metal size due to decreasing metal-carbonyl bond strengths. The electron densities at the BCPs vary accordingly. This decrease in the electron density is also consistent with the red-shifts observed experimentally and described in the previous section (*vide supra*). The M–N and M–O bond lengths obviously increase as the metal cation size increases. Also, the M–N bond lengths and M–O bond lengths are between 0.11 and 0.21 Å and between 0.02 and 0.06 Å, respectively, shorter for the deprotonated uracil compared to neutral uracil. All these trends are confirmed by the electron densities calculated at the corresponding BCPs.

These structural deviations away from the neutral, diketo tautomer as a result of the presence of the metal ion can have biological impacts through the disruption of hydrogen

bonding between base pairs [62–64]. Both the deprotonation as well as the keto-enol proton transfer change the hydrogen bonding environment and may have a negative effect on the structural integrity of the nucleic acid strand, specifically RNA in the case of uracil.

Two additional structures in Figure 2.2 found to be slightly higher in energy are labelled as N3O4/N3O4(O2–O2) and N3O2/N3O2(O4–O4). In the N3O4/N3O4(O2–O2) structure, the metal is coordinated to the N3 and O4 of the uracil where the proton has been transferred to O2, and an intermolecular hydrogen bond is formed between O2H of uracil, and O2 of deprotonated uracil. This structure increases in computed relative energy compared to N3O4/N3O2(O4–O2) as the metal cation increases in size. The third structure, N3O2/N3O2(O4–O4) instead has metal coordination to N3 and O2 of both uracils, proton transfer from N3 to O4, and an intermolecular hydrogen bond between O4H and the O4 of deprotonated uracil. The N3O4/N3O4(O2–O2) isomer is slightly lower in energy when compared to N3O2/N3O2(O4–O4) when bound by a Sr^{2+} or Ca^{2+} ion. However, this order is reversed when Ba^{2+} is the metal centre. For the complexes of Ba and Sr, these two isomers are within 1 kJ mol^{-1} of each other in terms of both enthalpy and Gibbs energy based upon the second calculation method. All other structures were determined to be significantly higher in energy by both methods of calculation by a minimum of about 15 kJ mol^{-1} in Gibbs energy.

All lowest energy structures are planar with method 1, but with method 2 the lowest energy Ba^{2+} and Sr^{2+} structures are slightly out of plane.

As a comparison, the three lowest energy isomers for the $[\text{Ca}(\text{Ura-H})(\text{Ura})]^+$ complex were re-optimized, with def2-TZVPP basis set on all atoms. These results are also

summarized in Table A1 (Appendix A), and minimal deviation was noted between these and the results of method 2.

2.3.2.1 Comparison of Computed and Experimental Spectra

A comparison between the experimental spectra and the three lowest energy structures computed via method 2 are given in Figure 2.3 for the $[M(\text{Ura-H})(\text{Ura})]^+$ ions. The five lowest energy structures, based on both calculation methods, are compared to the experimental spectra for all ions in Figures A5 to A12 (Appendix A). For $[\text{Ba}(\text{Ura-}$

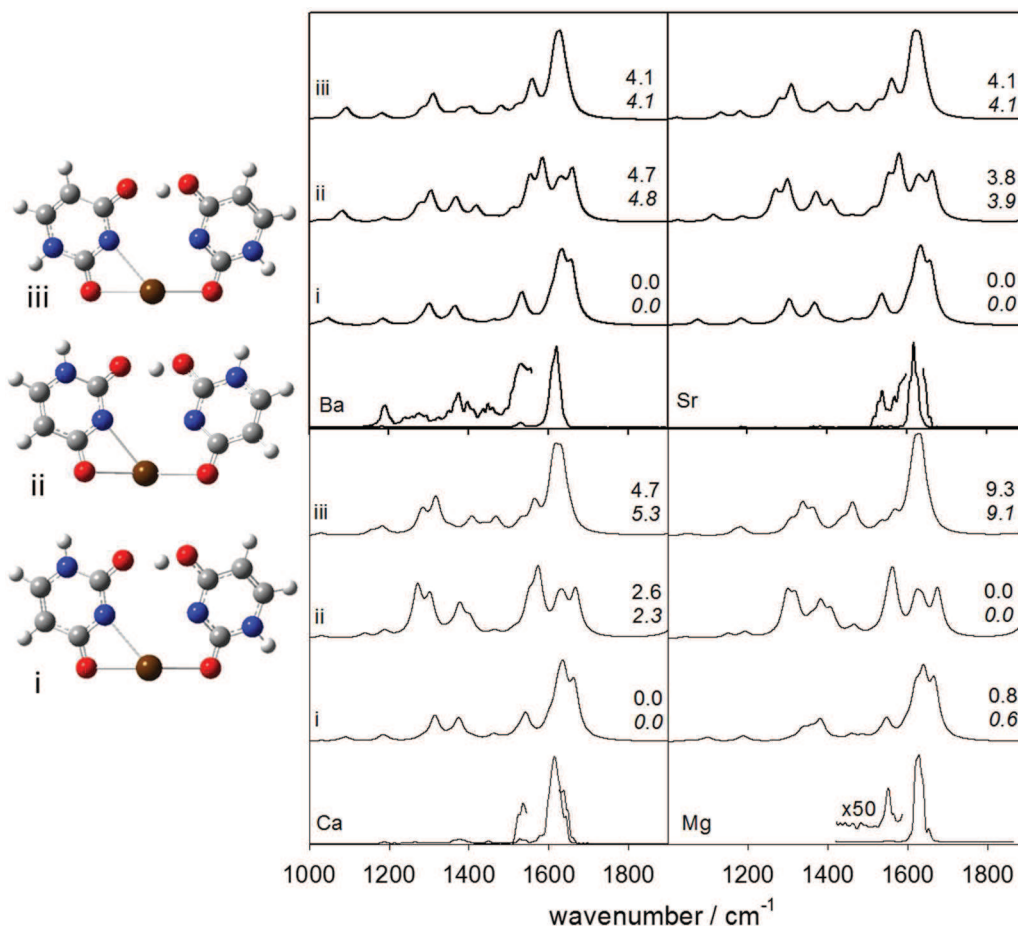


Figure 2.3. Experimental IRMPD spectrum (bottom) for $[\text{M}(\text{Ura-H})(\text{Ura})]^+$ compared with the B3LYP computed spectra using computational method 2 for the three lowest energy structures. Lowest energy structures represent the (i) N3O4/N3O2(O4–O2), (ii) N3O4/N3O4(O2–O2) and (iii) N3O2/N3O2(O4–O4) tautomers. The calculated relative enthalpies and 298 K Gibbs energies (italics) are also shown.

H)(Ura)]⁺ (Figure 2.3), there is good agreement between the experimental spectrum and those computed for structures i and iii. The major band of the experimental spectrum with a maximum at 1620 cm⁻¹ is expected to be composed of four modes corresponding mainly to the stretching of the three C=O bonds and the C=C bonds. Complexes of Ba²⁺, Sr²⁺, Ca²⁺ and Mg²⁺ each exhibit a second less intense band centred between 1530 – 1548 cm⁻¹, which according to the comparison with calculations, can be attributed to the enolic C4–O4H stretch expected in these dimers. In protonated uracil, the C4–O4 stretch was computed at 1487 cm⁻¹ and could account for an experimental signal observed at 1469 cm⁻¹ [65]. Consequently, if we strictly compare the same bond, one observes a blue-shift with respect to protonated uracil. This blue-shift is in agreement with the AIM analysis, the electron density at the C4–O4 bond BCP for protonated uracil being 0.330 e Å⁻³ while it ranges from 0.341 to 0.346 e Å⁻³ for the N3O4/N3O2(O4–O2) structures. The C4–O4H bond is therefore reinforced in the complexes. This blue-shift is even more pronounced with respect to the neutral form of uracil involved in the complexes (tautomeric form U2).

There are no distinguishing features with which we can experimentally differentiate between these two lowest energy structures as was the case in 3200 – 3800 cm⁻¹ region. It was not possible, in the 3200 – 3800 cm⁻¹ region, to rule out the BaN3O4/N3O4(O2–O2) structure based on comparing the experimental and computed spectra [31]. However, based upon the poor agreement between the present experimental spectra and that computed for BaN3O4/N3O4(O2–O2) we can safely rule it out as being a major contributor, though its presence cannot be discounted entirely. Similar results are obtained for both the [Sr(Ura-H)(Ura)]⁺ and [Ca(Ura-H)(Ura)]⁺ complexes (Figure 2.3), although in both cases, the

N3O4/N3O4(O2–O2) isomer which does not have an apparent significant contribution is computed to be lower in energy than N3O2/N3O2(O4–O4).

For [Mg(Ura-H)(Ura)]⁺, based on the computed spectra, we can safely rule out the second structure Mg N3O4/N3O4(O2–O2) as the primary contributor even though it is computed to be the lowest energy structure, albeit only slightly. Calculations using MP2 and dispersion corrected B3LYP result in very similar energies, the observed structure being slightly higher in energy (Table A3, Appendix A). The observation of the structure second highest in energy could be due to the presence of a solvent effect which could destabilize the Mg–N3O4/N3O4(O2–O2) structure in the solution from which the complexes are electrosprayed. As was the case for the other metals, neither the N3O4/N3O2(O4–O2) nor the N3O2/N3O2(O4–O4) structures can be ruled out by comparing the computed and experimental spectra, however, the latter is computed to be 9.3 kJ mol^{–1} higher in Gibbs energy. Due to time restrictions on the FEL we were not able to obtain the spectrum below 1400 cm^{–1} for the Mg complex, however, as for the other metals this region is not expected to differentiate between these isomers.

2.3.3 Computed Structures for [M(Ura-H)(Ura)(H₂O)]⁺

The isomers that were examined computationally were all based upon the three lowest energy isomers of the unsolvated complexes. A total of 12 isomers were identified for the Ba²⁺ metal centre, 13 isomers for Sr²⁺, 9 isomers for Ca²⁺, and 7 isomers for Mg²⁺, for calculation Method 1 and can be seen in Figures A13–A16 (Appendix A). For [Sr(Ura-H)(Ura)(H₂O)]⁺ using Method 2, only 11 isomers were obtained. The N3O4/N3O2(O4–O2)/wO4a isomer optimizes to N3O4/N3O2(O4–O2)/wO4b, while the N3O2/N3O2(O4–

O4)/wO2a optimizes to N3O2/N3O2(O4–O4)/wO2b. A comparison of computed thermochemistries for both computational methods and the five lowest energy structures is given in Table A2 (Appendix A).

As it was for the bare complexes, the lowest energy structure for the hydrated Ba^{2+} , Sr^{2+} and Ca^{2+} complexes share a common construction. The N3O4/N3O2(O4–O2) isomer which was determined to be the lowest energy configuration for the unsolvated complexes also forms the basis of these structures (Figure 2.4). The single water molecule is coordinated to the metal ion, and according to the Bader topological analysis (Appendix A Figure A26), also is participating in a hydrogen bond with O4 of the deprotonated uracil for Sr and Ba. Although a BCP is not localized for Ca, a weak interaction should be established as the water molecule is clearly oriented towards O4. This structure is identified

iii-w
M-N3O2/N3O2(O4-O4)/wO2b

M	$\Delta_{\text{rel}}H/\Delta_{\text{rel}}G$	a	b	c	d	e	f
Ba	6.3/5.3	1.271	1.258	1.253	1.293	1.471	2.047
Sr	5.9/5.8	1.272	1.260	1.253	1.290	1.444	2.223
Ca	5.7/4.6	1.273	1.262	1.254	1.287	1.421	2.595
Mg	8.2/8.1	1.273	1.267	1.255	1.285	1.421	3.407

ii-w
M-N3O4/N3O4(O2-O2)/wO4b

M	$\Delta_{\text{rel}}H/\Delta_{\text{rel}}G$	a	b	c	d	e	f
Ba	6.3/5.9	1.273	1.261	1.255	1.294	1.437	2.065
Sr	5.1/4.7	1.274	1.262	1.255	1.291	1.414	2.199
Ca	3.4/2.7	1.275	1.265	1.256	1.288	1.392	2.516
Mg	0/0	1.276	1.269	1.257	1.284	1.378	2.938

i-w
M-N3O4/N3O2(O4-O2)/wO4b

M	$\Delta_{\text{rel}}H/\Delta_{\text{rel}}G$	a	b	c	d	e	f
Ba	0/0	1.275	1.257	1.250	1.298	1.514	2.037
Sr	0/0	1.277	1.259	1.250	1.294	1.492	2.164
Ca	0/0	1.278	1.261	1.250	1.292	1.479	2.424
Mg	0.4/0.2	1.279	1.264	1.250	1.290	1.477	2.813

Figure 2.4. Comparison of the energies and structures for the three lowest energy $[\text{M}(\text{Ura-H})(\text{Ura})(\text{H}_2\text{O})]^+$ complexes, $\text{M} = \text{Ba}, \text{Sr}, \text{Ca}, \text{Mg}$. The thermochemistry reported here are those from method 2. For complexes of Mg, all/wO4b or/wO2b labels are replaced simply by/w.

as N3O4/N3O2(O4–O2)/wO4b, where ‘O4b’ is used to indicate hydrogen bonding between the water molecule and O4 of the deprotonated uracil (whereas the use of ‘a’ signifies a hydrogen bond involving the neutral uracil). The matching Mg complex is labelled without a reference to O4b, and is instead N3O4/N3O2(O4–O2)/w, since the water molecule does not demonstrate a preference to one uracil over the other. This alternative labelling, as well as the structures, can be seen in Figures A16, A23 and A24 (Appendix A). For all structures, the water molecule does not reside in the same plane as the remainder of the complex. The intramolecular hydrogen bond length between uracil molecules increased, and thus the strength decreased, with increasing size of the metal center, from 1.477 Å in the Mg²⁺ complex to 1.514 Å in the Ba²⁺ complex. This is consistent with the decrease in the electron density at the corresponding BCP. An opposite trend is observed for the hydrogen bond between water and uracil, which ranges from 2.037 Å in Ba²⁺ to 2.424 Å in Ca²⁺, and is virtually non-existent for Mg²⁺, presumably due to the very strong Mg–OH₂ bond. Once again a slight increase in the enol C–OH bond length is expected with increasing metal size, from 1.290 Å for Mg to 1.298 Å for Ba. This C–OH bond is clearly a single bond as confirmed by the computed ellipticity values. The single bond character is reinforced when increasing the size of the metal (decrease in ellipticities). There is no change in the length of the hydrogen bonded carbonyl bond, while the metal coordinated carbonyl bonds tend to increase in length with decreasing metal size, as was observed for the bare ions. Accordingly, the electron density at the BCP remains unchanged for this carbonyl group.

Similar to the unsolvated complexes, Mg²⁺ does not match the lowest energy structures of the other metals. As previously observed for the bare ion, the

N3O4/N3O4(O2–O2) isomer is the lowest in energy when solvated, although in both cases, they are virtually isoenergetic (Figure 2.4). The water molecule is not planar with the remainder of the complex, however in all isomers where water is coordinated to Mg^{2+} , the water molecule does not participate in hydrogen bonding with the neighbouring uracils to the same extent as for the other metal complexes. Indeed, no BCP were found between water and the carbonyl groups of uracils.

Upon addition of a water molecule to the N3O4/N3O2(O4–O2) the structure around the metal cation relaxes somewhat. For all metals, the M–N bond lengths increase by about 0.04 Å. The M–O bonds to the deprotonated and neutral uracils increase by between 0.05 and 0.09 Å and by between 0.02 and 0.03 Å, respectively. Consistently, one can see a decrease in the electron density at the BCPs with respect to bare complexes. This predicted loosening about the M–O and M–N bonds does not translate to a noticeable predicted decrease in the carbonyl bonds, and in some cases there are slight increases, but only in the thousandths of an Angström. Experimentally, it is likely that a very small increase in the carbonyl bond strength could be responsible for the blue-shifting observed in the infrared spectra upon hydration, however, the calculations are not sensitive enough to reproduce this.

2.3.3.1 Comparison of Computed and Experimental Spectra

The experimental spectra for the $[\text{M}(\text{Ura-H})(\text{Ura})(\text{H}_2\text{O})]^+$ ions are compared to the computed spectra for three of the lowest energy structures obtained computationally in Figure 2.5. The five lowest energy structures, based on both calculation methods, are compared to the experimental spectra for all ions in Figures A17 to A24 (Appendix A). In

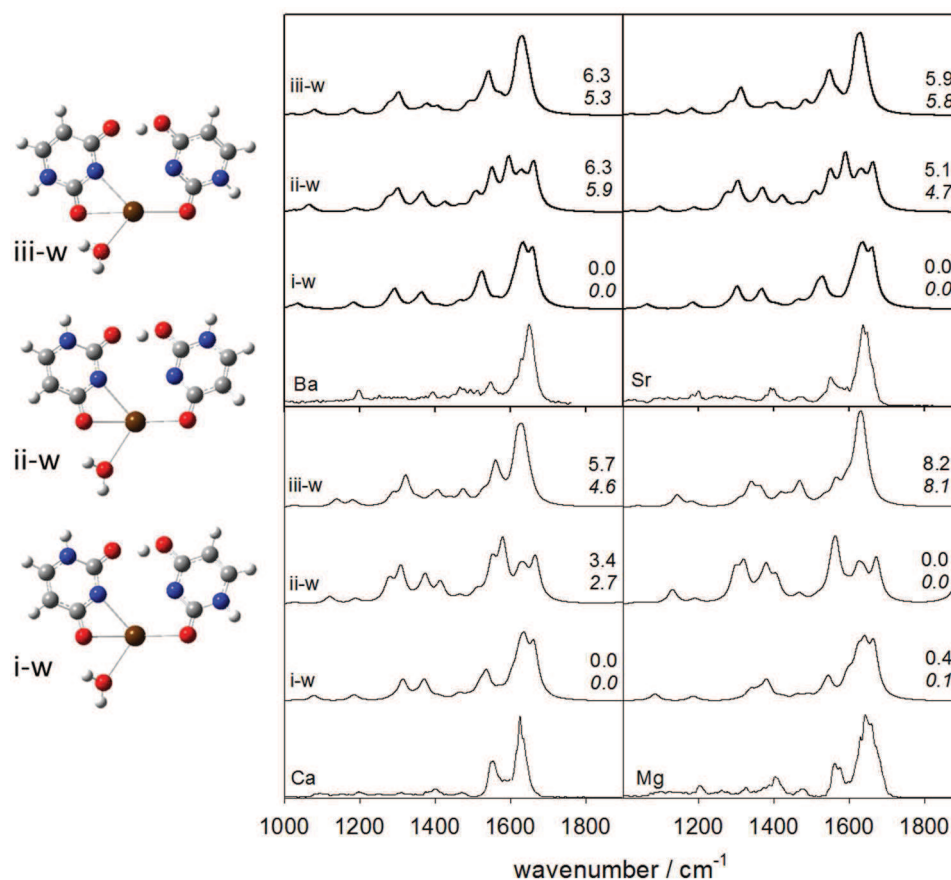


Figure 2.5. Experimental IRMPD spectrum (bottom) for $[M(\text{Ura-H})(\text{Ura})(\text{H}_2\text{O})]^+$ compared with the B3LYP computed spectra using computational method 2 for the three lowest energy structures. Lowest energy structures represent the (i-w) N3O4/N3O2(O4–O2)/wO4b, (ii-w) N3O4/N3O4(O2–O2)/wO4b and (iii-w) N3O2/N3O2(O4–O4)/wO2b tautomers. The calculated relative enthalpies and Gibbs energies (italic) are also shown.

the case of Ba, Sr and Ca exceptional agreement is obtained between the experimental and calculated lowest energy spectra for the N3O4/N3O2(O4–O2)/wO4b tautomer. The intense band at 1648 cm^{-1} for the Ba^{2+} complex has an asymmetry about it which is most likely an unresolved shoulder at a slightly lower wavenumber position. The main band and the asymmetry are identified in the spectrum of the lowest energy complex as carbonyl stretches. Through calculations, the highest frequency stretch is expected to be the carbonyl participating in the intramolecular hydrogen bond with the enol, followed by the metal-

coordinated carbonyl without water and then the metal-coordinated carbonyl hydrogen bonded to the water molecule, at scaled frequencies of 1662, 1637 and 1626 cm^{-1} , respectively. The enol C–OH stretch at 1547 cm^{-1} is evident in the lowest energy spectrum at 1535 cm^{-1} . The N3O4/N3O4(O2–O2)/wO4b structures can all be ruled out as major contributors based on the disagreement with the computed and experimental spectra. However, as was the case for the bare ions, the N3O2/N3O2(O4–O4)/wO2b structure cannot be experimentally ruled out although they are higher energy structures. Similar experimental and computed spectra are observed for the Sr^{2+} , Ca^{2+} , and Mg^{2+} complexes. In Figures A17 to A24 (Appendix A), comparisons between some higher energy structures and the experimental spectra are made. There is not as good agreement between the computed and experimental spectra and based on the computed thermochemistry, it is not expected that these structures would be present in any observable quantity.

2.3.4 Comparison of Computational Methods

Thermodynamic data for the five lowest energy structures can be seen in Table A1 for $[\text{M}(\text{Ura-H})(\text{Ura})]^+$ complexes, and Table A2 for $[\text{M}(\text{Ura-H})(\text{Ura})(\text{H}_2\text{O})]^+$ complexes (both found in Appendix A). Both methods identify the same isomer as being the lowest in energy for each case. As well, good agreement is obtained in the trend of relative enthalpies and Gibbs energies for all other configurations. There is larger deviation in the relative energies of the two high energy bare complexes for Ba^{2+} and Sr^{2+} (i.e. between the LANL2DZ and def2-TZPP basis sets) but the relative energies for all the isomers for Ca^{2+} and Mg^{2+} are virtually identical (i.e. 6–311+G(3df,3pd) and def2-TZVPP).

A comparison of computed spectra is shown in Figure A25 (Appendix A). For $[\text{Ba}(\text{Ura-H})(\text{Ura})]^+$ and $[\text{Ba}(\text{Ura-H})(\text{Ura})(\text{H}_2\text{O})]^+$ and shows that both spectra for each are remarkably similar. Either basis set (LANL2DZ or def2-TZVPP) on the metal proved to be suitable for comparison with experimental data.

2.4 Summary

The structures of $[\text{M}(\text{Ura-H})(\text{Ura})]^+$ and $[\text{M}(\text{Ura-H})(\text{Ura})(\text{H}_2\text{O})]^+$, where M corresponds to group 2 metal ions Ba^{2+} , Sr^{2+} , Ca^{2+} and Mg^{2+} , were examined using IRMPD spectroscopy in the mid-infrared 1000–1900 cm^{-1} region. Two different electronic structure calculation methods were used and compared to the experimental spectra and their energies were compared. There was good agreement between both computational methods in terms of the lowest energy structures and the IR spectra generated for these structures also correspond well to experimental IRMPD spectra. In the case of Mg^{2+} complexes, a second, virtually isoenergetic isomer, displays better agreement with experimental spectra, and corresponds to the lowest-energy forms obtained with the three other metals.

In all cases, experimental evidence suggests the deprotonation of uracil occurs at the N3 position and that the neutral uracil is the tautomer where hydrogen is transferred from N3 to O4. This hydrogen then participates in a strong hydrogen bond interaction with O2 of the deprotonated uracil. The metal ion is tetracoordinate, interacting with N3 and O4 of the deprotonated uracil, and N3 and O2 of the other uracil, as confirmed by the AIM analysis. In the case of solvated structures, the complex takes an identical form, with the water molecule coordinated directly to the metal ion, and also hydrogen bonds with O4 of the deprotonated uracil. In the case of Mg^{2+} complexes, although these particular

configurations are not calculated to be the lowest energy, the N3O4/N3O2(O4–O2) configuration does provide the best agreement with the experimental IRMPD spectra and is only very slightly higher ($\leq 0.8 \text{ kJ mol}^{-1}$) in energy.

Although for both the bare and solvated Mg^{2+} complexes two structures were computed to be very similar in energy, one could be ruled out as the primary structure based on spectroscopic evidence: The same one that could also be ruled out spectroscopically for the other metal ions. This second structure, that only differed slightly, could not be ruled out spectroscopically for Sr^{2+} and Ba^{2+} in a previous study focused on the N–H stretching region.

2.5 Acknowledgements

The authors wish to thank the CLIO team (J.M. Ortega, C. Six, G. Perilhous, J. P. Berthet) as well as P. Maître and V. Steinmetz for their support during the experiments. The authors also acknowledge the computational resources provided by ACE-Net and Westgrid. Finally, TDF acknowledges the financial contributions from NSERC, CFI, and Memorial University.

2.6 References

1. A.M. Pyle, *Science*, **1993**, *261*, 709.
2. V.K. Misra, D.E. Draper, *Biopolymers*, **1998**, *48*, 113.
3. E. Madore, C. Florentz, R. Giege, J. Lapointe, *J. Nucleic Acids Res.*, **1999**, *27*, 3583.
4. R. Hanna, J.A. Doundna, *Curr. Opin. Chem. Biol.*, **2000**, *4*, 166.

5. D.L. Nelson, M.M. Cox, A.L. Lehninger, *Principles of Biochemistry*, 3rd ed., W.H. Freeman, New York, NY, **2004**.
6. G.L. Eichhorn, L.G. Marzilli, *Advances in Inorganic Biochemistry: Metal Ions in Genetic Information Transfer*, Elsevier Science, New York, NY, **1981**.
7. G.L. Eichhorn, *Nature*, **1962**, 194, 474.
8. W. Förster, E. Bauer, H. Schutz, H. Berg, M. Akimenko, L.-E. Minchenkova, Y.M. Evdkimov, Y.M. Vershavsky, *Biopolymers*, **1979**, 18, 625.
9. A.M. Pyle, *J. Biol. Inorg. Chem.*, **2002**, 7, 679.
10. S. Basu, R.P. Rambo, J. Strauss-Soukup, J.H. Cate, A.R. Ferre-D'Amare, S.A. Strobel, J.A. Doudna, *Nat. Struct. Biol.*, **1998**, 5, 986.
11. R. Shiman, D.E. Draper, *J. Mol. Biol.*, **2000**, 302, 79.
12. Y.A. Shin, G.L. Eichhorn, *Biopolymers*, **1977**, 16, 225.
13. S. Burge, G.N. Parkinson, P. Hazel, A.K. Todd, S. Neidle, *Nucleic Acids Res.* **2006**, 34, 5402.
14. P.-O. Lowdin, *Rev. Mod. Phys.*, **1963**, 35, 724.
15. M.D. Topal, J.R. Fresco, *Nature*, **1976**, 263, 285.
16. P.O.P. Ts'o, *Basic Principles in Nucleic Acids Chemistry*, Academic Press, New York, NY, **1974**.
17. H. Ruterjans, E. Kaun, W.E. Hull, H.H. Limbach, *Nucleic Acid Res.*, **1982**, 10, 7.
18. S. Guillaumont, J. Tortajada, J.-Y. Salpin, A.M. Lamsabhi, *Int. J. Mass Spectrom.*, **2005**, 243, 279.
19. C. Gutlé, J.-Y. Salpin, T. Cartailier, J. Tortajada, M.-P. Gageot, *J. Phys. Chem. A*, **2006**, 110, 11684.
20. M. Kabeláč, P. Hobza, *J. Phys. Chem. B*, **2006**, 110, 14515.

21. J.-Y. Salpin, S. Guillaumont, J. Tortajada, A. Lamsabhi, *J. Am. Soc. Mass Spectrom.*, **2009**, 20, 359.
22. O.Y. Ali, T.D. Fridgen, *Int. J. Mass Spectrom.*, **2011**, 308, 167.
23. E.A.L. Gillis, K. Rajabi, T.D. Fridgen, *J. Phys. Chem. A*, **2009**, 113, 824.
24. E.A.L. Gillis, T.D. Fridgen, *Int. J. Mass Spectrom.*, **2010**, 297, 2.
25. E. Rincón, M. Yáñez, A. Toro-Labbé, O. Mó, *Phys. Chem. Chem. Phys.*, **2007**, 9, 2531.
26. A. Lamsabhi, M. Alcamí, O. Mó, M. Yáñez, J. Tortajada, *J. Phys. Chem. A*, **2006**, 110, 1943.
27. O.Y. Ali, T.D. Fridgen, *ChemPhysChem*, **2012**, 13, 588.
28. Y.-w. Nei, T.E. Akinyemi, C.M. Kaczan, J.D. Steill, G. Berden, J. Oomens, M.T. Rodgers, *Int. J. Mass Spectrom.*, **2011**, 308, 191.
29. J.-Y. Salpin, S. Guillaumont, D. Ortiz, J. Tortajada, P. Maître, *Inorg. Chem.*, **2011**, 50, 7769.
30. O.Y. Ali, N.M. Randell, T.D. Fridgen, *ChemPhysChem*, **2012**, 13, 1507.
31. A.A. Power, O.Y. Ali, M.B. Burt, T.D. Fridgen, *Int. J. Mass Spectrom.*, **2012**, 330–332, 233.
32. A. Eizaguirre, A.M. Lamsabhi, O. Mo, M. Yanez, *Theor. Chem. Acc.*, **2011**, 128, 457.
33. D. Dougherty, K. Wittel, J. Meeks, S.P. McGlynn, *J. Am. Chem. Soc.*, **1976**, 98, 3815.
34. R. Czerminski, B. Lesying, A. Pohorille, *Int. J. Quantum Chem.*, **1979**, 16, 605.
35. D. Shugar, K. Szczepaniak, *Int. J. Quantum Chem.*, **1981**, 20, 573.
36. P. Beak, J.M. White, *J. Am. Chem. Soc.*, **1982**, 104, 7073.
37. M. Szczesniak, M.J. Nowak, K. Szczepaniak, W.B. Person, D. Shugar, *J. Am. Chem. Soc.*, **1983**, 105, 5969.

38. S. Chin, I. Scott, K. Szczepani, W.B. Person, *J. Am. Chem. Soc.*, **1984**, *106*, 3415.
39. M.J. Scanlan, I.H. Hillier, *J. Am. Chem. Soc.*, **1984**, *106*, 3737.
40. J.S. Kwiatkowski, T.J. Zielinski, R. Rein, *Adv. Quantum Chem.*, **1986**, *18*, 85.
41. U. Norinder, *THEOCHEM*, **1987**, *36*, 259.
42. Y. Tsuchiya, M. Fujii, M. Ito, *J. Phys. Chem.*, **1988**, *92*, 1760.
43. B.B. Brady, L.A. Peteanu, D.H. Levy, *Chem. Phys. Lett.*, **1988**, *147*, 538.
44. R.D. Brown, P.D. Godfrey, D. McNaughton, A.P. Pierlot, *J. Am. Chem. Soc.*, **1988**, *110*, 2329.
45. A. Lés, L. Adamowicz, *J. Phys. Chem.*, **1989**, *93*, 7078.
46. I.R. Gould, I.H. Hiller, *J. Chem. Soc., Perkin Trans.*, **1990**, *2*, 329.
47. J. Leszczynski, *J. Phys. Chem.*, **1992**, *96*, 1649.
48. D.A. Estrin, L. Paglieri, G. Corongiu, *J. Phys. Chem.*, **1994**, *98*, 5653.
49. I.R. Gould, N.A. Burton, R.J. Hall, I.H. Hiller, *THEOCHEM*, **1995**, *331*, 147.
50. L. Paglieri, G. Corongiu, D.A. Estrin, *Int. J. Quantum Chem.*, **1995**, *56*, 615.
51. S.X. Tian, C.F. Zhang, Z.J. Zhang, X.J. Chen, K.Z. Xu, *Chem. Phys.*, **1999**, *242*, 217.
52. M. Sabat, B. Lippert, *Met. Ions Biol. Syst.*, **1996**, *33*, 143.
53. C. Trujillo, A.M. Lamsabhi, O. Mó, M. Yáñez, J.-Y. Salpin, *Org. Biomol. Chem.*, **2008**, *6*, 3695.
54. R. Prazeres, F. Glotin, C. Insa, D.A. Jaroszynski, J.M. Ortega, *Eur. Phys. J. D: At., Mol., Opt. Plasma Phys.*, **1998**, *3*, 87.
55. W. Paul, *Rev. Mod. Phys.*, **1990**, *62*, 531.

56. K. Rajabi, M.L. Easterling, T.D. Fridgen, *J. Am. Soc. Mass Spectrom.*, **2009**, *20*, 411.
57. M.J. Frisch, G.W. Trucks, H.B. Schlegel, G.E. Scuseria, M.A. Robb, J.R. Cheeseman, G. Scalmani, V. Barone, B. Mennucci, G.A. Petersson, H. Nakatsuji, M. Caricato, X. Li, H.P. Hratchian, A.F. Izmaylov, J. Bloino, G. Zheng, J.L. Sonnenberg, M. Hada, M. Ehara, K. Toyota, R. Fukuda, J. Hasegawa, M. Ishida, T. Nakajima, Y. Honda, O. Kitao, H. Nakai, T. Vreven, J.A. Montgomery, J.E. Peralta J., F. Ogliaro, M. Bearpark, J.J. Heyd, E. Brothers, K.N. Kudin, V.N. Staroverov, T. Keith, R. Kobayashi, J. Normand, K. Raghavachari, A. Rendell, J.C. Burant, S.S. Iyengar, J. Tomasi, M. Cossi, N. Rega, J.M. Millam, M. Klene, J.E. Knox, J.B. Cross, V. Bakken, C. Adamo, J. Jaramillo, R. Gomperts, R.E. Stratmann, O. Yazyev, A.J. Austin, R. Cammi, C. Pomelli, J.W. Ochterski, R.L. Martin, K. Morokuma, V.G. Zakrzewski, G.A. Voth, P. Salvador, J.J. Dannenberg, S. Dapprich, A.D. Daniels, O. Farkas, J.B. Foresman, J.V. Ortiz, J. Cioslowski, D.J. Fox, *Gaussian 09*, Revision D.01, Gaussian, Inc., Wallingford, CT, **2013**.
58. P.B. Armentrout, M. Citir, Y. Chen, M.T. Rodgers, *J. Phys. Chem. A*, **2012**, *116*, 11823.
59. P.B. Armentrout, Y. Chen, M.T. Rodgers, *J. Phys. Chem. A*, **2012**, *116*, 3989.
60. R.F.W. Bader, *Atoms in Molecules: A Quantum Theory*, Clarendon Press, Oxford University Press, New York, NY, **1990**.
61. P. Colarusso, K. Zhang, B. Gup, P.F. Bernath, *Chem. Phys. Lett.*, **1997**, *269*, 39.
62. S.J. Lippard, J.M. Berg, *Principles of Bioinorganic Chemistry*, University Science Books, Mill Valley, CA, **1994**.
63. W. Kaim, B. Schwedersky, *Bioinorganic Chemistry Inorganic Elements in the Chemistry of Life*, John Wiley & Sons, Chichester, UK, **1994**.
64. L.A. Loeb, A.R. Zakour, *Nucleic Acids-Metal Ion Interactions*, T.G. Spiro Ed., John Wiley & Sons, New York, NY, **1980**.
65. J.-Y. Salpin, S. Guillaumont, J. Tortajada, L. MacAleese, J. Lemaire, P. Maître, *ChemPhysChem*, **2007**, *8*, 223.

CHAPTER 3 – Structures of $[M(\text{Ura-H})(\text{H}_2\text{O})_n]^+$ ($M = \text{Mg, Ca, Sr, Ba}$; $n = 1-3$) Complexes in the Gas Phase by IRMPD Spectroscopy and Theoretical Studies

The structures of singly and doubly (and for Mg, triply) hydrated group 2 metal dications bound to deprotonated uracil were explored in the gas phase using infrared multiple photon dissociation spectroscopy in the mid-infrared region ($1000 - 1900 \text{ cm}^{-1}$) and the O–H/N–H stretching region ($2700 - 3800 \text{ cm}^{-1}$) in a Fourier transform ion cyclotron resonance mass spectrometer. The infrared multiple photon dissociation spectra were then compared with the computed IR spectra for various isomers. Calculations were performed using B3LYP with the 6-31+G(d,p) basis set for all atoms except Ba^{2+} and Sr^{2+} , for which the LANL2DZ or the def2-TZVPP basis sets with relativistic core potentials were used. Atoms-in-molecules analysis was conducted for all lowest energy structures. The lowest energy isomers in all cases are those in which the one uracil is deprotonated at the N3 position, and the metal is coordinated to the N3 and O4 of uracil. Regardless of the degree of solvation, all water molecules are bound to the metal ion and participate in a hydrogen bond with a carbonyl of the uracil moiety.

A version of this chapter has been published:

B. Power, V. Haldys, J.-Y. Salpin and T.D. Fridgen, *J. Mass Spectrom.*, **2016**, *51*, 236.

3.1 Introduction

Independently, both metal ions and solvents, notably water, have been thoroughly investigated for the roles they play in biological systems. In particular, the influence each holds on the behavior of DNA and RNA nucleobases has been of great interest. In the case of metal dications, it has been shown that they are crucial for the stability of DNA and RNA through charge neutralization and noncovalent interactions with the phosphate backbone of the nucleic acids [1–3]. However, when in an undesirable excess, the metal dications may also change the conformation of the individual nucleobases away from the preferred canonical form, leading to deviations from the predicted Watson–Crick pairings through modification of hydrogen bonding sites [4–7]. These unwanted conformational changes can lead to genetic defects.

When uracil is in aqueous solution, the conjugate bases resulting from the loss of both N1 and N3 protons exist in equilibrium with a pK_a measured to be 9.5 [8]. However, in the gas phase, the acidity of both sites is dramatically different. Loss of the proton at N3 is associated with a deprotonation enthalpy of $1452 \pm 17 \text{ kJ mol}^{-1}$ [9], whereas to deprotonate at N1 requires $1393 \pm 17 \text{ kJ mol}^{-1}$ [9,10]. Various calculation methods [10–12] are in agreement on these thermochemical values. To resolve the differences between the gas and solvent phase values, Bachrach and Dzierlenga [13] employed microsolvation to model this solvent effect using density functional theory methods and determine at what point bulk solvent effects become prevalent. It was determined that the gap in deprotonation energy decreases successively with each water molecule added up to the fourth water, at which point the gap in deprotonation energy has halved. Addition of a fifth and sixth water molecule has a negligible effect on the difference between deprotonation energies.

The focus of this current work is to examine the RNA nucleobase uracil and the complexes formed with group 2 metal dications at varying degrees of water solvation. The conventional uracil numbering scheme used throughout is presented in Scheme 2.1. Although the deprotonation energy at the N1 site of uracil is lower in the gas phase compared with N3, previous studies have all concluded that deprotonation occurs at N3 in the presence of alkaline earth metal cations [14–16], or heavy metals [17]. Of course, replicating the cellular environment in condensed phase analysis is difficult. To overcome this, gas-phase conditions are utilized, allowing for direct molecular examination and eliminating the interference of bulk solvent effects, which may otherwise influence the structure of such complexes. Action, or consequence spectroscopy, is a method that has successfully been applied to conduct such research. In particular, infrared multiple photon dissociation (IRMPD) is a technique frequently used and is the method of choice for this current work [18,19].

The current work aims to provide structural insight into the hydrated alkaline earth metal complexes, $[M(\text{Ura-H})(\text{H}_2\text{O})_n]^+$ ($M = \text{Mg, Ca, Sr, Ba}$), using IRMPD spectroscopy in both the O-H/N-H stretching region ($2700 - 3800 \text{ cm}^{-1}$) as well as the fingerprint region ($1000 - 1900 \text{ cm}^{-1}$). In this fingerprint region, carbonyl stretching frequencies are obtained, and differentiating features between the computed tautomers, previously indistinguishable, are now evident.

3.2 Methods

3.2.1 Experimental

All mid-infrared experiments were performed using a Fourier transform ion cyclotron resonance mass spectrometer coupled to a mid-infrared free electron laser (FEL) at the Centre Laser Infrarouge d'Orsay [20,21]. 0.01 mmol L⁻¹ solutions of the chloride salts of each of the metal ions and 1 mmol L⁻¹ uracil solutions were prepared in 18 MΩ water (Millipore). Mixtures were then prepared in a 1 to 10 ratio of metal solution to uracil solution and introduced via syringe injection to the electrospray ion source at a flow rate of 75 μL h⁻¹. Ions were mass selected with a quadrupole mass filter, isolated in the ion cyclotron resonance cell, and irradiated with the free electron laser. To accomplish hydration of the ions, the bare [M(Ura-H)]⁺ ion was first selected in the quadrupole filter and then stored in the hexapole storage cell, into which water vapour had been leaked [22]. Irradiation times varied from 0.1 to 3 s, with the more weakly bound and, therefore, faster dissociating ions being irradiated for the shortest time. Certain areas of the IRMPD spectra, which were saturated, were scanned after attenuation of the FEL. The laser was scanned at 5 cm⁻¹ intervals from ~1000 to 1900 cm⁻¹.

Experiments in the O–H/N–H region were conducted at the Laboratory for the Study of the Energetics, Structures, and Reactions of Gaseous Ions at Memorial University using a Bruker Apex Qe 7 T Fourier transform ion cyclotron resonance mass spectrometer (Billerica, MA, USA) coupled with an IR optical parametric oscillator tunable laser as previously described [23]. Solutions were prepared to 1 mmol L⁻¹ of both uracil and metal ion in a 50:50 methanol–water solvent system. The solutions were syringe injected into the electrospray ion source at a flow rate of 160 μL h⁻¹. The ions emerging from the source

were mass selected using a quadrupole mass filter, accumulated in the hexapole collision cell, then guided into the ion cyclotron resonance cell. The ions were then irradiated with tunable infrared radiation in the O–H/N–H stretching region from 2700 to 3800 cm^{-1} at an irradiation time between 1.5 and 3 s. The laser was scanned in 2 cm^{-1} intervals to yield the IRMPD spectra.

The IRMPD efficiency is the negative of the natural logarithm of parent ion intensity divided by the sum of parent and fragment ion signals.

3.2.2 Computational

Calculations for all structures were conducted using the Gaussian 09 suite of programmes [24]. Each structure was optimized and infrared spectra computed using B3LYP density functional theory. In the cases of the Ca^{2+} and Mg^{2+} complexes, the 6-31+G(d,p) basis set was used for all atoms. For the complexes of Ba^{2+} and Sr^{2+} , the LANL2DZ basis set with relativistic core potential was used for strontium and barium atoms, and the 6-31+G(d,p) basis was used for all other atoms. Single point energy calculations were then carried out using B3LYP with the 6-311+G(3df,3pd) basis set on all atoms except Sr and Ba, for which the LANL2DZ basis set with relativistic core potential was used. This computational method will be referred to as method 1.

All calculations were then repeated with the def2-TZVPP basis set, which has been found to work better for metal-cation amino acid complexes than the LANL2DZ [25,26], for all metal atoms during both the optimization and single-point energy calculations. The 6-31+G(d,p) basis set was again used for all other atoms (C, H, N and O) during

optimization, followed by the 6-311+G(3df,3pd) basis set for single point energy calculations. This computational method will be referred to as method 2.

These single-point electronic energies, using methods 1 and 2, were used to compute the enthalpies and Gibbs energies of isomeric species at 298 K, using the unscaled harmonic vibrational frequencies calculated based on the optimized geometry.

The bonding within the individual equilibrium structures was also analyzed by locating the bond critical points (BCPs) using atoms-in-molecules (AIM) theory [27], which is based on a topological analysis of the electronic density at the BCPs, and is a good descriptor of the bond strength or weakness. This analysis was conducted using AIMAll software [28] with the optimized structures from method 2. Data from the topological analysis are given collectively in Appendix B as Figure B20.

For comparison with the experimental spectra, the computed infrared spectra were scaled by a factor of 0.97 in the fingerprint region, by 0.96 in the O–H/N–H region, and convoluted with a Lorentzian profile with a width (FWHM) of 15 cm⁻¹.

3.3 Results and Discussion

3.3.1 Examination of the IRMPD Spectra

When complexes were irradiated by both the FEL and optical parametric oscillator, regardless of the metal or the degree of hydration, only water molecules were lost upon irradiation. This is in agreement with the loss of the water molecule in the singly hydrated complexes involving either Ba, Sr, or Pb and two uracil units, where only the loss of water was observed [14,29]. In these studies, only loss of a single water molecule is noted for the

doubly hydrated dimer complexes, whereas in the current work sequential dehydration corresponding to the losses of one and/or two water molecules is observed.

Figure 3.1 presents the IRMPD spectra for $[M(\text{Ura-H})(\text{H}_2\text{O})]^+$ in the 1000 – 1900 cm^{-1} region. All $[M(\text{Ura-H})(\text{H}_2\text{O})]^+$ spectra display a broad band centred between 1612 and 1620 cm^{-1} , which contains a combination of stretching modes; hydrogen-bonded C=O stretching, H₂O scissoring and C5=C6 stretching. This band is redshifted with respect to the position of the free carbonyl stretch of uracil, centred about 1750 cm^{-1} in the gas phase [30], because of hydrogen bonding, which has the effect of lengthening and weakening the carbonyl bond. Both the H₂O scissoring mode and the C=C stretch also occur in this region, with the C=C stretch in particular being previously observed at the same frequency in similar complexes [15].

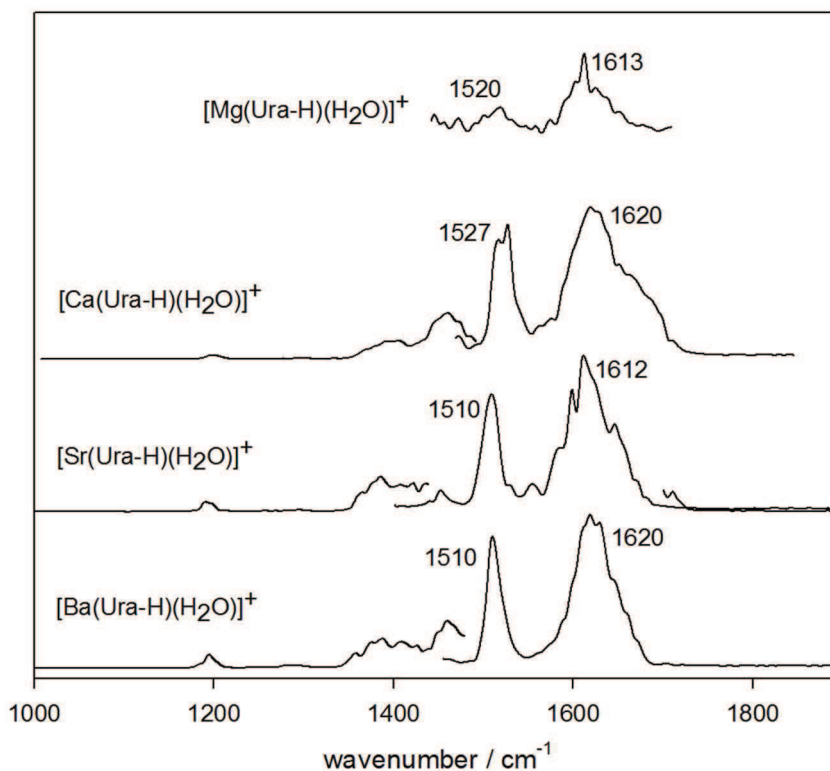


Figure 3.1. Infrared multiple photon dissociation spectra for $[\text{Ba}(\text{Ura-H})(\text{H}_2\text{O})]^+$, $[\text{Sr}(\text{Ura-H})(\text{H}_2\text{O})]^+$, $[\text{Ca}(\text{Ura-H})(\text{H}_2\text{O})]^+$ and $[\text{Mg}(\text{Ura-H})(\text{H}_2\text{O})]^+$ in the 1000 – 1900 cm^{-1} region.

Another intense band for all $[M(\text{Ura-H})(\text{H}_2\text{O})]^+$ complexes is centred around $1510 - 1527 \text{ cm}^{-1}$. This band is attributed to the metal-coordinated carbonyl stretch. Again this band is red-shifted compared with the free carbonyl stretch of uracil, which occurs about 1750 cm^{-1} as previously mentioned [30]. It is also a significant red-shift in comparison with the sodium-coordinated carbonyl stretch in uracil, observed to absorb between 1630 cm^{-1} and 1675 cm^{-1} [31] and is due to the metals in the present complexes being dications, binding more strongly to uracil than Na^+ . The red shift is also more pronounced than in the hydrated $[M(\text{Ura-H})(\text{Ura})]^+$ complexes with the same metal dications, where the corresponding absorptions were found between 1614 cm^{-1} and 1627 cm^{-1} , depending on the metal [15]. In fact, the observed bands in the present work correspond more closely to the enol stretches in the dimer complexes, which absorbed between 1530 cm^{-1} and 1548 cm^{-1} , an indication that the carbonyl bond is significantly weakened in these monomeric complexes when compared with the dimers. The carbonyl weakening in the present monomeric complexes is because of the metal ion is now coordinated to a single carbonyl, instead of two.

Weaker features are visible at approximately 1400 cm^{-1} and 1200 cm^{-1} for the complexes of Ba, Sr and Ca. The broad band around 1400 cm^{-1} contains C–N stretches within the uracil ring, as well as the N1 hydrogen wagging vibration. At 1200 cm^{-1} , the C5 and C6 hydrogen wagging modes occur.

The IRMPD spectra in the fingerprint region of $[M(\text{Ura-H})(\text{Ura})(\text{H}_2\text{O})_2]^+$ complexes are shown in Figure 3.2. The doubly hydrated Mg complex could not be isolated during these particular experiments, although a spectrum was obtained in the O–H/N–H region. The spectra are consistent with the singly hydrated complexes; however the

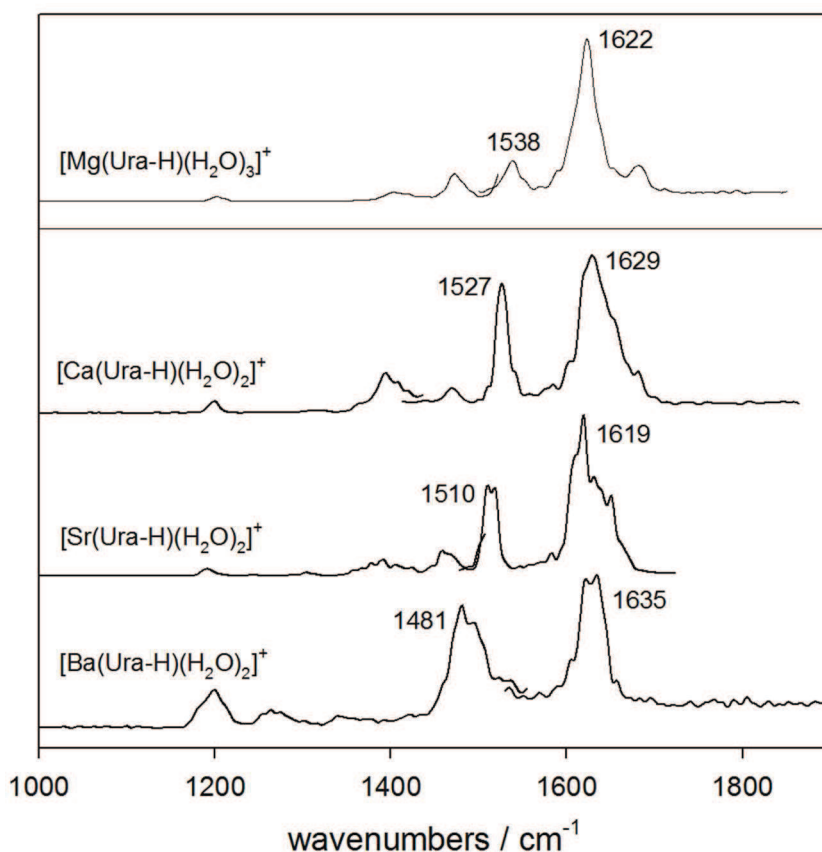


Figure 3.2. Infrared multiple photon dissociation spectra for $[\text{Ba}(\text{Ura-H})(\text{H}_2\text{O})_2]^+$, $[\text{Sr}(\text{Ura-H})(\text{H}_2\text{O})_2]^+$, $[\text{Ca}(\text{Ura-H})(\text{H}_2\text{O})_2]^+$ and $[\text{Mg}(\text{Ura-H})(\text{H}_2\text{O})_3]^+$ in the 1000 – 1900 cm^{-1} region.

narrowing and a slight blue-shift ($\sim 10 \text{ cm}^{-1}$) of the major feature are presently observed. Calculations show that the band contains hydrogen-bonded carbonyl stretching, H_2O scissoring and $\text{C5}=\text{C6}$ stretching, similar to the singly hydrated complex. The secondary feature, now detected between 1481 and 1527 cm^{-1} , once again is indicative of the metal-coordinated carbonyl stretching mode. This band noticeably blue-shifts as the metal decreases in size. This can be explained in terms of hard-soft acid-base theory. As the metal cation decreases in size, it is a harder acid and binds more strongly to the harder base, water, thereby weakening the bonding with the softer NCO^- moiety of deprotonated uracil, increasing the $\text{C}=\text{O}$ bond strength and causing a blue-shift.

Even though the doubly hydrated Mg complex could not be isolated in enough abundance to be examined during the experiments at Centre Laser Infrarouge d'Orsay, the triply hydrated complex was easily detected. The IRMPD spectrum for $[\text{Mg}(\text{Ura-H})(\text{H}_2\text{O})_3]^+$ is presented in Figure 3.2 (top). There is now some distinction made between the stretches occurring between 1580 and 1680 cm^{-1} . The main band centred about 1622 cm^{-1} is now much narrower than it was for the singly and doubly hydrated species. The carbonyl stretch at the O2 position has been blue-shifted to 1680 cm^{-1} and is now separated from the predominant band, which contains the scissoring stretch of the water molecule hydrogen-bonded to O2, as well as the C5=C6 stretch. Both synchronous and asynchronous scissoring of the other water molecules hydrogen-bonded to O4 appears as a shoulder on the red side of the main band. The secondary carbonyl stretching feature, the metal-coordinated carbonyl, is also blue-shifted in comparison with the singly and doubly hydrated species, to 1538 cm^{-1} . Blue shifting of carbonyl stretches has been previously observed upon hydration of these types of complexes [15]. The effect is likely the result of water binding to the metal, thus donating electron density back to the complex and particularly to the carbonyl bonds. This leads to a mild strengthening of the C=O bond, and in turn, a higher stretching frequency.

Figure 3.3 presents the experimental spectra of the hydrated complexes of Ca and Mg in the O–H/N–H stretching region. Similar complexes of Ba and Sr have been examined previously [14]. All spectra exhibit the same key features; first, a band centred about 3455 cm^{-1} for the singly hydrated complexes, which gradually blue-shifts with increasing hydration, indicative of the N–H stretch of uracil, and secondly, the free O–H stretching modes of water, located in the range of $3600 - 3700\text{ cm}^{-1}$. As the degree of hydration

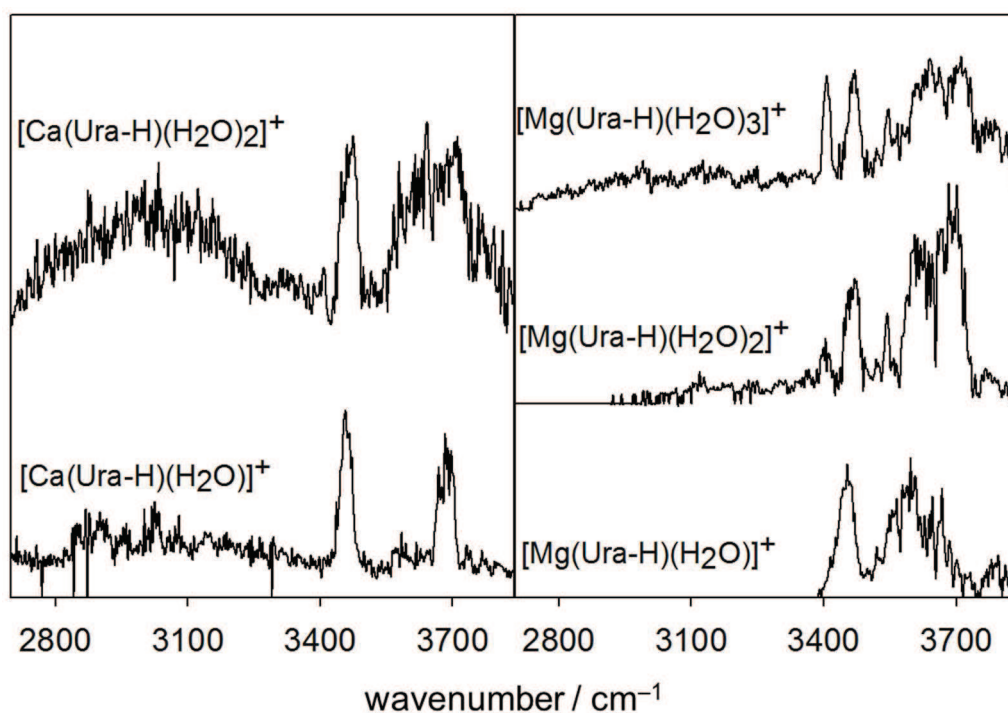


Figure 3.3. Infrared multiple photon dissociation spectra for $[\text{Ca}(\text{Ura-H})(\text{H}_2\text{O})_2]^+$, $[\text{Ca}(\text{Ura-H})(\text{H}_2\text{O})]^+$, $[\text{Mg}(\text{Ura-H})(\text{H}_2\text{O})_3]^+$, $[\text{Mg}(\text{Ura-H})(\text{H}_2\text{O})_2]^+$ and $[\text{Mg}(\text{Ura-H})(\text{H}_2\text{O})]^+$ in the 2700 – 3800 cm^{-1} region.

increases, more of these stretches are logically observed. In the singly hydrated complexes, there is a single free O–H stretching mode; however as more water molecules added, symmetric and asymmetric modes are also observed.

3.3.2 Computed Structures for $[\text{M}(\text{Ura-H})(\text{H}_2\text{O})]^+$

A total of seven isomers were located for the singly hydrated complexes of all metals. Figure 3.4 gives the structures and energetics for the three lowest energy structures. All structures obtained for both calculation methods are given in Figures B1–B8 (Appendix B) along with the thermochemistries, while Table B1 compares the relative energies obtained with both calculations methods. In all instances, the N3O4/wbO2 isomer is the most stable form in relative enthalpy. It is also the global minimum in relative Gibbs energy

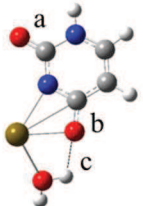
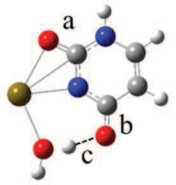
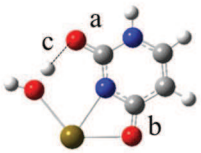
iii		M	$\Delta_{rel}H/\Delta_{rel}G$	a	b	c
		Ba	39.6/34.4	1.225	1.293	2.074
		Sr	39.3/33.0	1.223	1.296	2.264
		Ca	35.1/23.6	1.221	1.299	3.577
		Mg	1.2/0	1.217	1.301	n/a
ii		M	$\Delta_{rel}H/\Delta_{rel}G$	a	b	c
		Ba	5.6/5.8	1.273	1.251	1.549
		Sr	6.1/6.3	1.275	1.251	1.556
		Ca	6.9/7.1	1.278	1.249	1.580
		Mg	13.1/16.7	1.290	1.245	1.737
i		M	$\Delta_{rel}H/\Delta_{rel}G$	a	b	c
		Ba	0/0	1.246	1.279	1.619
		Sr	0/0	1.245	1.281	1.638
		Ca	0/0	1.243	1.285	1.673
		Mg	0/5.6	1.236	1.297	1.942

Figure 3.4. Comparison of the energies and structures for the three lowest energy $[M(\text{Ura-H})(\text{H}_2\text{O})]^+$ complexes, $M = \text{Ba}, \text{Sr}, \text{Ca}, \text{Mg}$. The thermochemistry reported here are those from method 2. Energies are expressed in kJ mol^{-1} and distances in Angströms.

(298 K) for all complexes, with the exception of the Mg complex, for which the N3O4/w structure is the global minimum. This result is identical to previous results obtained for the complexes of Ba and Sr [14]. This particular N3O4/w structure is deprotonated at the N3 of uracil, with metal coordination between N3 and O4. In addition, the water molecule is oriented away from the uracil moiety and does not interact with uracil (Figure B7, Appendix B). It is interesting that the hydrogen bonds (distance c in Figure 3.4) increase in length as the metal cation gets smaller. This is due to the metal cation to water–O bond distance being smaller for the smaller cations rendering the water–H to uracil–O hydrogen bond longer; in the case of N3O4/w for Mg, the water is not coordinated at all to the uracil.

For N3O4/wbO2 forms, the AIM topological analysis confirms the bidentate interaction, with two BCPs connecting the metal to uracil in all complexes, and with corresponding positive values of the Laplacian of the electron density, $\nabla^2\rho$, suggesting electrostatic interactions (Appendix B Figure B20). Water is bound to the metal centre, with a hydrogen bond formed between the water and O2 of uracil, which is also confirmed through AIM analysis. The hydrogen bond is particularly strong for the Ba, Sr and Ca complexes, measuring ~ 1.6 Å for each, with the hydrogen bond length increasing (and thus, decreasing in strength) with decreasing the metal ion size. For the Mg complex, the hydrogen bond length is 1.942 Å. This is similar to the results observed for the water–carbonyl hydrogen bond in metal–uracil dimers [15], although the hydrogen bonds were much stronger in the case of the monomers. The carbonyl bond lengths vary, with the hydrogen-bonded carbonyl slightly shorter (~ 1.24 Å) than the metal-coordinated carbonyl bond length (1.28 Å). Distinct patterns are observed based on the size of the metal. As the metal size increases, the metal-coordinated carbonyl bond lengths decrease slightly, an expected result based upon decreasing metal–carbonyl bond strengths and confirmed by the computed electron densities at the BCPs. The increasing metal size also leads to the lengthening of the hydrogen-bonded carbonyl groups.

For the complexes of Ba, Sr and Ca, only one other form comes relatively close in terms of energy. In the N3O2/wbO4 conformation, uracil is again deprotonated at the N3 position. However, metal coordination now occurs between N3 and O2, with the water molecule coordinated to the metal centre and hydrogen-bonded to the O4 position. For these metals, the difference in enthalpy and Gibbs energy between these two structures is between 5.8 and 7.1 kJ mol⁻¹. All other structures were found to be significantly higher in

energy, using both calculation methods, by at least 23 kJ mol⁻¹. For the complex of Mg, the N3O4/wbO2 structure is, like the other metals, lowest in enthalpy. However, the structure, which is lowest in Gibbs energy (N3O4/w), was deemed as an insignificant contributor for the other metal complexes.

To conclude, all lowest energy structures exhibit planar geometry, regardless of calculation method.

3.3.2.1 Comparison of Computed and Experimental Spectra

A comparison between the experimental spectra and the three lowest energy structures computed via method 2 is given in Figure 3.5 for the [M(Ura-H)(H₂O)]⁺ ions. IR spectra for all optimized structures are compared with the experimental fingerprint spectra for all ions in Figures B1–B8 (Appendix B), including those for both methods of computation.

Although no distinction could be made between the computed structures of Ba and Sr complexes in the 3200 – 3800 cm⁻¹ region [14], enough evidence now exists to support definitive assignment of structure (i) as being the primary experimental structure for both ions, as is also the case for the Ca complex, although a hydrogen-bonded O–H stretch is not experimentally observed. The feature in the area of 1610 – 1620 cm⁻¹ (hydrogen-bonded C=O stretching, H₂O scissoring and C5=C6 stretching combined modes) is more intense and broader than the one at 1510 cm⁻¹ (metal-coordinated carbonyl stretch). These two features are better reproduced by the calculated spectra of structure (i) in all three cases. Even more so, the small band observed at 1460 cm⁻¹, attributed to N1 hydrogen wagging, is matched in the calculated spectra for structure (i) but absent in structure (ii) in all three

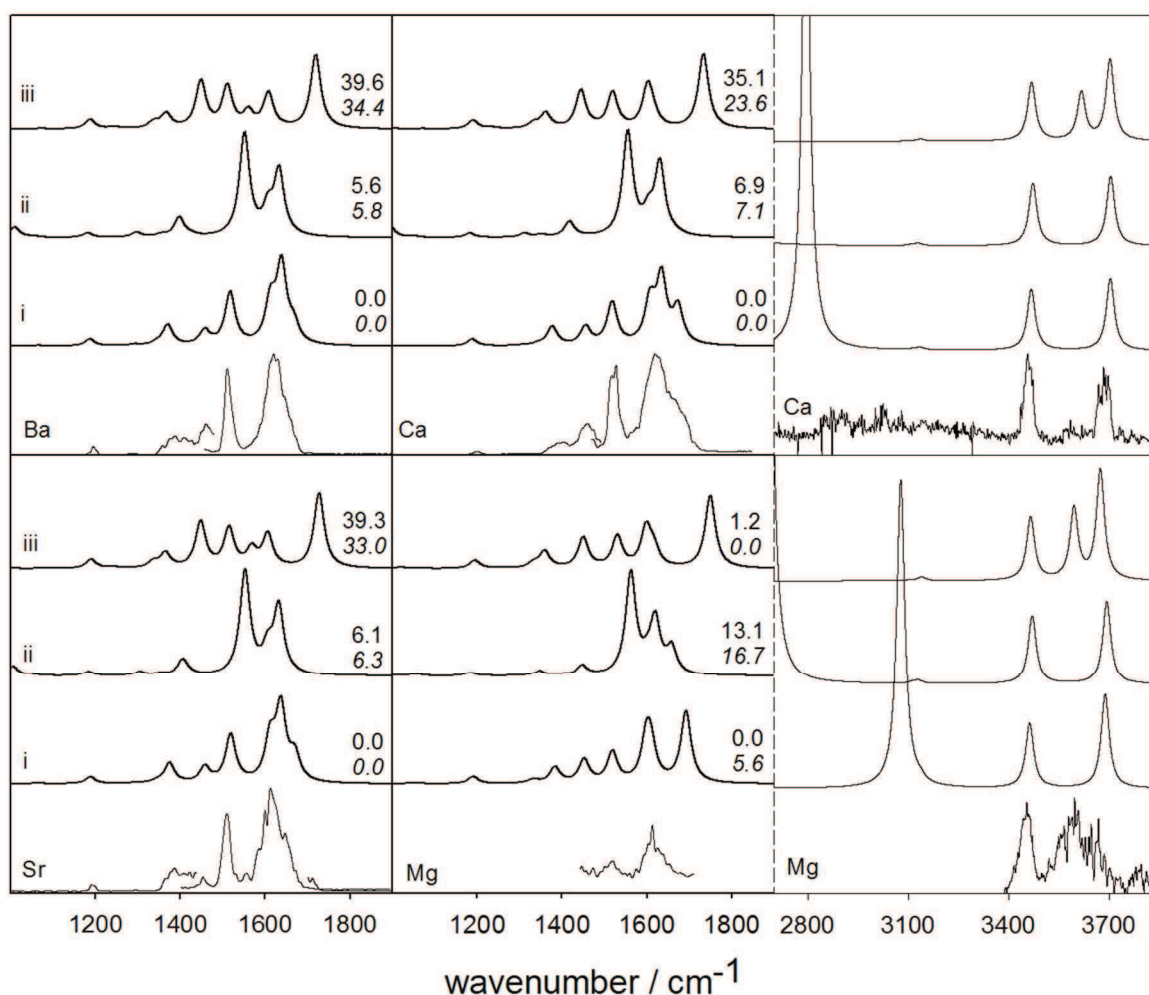


Figure 3.5. Experimental infrared multiple photon dissociation spectrum (bottom) for $[M(\text{Ura-H})(\text{H}_2\text{O})]^+$ compared with the B3LYP computed spectra using computational method 2 for the three lowest energy structures. Lowest energy structures represent the (i) N3O4/wbO2, (ii) N3O2/wbO4 and (iii) N3O4/wbO4 tautomers. The relative enthalpies and Gibbs energies (*italics*) calculated at 298 K are shown in kJ mol^{-1} .

cases. It is worth noting that for the complexes obtained with Ca, Sr and Ba, the shoulder experimentally observed on the blue side of the broad feature detected above 1610 cm^{-1} is also quite well reproduced by the calculated spectra of N3O4/wb2 forms (i). In the stretch region, both the N–H stretch of uracil as well as the free O–H stretch of the water molecule in structure (i) of the Ca complex match well with the experimental spectra.

The experimental spectrum of the Mg complex only offers two distinct bands, which may be used for assignment in the fingerprint region, while the O–H/N–H region offers more detailed information. The bands in the fingerprint regions correspond to the same predominant bands that are visible in the spectra for all other complexes; 1613 cm^{-1} for the hydrogen-bonded C=O stretching, H₂O scissoring and C5=C6 stretching combined modes, and 1520 cm^{-1} for the metal-coordinated carbonyl stretch. Both bands are prominently displayed in the calculated spectra for structures (i) and (iii). However, a lack of hydrogen bonding within the complex is suggested in the experimental spectrum through the broad band centred about 3595 cm^{-1} . This would correlate more so with structure (iii), in which the symmetric and asymmetric stretches of water are plainly observed.

3.3.3 Computed Structures for $[\text{M}(\text{Ura-H})(\text{H}_2\text{O})_2]^+$

A total of seven isomers were obtained for the doubly hydrated complexes of Ba, while six isomers were found for the complexes of Sr and Ca via method 1. Method 2 gives only five isomers for the Sr complex, the N3O2/wbO4/wbw structure obtained with method 1 evolving towards the N3O2/wbO4/wbO2 when using method 2. There are five distinct isomers optimized for complexes of Mg through both methods. For both computational methods, the hypothesized Mg-N3O2/wbO4/wbw input collapses towards a Mg-N3O2/wbO4/w structure, similar to the behaviour of Sr. Figure 3.6 gives binding schemes and energetics for the three lowest energy structures. All structures obtained for both calculation methods are given in Figures B9–B14 (Appendix B) along with energetics, while Table B2 summarizes the relative energies obtained with both calculations methods.

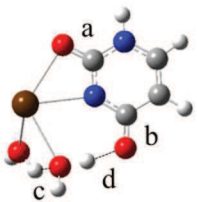
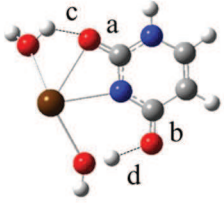
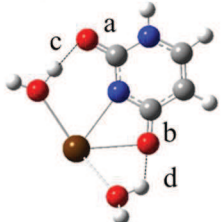
iii		M	$\Delta_{rel}H/\Delta_{rel}G$	a	b	c	d
		Ba	10.3/11.2	1.270	1.255	2.201	1.525
		Ca	14.6/9.2	1.275	1.252	4.640	1.597
ii		M	$\Delta_{rel}H/\Delta_{rel}G$	a	b	c	d
		Ba	7.0/7.0	1.274	1.251	2.061	1.559
		Sr	7.1/7.2	1.275	1.251	2.186	1.567
		Ca	7.5/7.2	1.276	1.250	2.417	1.586
		Mg	10.5/10.2	1.279	1.247	3.004	1.667
i		M	$\Delta_{rel}H/\Delta_{rel}G$	a	b	c	d
		Ba	0/0	1.246	1.280	1.629	2.048
		Sr	0/0	1.246	1.281	1.644	2.166
		Ca	0/0	1.244	1.283	1.675	2.359
		Mg	0/0	1.240	1.286	1.802	2.982

Figure 3.6. Comparison of the energies and structures for the three lowest energy $[M(\text{Ura-H})(\text{H}_2\text{O})_2]^+$ complexes, $M = \text{Ba}, \text{Sr}, \text{Ca}, \text{Mg}$. The thermochemistry reported here are those from method 2. Energies are expressed in kJ mol^{-1} and distances in Angströms.

For each metal centre, the N3O4/wbO2/wbO4 complex is the lowest energy form in both enthalpy and Gibbs energy. This result is consistent with previous findings obtained for the complexes of Ba and Sr [14]. In this structure, deprotonation occurs at the N3 of uracil, with metal coordination between N3 and O4, again confirmed by the presence of two BCPs of an electrostatic nature (positive values of $\nabla^2\rho$). Both water molecules are bound to the metal centre, with a hydrogen bond formed between one water molecule and O2, with the other water molecule hydrogen-bonded to O4. Note that in the case of both Ca and Mg, no hydrogen bonding is apparent between the water molecule and the O4

carbonyl (structures instead labelled as N3O4/wbO2/w). Consistently, the hydrogen bonds can be observed in the AIM analysis for complexes of Ba and Sr; however, no BCP is localized between the water molecule and O4 for the Ca or Mg complex. As already observed for the singly hydrated complexes, the hydrogen bond length increases (and therefore their strength decreases), with decreasing the size of the metal ion. The hydrogen bond between water and O2 is far stronger than the hydrogen bond involving O4, presumably because of the O4 position is also the metal binding site. The carbonyl bond lengths are similar to those computed for singly hydrated species, with the O2 carbonyl being shorter, $\sim 1.24 \text{ \AA}$, than the metal-coordinated O4 carbonyl, $\sim 1.28 \text{ \AA}$. Similar patterns are observed based on the size of the metal, although these trends are not as pronounced. As metal size increases, the metal-coordinated O4 carbonyl bond length decreases slightly. The length of the O2 carbonyl is the same for both the Ba and Sr complexes and marginally shorter for the Ca complex.

The nearest isomer in terms of energy for the Sr and Ca complexes, which is at least 7.0 kJ mol^{-1} higher in both enthalpy and Gibbs energy for all, is the N3O2/wbO4/wbO2 structure. The structure is very similar to the second lowest energy structure determined for singly hydrated complexes, uracil being again deprotonated at the N3 position, and metal coordination occurring between N3 and O2. Two water molecules are coordinated to the metal centre, one being hydrogen-bonded to the O4 position and the other seemingly hydrogen-bonded to O2. However, the distance between the water molecule and O2 in the Ca complex suggests there is likely no interaction. Even so, the N3O2/wbO4/wbO2 label is still applied to this structure in order to differentiate this particular form and the structure (iii) (Figure 3.6). For Ba, the N3O4/wbO2/wbw complex sits just slightly higher in energy.

This structure takes the same conformation as the lowest energy singly hydrated complex, with the additional water molecule bound between the metal centre and the other water molecule. This complex does not represent a local energy minimum for the other metals.

3.3.3.1 Comparison of Computed and Experimental Spectra

A comparison between the experimental spectra and the three lowest energy structures computed via method 2 is given in Figure 3.7 for the $[M(\text{Ura-H})(\text{H}_2\text{O})_2]^+$ ions. Spectra for all optimized structures, based on both calculation methods, are compared with the experimental spectra for all ions in Figures B9–B14 (Appendix B). Good agreement is obtained in all cases between the experimental spectra and those calculated for structure (i). Previous studies could not distinguish between the doubly hydrated structures of Ba and Sr in the $3200 - 3800 \text{ cm}^{-1}$ region [14], but as was the case for the singly solvated structures in this work, key features that are absent in the theoretical spectra for structures (ii) and (iii) allows structure (i) to be assigned to the observed ions.

Similar to the singly hydrated species, the two prominent bands in the fingerprint regions give good agreement across all calculated spectra. The experimental bands in the area of $1620 - 1635 \text{ cm}^{-1}$ (hydrogen-bonded C=O stretching, H₂O scissoring and C5=C6 stretching combined modes) as well as those at $1480 - 1530 \text{ cm}^{-1}$ (metal-coordinated carbonyl stretch) agree well with the computed spectra for structure (i), especially for Sr and Ca (Figure 3.7). The feature centred at 1481 cm^{-1} for Ba is broader than the others and does not match as well with the spectrum for (i), as it does for Sr and Ca. The small band occurring between 1455 and 1480 cm^{-1} , which in the Ba spectrum appears as, at best, a shoulder to the red of the metal bound carbonyl stretch, is the result of N1 hydrogen

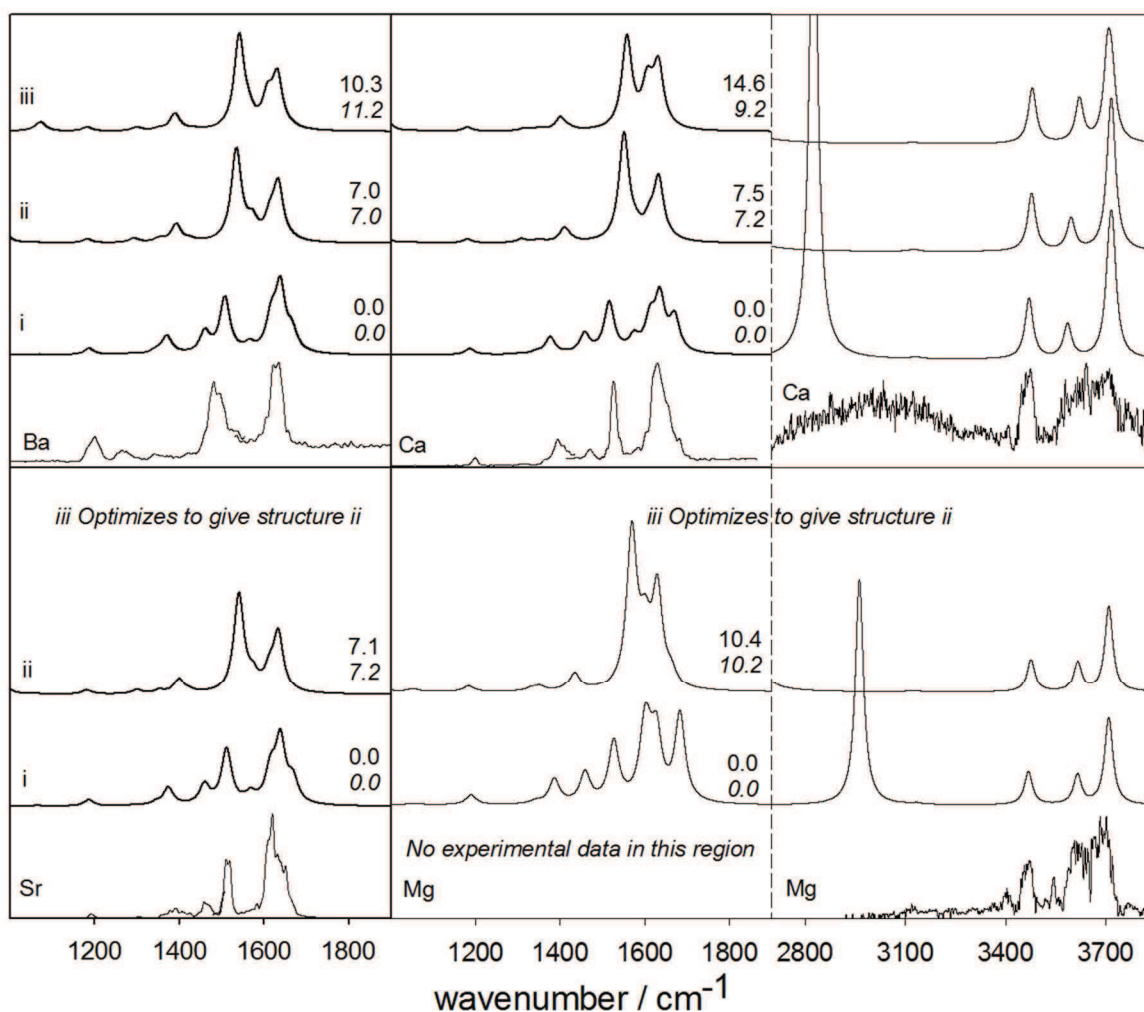


Figure 3.7. Experimental infrared multiple photon dissociation spectrum (bottom) for $[M(\text{Ura-H})(\text{H}_2\text{O})_2]^+$ compared with the B3LYP computed spectra using computational method 2 for the three lowest energy structures. Lowest energy structures represent the (i) N3O4/wbO2/w(bO4), (ii) N3O2/wbO4/w(bO2) and (iii) N3O2/wbO4/w tautomers. The relative enthalpies and Gibbs energies (italics) calculated at 298 K are also shown in kJ mol^{-1} .

wagging. The location of this vibration is only matched by the calculated spectra for structure (i) for each of the complexes.

As was the case for the singly hydrated species, both the N–H and free O–H stretches provide good agreement in the Ca and Mg complexes; however, all computed lowest energy structures display exactly the same features. An N–H stretch is observed at

3475 cm^{-1} for complexes of both metals. Two distinct free O–H stretching bands of water are found in the spectrum of the Mg complex, with both the asymmetric stretch as well as the free O–H stretch of the water hydrogen-bonded to uracil occurring at 3700 cm^{-1} and the symmetric stretch at 3630 cm^{-1} . Again, the lowest energy structure exhibits a strong hydrogen-bonded O–H band, which is not observed in the experimental spectrum which prevents a definitive assignment of the experimental structure. For the Ca complex, similar O–H stretches are observed at 3700 cm^{-1} and 3640 cm^{-1} , as well as a seeming broad band below 3400 cm^{-1} , indicative of the hydrogen bonded O–H stretch, further supporting structure (i) as the experimental structure of the Ca complex.

3.3.4 Computed Structures for $[\text{Mg}(\text{Ura-H})(\text{H}_2\text{O})_3]^+$

Fifteen isomers of the triply hydrated $[\text{Mg}(\text{Ura-H})]^+$ ion were obtained through method 1. Of those, the five lowest energy structures were re-optimized using method 2. Figure 3.8 gives the structures and energetics for the three lowest energy structures, with all optimized structures given in Figure B17 (Appendix B). Table B3 presents a comparison of thermochemistries deduced from both computational methods for the five lowest energy structures.

The lowest energy structure is deprotonated at the N3 position, with bidentate electrostatic Mg coordination to N3 and O4, as confirmed by AIM analysis. Three water molecules are all coordinated to the metal centre and are participating in hydrogen bonding with the uracil moiety – two water molecules presumably weakly interacting with O4 (although no localized BCPs are observed), and staggered on opposite sides of uracil, and the third water molecule hydrogen-bonded to O2 is found in the same plane as uracil.

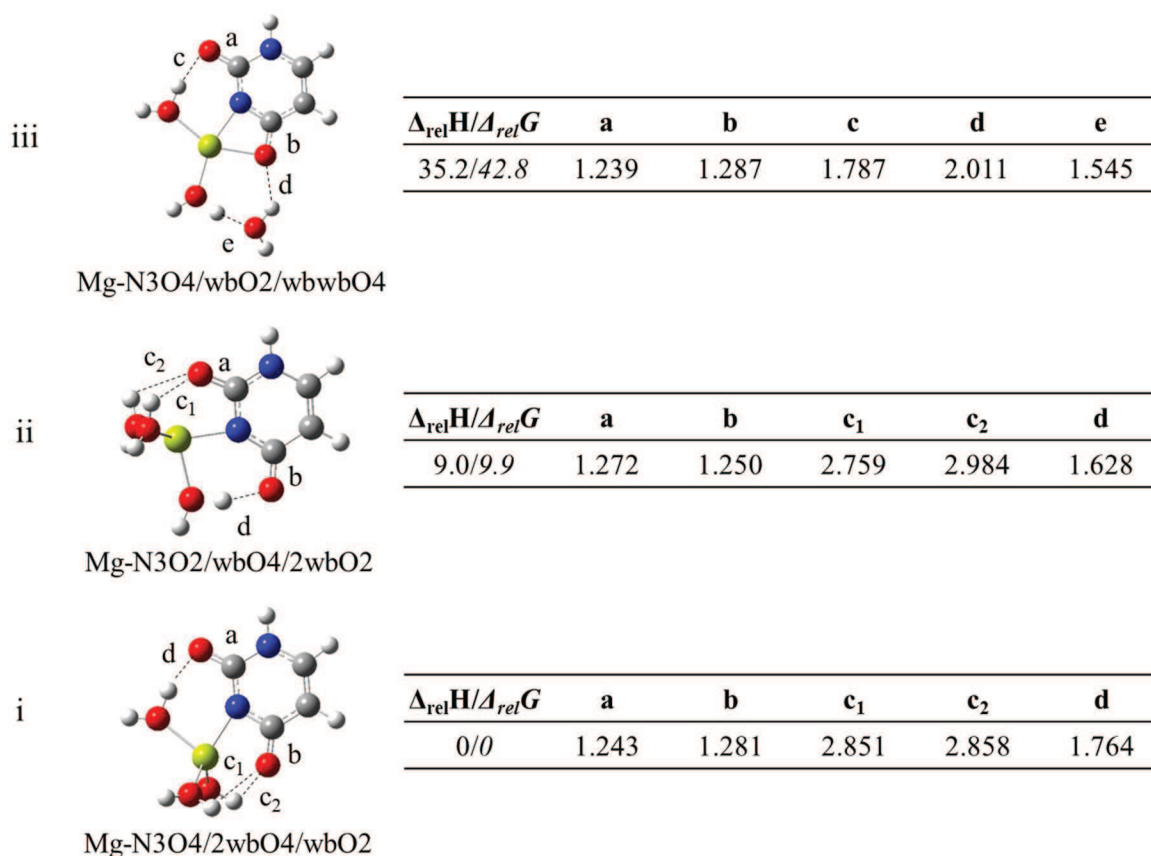


Figure 3.8. Comparison of the energies and structures for the three lowest energy $[\text{Mg}(\text{Ura-H})(\text{Ura})(\text{H}_2\text{O})_3]^+$ complexes. The thermochemistry reported here are those from method 2. Energies are expressed in kJ mol^{-1} and distances in Angströms.

This particular structure is labelled as N3O4/2wbO4/wbO2 in Figure 3.8.

The O4 carbonyl, which participates in the metal coordination, has a length of 1.280 Å; predictably shorter than the same carbonyl bond in the singly hydrated complex (1.297 Å) and doubly hydrated (1.286 Å). This shortening, and hence strengthening, of the carbonyl bond is attributed to the donation of electron density from the increased presence of water molecules weakening the M–O interaction, confirmed through AIM analysis by successively decreasing electron density at the BCPs as hydration increases. The O2 carbonyl length is 1.243 Å, which is only very slightly longer than the corresponding bond

in the singly hydrated (1.236 Å) and doubly hydrated (1.240 Å) species. Both water–O4 hydrogen bonds measure ~2.85 Å, while the water–O2 hydrogen bond has a length of 1.764 Å.

The only other isomer computed to be close in energy to the lowest energy structure is N3O2/wbO4/2wbO2, which is located about 9 kJ mol⁻¹ higher than N3O4/2wbO4/wbO2. In this particular isomer, deprotonation occurs at N3, with magnesium coordination now between N3 and O2. All three water molecules are again coordinated to magnesium. Two out of plane water molecules are hydrogen-bonded to O2, while the third interacts with O4 and lies in the same plane as uracil. The next lowest energy structure found is 35 kJ mol⁻¹ higher than the global minimum.

3.3.4.1 Comparison of Computed and Experimental Spectra

A comparison between the experimental spectra and the three lowest energy structures computed with method 2 is given in Figure 3.9 for the [Mg(Ura-H)(H₂O)₃]⁺ ion. The five lowest energy structures, based on both calculation methods, are compared with the experimental spectra in Figures B18 and B19 (Appendix B).

The agreement between the experimental IRMPD spectrum and the lowest energy structure is not bad, although the most intense band is predicted to have a shoulder, which is not observed. Structure iii also is in decent agreement although it is predicted to be considerably higher in energy. The O2 carbonyl stretch, calculated for structure (i) to be at 1677 cm⁻¹, is visible in the experimental spectrum as a band of its own at 1681 cm⁻¹; the intense band centred about 1623 cm⁻¹ is consistent with both scissoring of the water molecule hydrogen-bonded to O2 (calculated at 1624 cm⁻¹ for structure i) and the C5=C6

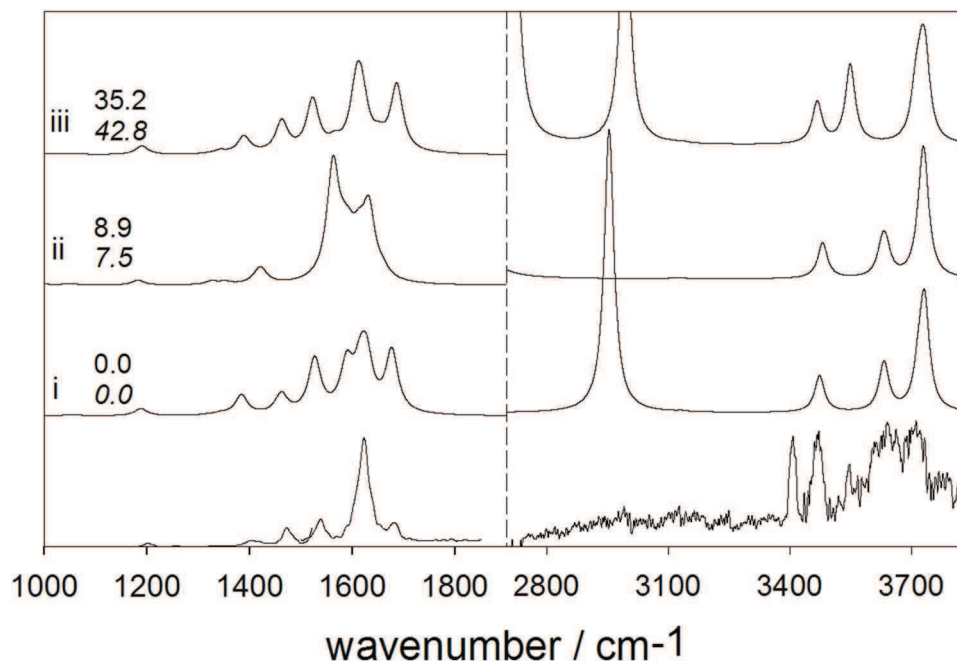


Figure 3.9. Experimental infrared multiple photon dissociation spectrum (bottom) for $[\text{Mg}(\text{Ura-H})(\text{H}_2\text{O})_3]^+$ compared with the B3LYP computed spectra using computational method 2 for the three lowest energy structures. Lowest energy structures represent the (i) N3O4/2wbO4/wbO2, (ii) N3O2/wbO4/2wbO2 and (iii) N3O4/wbO2/wbwbO4 tautomers. The relative enthalpies and Gibbs free energies (*italics*) calculated at 298 K are also shown in kJ mol^{-1} .

stretch (1615 cm^{-1} for structure i). The slight shoulder experimentally observed at 1590 cm^{-1} may be the result of synchronous (1592 cm^{-1}) and asynchronous (1588 cm^{-1}) scissoring of the out of plane water molecules, which may be isoenergetic with the most intense band in the experimental spectrum and could account for the higher than predicted intensity of this band. The scissoring motions of the two water molecules close to O4 in structure (iii) do not absorb with any appreciable intensity and are thus not observed in the calculated spectrum. A poor agreement between the spectrum of structure (ii) and the experimental trace is observed. Notably it cannot account for the two experimental bands detected at 1539 cm^{-1} and 1472 cm^{-1} . Both structure (i) and (iii) display the O carbonyl stretch at 1527 cm^{-1} and 1523 cm^{-1} , respectively, as well as N1 hydrogen wagging, computed at 1463 cm^{-1} for both.

The experimental spectra in the O–H/N–H region is nearly identical to that of the doubly hydrated Mg complex – an N–H stretch at 3475 cm^{-1} , and two O–H stretches at 3720 and 3650 cm^{-1} , corresponding to the asymmetric and symmetric O–H stretches in water, respectively. All stretches are noticeably blue-shifted with increasing hydration. A feature at 3410 cm^{-1} does not correspond to any of the calculated structures and cannot be accounted for. As with the other complexes, a hydrogen-bonded O–H stretch is not experimentally observed.

3.4 Summary

The structures of $[\text{M}(\text{Ura-H})(\text{H}_2\text{O})]^+$, where M corresponds to group 2 metal ions Ba^{2+} , Sr^{2+} , Ca^{2+} and Mg^{2+} , along with $[\text{M}(\text{Ura-H})(\text{H}_2\text{O})_2]^+$ for Ba^{2+} , Sr^{2+} and Ca^{2+} , as well as $[\text{Mg}(\text{Ura-H})(\text{H}_2\text{O})_3]^+$, were examined using IRMPD spectroscopy in the $1000 - 1900\text{ cm}^{-1}$ mid-infrared region. The same complexes were also examined in the $2700 - 3800\text{ cm}^{-1}$ O–H/N–H stretching region for Ca and Mg. Two different electronic structure calculation methods were employed for energy comparison of the various isomers, as well as for comparison with experimental spectra. There was good agreement between both computational methods for the structures, energies and computed IR spectra. The IR spectra generated for these lowest energy structures also generally agreed best with the experimental IRMPD spectra.

For all complexes, the lowest energy structures are deprotonated at N3 of uracil with the metal bound by a bidentate electrostatic interaction with N3 and O4, confirmed through AIM analysis. Any water molecules present are bound to the metal ion and participate in hydrogen bonding with the neighbouring carbonyls. In the case of singly

hydrated complexes, a hydrogen bond between water and uracil is established at the O2 position; for doubly hydrated ions, one water molecule is hydrogen-bonded to O2 while the second one is hydrogen-bonded to O4 (except for Ca and Mg, for which AIM analysis does not detect any water–O4 interaction). For the triply hydrated Mg/uracil complex, two water molecules are oriented towards O4, although no hydrogen bonds seem to be established, and the third water molecule is hydrogen-bonded to O2.

For the complexes of Ba, Sr and Ca, only the lowest energy structure gave calculated spectra in suitable agreement with the experimental IRMPD spectra, and in each case, the predominant contributor was easily assessed. For magnesium, however, even if the spectra of the lowest energy isomer did provide suitable agreement, it could not be conclusively determined as the major contributor because of good spectral agreement from other isomers.

3.5 Acknowledgements

The authors wish to thank the CLIO team (J.M. Ortega, C. Six, G. Perilhous, J. P. Berthet) as well as P. Maître and V. Steinmetz for their support during the experiments. The authors also acknowledge the computational resources provided by ACE-Net and Westgrid. Finally, T.D.F acknowledges the financial contributions from the NSERC, the Canadian Foundation for Innovation, and Memorial University of Newfoundland.

3.6 References

1. A.M. Pyle, *Science*, **1993**, 261, 709.
2. D.L. Nelson, M.M. Cox, A.L. Lehninger, *Principles of Biochemistry*, 3rd ed., W.H. Freeman, New York, NY, **2004**.
3. G.L. Eichhorn, L.G. Marzilli, *Advances in Inorganic Biochemistry: Metal Ions in Genetic Information Transfer*, Elsevier Science, New York, NY, **1981**.
4. P.-O. Lowdin, *Rev. Mod. Phys.*, **1963**, 35, 724.
5. P.O.P. Ts'o, *Basic Principles in Nucleic Acids Chemistry*, Academic Press, New York, NY, **1974**.
6. M.D. Topal, J.R. Fresco, *Nature*, **1976**, 263, 285.
7. H. Ruterjans, E. Kaun, W.E. Hull, H.H. Limbach, *Nucleic Acid Res.*, **1982**, 10, 7.
8. K. Nakanishi, N. Suzuki, F. Yamazaki, *Bull. Chem. Soc. Jpn.*, **1961**, 34, 53.
9. M.A. Kurinovich, J.K. Lee, *J. Am. Chem. Soc.*, **2000**, 122, 6258.
10. T.M. Miller, S.T. Arnold, A.A. Viggiano, A.E. Stevens Miller, *J. Phys. Chem. A*, **2004**, 108, 3439.
11. M.T. Nguyen, A.K. Chandra, T. Zeegers-Huyskens, *J. Chem. Soc., Faraday Trans.*, **1998**, 94, 1277.
12. Y. Huang, H. Kenttamaa, *J. Phys. Chem. A*, **2003**, 107, 4893.
13. S.M. Bachrach, M.W. Dzierlenga, *J. Phys. Chem. A*, **2011**, 115, 5674.
14. A.A. Power, O.Y. Ali, M.B. Burt, T.D. Fridgen, *Int. J. Mass Spectrom.*, **2012**, 330–332, 233.
15. B. Power, V. Haldys, J.-Y. Salpin, T.D. Fridgen, *Int. J. Mass Spectrom.*, **2015**, 378, 328.

16. O.Y. Ali, N.M. Randell, T. D. Fridgen, *ChemPhysChem*, **2012**, *13*, 1507.
17. S. Guillaumont, J. Tortajada, J.-Y. Salpin, A.M. Lambashi, *Int. J. Mass Spectrom.*, **2005**, *243*, 279.
18. T.D. Fridgen, *Mass Spectrom. Rev.*, **2009**, *28*, 586.
19. N.C. Polfer, J. Oomens, *Mass Spectrom. Rev.*, **2009**, *28*, 468.
20. R. Prazeres, F. Glotin, C. Insa, D. A. Jaroszynski, J. M. Ortega, *Eur. Phys. J. D*, **1998**, *3*, 87.
21. W. Paul, *Rev. Mod. Phys.*, **1990**, *62*, 531.
22. K. Rajabi, M. L. Easterling, T. D. Fridgen, *J. Am. Soc. Mass Spectrom.*, **2009**, *20*, 411.
23. M. Azargun, T.D. Fridgen, *Phys. Chem. Chem. Phys.*, **2015**, *17*, 25778.
24. M.J. Frisch, G.W. Trucks, H.B. Schlegel, G.E. Scuseria, M.A. Robb, J.R. Cheeseman, G. Scalmani, V. Barone, B. Mennucci, G.A. Petersson, H. Nakatsuji, M. Caricato, X. Li, H.P. Hratchian, A.F. Izmaylov, J. Bloino, G. Zheng, J.L. Sonnenberg, M. Hada, M. Ehara, K. Toyota, R. Fukuda, J. Hasegawa, M. Ishida, T. Nakajima, Y. Honda, O. Kitao, H. Nakai, T. Vreven, J.A. Montgomery, J.E. Peralta J., F. Ogliaro, M. Bearpark, J.J. Heyd, E. Brothers, K.N. Kudin, V.N. Staroverov, T. Keith, R. Kobayashi, J. Normand, K. Raghavachari, A. Rendell, J.C. Burant, S.S. Iyengar, J. Tomasi, M. Cossi, N. Rega, J.M. Millam, M. Klene, J.E. Knox, J.B. Cross, V. Bakken, C. Adamo, J. Jaramillo, R. Gomperts, R.E. Stratmann, O. Yazyev, A.J. Austin, R. Cammi, C. Pomelli, J.W. Ochterski, R.L. Martin, K. Morokuma, V.G. Zakrzewski, G.A. Voth, P. Salvador, J.J. Dannenberg, S. Dapprich, A.D. Daniels, O. Farkas, J.B. Foresman, J.V. Ortiz, J. Cioslowski, D.J. Fox, *Gaussian 09*, Revision D.01, Gaussian, Inc., Wallingford, CT, **2013**.
25. P.B. Armentrout, M. Citir, Y. Chen, M.T. Rodgers, *J. Phys. Chem. A*, **2012**, *116*, 11823.
26. P.B. Armentrout, Y. Chen, M.T. Rodgers, *J. Phys. Chem. A*, **2012**, *116*, 3989.
27. R.F.W. Bader, *Atoms in Molecules: A Quantum Theory*, Clarendon Press, Oxford University Press, New York, NY, **1990**.

28. T.A. Keith, *AIMAll*, Version 14.10.27, TK Gristmill Software, Overland Park, KS, **2014**, aim.tkgristmill.com.
29. O.Y. Ali, T.D. Fridgen, *Int. J. Mass Spectrom.*, **2011**, 308, 167.
30. P. Colarusso, K. Zhang, B. Gup, P.F. Bernath, *Chem. Phys. Lett.*, **1997**, 269, 39.
31. Y.-w. Nei, T.E. Akinyemi, C.M. Kaczan, J.D. Steill, G. Berden, J. Oomens, M.T. Rodgers, *Int. J. Mass Spectrom.*, **2011**, 308, 191.

CHAPTER 4 – Structures of $[M(\text{Ura-H})(\text{Ura})]^+$ and $[M(\text{Ura-H})(\text{H}_2\text{O})_n]^+$ ($M = \text{Cu}, \text{Zn}, \text{Pb}; n = 1 - 3$) Complexes in the Gas Phase by IRMPD Spectroscopy in the Fingerprint Region and Theoretical Studies

The gas-phase structures of the bare dimers, $[M(\text{Ura-H})(\text{Ura})]^+$, and hydrated monomers, $[M(\text{Ura-H})(\text{H}_2\text{O})_n]^+$, were examined using infrared multiple photon dissociation spectroscopy in the fingerprint region ($1000 - 1900 \text{ cm}^{-1}$) for $M = \text{Cu}, \text{Zn}$, and Pb and $n = 1 - 3$. The experimental results were compared to those calculated using density functional methods. The dimeric structures all show deprotonation of one uracil moiety at N3, and each forms a tetracoordinate interaction with N3 and O4 of the deprotonated uracil, and N3 and O2 of the neutral uracil. The hydrated monomers, $[M(\text{Ura-H})(\text{H}_2\text{O})]^+$, all have rather different structures. Uracil is deprotonated at N3 for $M = \text{Zn}$ and Pb , but for Cu , uracil is deprotonated at N1 and Cu^{2+} is bound to N1 and O2. Like the $[M(\text{Ura-H})(\text{Ura})]^+$ complexes, in $[\text{Pb}(\text{Ura-H})(\text{H}_2\text{O})]^+$ the metal is bound to N3 and O4. The Zn^{2+} complex actually better resembles $[\text{M}(\text{Ura})(\text{OH})]^+$ with a proton apparently transferred from water to O4 of uracil and the metal cation coordinated to O2. Unlike the singly hydrated complex, uracil is deprotonated at N3 in $[\text{Cu}(\text{Ura-H})(\text{H}_2\text{O})_2]^+$. In all singly, doubly, and triply solvated complexes studied, water is found to be coordinated to the metal cation.

A version of this chapter has been published:

B. Power, V. Haldys, J.-Y. Salpin, T.D. Fridgen, *Int. J. Mass Spectrom.*, **2017**, dx.doi.org/10.1016/j.ijms.2017.05.003.

4.1 Introduction

The sequencing of nucleobases in DNA and RNA forms the basis of our genetic code. The formation of proteins relies upon proper transcription of the DNA sequence to messenger RNA, through the Watson-Crick pairing of nucleobases [1]. This proper base pairing is mainly dependent upon hydrogen bonding interactions. Should the configuration of a nucleobase be altered, resulting in changes to hydrogen bonding sites, disruption of proper Watson-Crick pairing can result, leading to errors in transcription and thus genetic mutations. Among other biological processes, metal ions play an important role in RNA stability and activity [2–4], but their presence also has the ability to affect the tautomerization of nucleobases [5], thus impacting the hydrogen bonding sites and potentially leading to mis-matched base pairs and genetic mutations [6]. Transition metal dications have shown an increased affinity towards nucleobases compared to their group 2 counterparts [7], with copper having the greatest affinity of the divalent cations [8]. Cu^{2+} is one of the metal ions of interest in this current work, along with Zn^{2+} and Pb^{2+} , and the impact they have on the structure of both bare and hydrated uracil complexes.

Each of these metals has been thoroughly explored in terms of their enhancement of or interference in biological processes. While copper is important to nucleotide stability, it can also reach toxic levels in cells, causing reduction of hydrogen peroxide in the mitochondria. As a result, this produces highly reactive hydroxyl radicals which can negatively impact DNA and cause membrane damage [9,10]. Zinc is one of the most abundant d-block elements found in cell cytoplasm, and has a role in gene regulation and protein folding [11,12], making its inclusion in this work particularly interesting. The toxic impact and detrimental effect Pb^{2+} has on human health has been well documented, in

particular its disruption of biological homeostasis and its targeting of the heart, liver and kidneys [13].

While several stable tautomers of uracil exist, as well as its DNA replacement thymine, it is the diketo form that is favoured [14–18]. The diketo tautomer of uracil, along with the numbering scheme for uracil, is presented in Scheme 2.1. The interaction of the Cu^{2+} , Zn^{2+} and Pb^{2+} ions with both uracil and thymine have been explored both experimentally and computationally. Both Cu^{2+} and Zn^{2+} have been shown to stabilize the keto-enol tautomer of thymine [19]. When complexed with uracil, each of these dications will deprotonate uracil to form a singly charged ion of the form $[\text{M}(\text{Ura-H})]^+$. However, the site of deprotonation is dependent upon the metal. Both Pb^{2+} [20] and Zn^{2+} [21] will deprotonate uracil from the N3 position, and form a bidentate interaction with uracil at N3 and O4. This binding is also characteristic of the $[\text{M}(\text{Ura-H})]^+$ moiety in $[\text{M}(\text{Ura-H})(\text{Ura})]^+$ (loosely termed “dimeric complex”) when M is Zn or Pb [22,23] or the group 2 cations [24–26]. By contrast, the $[\text{Cu}(\text{Ura-H})]^+$ complex was shown to be deprotonated at the N1 position of uracil, with Cu bound to N1 and O2 [27,28]. However, the dimeric complex adopts a similar structure to the Pb and Zn dimers, where deprotonation occurs at N3 and metal binding is to N3 and O4 of the deprotonated moiety [23,29,30].

The current work uses IRMPD spectroscopy in the fingerprint region ($1000 - 1900 \text{ cm}^{-1}$) to explore the structures of bare dimeric $[\text{M}(\text{Ura-H})(\text{Ura})]^+$ complexes, as well as hydrated monomers $[\text{M}(\text{Ura-H})(\text{H}_2\text{O})]^+$, where M = Cu, Zn, and Pb. The doubly hydrated monomers of Cu and Zn are also examined, along with the triply hydrated Zn monomer. The chief feature in the fingerprint region is carbonyl stretching, which is then compared to the computed spectra for several lowest energy isomers for each complex.

4.2 Methods

4.2.1 Experimental

All experiments were performed using a Fourier-transform ion cyclotron resonance mass spectrometer (FT-ICR-MS) coupled to a mid-infrared free electron laser (FEL) at the Centre Laser Infrarouge d'Orsay (CLIO) [31,32]. 0.01 mmol L⁻¹ solutions of the chloride salts of each metal ion were prepared using 18 MΩ-cm water (Millipore). Uracil solutions were prepared to 1 mmol L⁻¹ in 18 MΩ-cm water (Millipore). Mixtures were then prepared in a 1 to 10 ratio of metal solution to uracil solution, and introduced via syringe injection to the electrospray ion source at a flow rate of 75 μL h⁻¹. The ions were mass selected with a quadrupole mass filter and introduced in to the ICR cell, where they are then isolated and irradiated with the free electron laser. To accomplish hydration, bare [M(Ura-H)]⁺ ions were mass selected in the quadrupole mass filter and stored in the hexapole storage cell, where water vapour had been introduced [33]. Irradiation times varied from 0.1 to 3 s, with the shorter irradiation times corresponding to the more weakly bound hydrated ions. Areas of the IRMPD spectra which experienced saturation were scanned after attenuation of the FEL. The laser was scanned at 5 cm⁻¹ intervals from ~1000 to 1900 cm⁻¹. The IRMPD efficiency is the negative of the natural logarithm of parent ion intensity divided by the sum of parent and fragment ion signals.

4.2.2 Computational

Calculations for all structures were conducted using the Gaussian 09 suite of programs [34]. Each structure was optimized, and infrared spectra computed, using B3LYP density functional theory. For the complexes of Cu and Zn, the 6-31+G(d,p) basis set was

applied to all atoms. For complexes of Pb, the LANL2DZ basis set with relativistic core potential was applied to the Pb atom and the 6–31+G(d,p) basis was used for all other atoms. Single point energy calculations were then carried out using B3LYP with the 6–311+G(3df,3pd) basis set on all atoms except Pb, for which the LANL2DZ basis set with relativistic core potential was used. This computational method will be referred to as method 1.

All calculations were then repeated, for the five lowest energy structures, with the def2-TZVPP basis set which has been found to work better for metal-cation amino acid complexes than the LANL2DZ [35,36] for all metals during both the optimization and single point energy calculations. The def2-TZVPP basis set contains polarization functions, which are not included in the LANL2DZ basis set. The 6–31+G(d,p) basis set was again used for all other atoms (C, H, N and O) during optimization, followed by the 6–311+G(3df,3pd) basis set for single point energy calculations. This computational method will be referred to as method 2.

These single-point electronic energies, using methods 1 and 2 were used to compute the enthalpies and Gibbs energies of isomeric species at 298 K, using the unscaled harmonic vibrational frequencies calculated for the optimization geometries.

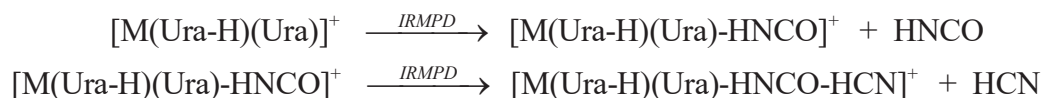
The bonding within the individual equilibrium structures was also explored by locating the bond critical points (BCPs) using atoms-in-molecules (AIM) theory [37], which is based on a topological analysis of the electronic density at the BCPs, and is a good descriptor of the bond character; electrostatic or covalent. This analysis was conducted using optimized structures from method 2 using the AIMAll software [38]. Data from the topological analysis are given collectively in the Appendix C as Figure C13.

Due to errors with the computational method and basis set as well as errors with the harmonic approximation, when comparing the calculated IR spectra to the experimental IRMPD spectra, it is typical that a scaling of the computed spectra to better match the experimental spectra is done. In this work, for comparison with the experimental spectra, the computed infrared spectra were all scaled by a factor of 0.97, consistent with other molecules of this type in this region of the infrared [25,26,30]. Further the computed spectra were convoluted with a Lorentzian profile with a width (FWHM) of 15 cm⁻¹.

4.3 Results and Discussion

4.3.1 Examination of the IRMPD Spectra

For the hydrated monomers of all metals, the primary fragmentation pathway results from the sequential loss of water solvent molecules. For the case of the bare dimer complexes, the primary fragmentation pathway is dependent upon the identity of the metal center [22,23,29]. For M = Cu and Zn,



where the identity of the fragment ions for the Cu²⁺ complex was explored previously [29]. [Pb(Ura-H)(Ura)]⁺ simply loses uracil upon IRMPD activation. The hydrated complexes were found to simply lose solvent.

Figure 4.1 is a comparison of the experimental spectra for all [M(Ura-H)(Ura)]⁺ complexes in the 1000 – 1900 cm⁻¹ region. All three complexes exhibit similar features in the 1517 – 1553 cm⁻¹ region, corresponding to an enolic C–OH stretch, characteristic of the lowest energy structures of each which will be discussed later. Above 1600 cm⁻¹, only

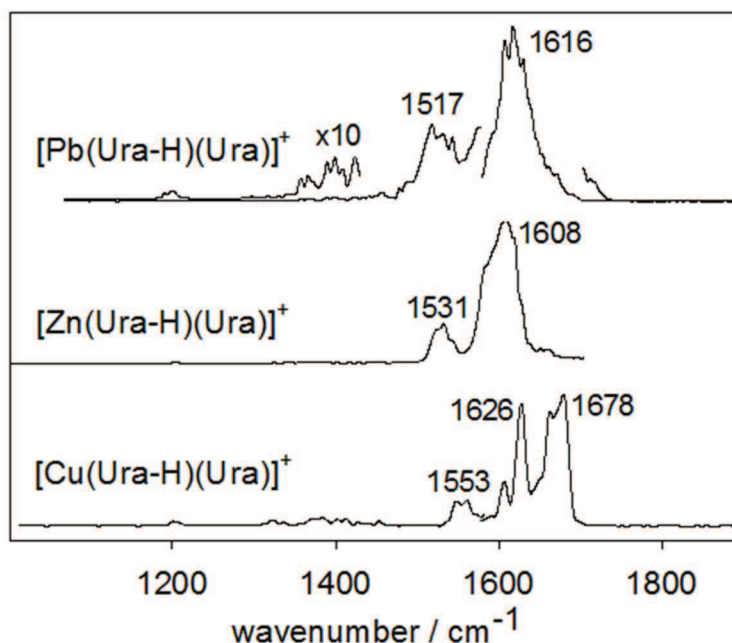


Figure 4.1. Infrared multiple photon dissociation spectra for $[M(\text{Ura-H})(\text{Ura})]^+$ ($M = \text{Cu}, \text{Zn}, \text{Pb}$) in the 1000–1900 cm^{-1} region.

one band is observed for the Zn and Pb complexes, while two major bands are observed in the Cu complex. For the Cu complex, blue shifting of the C=O stretch, by approximately 60 – 70 cm^{-1} in comparison to the other metals, allows the intense C=C stretch (1626 cm^{-1}), and the carbonyl stretches centered at 1678 cm^{-1} to be resolved. This separation is not seen in the Zn and Pb complexes, as one broad band encompasses both the C=C and C=O stretching modes. For the Cu^{2+} complex, a slight distinction between the different carbonyl stretching modes is observed, with the metal coordinated carbonyl stretch emerging as a shoulder on the red side of this band. The carbonyl stretching bands, for all complexes, are red-shifted in comparison to the free C=O stretch of uracil, at 1750 cm^{-1} in the gas phase [39], as metal coordination weakens the carbonyl bond. When compared to the $[M(\text{Ura-H})(\text{Ura})]^+$ complexes of group 2 dications, these carbonyl stretches occur in roughly the same position [25], with the exception of the Cu^{2+} complex. The blue-shifting

of the carbonyl stretches of the $[\text{Cu}(\text{Ura-H})(\text{Ura})]^+$ complex in comparison to the other metals is rationalized in the following way; It has previously been demonstrated that Cu^{2+} exhibits greater binding energy to carbonyl groups of peptide ligands [40]. Though this would intuitively suggest a weakening of the carbonyl bond, metal-to-ligand charge transfer is facilitated as a result of this increased binding energy, donating electron density back to the carbonyl, which serves to strengthen the carbonyl bond. It would be reasonable to expect a similar result in the present complexes.

For the bare monomeric species, $[\text{M}(\text{Ura-H})]^+$, an IRMPD spectrum has been recently obtained for $\text{M} = \text{Pb}$ [41] by coupling the FEL to a quadrupole ion trap. For this complex, Pb interacts with uracil at the O4 carbonyl [20], and a very intense signal at 1755 cm^{-1} corresponds to the free carbonyl stretch at O2. Consequently, the free $\text{C}=\text{O}$ stretch can result in a very intense feature under IRMPD conditions. Within this current work, IRMPD spectra could not be obtained for the $[\text{M}(\text{Ura-H})]^+$ complexes, presumably because the dissociation energy was too high to be reached under our experimental conditions. However, the solvated monomers are easily dissociated and were examined using IRMPD spectroscopy. In Figure 4.2, the IRMPD spectrum for the $[\text{M}(\text{Ura-H})(\text{H}_2\text{O})]^+$ complexes in the $1000 - 1900 \text{ cm}^{-1}$ region are presented. The spectrum of the $[\text{Pb}(\text{Ura-H})(\text{H}_2\text{O})]^+$ complex offers many distinct features to assist in characterization, such as the carbonyl stretch (centered at 1702 cm^{-1}), $\text{C}=\text{C}$ stretching and H_2O scissoring (1595 cm^{-1}), metal coordinated carbonyl stretch (1534 cm^{-1}) and N-H wagging (1454 cm^{-1}). An additional signal is also observed around 1750 cm^{-1} , in the area of a free carbonyl stretch. The spectrum for Cu contains a band in the carbonyl stretching region, although it is significantly red-shifted in comparison to the Pb spectrum. Aside from that, there is a large,

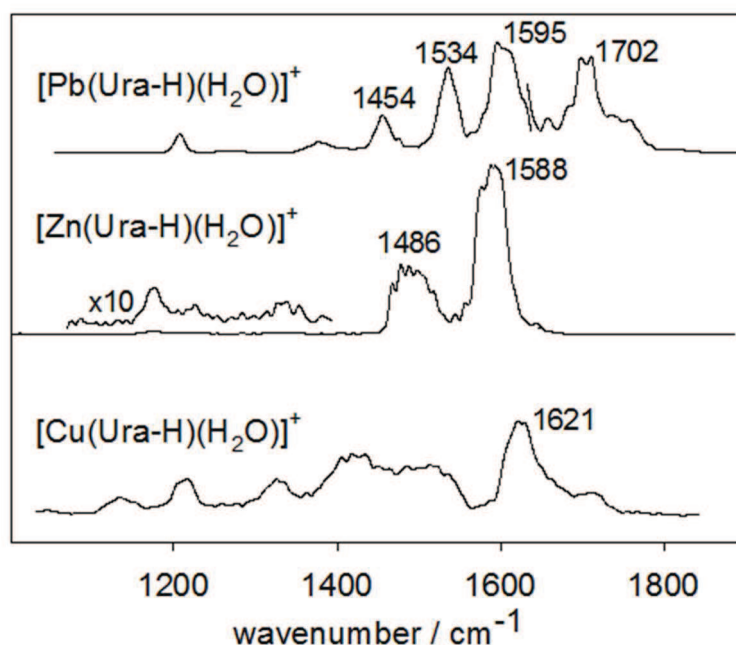


Figure 4.2. Infrared multiple photon dissociation spectra for $[M(\text{Ura-H})(\text{H}_2\text{O})]^+$ ($M = \text{Cu}, \text{Zn}, \text{Pb}$) in the 1000–1900 cm^{-1} region.

broad absorption between 1400 cm^{-1} and 1550 cm^{-1} . Interestingly, the spectrum for $[\text{Zn}(\text{Ura-H})(\text{H}_2\text{O})]^+$ shows no features above 1600 cm^{-1} , only an intense band at 1588 cm^{-1} and a broad feature centred at 1486 cm^{-1} . The intense band is in the C=C and red shifted C=O stretching regions, while the 1486 cm^{-1} feature is in the protonated carbonyl stretching region.

Figure 4.3 shows the IRMPD spectrum for the doubly and triply hydrated monomers in the fingerprint region. An experimental spectrum for $[\text{Pb}(\text{Ura-H})(\text{H}_2\text{O})_2]^+$ could not be obtained due to the inability to isolate enough of the ion, and only the triply hydrated Zn species was isolated. Neither of the spectra for the doubly or triply hydrated Zn^{2+} complexes offer much in the way of band resolution, although broad absorptions with a sharp onset at about 1720 cm^{-1} are observed down to about 1375 cm^{-1} . The $[\text{Cu}(\text{Ura-H})(\text{H}_2\text{O})_2]^+$ complex, on the other hand, gives a very well resolved spectrum with bands at

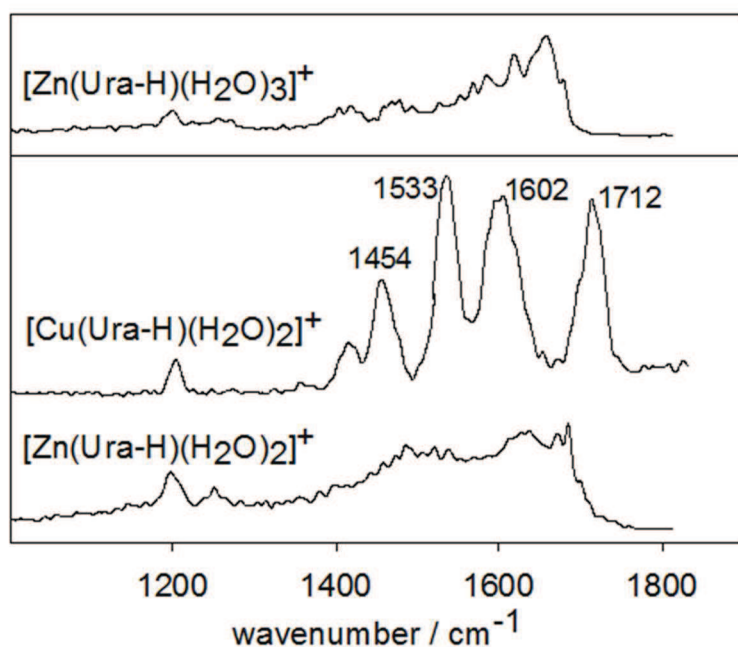


Figure 4.3. Infrared multiple photon dissociation spectra for $[\text{Zn}(\text{Ura-H})(\text{H}_2\text{O})_2]^+$, $[\text{Cu}(\text{Ura-H})(\text{H}_2\text{O})_2]^+$ and $[\text{Zn}(\text{Ura-H})(\text{H}_2\text{O})_3]^+$ in the 1000–1900 cm^{-1} region.

1712 cm^{-1} (carbonyl stretching), 1602 cm^{-1} (H_2O scissoring), 1533 cm^{-1} ($\text{C}=\text{C}/\text{C}=\text{O}$ stretching) and 1454 cm^{-1} (N-H wagging). As noted above, the carbonyl stretching is shown to be higher in energy when Cu is the metal center, but the inclusion of two water molecules leads to donation of electron density back to the carbonyl bonds, strengthening them even further, which blue-shifts this carbonyl stretch even more.

4.3.2 Computed Structures for $[\text{M}(\text{Ura-H})(\text{Ura})]^+$

A total of 27 minima were found for the Cu^{2+} complex, 25 for the Zn^{2+} complex and 16 for the Pb^{2+} complex. In Figure 4.4, the geometries and energetics for the lowest energy isomers of each complex are presented, based upon the results of calculation method 2. In Figures C1 to C3 (Appendix C), all structures and energetics are presented for the method 1, along with a comparison of energetics by method 2 for the five lowest energy

structures, where relatively good agreement is noted across both methods. In the isomer labelled as structure i in Fig. 4.4, one uracil is deprotonated at N3, and metal coordination occurs between N3 and O4. The neutral uracil is a tautomer where hydrogen has been transferred from N3 to O4, and the metal is coordinated to N3 and O2. An intramolecular hydrogen bond occurs between the O4 enol of the neutral uracil and O2 carbonyl of the deprotonated uracil. With a bond length of ~ 1.5 Å, this interaction is relatively strong. This isomer is the lowest in energy for the M = Cu and Pb complexes, which is consistent with results previously obtained for Cu [23,29] and Pb [22], and comparable to the ammoniated dimer of Cu [30] as well as similar bare dimers metalated by group 2 dications [24,25]. This structure is only slightly higher in energy for the Zn complex by a nominal amount.

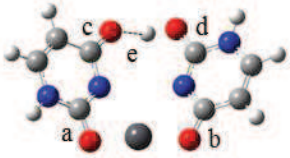
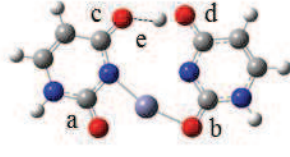
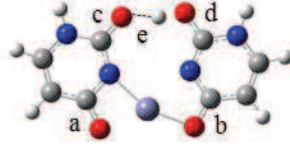
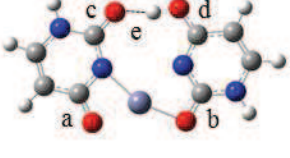
iv		M	$\Delta_{\text{rel}}H/\Delta_{\text{rel}}G$	a	b	c	d	e
		Pb	8.5/8.6	1.268	1.269	1.258	1.285	1.373
iii		M	$\Delta_{\text{rel}}H/\Delta_{\text{rel}}G$	a	b	c	d	e
		Pb	8.8/8.9	1.270	1.263	1.248	1.294	1.509
		Zn	12.7/12.2	1.273	1.277	1.248	1.288	1.487
		Cu	7.6/7.4	1.274	1.263	1.248	1.284	1.452
ii		M	$\Delta_{\text{rel}}H/\Delta_{\text{rel}}G$	a	b	c	d	e
		Pb	3.4/4.1	1.276	1.267	1.250	1.295	1.475
		Zn	0.0/0.0	1.280	1.281	1.249	1.289	1.460
		Cu	1.8/2.3	1.278	1.267	1.250	1.285	1.435
i		M	$\Delta_{\text{rel}}H/\Delta_{\text{rel}}G$	a	b	c	d	e
		Pb	0.0/0.0	1.278	1.262	1.244	1.299	1.566
		Zn	1.3/0.7	1.281	1.277	1.243	1.293	1.543
		Cu	0.0/0.0	1.282	1.261	1.243	1.290	1.526

Figure 4.4. Comparison of the energies and structures for the lowest energy $[\text{M}(\text{Ura-H})(\text{Ura})]^+$ complexes, M = Cu, Zn, Pb. The thermochemistry reported here are those from method 2.

AIM topological analysis (Appendix C, Fig. C13) was conducted for isomer i for each complex, as well as isomer ii for the Zn complex, which is lowest in energy for that metal. The tetradentate metal interactions are confirmed by the topological analysis, as four bond critical points (BCPs) are observed connecting the metal to the two uracil units. The metal-uracil and hydrogen bonding interactions are electrostatic as indicated by the positive values of the Laplacian of the electron density, $\nabla^2\rho$, (Appendix C, Fig. C13). The free carbonyl is the shortest of all C=O bonds, followed by the metal coordinated carbonyls and then the protonated carbonyl C=O bond. In terms of the two metal coordinated carbonyls, that of the deprotonated uracil is slightly longer.

These structural differences relative to the neutral diketo tautomer, as a result of the presence of the metal ion, can have biological impacts through the disruption of hydrogen bonding between base pairs [42–44]. Both the deprotonation as well as the keto-enol proton transfer change the hydrogen bonding environment and may have a negative effect on the structural integrity of the nucleic acid strand, specifically RNA in the case of uracil.

Two additional structures in Figure 4.4 found to be comparable in terms of energy show only slight differences from the first structure. In structure ii, the metal is coordinated to the N3 and O4 of the uracil where the proton has been transferred to O2, and an intermolecular hydrogen bond is formed between O2 enol of uracil, and O2 of deprotonated uracil. This particular structure is the lowest in energy when Zn is the metal center. Structure iii instead has metal coordination to N3 and O2 of both uracils, proton transfer from N3 to O4, and an intermolecular hydrogen bond between the O4 enol and the O4 of deprotonated uracil. Specific to the Pb complex is a fourth structure nearly identical to the first, labelled as structure iv. In this configuration, Pb is coordinated at the N3 and O2

position of deprotonated uracil, and N3 and O4 of the neutral uracil where proton transfer from N3 results in a tautomer with an enol at O2. This enol then hydrogen bonds to the O4 of the deprotonated uracil. This particular isomer is observed using method 1 for Zn, but optimizes to give the structure i using method 2, as the enol proton is transferred between uracil moieties. When Cu is the metal center, this configuration optimizes as structure i for both calculation methods. All other isomers were determined to be significantly higher in energy by both methods of calculation.

All lowest energy structures are planar for Cu and Zn, but are bent for Pb at an angle of approximately 125°. This is to be expected, given the much larger size of the Pb ion ($\text{Cu}^{2+} = 87 \text{ pm}$, $\text{Zn}^{2+} = 88 \text{ pm}$ and $\text{Pb}^{2+} = 133 \text{ pm}$), in combination with repulsion from the lone pair of electrons in a hybridized sp orbital.

4.3.2.1 Comparison of Computed and Experimental Spectra

A comparison of the experimental spectra for the $[\text{M}(\text{Ura-H})(\text{Ura})]^+$ structures with the calculated spectra for isomers i – iv is shown in Figure 4.5. In the Cu^{2+} complex, the bands above 1600 cm^{-1} are resolved, which contrasts with the Zn and Pb complexes. This resolution offers three distinct maxima – a band centered at 1678 cm^{-1} with a shoulder at 1663 cm^{-1} (hydrogen bonded and metal coordinated carbonyls, respectively), and another band at 1626 cm^{-1} , reflective of the C=C stretch. Each of these vibrations are observed in the computed spectrum for structure i, although a large, unresolved band in this area appears for structure iii which cannot be discredited. Perhaps the most distinguishing feature is the less intense protonated C=O stretch at 1553 cm^{-1} in the experimental spectrum, which only occurs in structure i.

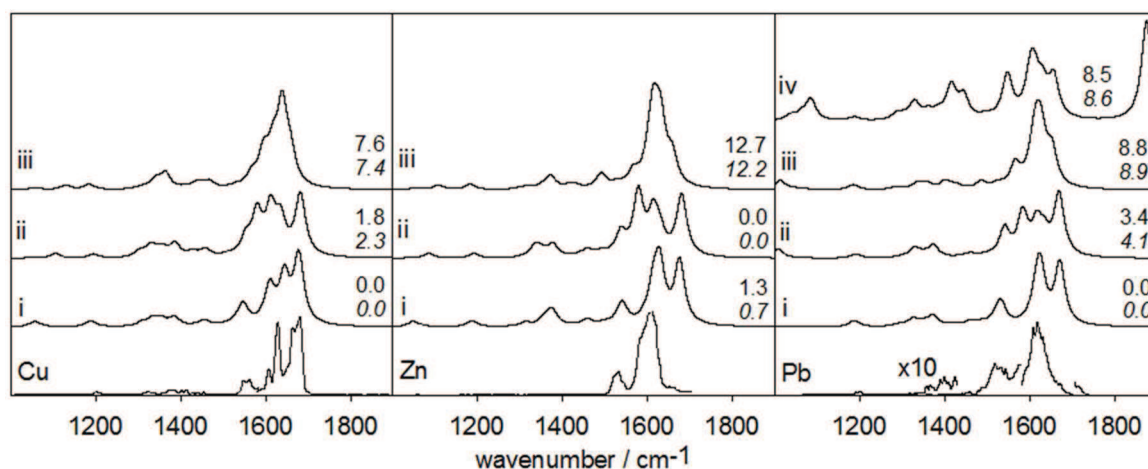


Figure 4.5. Experimental IRMPD spectrum (bottom) for $[M(\text{Ura-H})(\text{Ura})]^+$ compared with the B3LYP computed spectra using computational method 2 for the lowest energy structures. The calculated relative enthalpies and 298 K Gibbs energies (italics) are also shown.

In the experimental IRMPD spectra for Zn^{2+} and Pb^{2+} complexes, the same resolution in the C=O and C=C region is not observed as it was for the Cu^{2+} complex. The calculated spectra for structure i does differentiate between these stretches, with the hydrogen bonded carbonyl, $\sim 1670 \text{ cm}^{-1}$, appearing to the blue of the metal coordinated carbonyl band, which is the one corresponding to the experimental spectrum. In the experimental spectrum of the Zn complex, a very weak feature is observed that corresponds to the calculated position of the hydrogen bonded carbonyl stretch by structure i. The protonated C=O stretches, however, exhibit good agreement between experimental and structure i. Given the lack of resolution between carbonyl stretches in experimental spectra, which is more consistent with structure iii, no definitive assignment can be made to the primary contributing structure for the Zn and Pb dimers. Structure ii, which is actually lowest in energy for the Zn complex, could also be considered although it offers resolution of all carbonyl and C=C stretches which was not observed experimentally.

The Boltzmann distribution of the lowest energy isomers was calculated, using $e^{-\Delta G/RT}$ to determine the percentage of each isomer in the mixture. A spectrum is then created based upon this distribution, using a percentage of the calculated IR intensity corresponding to the Boltzmann distribution for each isomer, and combining those together into a new spectrum. This spectrum is included in Figure C10 (Appendix C), however does not offer better agreement than any of the individual isomers independently.

4.3.3 Computed Structures for $[M(\text{Ura-H})(\text{H}_2\text{O})]^+$

There are 7 different isomers obtained for the $[\text{Pb}(\text{Ura-H})(\text{H}_2\text{O})]^+$ complex, along with 25 for Zn and 19 for Cu by computational method 1. These structures, along with energetics, are presented in Figures C4 to C6 (Appendix C), along with a comparison of the computed relative energetics to method 2 for the five lowest energy structures. Once again, good agreement is obtained across both methods. The lowest energy structures were re-optimized using method 2 and are summarized in Figure 4.6. The structures of $[\text{Pb}(\text{Ura-H})(\text{H}_2\text{O})]^+$ are consistent with those calculated previously [22], in which the lowest energy structure is deprotonated at the N3 position, Pb coordinates to N3 and the O4 carbonyl, and the water molecule is bound directly to the Pb center with a hydrogen bonding interaction to the O2 carbonyl. This structure is identified as 1-i(Pb). Through the AIM topological analysis (Appendix C, Fig. C13), the electrostatic nature of this bidentate interaction is confirmed, as is the hydrogen bonding relationship. A second structure just slightly higher in energy, 1-ii(Pb), once again demonstrates deprotonation at N3 and water coordination directly to Pb, but now shows Pb coordination to N3 and O2, with water hydrogen bonding to the O4 carbonyl. For both isomers, the carbonyl involved in metal coordination is

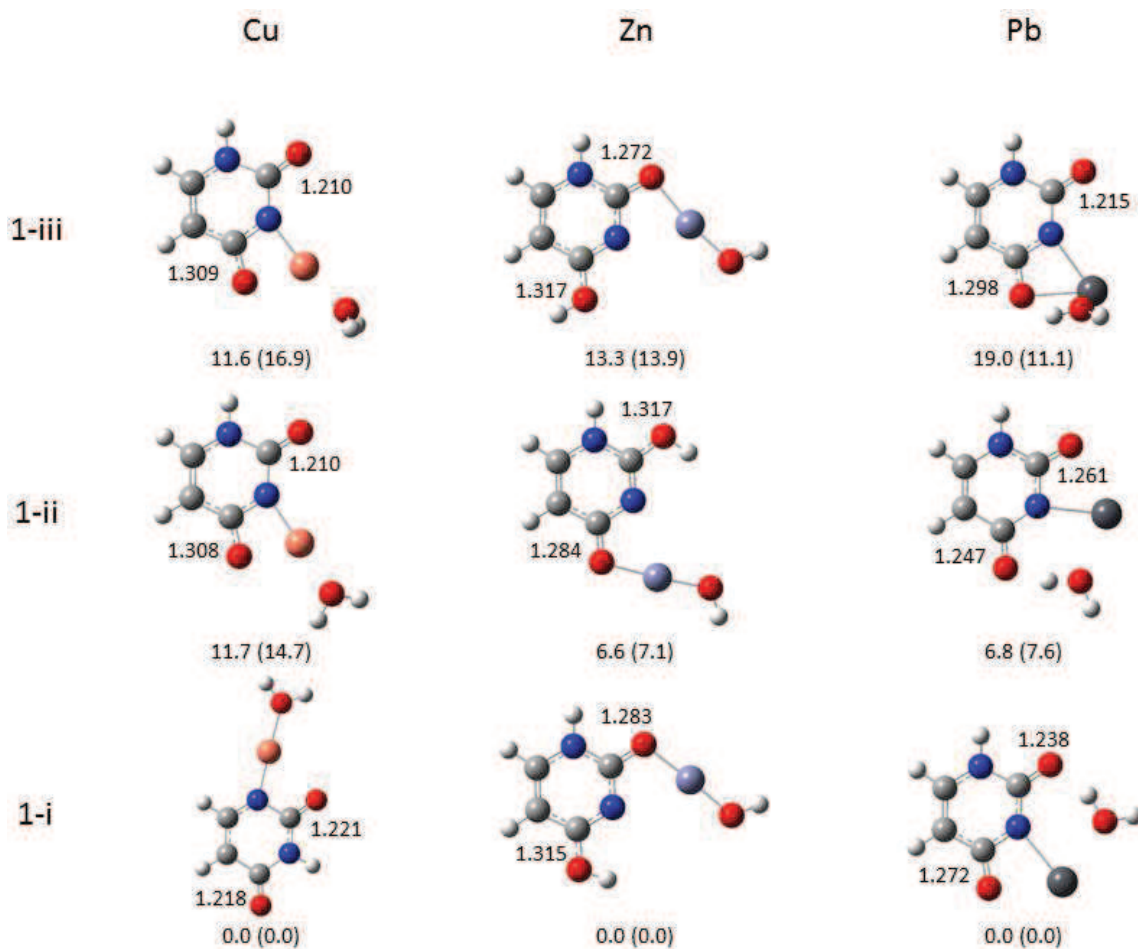


Figure 4.6. Comparison of the energies and structures for the lowest energy $[M(\text{Ura-H})(\text{H}_2\text{O})]^+$ complexes, $M = \text{Cu}, \text{Zn}, \text{Pb}$. The thermochemistry reported here are those from method 2.

consistently longer ($\sim 1.26 \text{ \AA} - 1.27 \text{ \AA}$) than the other carbonyl bond ($\sim 1.24 \text{ \AA} - 1.25 \text{ \AA}$), although this discrepancy in bond lengths is much larger in structure 1-i(Pb).

Given the lack of a carbonyl feature in the experimental spectrum for $[\text{Zn}(\text{Ura-H})(\text{H}_2\text{O})]^+$, additional structures were optimized in which the water solvent transfers a proton to the uracil moiety, resulting in a $[\text{Zn}(\text{Ura})(\text{OH})]^+$ complex. This particular configuration proved to be lowest in energy. Deprotonation is again at the N3 position. One would expect a bidentate interaction of Zn with the N3 and O2 positions, however the AIM analysis indicates there is only a single interaction between Zn and O2, with no BCP

present between Zn and N3. Proton transfer apparently occurs from water to O4, resulting in a neutral keto-enol tautomer of uracil. The resulting hydroxide is bound directly to Zn, and does not participate in any hydrogen bonding interactions with the uracil moiety. As this structure is a keto-enol tautomer, the carbonyl bond lengths are notably longer, at 1.31 Å for the enol and 1.28 Å for the metal coordinated carbonyl. A similar structure just slightly higher in energy has Zn coordination to O4, with a proton transferred from water to the O2 position, resulting in an enol. It has been shown that water bound to Zn^{2+} experiences a decrease in pK_a from 15.7 to 7.9 [45], facilitating the loss of a proton from water. The deprotonation of water by Zn^{2+} has been observed previously, particularly in metalloenzymes. Zn^{2+} has a d^{10} configuration, and thus is not subject to ligand field stabilization effects, making it suitable for interaction with protein-binding sites that deviate from an octahedral geometry or coordination number of 6 [45], nor is it capable of any redox activity. In carbonic anhydrase, zinc-bound hydroxide attacks CO_2 to form zinc-bound bicarbonate, and the bicarbonate is subsequently replaced by a water molecule. The water molecule very rapidly ionizes to regenerate zinc-bound hydroxide, a process facilitated by histidine-64, where the proton is shuttled to the non-hydrogenated imidazole nitrogen [45]. The $[\text{Zn}(\text{Ura-H})(\text{H}_2\text{O})]^+$ isomers where the water molecule remains intact are $> 25 \text{ kJ mol}^{-1}$ higher in energy.

In the case of $[\text{Cu}(\text{Ura-H})(\text{H}_2\text{O})]^+$, the lowest energy structure is deprotonated at the N1 position, similar to the bare monomer. Much like the Zn complex, there is seemingly a bidentate interaction with copper coordinated to the N1 and O2 position, however the AIM topological analysis does not show a BCP between Cu and O2. The water molecule, bound directly to Cu, does not interact with the uracil moiety. This structure is labelled as 1-i(Cu)

in Fig. 4.6. Now that both carbonyl bonds are free, they display a similar length at ~ 1.22 Å. Even though the 1-i(Cu) structure is lowest in energy, the N3 deprotonated structure, 1-ii(Cu), is now relatively closer in terms of energy when compared to the bare structures, which were separated by approximately $15 - 35 \text{ kJ mol}^{-1}$ [27,29]. Considering that these two bare monomers were virtually isoenergetic when solvent model calculations were performed [29], one would expect that the inclusion of solvent molecules would close the gap in energy between the N1 and N3 deprotonated structures.

4.3.3.1 Comparison of Computed and Experimental Spectra for $[\text{Zn}(\text{Ura-H})(\text{H}_2\text{O})]^+$ and $[\text{Pb}(\text{Ura-H})(\text{H}_2\text{O})]^+$

A comparison of the experimental spectra for the $[\text{M}(\text{Ura-H})(\text{Ura})]^+$ structures with the calculated spectra for isomers 1-i – 1-iii is shown in Figure 4.7. For the Zn complex, good agreement is observed between the experimental spectrum and the calculated spectra for each of the three lowest energy isomers. Structure 1-i(Zn) is the best match with the experimental spectrum in terms of both band shape and position, although neither 1-ii(Zn) nor 1-iii(Zn) can be discounted entirely. The intense band at 1588 cm^{-1} in the experimental spectrum, a combination of both metal coordinated carbonyl and C=C stretching, is observed at 1611 cm^{-1} for isomer 1-i(Zn). These two modes are separated in isomer 1-ii(Zn) and is blue-shifted to 1628 cm^{-1} in structure 1-iii(Zn). The protonated C=O stretch experimentally observed at 1486 cm^{-1} occurs at 1492 cm^{-1} in isomer 1-i(Zn), demonstrating remarkable agreement. Congruence is also noted at the enlarged feature at 1175 cm^{-1} , where both C-H wagging and enolic O-H wagging occur.

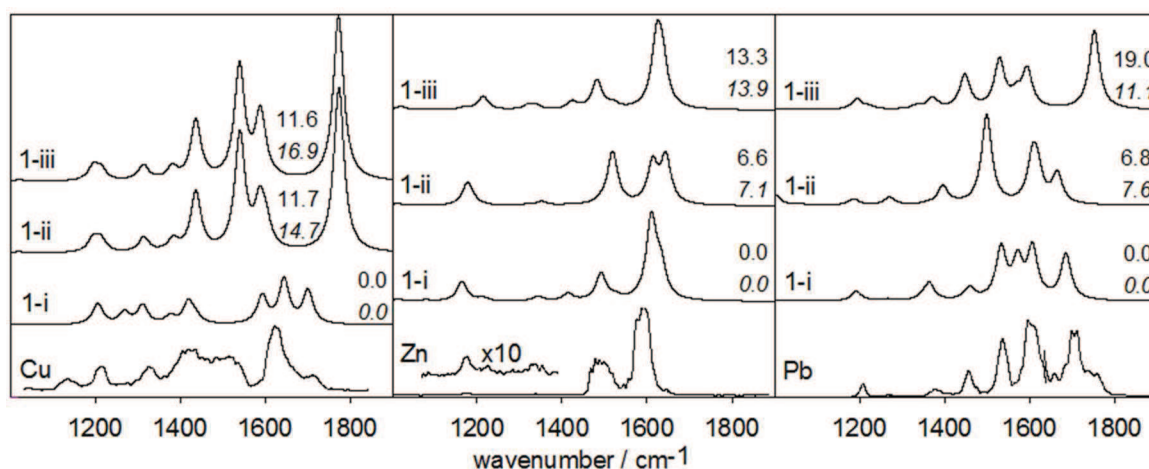


Figure 4.7. Experimental IRMPD spectrum (bottom) for $[M(\text{Ura-H})(\text{H}_2\text{O})]^+$ compared with the B3LYP computed spectra using computational method 2 for the lowest energy structures. The calculated relative enthalpies and 298 K Gibbs energies (italics) are also shown.

In previous work involving the Pb complex, both structure 1-i and 1-ii were identical to the experimental spectrum in the O-H/N-H region, and could not be distinguished from one another [22]. With the current work in the mid-infrared region, differences between the calculated spectra of these isomers are observed, and structure 1-i corresponds most closely with the experimental spectrum. In particular, there is good alignment with all features below 1550 cm^{-1} , namely the metal coordinated carbonyl (1534 cm^{-1}) and N-H wagging (1454 cm^{-1}), along with the more minor features of C-N stretching at 1360 cm^{-1} and C-H wagging at 1190 cm^{-1} . The most predominant feature in the experimental spectrum, an intense band with a maximum at 1595 cm^{-1} with a shoulder to the blue, aligns closely with the two better-resolved bands in the spectrum for 1-i, attributed to H_2O scissoring, at the lower frequency, and C=C stretching. The carbonyl stretch is in a position slightly lower in frequency in the calculated spectra for structure 1-i, at 1684 cm^{-1} , however it offers the closest agreement with the experimental carbonyl stretch of all computed structures. Structure 1-ii cannot be ignored entirely as a contributor, especially

considering the good agreement in the most intense band at 1595 cm^{-1} , in addition to a small band at 1660 cm^{-1} in the experimental spectrum, between two far more intense bands which is in good agreement with the carbonyl stretch of structure 1-ii. Finally, note that an experimental signal is also observed around 1750 cm^{-1} . Comparison with the IRMPD spectrum obtained for the $[\text{Pb}(\text{Ura-H})]^+$ complex [41] suggests that this experimental feature probably corresponds to the stretching of a free C=O group. This signal proves to be in good agreement with the free C=O stretch computed for the 1-iii structure, which is located only 11.1 kJ mol^{-1} higher in Gibbs energy. Therefore, a mixture of at least two different forms may be obtained for the $[\text{Pb}(\text{Ura-H})(\text{H}_2\text{O})]^+$ complex, with a minor contribution of 1-iii as suggested by the weak abundance of the experimental signal. Note that the bond length computed for the O2 carbonyl in 1-iii (1.215 \AA) is similar to the bond length obtained for the $[\text{Pb}(\text{Ura-H})]^+$ ion (1.213 \AA), consistent with a similar position of the experimental band. The Boltzmann distribution spectra were not examined in this case, with the lowest energy isomers accounting for approximately 93% of the composition of the mixture in each case.

4.3.3.2 Spectra for $[\text{Cu}(\text{Ura-H})(\text{H}_2\text{O})]^+$

The singly hydrated monomer of Cu presents a perplexing result when compared to the experimental spectrum, where none of the calculated spectra are in good agreement. The calculated spectra for structures 1-ii and 1-iii are nearly identical, as the structures differ only by rotation in the water molecule. Based on the lowest energy structures, the free carbonyl stretching should be readily observed, a feature that is present experimentally, but is not as intense as one would expect from the computed spectra. A minor band

observed experimentally at 1712 cm^{-1} does offer agreement with the band observed for structure 1-i corresponding to the O2 carbonyl stretch. The sharpest and most intense band in the experimental spectrum is 1621 cm^{-1} , and one broad band covering the area from 1400 cm^{-1} to 1550 cm^{-1} , neither of which can be accounted for in the spectra in the lowest energy structures.

The number of initial input geometries used to determine the lowest energy structure through calculations was greatly expanded for these complexes, although a lower energy isomer was not found. Isomers having the form $[\text{Cu}(\text{Ura})(\text{OH})]^+$, the configuration adopted by the Zn complex, were also explored resulting in 13 additional structures, none of which were lower in energy than structure 1-i(Cu) by calculation method 1. A comparison of these structures is presented in Figure C11 of the Appendix C. Solvent modelling using the Polarizable Continuum Model (PCM) as well as an empirical dispersion correction were both added to the $[\text{Cu}(\text{Ura-H})(\text{H}_2\text{O})]^+$ complexes when calculating in an effort to find another structure lower in energy that may match the experimental spectra, but to no avail. Although the experimental spectra in the high frequency O-H/N-H stretching region has not been collected, a comparison of the calculated spectra in this region for the three lowest energy structures (Appendix C, Figure C12) suggests that this region would not offer any useful information in terms of complex determination, as the calculated spectra are all identical.

4.3.4 Computed Structures for $[\text{M}(\text{Ura-H})(\text{H}_2\text{O})_2]^+$

For the doubly hydrated monomers, only calculations of the Cu and Zn species were conducted since the Pb complex was not observed experimentally. For the Cu complex, a

total of 57 isomers were optimized by method 1, along with 39 distinct isomers of the Zn complex. All of these isomers are given in Figures C7 and C8 (Appendix C), along with a comparison of energetics to method 2 for the five lowest energy structures. The calculations were repeated on the lowest energy structures using method 2, with the results presented in Figure 4.8 along with the calculated energetics and spectra.

For $[\text{Cu}(\text{Ura-H})(\text{H}_2\text{O})_2]^+$, the inclusion of a second water molecule leads to the lowest energy structure now exhibiting deprotonation at N3, with Cu coordinated to N3 and O4, and two solvent molecules are bound directly to Cu. One of these water molecules participates in a hydrogen bond with the O2 carbonyl, which is not involved in metal binding. This isomer is referred to as 2-i. This presents a noticeable change in structure in comparison to the bare $[\text{Cu}(\text{Ura-H})]^+$ [27], as well as the structure currently determined as lowest in energy for $[\text{Cu}(\text{Ura-H})(\text{H}_2\text{O})]^+$, both of which are deprotonated at the N1 position,

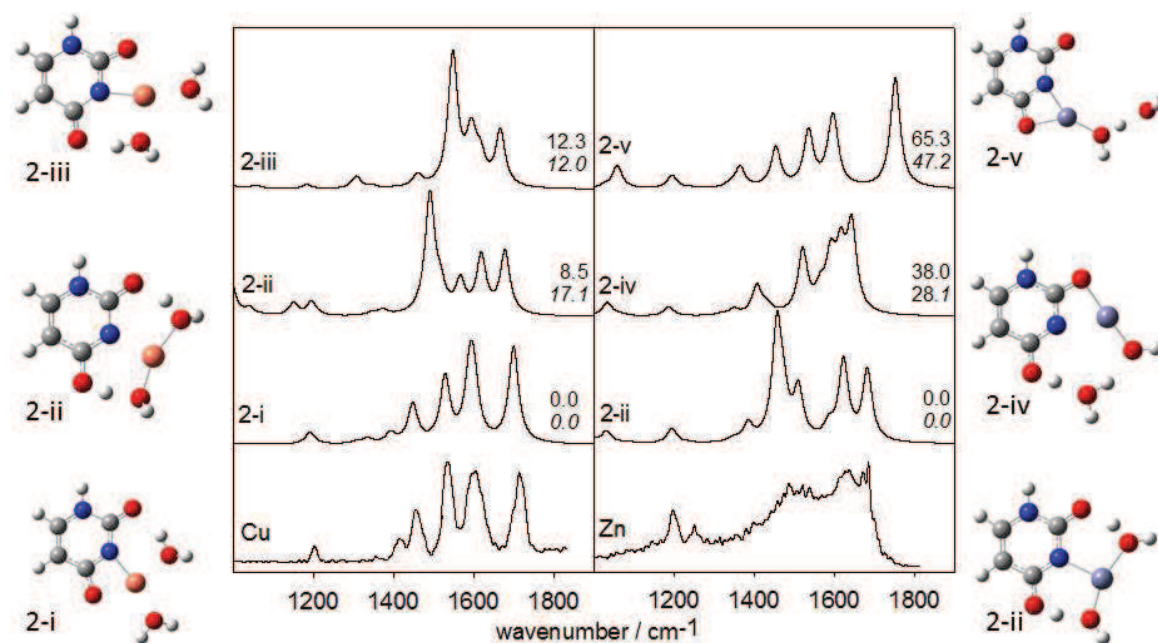


Figure 4.8. Experimental IRMPD spectrum (bottom) for $[\text{M}(\text{Ura-H})(\text{H}_2\text{O})_2]^+$, $\text{M} = \text{Cu}$ (left) and Zn (right), compared with the B3LYP computed spectra using computational method 2 for the three lowest energy structures. The calculated relative enthalpies and Gibbs energies (italics) are also shown.

demonstrating a clear solvent effect. Structure 2-iii is opposite in terms of the behaviour of the carbonyl groups, with the metal now bound to N3 and O2, two water molecules bound directly to Cu, one of which interacting with O4 through hydrogen bonding. The middle isomer, structure 2-ii, is interesting in that there is no bidentate interaction between Cu and uracil. Rather, Cu is bound only to the deprotonated N3 position. Both water molecules are still coordinated directly to Cu, which is common to all isomers. However, since neither carbonyl interacts with the metal ion, they are both available for hydrogen bonding with the solvent. When using structures 2-i, 2-ii and 2-iii as the initial input for optimization calculations for $[\text{Zn}(\text{Ura-H})(\text{H}_2\text{O})_2]^+$, each results in the 2-ii isomer, which is significantly lower in energy than any other isomer. It is interesting to note that the Zn complex prefers the configuration where the metal has just a single interaction with uracil. However, the characteristics of N3 deprotonation and solvent coordination directly to the metal are consistent.

The AIM topological analysis (Appendix C, Fig. C13) confirms all metal interactions with uracil, including the single interaction for $[\text{Zn}(\text{Ura-H})(\text{H}_2\text{O})_2]^+$, through the presence of BCPs. The positive nature of the Laplacian of the electron density, $\nabla^2\rho$, also confirms the electrostatic nature of these interactions. The solvent coordination to the metals, as well as the hydrogen bonds between water and carbonyl, are also observed through the presence of BCPs.

4.3.4.1 Comparison of Computed and Experimental Spectra

The experimental spectra for $[\text{M}(\text{Ura-H})(\text{H}_2\text{O})_2]^+$ are compared to the spectra of the three lowest energy structures as determined by method 2 in Figure 4.8. For the Cu

complex, remarkable agreement is obtained between the experimental spectrum and structure 2-i, allowing for confident assignment of structure 2-i as the principal contributor. Both the intensity as well as the scaled positions of the carbonyl stretching modes (1712 cm^{-1}), H_2O scissoring modes (1602 cm^{-1}), $\text{C}=\text{C}$ stretching mode (1533 cm^{-1}) and N-H wagging mode (1454 cm^{-1}) are in excellent alignment with the experimental spectrum. Another minor feature, C-H wagging at 1200 cm^{-1} , also matches between the experimental spectrum and structure 2-i. Though a case could be made for a contribution from structure 2-ii based on majority of the spectral features, it is the intense band at 1491 cm^{-1} , which corresponds to the H_2O scissoring in this isomer, which allows for this structure to be ruled out.

While the experimental spectrum for the Zn complex is not very well resolved, structure 2-ii still presents a compelling case. Even though there is a large band encompassing frequencies from approximately 1400 cm^{-1} to 1700 cm^{-1} , there are still local maxima that are evident that correspond to the scaled computed spectra for structure 2-ii. Of particular note, major bands in the spectrum for structure 2-ii occur at 1682 cm^{-1} , 1623 cm^{-1} , and 1457 cm^{-1} , corresponding to the hydrogen bonded carbonyl stretches, $\text{C}=\text{C}$ stretch and H_2O scissoring, respectively. These bands correspond to maxima observed within the broad band of the experimental spectrum. As was the case for the Cu complex, the less intense C-H wagging vibration at 1200 cm^{-1} also corresponds well. A more compelling argument, however, may be that structures 2-iv and 2-v are considerably higher in energy, and 2-v contains an intense free carbonyl stretching frequency at $\sim 1750\text{ cm}^{-1}$, which is absent in the experimental spectrum.

4.3.5 Computed Structures for $[\text{Zn}(\text{Ura-H})(\text{H}_2\text{O})_3]^+$

Using the 10 lowest energy isomers of $[\text{Zn}(\text{Ura-H})(\text{H}_2\text{O})_2]^+$ as a starting point, a total of 46 isomers were obtained for the triply hydrated Zn complex using computational method 1, all of which are given in Figure C9 (Appendix C), with a comparison of energetics based upon method 2 for the five lowest energy structures. Based upon method number 2, the four lowest energy structures along with their computed energetics and spectra are presented in Figure 4.9. All structures demonstrate deprotonation of the uracil at the N3 position, which has been a consistent theme throughout. As we have seen with Zn previously, it does not participate in a bidentate interaction in this monomeric complex, instead binding directly to the N3 site. The lowest energy structure, labelled as structure 3-i, has all three solvent molecules bound directly to the metal center, two of which participate in a hydrogen bond to each of the neighbouring carbonyls. Both the single interaction between Zn and N3, as well as the hydrogen bonds between the water molecules

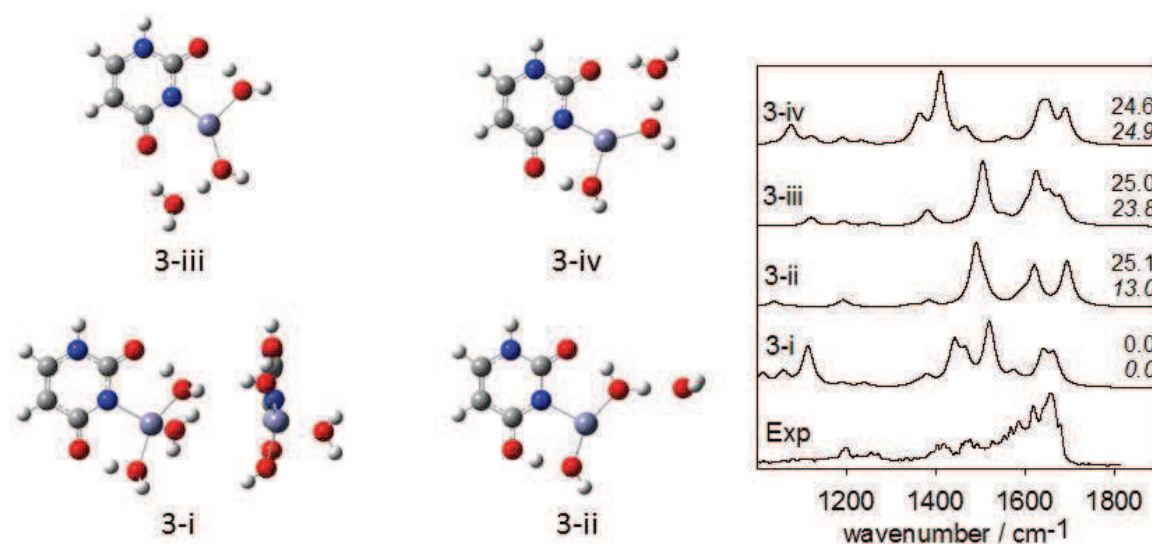


Figure 4.9. Experimental IRMPD spectrum (bottom) for $[\text{Zn}(\text{Ura-H})(\text{H}_2\text{O})_3]^+$, compared with the B3LYP computed spectra using computational method 2 for the four lowest energy structures. Isomer 3-i is also shown rotated 90° clockwise about a vertical axis. The calculated relative enthalpies and Gibbs energies (italics) are also shown.

and carbonyl positions are confirmed by the presence of BCPs in the AIM topological analysis (Figure C13, Appendix C).

The other structures presented in Fig 4.9 also have Zn bound solely to N3, but with only two water molecules bound to the metal center. However, in each case, the third water molecule hydrogen bonds to one of the water molecules linked directly to the metal. These structures are considerably higher in energy than structure 3-i.

4.3.5.1 Comparison of Computed and Experimental Spectra

The comparison between the experimental spectrum and the computed spectra of the lowest energy complexes is also given in Fig. 4.9. The experimental spectrum for the triply hydrated Zn complex is very similar to that for the doubly solvated complex in shape and resolution. The most prominent feature, carbonyl stretching at 1658 cm^{-1} , corresponds well to the calculated spectrum from structure 3-i. However, there is an absence of distinct bands in the experimental spectrum between 1430 cm^{-1} and 1530 cm^{-1} , a region with prominent bands in the spectra of each of the lowest energy structures. These bands, in the area of H_2O scissoring motion as well as N-H wagging, represent features that would be present regardless of the configuration of the complex. However, these motions are not obvious in the experimental spectrum, and although there are two minor bands near this region, their intensity is minimal. The calculated spectra of isomers 3-i, 3-iii and 3-iv are relatively consistent with the bands observed in the experimental spectrum above 1600 cm^{-1} , although both 3-iii and 3-iv are significantly higher in terms of relative energy.

4.4 Summary

The structures of $[M(\text{Ura-H})(\text{Ura})]^+$ as well as $[M(\text{Ura-H})(\text{H}_2\text{O})]^+$ where M corresponds to metal ions Cu^{2+} , Zn^{2+} , and Pb^{2+} , along with $[M(\text{Ura-H})(\text{H}_2\text{O})_2]^+$ for Cu^{2+} and Zn^{2+} , as well as $[\text{Zn}(\text{Ura-H})(\text{H}_2\text{O})_3]^+$, were examined using IRMPD spectroscopy in the $1000 - 1900 \text{ cm}^{-1}$ mid-infrared region. Two different electronic structure calculation methods were employed for energy comparison of the various isomers, as well as for comparison with experimental spectra. There was good agreement between both computational methods for the structures and energetics. The IR spectra generated for these lowest energy structures also generally agreed best with the experimental IRMPD spectra in most cases, with some notable exceptions where assignment of a structure could not be confidently made. $[\text{Cu}(\text{Ura-H})(\text{H}_2\text{O})]^+$ does not present adequate agreement between the experimental spectra and any of the computed spectra to allow for the assignment of a structure. Although experimental data in the O-H/N-H region was not collected, the calculated spectra of all lowest energy structures are identical in this region, and so no additional information could be gathered from this region in an attempt to assign the structures.

For all dimeric complexes, the lowest energy structures are deprotonated at N3 of uracil with the metal bound by a bidentate electrostatic interaction with N3 and O4, confirmed through AIM analysis. For hydrated monomeric species, the same pattern of deprotonation is observed, with the exception of $[\text{Cu}(\text{Ura-H})(\text{H}_2\text{O})]^+$ which is coordinated at the deprotonated N1 position. As this complex becomes doubly hydrated, the uracil is then deprotonated at N3, demonstrating a solvent effect in the Cu complexes. Though the $[\text{Zn}(\text{Ura-H})(\text{H}_2\text{O})]^+$ deprotonates at N3, the metal coordination is to O2 only, with the

solvent transferring a proton to the uracil, resulting in $[\text{Zn}(\text{Ura})(\text{OH})]^+$, with the uracil moiety being a neutral keto-enol tautomer. Any water molecules present are bound to the metal ion and, for the most part, participate in hydrogen bonding with the neighbouring carbonyls, with the exception of $[\text{Cu}(\text{Ura-H})(\text{H}_2\text{O})]^+$ and $[\text{Zn}(\text{Ura})(\text{OH})]^+$ where no hydrogen bonding is observed. For the doubly and triply hydrated Zn species, metal coordination is monodentate to N3 only, while the water molecules bound to Zn insert themselves between the metal and the neighbouring carbonyl groups for hydrogen bonding. The experimental spectrum of $[\text{Zn}(\text{Ura-H})(\text{H}_2\text{O})_3]^+$ does not contain many well defined spectral features, and as a result, multiple isomers are consistent with the bands that are experimentally observed.

4.5 Acknowledgements

The authors wish to thank the CLIO team (J.M. Ortega, C. Six, G. Perilhous, J.P. Berthet) as well as P. Maître and V. Steinmetz for their support during the experiments. The authors also acknowledge the computational resources provided by ACE-Net and Westgrid. Finally, T.D.F. acknowledges the financial contributions from NSERC, Canadian Foundation for Innovation, and Memorial University of Newfoundland.

4.6 References

1. J.D. Watson, F.H. Crick, *Nature*, **1953**, 171, 737.
2. A.M. Pyle, *Science*, **1993**, 261, 709.
3. V.K. Misra, D.E. Draper, *Biopolymers*, **1998**, 48, 113.

4. E. Madore, C. Florentz, R. Giege, J. Lapointe, *J. Nucleic Acids Res.*, **1999**, 27, 3583.
5. J.V. Burda, J. Sponer, J. Leszczynski, P. Hobza, *J. Phys. Chem. B*, **1997**, 101, 9670.
6. P.O. Lowdin, *Rev. Mod. Phys.*, **1963**, 35, 724.
7. M. Sabat, B. Lippert, *Met. Ions Biol. Syst.*, **1996**, 33, 143.
8. M. Burkitt, *Methods Enzymol.*, **1994**, 234, 66.
9. W. Bal, K.S. Kaprzak, *Toxicol Lett.*, **2002**, 127, 55.
10. B. Halliwell, J.M.C. Gutteridge, *Arch. Biochim. Biophys. Acta*, **1986**, 246, 501.
11. J.M. Berg, Y. Shi, *Science*, **1996**, 271, 1081.
12. J.W.R. Schwabe, A. Klug, *Nat. Struct. Mol. Biol.*, **1994**, 1, 345.
13. R.A. Goyer, H.G. Seiler, H. Sigel, A. Sigel, *Handbook on Toxicity of Inorganic Compounds*, Dekker, New York, NY, **1988**.
14. Y. Tsuchiya, T. Tamura, M. Fujii, M. Ito, *J. Phys. Chem.*, **1988**, 92, 1760.
15. M.J. Scanlan, I.H. Hillier, *J. Am. Chem. Soc.*, **1984**, 106, 3737.
16. M. Piacenza, S. Grimme, *J. Comput. Chem.*, **2004**, 25, 83.
17. J.K. Wolken, F. Turecek, *J. Am. Soc. Mass Spectrom.*, **2000**, 11, 1065.
18. E.S. Kryachko, M.T. Nguyen, T. Zeegers-Huyskens, *J. Phys. Chem. A*, **2001**, 105, 1288.
19. E. Rincón, M. Yáñez, A. Toro-Labbé, O. Mo, *Phys. Chem. Chem. Phys.*, **2007**, 9, 2531.
20. S. Guillaumont, J. Tortajada, J.Y. Salpin, A.M. Lamsabhi, *Int. J. Mass Spectrom.*, **2005**, 243, 279.
21. T. Marino, D. Mazzuca, M. Toscano, N. Russo, A. Grand, *Int. J. Quantum Chem.*, **2007**, 107, 311.

22. O.Y. Ali, T.D. Fridgen, *Int. J. Mass Spectrom.*, **2011**, 308, 167.
23. O.Y. Ali, N.M. Randell, T. D. Fridgen, *ChemPhysChem*, **2012**, 13, 1507.
24. A.A. Power, O.Y. Ali, M.B. Burt, T.D. Fridgen, *Int. J. Mass Spectrom.*, **2012**, 330–332, 233.
25. B. Power, V. Haldys, J.-Y. Salpin and T.D. Fridgen, *Int. J. Mass Spectrom.*, **2015**, 378, 328.
26. B. Power, V. Haldys, J.-Y. Salpin and T.D. Fridgen, *J. Mass Spectrom.*, **2016**, 51, 236.
27. A.M. Lamsabhi, M. Alcamí, M. Otilia, M. Yañez, J. Tortajada, *J. Phys. Chem. A*, **2006**, 110, 1943.
28. A.M. Lamsabhi, M. Alcamí, O. Mó, M. Yañez, J. Tortajada, J.-Y. Salpin, *ChemPhysChem*, **2007**, 8, 181.
29. O.Y. Ali, T.D. Fridgen, *ChemPhysChem*, **2012**, 13, 588.
30. B. Power, S.A. Rowe, T.D. Fridgen, *J. Phys. Chem. B*, **2017**, 121, 58.
31. R. Prazeres, F. Glotin, C. Insa, D.A. Jaroszynski, J.M. Ortega, *Eur. Phys. J. D: At., Mol., Opt. Plasma Phys.*, **1998**, 3, 87.
32. W. Paul, *Rev. Mod. Phys.*, **1990**, 62, 531.
33. K. Rajabi, M.L. Easterling, T.D. Fridgen, *J. Am. Soc. Mass Spectrom.*, **2009**, 20, 411.
34. M.J. Frisch, G.W. Trucks, H.B. Schlegel, G.E. Scuseria, M.A. Robb, J.R. Cheeseman, G. Scalmani, V. Barone, B. Mennucci, G.A. Petersson, H. Nakatsuji, M. Caricato, X. Li, H.P. Hratchian, A.F. Izmaylov, J. Bloino, G. Zheng, J.L. Sonnenberg, M. Hada, M. Ehara, K. Toyota, R. Fukuda, J. Hasegawa, M. Ishida, T. Nakajima, Y. Honda, O. Kitao, H. Nakai, T. Vreven, J.A. Montgomery, J.E. Peralta J., F. Ogliaro, M. Bearpark, J.J. Heyd, E. Brothers, K.N. Kudin, V.N. Staroverov, T. Keith, R. Kobayashi, J. Normand, K. Raghavachari, A. Rendell, J.C. Burant, S.S. Iyengar, J. Tomasi, M. Cossi, N. Rega, J.M. Millam, M. Klene, J.E. Knox, J.B. Cross, V. Bakken, C. Adamo, J. Jaramillo, R. Gomperts, R.E. Stratmann, O. Yazyev, A.J. Austin, R. Cammi, C. Pomelli, J.W. Ochterski, R.L. Martin, K. Morokuma, V.G. Zakrzewski, G.A. Voth, P. Salvador, J.J.

- Dannenberg, S. Dapprich, A.D. Daniels, O. Farkas, J.B. Foresman, J.V. Ortiz, J. Cioslowski, D.J. Fox, *Gaussian 09*, Revision D.01, Gaussian, Inc., Wallingford, CT, **2013**.
35. P.B. Armentrout, M. Citir, Y. Chen, M.T. Rodgers, *J. Phys. Chem. A*, **2012**, *116*, 11823.
36. P.B. Armentrout, Y. Chen, M.T. Rodgers, *J. Phys. Chem. A*, **2012**, *116*, 3989.
37. R.F.W. Bader, *Atoms in Molecules: A Quantum Theory*, Clarendon Press, Oxford University Press, New York, NY, **1990**.
38. T.A. Keith, AIMAll, Version 14.10.27, TK Gristmill Software, Overland Park, KS, **2014**, aim.tkgristmill.com.
39. P. Colarusso, K. Zhang, B. Gup, P.F. Bernath, *Chem. Phys. Lett.*, **1997**, *269*, 39.
40. J.-W. Shin, *Int. J. Mass Spectrom.*, **2014**, *372*, 39.
41. J.-Y. Salpin, V. Haldys, S. Guillaumont, J. Tortajada, M. Hurtado, A.M. Lamsabhi, *ChemPhysChem*, **2014**, *15*, 2959.
42. S.J. Lippard, J.M. Berg, *Principles of Bioinorganic Chemistry*, University Science Books, Mill Valley, CA, **1994**.
43. W. Kaim, B. Schwedersky, *Bioinorganic Chemistry Inorganic Elements in the Chemistry of Life*, John Wiley & Sons, Chichester, UK, **1994**.
44. L.A. Loeb, A.R. Zakour, *Nucleic Acids-Metal Ion Interactions*, T.G. Spiro Ed., John Wiley & Sons, New York, NY, **1980**.
45. D.W. Christianson, J.D. Cox, *Annu. Rev. Biochem.*, **1999**, *68*, 33.

CHAPTER 5 – Ammoniated Complexes of Uracil and Transition Metal Ions: Structures of $[M(\text{Ura-H})(\text{Ura})(\text{NH}_3)]^+$ by IRMPD Spectroscopy and Computational Methods (M = Fe, Co, Ni, Cu, Zn, Cd)

The structures of deprotonated d-block metal dication bound uracil dimers, solvated by a single ammonia molecule, were explored in the gas phase using infrared multiple photon dissociation (IRMPD) spectroscopy in a Fourier transform ion cyclotron resonance mass spectrometer (FTICR-MS). The IRMPD spectra were then compared to computed IR spectra for various isomers. Calculations were performed using B3LYP with the 6-31+G(d,p) basis set for all atoms, with the exception of Cd, for which the LANL2DZ basis set with relativistic core potentials were used. The calculations were then repeated using the def2-TZVPP basis set on all atoms and compared to the first set of calculations. The lowest energy structures are those in which one uracil is deprotonated at the N3 position and, aside from the Cu complex, the intact uracil is a tautomer where the N3 hydrogen is at the O4 carbonyl oxygen. The metal displays a tetradentate interaction to the uracil moieties, with the exception of Cu which is tridentate, and the ammonia molecule is bound directly to the metal center. In the Cu complex, a square planar geometry is observed about the metal center, consistent with Jahn-Teller distortions commonly observed in Cu(II) complexes. The IRMPD spectroscopic data are consistent with the computed infrared spectra for the lowest-energy structures.

A version of this chapter has been published:

B. Power, S.A. Rowe, T.D. Fridgen, *J. Phys. Chem. B*, **2017**, *121*, 58.

5.1 Introduction

The effect that metal ions have on the structural behavior of biological molecules has been widely examined, including the potential impacts that such an interaction would have on routine biological processes. Differences in the configuration of specific complexes have been observed between the gas phase and aqueous solution, and so microsolvation has been utilized in gas phase experiments to determine what impact solvents may have, while eliminating any potential bulk solvent effects [1]. Gas phase experiments allow for direct molecular observation, and offer the best replication of the cellular environment. While water has understandably been the solvent of choice in such studies, the current work presents an examination of various transition metal – uracil dimers, solvated by a single ammonia molecule in the gas phase. These experiments were conducted using infrared multiple photon dissociation (IRMPD), a form of consequence spectroscopy frequently employed to examine such complexes.

While water is the most abundant solvent in the human body, ammonia also has an interesting role in biological processes. The toxicity of ammonia in the human body is well documented, with increasing ammonia blood levels being linked to more severe cases of hepatic encephalopathy, with stages of consciousness ranging from lethargy and confusion between 50 and 100 $\mu\text{mol L}^{-1}$ to coma at 200 $\mu\text{mol L}^{-1}$ [2]. However, ammonia is produced naturally and spontaneously through deamination of cytosine, at a rate of approximately 100 bases per cell per day – the product of which is uracil [3]. At the site of deamination, guanine is now mis-matched in a pair with uracil rather than the typical cytosine, a mutation which threatens to propagate through any replication steps [4]. However, this uracil is eliminated from DNA by Uracil-DNA glycosylase, which cleaves the N-glycosylic bond

of uracil. Once the DNA strand has been unzipped, DNA polymerase introduces the complimentary base pair to each daughter strand, establishing the correct guanine-cytosine and adenine-uracil linkages [5]. Even though the potential mutations are easily corrected, considering that both uracil and ammonia are spontaneously produced as part of the same reaction, any possible interactions between them is a point of intrigue.

Metal ions have proven to be essential in biological processes including structure stabilization, RNA folding and biochemical activity [6–8]. The interaction between metal ions and nucleobases have been thoroughly examined using a variety of techniques [9–24]. Transition metal dications in particular have demonstrated an increased affinity towards nucleobases in comparison to alkaline earth metals [25], and in the particular cases of Ni, Cu and Zn, have been found to preferentially stabilize the keto-enol form of uracil rather than the diketo form [26]. In the case of deprotonated uracil complexes, particularly those with Cu [27,28], deprotonation can occur at the N1 or N3 site, with the latter being 30 kJ mol⁻¹ higher in energy in the gas phase than deprotonation at N1, but the two are nearly identical in solution [29]. Interaction between the metal cation and deprotonated uracil incorporates both the deprotonated N and the neighbouring carbonyl. In dimeric complexes, one uracil is deprotonated while the other is tautomerized, while both are bridged by the metal ion. This has been evident in complexes Cu [29,30], Pb [31] and of alkaline metal dications, both solvated and unsolvated [32,33].

This current work aims to provide structural insight into ammoniated transition metal – uracil dimeric complexes, $[M(\text{Ura-H})(\text{Ura})(\text{NH}_3)]^+$ ($M = \text{Fe, Co, Ni, Cu, Zn}$ and Cd), using IRMPD spectroscopy in the fingerprint region (1000 – 1900 cm⁻¹). In this region, carbonyl stretching frequencies are obtained and compared to those determined

through computational methods for a number of different isomers in order to offer a structural comparison. The conventional uracil numbering scheme used throughout is presented in Scheme 2.1.

5.2 Methods

5.2.1 Experimental

All experiments were performed using an FT-ICR-MS coupled to a mid-infrared free electron laser (FEL) at the Centre Laser Infrarouge d'Orsay (CLIO) [34,35]. Metal chloride solutions (0.01 mol L^{-1}) were prepared for each metal using $18 \text{ M}\Omega \text{ cm}$ water (Millipore). Uracil solutions were made to 1 mmol L^{-1} in $18 \text{ M}\Omega \text{ cm}$ water. A mixture made at a ratio of 1 part metal solution to 10 parts uracil solution was then prepared for each metal, and introduced via syringe injection to the electrospray ion source at a flow rate of $75 \text{ }\mu\text{L h}^{-1}$. The complexes were mass selected in the quadrupole mass filter and transferred to the octopole storage cell for 0.5 s where they were ammoniated by residual ammonia in the storage cell [36]. The ions were then transferred to the ICR cell where they were isolated and irradiated with the free electron laser. Irradiation times varied between 0.5 and 1 s. Areas of the IRMPD spectra displaying saturation were scanned again, after attenuation of the FEL. The laser was scanned at 5 cm^{-1} intervals from ~ 1000 to 1900 cm^{-1} . The IRMPD efficiency is defined as the negative of the natural logarithm of parent ion intensity divided by the sum of parent and fragment ion signals.

5.2.2 Computational

Calculations for all structures were conducted using the Gaussian 09 suite of programs [37]. Each structure was optimized and infrared spectra computed using B3LYP density functional theory. For complexes of all metals other than Cd, the 6-31+G(d,p) basis set was used for all atoms. For the complex of Cd, the LANL2DZ basis set with relativistic core potential was used for the cadmium atom, and the 6-31+G(d,p) basis was used for all other atoms. Single point energy calculations were then carried out using B3LYP with the 6-311+G(3df,3pd) basis set on all atoms except Cd, for which the LANL2DZ basis set with relativistic core potential was again used. This computational method will be referred to as method 1.

Both the optimization and single point energy calculations were then repeated for each complex with the def2-TZVPP basis set applied to all atoms. This particular basis has been found to work better for metal-cation amino acid complexes in comparison to the LANL2DZ basis set [38,39]. This computational method will be referred to as method 2.

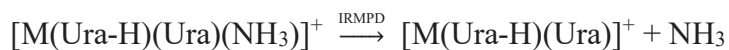
These single-point electronic energies, using methods 1 and 2, were used to compute the enthalpies and Gibbs energies of isomeric species at 298 K, using the unscaled harmonic vibrational frequencies calculated for optimization geometry.

The bonding within the individual equilibrium structures was also analyzed by locating the bond critical points (BCPs) using atoms-in-molecules (AIM) theory [40], which is based on a topological analysis of the electronic density at the BCPs, and is a good descriptor of the bond strength or weakness. This analysis was conducted using AIMAll software [41] with the lowest energy structures optimized from method 2. Data from the topological analysis are given collectively in Appendix D as Figure D14.

5.3 Results and Discussion

5.3.1 IRMPD Spectroscopy

When irradiated with the FEL, all complexes underwent the loss of ammonia as the only observed fragmentation pathway:



This result is consistent with the hydrated uracil dimers of alkaline earth metals in which fragmentation occurred simply through the loss of water [32,33].

Figure 5.1 depicts the IRMPD spectra for $[\text{M}(\text{Ura-H})(\text{Ura})(\text{NH}_3)]^+$ in the 1000 – 1900 cm^{-1} region. The spectra of the Fe, Co, Ni, Zn and Cd complexes are all strikingly similar, with the Cu complex exhibiting different spectroscopic features compared with the other metal ion complexes. Each of the spectra for the Fe, Co, Ni, Zn and Cd complexes have a strong feature with maxima between 1650 cm^{-1} and 1670 cm^{-1} , corresponding to C=O stretching and N-H scissoring in ammonia. These bands encompass both the metal coordinated and hydrogen bonded C=O stretches. The position of these carbonyl stretches are red-shifted in comparison to the free carbonyl stretch of uracil which is centered about 1750 cm^{-1} in the gas phase [42] and is expected due to the lengthening (and therefore weakening) effect that complexation with a metal cation or a hydrogen bond has on the carbonyl bond. In metal ion-amino acid complexes, similar positioning has also been observed in the metal bound carbonyl stretch, including in singly-charged Zn and Cd complexes with glutamine [43] and cysteine [44]. However, the positions of the bands in the present NH_3 -solvated complexes are also slightly blue shifted when compared to the maxima of the same carbonyl stretches observed in the hydrated uracil dimers of alkaline

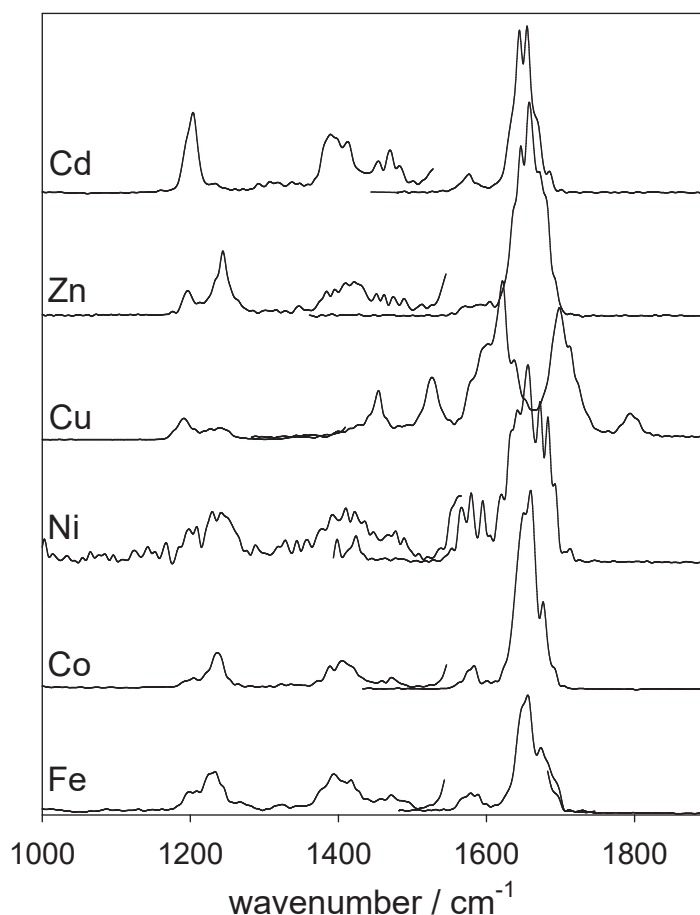


Figure 5.1. IRMPD spectra for $[M(\text{Ura-H})(\text{Ura})(\text{NH}_3)]^+$ ($M = \text{Fe}, \text{Co}, \text{Ni}, \text{Cu}, \text{Zn}, \text{Cd}$) in the 1000 – 1900 cm^{-1} region.

earth metals, which are observed between 1625 cm^{-1} and 1648 cm^{-1} [33]. A Lewis base, ammonia donates electron density back to the complex leading to the strengthening of the uracil carbonyl bonds, increasing the stretching frequency. Since ammonia is a slightly better electron donor than water, the blue shift observed here in comparison to the hydrated complexes is reasonable.

Other minor features observed in these spectra include an enolic C–OH stretch between 1560 cm^{-1} and 1600 cm^{-1} ; C–N stretching within the uracil ring between 1370 cm^{-1} and 1440 cm^{-1} ; N–H wagging in ammonia between 1220 cm^{-1} and 1260 cm^{-1} , and a

shoulder to the red of this band attributed to the C5 and C6 hydrogen wagging modes, although this is not evident in the spectrum on the Cd complex.

As previously mentioned, the experimental spectrum for the Cu complex is significantly different. Most notably, there is a distinct separation of the carbonyl stretches. The band centered at 1700 cm^{-1} is indicative of the hydrogen bonded carbonyl, while the metal coordinated carbonyl stretch is centered at 1621 cm^{-1} . There is also a free carbonyl stretch observed at 1794 cm^{-1} , which is not observed in any of the other complexes.

5.3.2 Computed Structures for $[M(\text{Ura-H})(\text{Ura})(\text{NH}_3)]^+$

Though many isomers exist for metal complexed uracil dimers, three particular structures are consistently significantly lower in energy than the others, regardless of the metal cation [29,31–33]. As a result, these three particular configurations were used as the starting point in all calculations, with an ammonia molecule introduced in various positions. The parent structures (shown with NH_3 attached) are depicted in Figure 5.2. In all structures, one uracil is deprotonated at N3 and the metal cation is tetracoordinate. In the first such structure, parent i, metal coordination is to N3 and O4 of deprotonated uracil. The neutral uracil is a tautomer where hydrogen has been transferred from N3 to O4, and the metal is coordinated to N3 and O2. The hydrogen which has been transferred to the O2 position participates in a hydrogen bond with the O4 carbonyl of the deprotonated uracil. In structure ii, metal coordination occurs at the N3 and O4 positions of both uracils, while in parent iii metal coordination is at N3 and O2 of both uracils. The tautomers of uracil in these lowest energy ionic complexes are considerably higher in energy when not part of an ionic complex [27–29].

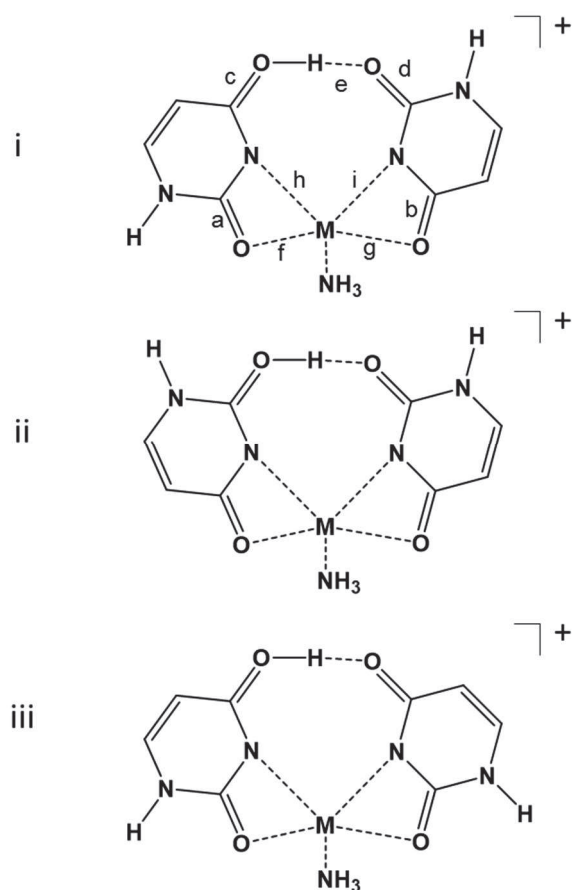


Figure 5.2. Comparison of the structures for the lowest energy $[M(\text{Ura-H})(\text{Ura})(\text{NH}_3)]^+$ isomers, $M = \text{Fe}, \text{Co}, \text{Ni}, \text{Zn}, \text{Cd}$. The unsolvated structures are representative of the parent dimers used as a starting point for calculations to determine the lowest energy $[M(\text{Ura-H})(\text{Ura})(\text{NH}_3)]^+$ structures.

From the result of these initial NH_3 -complex calculations, 9 Fe isomers (7 isomers by method 1), 9 Co isomers, 9 Ni isomers, 10 Cu isomers, 9 Zn isomers and 8 Cd isomers were minimized. When comparing the spectra of the structures calculated as lowest in energy to the experimental spectra, differences were observed in the Cu complex; This will be examined in more detail below. For the other five metals, Figure 5.2 depicts the lowest energy isomer for each metal ion based on calculation method 2, along with a summary of thermochemistry and bond lengths in Table 5.1. Appendix D Figures D1 to D12 give the

structures and energetics for the isomeric structures obtained using both calculation methods. Both calculation methods give similar results in terms of the relative thermochemistries for the three lowest energy structures of each complex with only minor discrepancies. For complexes of Fe, Co and Ni, where different spin multiplicities are possible, distorted octahedral (square pyramidal) d orbital splitting with high spin multiplicity was determined to be lower in energy when compared to the other possible spin states for the analogues of the three lowest energy structures. For the Fe complexes, the low spin distorted octahedral (square pyramidal) singlet and high spin tetrahedral triplet structures are approximately 130 kJ mol^{-1} and 80 kJ mol^{-1} higher in energy, respectively. The low spin doublet structures of Co complexes, as well as the square planar singlet structures of the Ni complexes are also approximately 60 kJ mol^{-1} higher in energy when compared to the high spin analogues of the three lowest energy structures. As a result of this, these high spin square pyramidal structures (quintet for Fe; quartet for Co and triplet for Ni) are reported herein. This is consistent with previous examination of metal ion–uracil complexes, in which uracil is identified as a weak field ligand, given the high π -charge density of the oxygen atoms in uracil [45]. For the remainder, only one possible spin state exists, that being singlet for Zn and Cd, and doublet for Cu.

Apart from the Cu complexes, the three lowest energy structures are the result of direct ammonia coordination to the metal ion in each of the three dimers previously described as the starting point for the theoretical work. This is consistent with studies of similar uracil dimers, in which the water solvent is directly bound to the metal center [32,33]. The structure in which ammonia is coordinated to the metal of parent i is the lowest energy structure in all cases. This isomer will be referred to as structure i. Similarly,

the parent ii and parent iii conformations in which ammonia is bound directly to the metal center will be referred to as structures ii and iii, respectively. The ammonia coordination and planarity of the uracil molecules also differ noticeably depending on metal ion, as highlighted in Figure 5.3. In all complexes, a slight bend is observed between uracil moieties, and ammonia coordination is orthogonal to the $[M(\text{Ura-H})(\text{Ura})]^+$ framework. Bending between uracil moieties in both the Fe and Ni complex is not as pronounced as the others, with approximately 165° between uracil molecules, compared to roughly 145° in the Co, Zn and Cd structures.

As one would expect, given the noticeable difference between the Cu experimental IRMPD spectrum compared to all others, the structure for this complex is likely quite

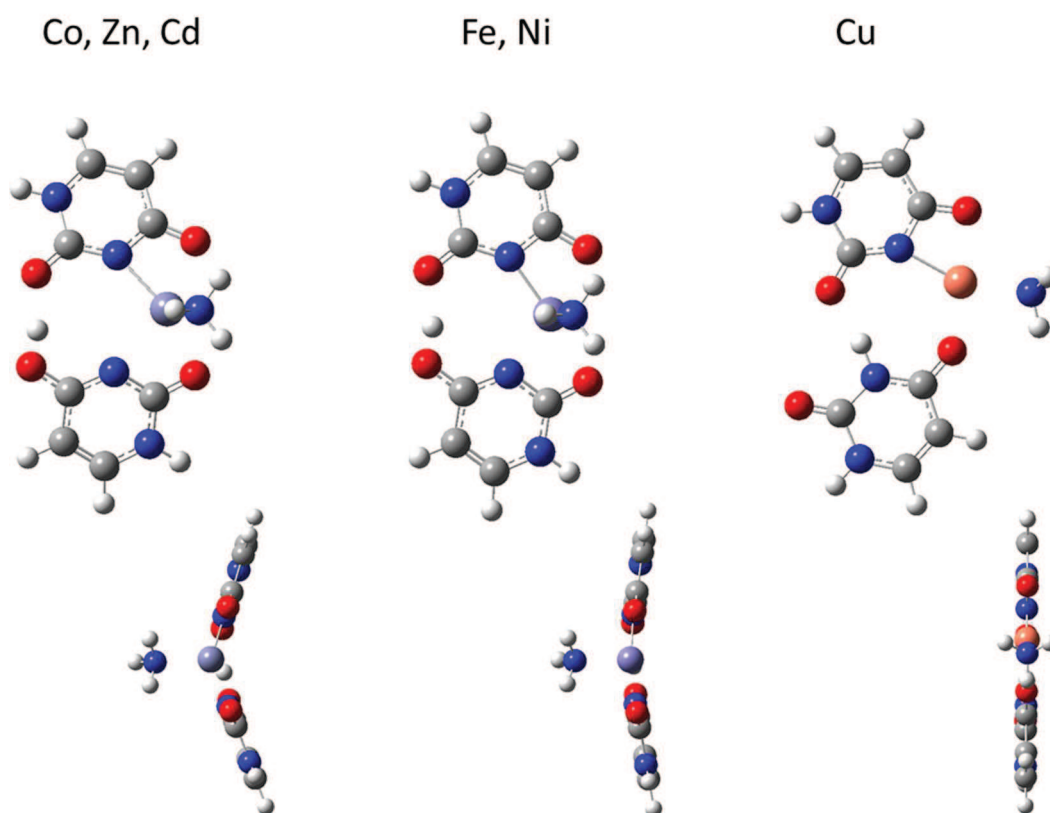


Figure 5.3. Comparison of the ammonia coordination in the lowest energy $[M(\text{Ura-H})(\text{Ura})(\text{NH}_3)]^+$ complexes, $M = \text{Fe}, \text{Co}, \text{Ni}, \text{Cu}, \text{Zn}, \text{Cd}$. Rotation is 90° clockwise about the vertical axis.

different. When the initial calculations were completed based on the parent structures in Figure 5.2, and no adequate comparison was found between the experimental and calculated spectra, 20 other isomers were located resulting in three different structures which are lowest in energy, labelled as I, II and III in Figure 5.4. Table 5.2 provides a summary of thermochemistry and bond lengths for these structures. All of these lowest energy structures are square planar complexes. Structure I displays a tridentate interaction between the Cu ion with the N3 and O4 positions of the deprotonated uracil moiety, along with the O4 of the neutral uracil. An intramolecular hydrogen bond occurs in this complex as well, however it is the N3 hydrogen of the neutral uracil that is hydrogen bonded to the

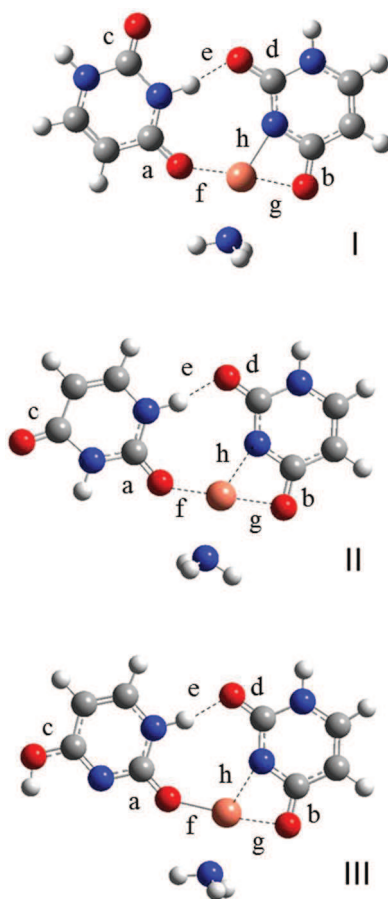


Figure 5.4. Comparison of the structures for the lowest energy $[\text{Cu}(\text{Ura-H})(\text{Ura})(\text{NH}_3)]^+$ complexes.

Table 5.1. Thermochemistry and bond distances for the lowest energy $[M(\text{Ura-H})(\text{Ura})(\text{NH}_3)]^+$ complexes, $M = \text{Fe}, \text{Co}, \text{Ni}, \text{Zn}, \text{Cd}$. The thermochemistry reported here are those from method 2. Energies are expressed in kJ mol^{-1} and distances in Angströms.

Structure	M	$\Delta_{\text{rel}}H/\Delta_{\text{rel}}G$	a	b	c	d	e	f	g	h	i
i	Fe	0/0	1.256	1.264	1.287	1.238	1.510	2.125	2.152	2.305	2.098
	Co	0/0	1.244	1.262	1.287	1.238	1.525	2.233	2.166	2.128	2.023
	Ni	0/0	1.254	1.264	1.288	1.238	1.533	2.193	2.128	2.086	1.990
	Zn	0/0	1.254	1.262	1.290	1.238	1.550	2.105	2.145	2.288	2.043
	Cd	0/0	1.250	1.257	1.290	1.238	1.543	2.331	2.368	2.454	2.225
ii	Fe	0.3/1.0	1.261	1.263	1.282	1.243	1.431	2.096	2.144	2.287	2.124
	Co	2.3/2.8	1.251	1.260	1.283	1.245	1.439	2.178	2.172	2.122	2.039
	Ni	2.4/2.7	1.251	1.261	1.283	1.244	1.448	2.150	2.138	2.073	2.002
	Zn	1.2/1.9	1.259	1.261	1.287	1.243	1.474	2.072	2.141	2.282	2.064
	Cd	1.5/2.1	1.255	1.257	1.287	1.243	1.466	2.291	2.354	2.448	2.250
iii	Fe	7.7/8.0	1.257	1.255	1.282	1.241	1.464	2.132	2.238	2.258	2.078
	Co	6.5/6.1	1.246	1.254	1.282	1.243	1.466	2.226	2.247	2.108	2.015
	Ni	6.9/6.7	1.247	1.257	1.282	1.243	1.467	2.187	2.187	2.068	1.990
	Zn	8.9/8.3	1.239	1.230	1.284	1.245	1.484	2.312	2.773	2.063	1.957
	Cd	7.4/6.0	1.248	1.245	1.286	1.242	1.503	2.373	2.531	2.387	2.187

Table 5.2. Thermochemistry and bond distances for the lowest energy $[\text{Cu}(\text{Ura-H})(\text{Ura})(\text{NH}_3)]^+$ complexes. The thermochemistry reported here are those from method 2. Energies are expressed in kJ mol^{-1} and distances in Angströms.

Structure	$\Delta_{\text{rel}}H/\Delta_{\text{rel}}G$	a	b	c	d	e	f	g	h
a	0/0	1.264	1.280	1.200	1.222	1.735	1.960	2.017	1.974
b	3.9/4.2	1.264	1.279	1.204	1.226	1.713	1.956	2.004	1.994
c	9.3/12.6	1.268	1.276	1.324	1.227	1.718	1.934	2.012	1.995

O2 position of the deprotonated uracil. Ammonia coordination still occurs directly to the metal center, and there is no interaction between any of the hydrogens of ammonia with the remainder of the complex. Another key difference in this structure is that it is planar about the Cu ion. Structure II is again deprotonated at the N3 position with Cu coordination between N3 and O4, however the neutral uracil is coordinated to Cu at O2. The intramolecular hydrogen bond is N3 of neutral uracil to O2 of the deprotonated uracil. Structure III is nearly identical to structure II, except the neutral uracil is an N3 to O4 tautomer of canonical uracil. Structures I through III are all lower in energy in comparison to the lowest energy structure initially determined using the parent structures from Fig 5.2 as a starting point. Given that these structures were lowest in energy for Cu, similar structures of I, II, and III were then examined for the remaining metals but found to be between 15 – 40 kJ mol⁻¹ higher in energy in all cases. For Fe, Co, Ni, Zn and Cd, a comparison between the lowest energy structure, structure i, and structure I using computational method 2 is given in Appendix D Figure D13.

The difference in the structure observed and computed for the Cu complex when compared to the others is rather intriguing. Jahn-Teller distortions in Cu(II) complexes are quite common [46]. Jahn-Teller distortions occur due to the instability of a degenerate energy state. The degenerate orbitals split and typically result in elongation of bonds. The square planar complex might be considered a limiting elongation of the axial “ligand(s)” in an octahedral or square pyramidal complex. For the metal cation complexes other than Cu, the intact uracil adopts an N3 to O4 tautomer – presenting two basic binding sites, N3 and O2 – that is lower in energy when bound to a cation (i.e. M(Ura-H)⁺) resulting in a square pyramidal structure for the [M(Ura-H)(Ura)NH₃]⁺. However, for [Cu(Ura-H)(Ura)NH₃]⁺,

it seems that the propensity for a square planar complex with uracil in its canonical tautomer – with one binding site – is preferable.

The tetradentate interaction between the metal center and both uracils is confirmed through AIM topological analysis (Appendix D Fig. D14), as there are two BCPs from the metal to each uracil, except for the Cu complex where there is only one interaction between Cu and neutral uracil. All intramolecular hydrogen bonds are also confirmed through the presence of BCPs in the AIM analysis. The positive value of the Laplacian of the electron density, $\nabla^2\rho$, which corresponds to these BCPs between the metal and uracil suggests these interactions are all primarily electrostatic in nature. In all complexes, NH_3 is also determined to be electrostatically bound to the metal cation.

The length of each carbonyl bond in structure i is quite consistent among the metals where this structure is lowest in energy (Fe, Co, Ni, Zn, Cd). As denoted in Table 5.1, the metal-coordinated carbonyl of the neutral uracil (distance ‘a’, ~ 1.25 Å for all) is consistently shorter than the metal-coordinated carbonyl of the deprotonated uracil (distance b, ~ 1.26 Å). Each enolic C–OH bond, distance c, is approximately 1.29 Å and the carbonyl participating in the hydrogen bond between uracils, distance d, is 1.238 Å in all cases. Altering the metal ion does not prove to have any impact on the carbonyl bond lengths. The experimental IRMPD spectra for the complexes in the C=O stretch region shows little variation, verifying the absence of a metal effect between Fe, Co, Ni, Zn, and Cd.

The length of the metal-coordinated carbonyl bonds in the Cu complex are somewhat longer than in comparison to the other metals, at approximately 1.27 Å. As the Cu interaction is tridentate in this complex as opposed to tetradentate, each carbonyl is

subjected to an enhanced electrostatic interaction, further lengthening the carbonyl bonds. When examining Cu coordination lengths f, g and h and comparing to the other complexes, the Cu ion is closer to the uracil moieties than other metals. This can be observed in the AIM analysis as well, as the Laplacian of the electron density, $\nabla^2\rho$, is greater for the metal-carbonyl bonds in the Cu complex compared to the others, indicating a stronger electrostatic interaction. The O2 carbonyl of the neutral uracil, labelled as bond d, is slightly longer in comparison to carbonyl bond c, due to the hydrogen bond occurring at position d. The exception to this is in structure III where proton transfer occurs, and carbonyl c is now in the much longer enol form. As a result, this can account for the differences in the carbonyl stretches in the Cu spectrum with reference to the other metals.

5.3.3 Comparison of the Computed and Experimental Spectra

A comparison between the experimental spectra and the three lowest energy structures computed *via* method 2 are given in Figure 5.5 for all $[M(\text{Ura-H})(\text{Ura})(\text{NH}_3)]^+$ ions. For the complexes identified as having structure i as the lowest in terms of both enthalpy and Gibbs energy (Fe, Co, Ni, Zn, Cd), satisfactory agreement is observed between the experimental spectra for each and the calculated spectra of structure i. Structure ii can be eliminated as a major contributor in each instance, most notably because the bands experimentally observed just below 1600 cm^{-1} , attributed to the enolic C–OH stretch, are predicted to be far more intense for structure ii. However, due to the similarity between the calculated spectra for structures i and iii, the possibility of structure iii being a major contributor cannot be ignored and are only computed to be higher in energy by between 6 and 8 kJ mol^{-1} in Gibbs energy and, so, cannot be definitively ruled out.

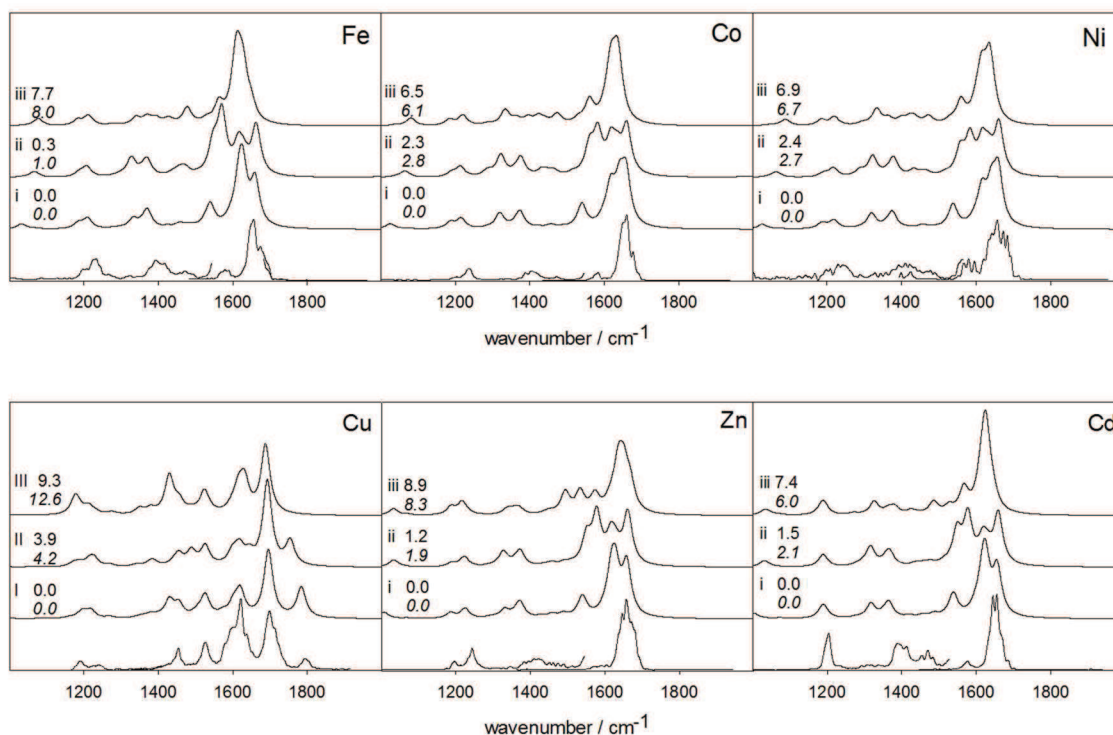


Figure 5.5. Experimental IRMPD spectrum (bottom) for $[M(\text{Ura-H})(\text{Ura})(\text{NH}_3)]^+$ compared with the B3LYP computed spectra using computational method 2 for the lowest energy structures. The relative enthalpies and Gibbs free energies (italics) calculated at 298 K are also shown in kJ mol^{-1} .

For the $[\text{Cu}(\text{Ura-H})(\text{Ura})(\text{NH}_3)]^+$, in which the experimental spectrum was significantly different than the others, structure I can be assigned as the correct structure. The three resolved peaks in the carbonyl stretching region correspond well with the calculated spectrum for I. In particular, the free $\text{C}=\text{O}$ stretch observed at 1794 cm^{-1} in the $[\text{M}(\text{Ura-H})(\text{Ura})(\text{NH}_3)]^+$ IRMPD spectrum was not reproduced by computed structures such as i – iii as for the other metals. It is this peak that is observed experimentally and ruled out all of the calculated structures initially obtained using parents i – iii from Figure 5.2. This band is predicted by the calculations to occur at 1784 cm^{-1} for structure I, with further separation from the coordinated carbonyl stretches in comparison to structure II, which is better reflective of the experimental spectra. Structure III, which is roughly 10

kJ mol^{-1} higher in energy, does not display this free $\text{C}=\text{O}$ stretch. Features observed below 1600 cm^{-1} in the experimental spectrum also demonstrate excellent agreement with the spectrum of structure a, including $\text{C}=\text{C}$ stretching within the uracil ring at 1526 cm^{-1} , N-H wagging in uracil between 1490 cm^{-1} (hydrogen bonded) and 1455 cm^{-1} (free), as well as N-H wagging in ammonia and C-H wagging in uracil about 1200 cm^{-1} .

5.4 Summary

The structures of $[\text{M}(\text{Ura-H})(\text{Ura})(\text{NH}_3)]^+$, where $\text{M} = \text{Fe}, \text{Co}, \text{Ni}, \text{Cu}, \text{Zn}$ and Cd , were examined using IRMPD in the $1000 - 1900\text{ cm}^{-1}$ mid-infrared region. Two different electronic structure calculation methods were employed for energy comparison between the various isomers, as well as for comparison to the experimental spectra. Good agreement was obtained in each instance between the experimental structure and those computed to be lowest in enthalpy and/or Gibbs energy.

Consistent with other studies, deprotonation occurs at the N3 position in all cases, and the other uracil displays hydrogen transfer from N3 to O4, except for the complex of Cu. This transferred hydrogen participates in a strong intramolecular hydrogen bond, as confirmed by AIM analysis, with a carbonyl group of the neighbouring uracil. In the cases where this transfer occurs, the hydrogen bond is to the O2 position of this neighbouring uracil. No proton transfer occurs in the neutral uracil of the Cu complex, and while the metal ion is still bound to N3 and O4 of the deprotonated uracil, it only interacts with O2 of the neighbouring moiety. In this case, the intramolecular hydrogen bond is from the N1 hydrogen to O3. The solvent molecule is bound directly to the metal ion in all lowest energy structures. For Fe, Co, Ni, Zn, and Cd complexes, the metal ion is tetracoordinate,

interacting with N3 and O2 of the neutral uracil and N3 and O4 of the deprotonated uracil. In the lowest energy Cu structure, the coordination is tridentate with N3 and O4 of the deprotonated uracil and O4 of the neutral uracil. This deviation in complex configuration is potentially contributed to copper's preference for a square planar complex.

5.5 Acknowledgements

The authors wish to thank the CLIO team (J. M. Ortega, G. Perilhous, J. P. Berthet) as well as P. Maître and V. Steinmetz for their support during the experiments conducted at CLIO. We are indebted to Dr. Paul Mayer for his help in collecting data at CLIO. The authors also acknowledge the computational resources provided by ACE-Net and Westgrid. Finally, TDF acknowledges the financial contributions from NSERC, CFI, and Memorial University.

5.6 References

1. S.M. Bachrach, M.W. Dzierlenga, *J. Phys. Chem. A*, **2011**, *115*, 5674.
2. J.P. Ong, A. Aggarwal, D. Krieger, K.A. Easley, M.T. Karafa, F. Van Lente, A.C. Arroliga, K.D. Mullen, *Am. J. Med.*, **2003**, *114*, 188.
3. B. Alberts, A. Johnson, J. Lewis, M. Raff, K. Roberts, P. Walter, *Molecular Biology of the Cell*, 4th ed., Garland Science, New York, NY, **2002**.
4. M.C. Longo, M.S. Berninger, J.L. Hartley, *Gene*, **1990**, *93*, 125.
5. L.H. Pearl, *Mutat. Res.*, **2000**, *460*, 165.
6. A.M. Pyle, *Science*, **1993**, *261*, 709.
7. V.K. Misra, D.E. Draper, *Biopolymers*, **1998**, *48*, 113.

8. E. Madore, C. Florentz, R. Giege, J. Lapointe, *Nucl. Acids Res.*, **1999**, 27, 3583.
9. S. Guillaumont, J. Tortajada, J.-Y. Salpin, A.M. Lamsabhi, *Int. J. Mass Spectrom.*, **2005**, 243, 279.
10. C. Gutlé, J.-Y. Salpin, T. Cartailier, J. Tortajada, M.-P. Gaigeot, *J. Phys. Chem. A*, **2006**, 110, 11684.
11. M. Kabeláč, P. Hobza, *J. Phys. Chem. B*, **2006**, 110, 14515.
12. J.-Y. Salpin, S. Guillaumont, J. Tortajada, A.M. Lamsabhi, *J. Am. Soc. Mass Spectrom.*, **2009**, 20, 359.
13. E.A.L. Gillis, K. Rajabi, T.D. Fridgen, *J. Phys. Chem. A*, **2009**, 113, 824.
14. E.A.L. Gillis, T.D. Fridgen, *Int. J. Mass Spectrom.*, **2010**, 297, 2.
15. Y.-w. Nei, T.E. Akinyemi, C.M. Kaczan, J.D. Steill, G. Berden, J. Oomens, M.T. Rodgers, *Int. J. Mass Spectrom.*, **2011**, 308, 191.
16. J.-Y. Salpin, S. Guillaumont, D. Ortiz, J. Tortajada, P. Maître, *Inorg. Chem.*, **2011**, 50, 7769.
17. O.Y. Ali, N.M. Randell, T.D. Fridgen, *ChemPhysChem*, **2012**, 13, 1507.
18. A. Eizaguirre, A.M. Lamsabhi, O. Mó, M. Yáñez, *Theor. Chem. Acc.*, **2011**, 128, 457.
19. M. Azargun, T.D. Fridgen, *Phys. Chem. Chem. Phys.*, **2015**, 17, 25778.
20. B. Yang, R.R. Wu, N.C. Polfer, G. Berden, J. Oomens, M.T. Rodgers, *J. Am. Soc. Mass Spectrom.*, **2013**, 24, 1523.
21. J.-Y. Salpin, V. Haldys, S. Guillaumont, J. Tortajada, M. Hurtado, A.M. Lamsabhi, *ChemPhysChem*, **2014**, 15, 2959.
22. C.M. Kaczan, A.I. Rathur, R.R. Wu, Y. Chen, C.A. Austin, G. Berden, J. Oomens, M.T. Rodgers, *Int. J. Mass Spectrom.*, **2015**, 378, 76.

23. M. Berdakin, V. Steinmetz, P. Maitre, G.A. Pino, *Phys. Chem. Chem. Phys.*, **2015**, *17*, 25915.
24. B. Power, V. Haldys, J.-Y. Salpin, T.D. Fridgen, *J. Mass Spectrom.*, **2016**, *51*, 236.
25. M. Sabat, B. Lippert, *Met. Ions Biol. Syst.*, **1996**, *33*, 143.
26. E. Rincón, M. Yáñez, A. Toro-Labbé, O. Mó, *Phys. Chem. Chem. Phys.*, **2007**, *9*, 2531.
27. A.M. Lamsabhi, M. Alcamí, O. Mó, M. Yáñez, J. Tortajada, *J. Phys. Chem. A*, **2006**, *110*, 1943.
28. A.M. Lamsabhi, M. Alcamí, O. Mó, M. Yáñez, J. Tortajada, J.-Y. Salpin, *ChemPhysChem*, **2007**, *8*, 181.
29. O.Y. Ali, T.D. Fridgen, *ChemPhysChem*, **2012**, *13*, 588.
30. O. Brea, M. Yáñez, O. Mó, A.M. Lamsabhi, *Org. Biomol. Chem.*, **2013**, *11*, 3862.
31. O.Y. Ali, T.D. Fridgen, *Int. J. Mass Spectrom.*, **2011**, *308*, 167.
32. A.A. Power, O.Y. Ali, M.B. Burt, T.D. Fridgen, *Int. J. Mass Spectrom.*, **2012**, *330-332*, 233.
33. B. Power, V. Haldys, J.-Y. Salpin, T.D. Fridgen, *Int. J. Mass Spectrom.*, **2015**, *378*, 328.
34. R. Prazeres, F. Glotin, C. Insa, D.A. Jaroszynski, J.M. Ortega, *Eur. Phys. J. D*, **1998**, *3*, 87.
35. W. Paul, *Rev. Mod. Phys.*, **1990**, *62*, 531.
36. K. Rajabi, M.L. Easterling, T.D. Fridgen, *J. Am. Soc. Mass Spectrom.*, **2009**, *20*, 411.
37. M.J. Frisch, G.W. Trucks, H.B. Schlegel, G.E. Scuseria, M.A. Robb, J.R. Cheeseman, G. Scalmani, V. Barone, B. Mennucci, G.A. Petersson, H. Nakatsuji, M. Caricato, X. Li, H.P. Hratchian, A.F. Izmaylov, J. Bloino, G. Zheng, J.L. Sonnenberg, M. Hada, M. Ehara, K. Toyota, R. Fukuda, J. Hasegawa, M. Ishida, T. Nakajima, Y. Honda, O. Kitao, H. Nakai, T. Vreven, J.A. Montgomery, J.E. Peralta J., F. Ogliaro, M. Bearpark, J.J.

- Heyd, E. Brothers, K.N. Kudin, V.N. Staroverov, T. Keith, R. Kobayashi, J. Normand, K. Raghavachari, A. Rendell, J.C. Burant, S.S. Iyengar, J. Tomasi, M. Cossi, N. Rega, J.M. Millam, M. Klene, J.E. Knox, J.B. Cross, V. Bakken, C. Adamo, J. Jaramillo, R. Gomperts, R.E. Stratmann, O. Yazyev, A.J. Austin, R. Cammi, C. Pomelli, J.W. Ochterski, R.L. Martin, K. Morokuma, V.G. Zakrzewski, G.A. Voth, P. Salvador, J.J. Dannenberg, S. Dapprich, A.D. Daniels, O. Farkas, J.B. Foresman, J.V. Ortiz, J. Cioslowski, D.J. Fox, *Gaussian 09*, Revision D.01, Gaussian, Inc., Wallingford, CT, **2013**.
38. P.B. Armentrout, M. Citir, Y. Chen, M.T. Rodgers, *J. Phys. Chem. A*, **2012**, *116*, 11823.
39. P.B. Armentrout, Y. Chen, M.T. Rodgers, *J. Phys. Chem. A*, **2012**, *116*, 3989.
40. R.F.W. Bader, *Atoms in Molecules: A Quantum Theory*, Clarendon Press, Oxford University Press, New York, NY, **1990**.
41. T.A. Keith, *AIMAll*, Version 14.10.27, TK Gristmill Software, Overland Park, KS, **2014**, aim.tkgristmill.com.
42. P. Colarusso, K. Zhang, B. Gup, P.F. Bernath, *Chem Phys Lett*, **1997**, *269*, 39.
43. G.C. Boles, R.A. Coates, G. Berden, J. Oomens, P.B. Armentrout, *J. Phys. Chem. B*, **2015**, *119*, 11607.
44. R.A. Coates, C.P. McNary, G.C. Boles, G. Berden, J. Oomens, P.B. Armentrout, *Phys. Chem. Chem. Phys.*, **2015**, *17*, 25799.
45. M. Goodgame, K.W. Johns, *J. Chem. Soc., Dalton Trans.*, **1977**, *17*, 1680.
46. M.A. Halcrow, *Chem. Soc. Rev.*, **2013**, *42*, 1784.

CHAPTER 6 – Conclusions and Future Work

6.1 Summary

A wide range of metal ion – uracil complexes, both bare and solvated, were examined through the use of IRMPD spectroscopy in concert with DFT electronic structure calculations. This combination of experimental and theoretical techniques has proven to be very effective in identifying the preferred configuration of such species, with calculations revealing the lowest energy isomers of each complex and comparisons between these calculated and the experimental spectra allowing for the determination of structures. The different basis sets used in structure calculations did not lead to any significant differences in either the relative energies of the isomers or the calculated spectra. Although the preferred isomer of every complex could not be definitively assigned, there is substantial new understanding into how uracil will tautomerize under various metal and solvent combinations. In some instances, complexes with a number of possible isomers that were indistinguishable from each other in previous experiments conducted in the O-H/N-H region ($2700 - 3800\text{ cm}^{-1}$), had been further narrowed down or identified in the current work based on the observations in the IR fingerprint region ($1000 - 1900\text{ cm}^{-1}$).

In chapter 2, the structures of $[\text{M}(\text{Ura-H})(\text{Ura})]^+$ and $[\text{M}(\text{Ura-H})(\text{Ura})(\text{H}_2\text{O})]^+$, where M corresponds to group 2 metal ions Ba^{2+} , Sr^{2+} , Ca^{2+} and Mg^{2+} , were examined using IRMPD spectroscopy in the IR fingerprint region. Deprotonation of one uracil moiety was found to occur at the N3 position, and the other neutral uracil is a keto-enol tautomer where hydrogen is transferred from N3 to O4. This transferred hydrogen participates in a hydrogen bond interaction with O2 of the deprotonated uracil. Each of the metal ions are tetracoordinate in all complexes, interacting with N3 and O4 of the deprotonated uracil,

and N3 and O2 of the other uracil. The carbonyl bonds are notably affected by the metal, as decreasing metal size leads to stronger binding between the metal and carbonyls. This lengthens (and weakens) the carbonyl bond, a trend that is observed by red-shifting of the carbonyl bands. However, the Mg^{2+} complexes do not follow this trend for reasons we are unsure of.

In the case of solvated structures, the water molecule coordinates directly to the metal ion and also hydrogen bonds with O4 of the deprotonated uracil. This hydrogen bond between water and uracil becomes increasingly weak as the metal ion decreases in size and, as confirmed by the AIM analysis, the interaction between water and the metal ion becomes increasingly electrostatic in nature as the metal ion decreases in size. The interaction between the metal ion and uracil moieties remains unchanged, indicating no solvent effect on the inclusion of a single water molecule. The water molecule donates electron density back to the carbonyl bonds, which can be observed in a blue-shift of these bands when compared to the bare structures. The same metal effect on the carbonyl stretching frequencies is observed; once again, Mg^{2+} does not follow this trend.

For the Mg^{2+} complexes, the configuration previously described offers the best agreement with the experimental spectra even though these isomers are not calculated to be the lowest energy. However, the difference between these isomers and those lower in energy is almost negligible ($\leq 0.8 \text{ kJ mol}^{-1}$) and these lower energy structures were ruled out spectroscopically as a major contributor.

Chapter 3 continued with similar complexes involving alkaline earth metals – this time, the degree of solvation varied from $n = 1 - 3$ in $[\text{M}(\text{Ura-H})(\text{H}_2\text{O})_n]^+$ complexes. When $n = 3$, only the $[\text{Mg}(\text{Ura-H})(\text{H}_2\text{O})_3]^+$ complex was experimentally detected, potentially due

to the smaller size, and thus increased charge density, of the Mg^{2+} ion. Both the O-H/N-H stretching and fingerprint regions were explored. The IR spectra generated for these lowest energy structures generally agreed best with the experimental IRMPD spectra.

For all complexes, the lowest energy isomers are once again deprotonated at N3 of uracil with the metal bound by a bidentate electrostatic interaction to N3 and O4, a pattern similar to that observed in the dimeric complexes. As this configuration is consistent regardless of the degree of hydration, no solvent effect is apparent. Any water molecules present are directly bound to the metal ion and participate in hydrogen bonding with neighbouring carbonyls, again following what was observed in the hydrated dimers. For singly hydrated complexes, a hydrogen bond between water and uracil is formed at the O2 position; for doubly hydrated ions, one water molecule is hydrogen-bonded to O2. In the Ba and Sr complexes, the second water molecule is hydrogen-bonded to O4. In the Ca and Mg complexes, the AIM analysis does not detect any water–O4 interaction. For $[\text{Mg}(\text{Ura-H})(\text{H}_2\text{O})_3]^+$, two water molecules are oriented towards O4, although the AIM analysis indicates no hydrogen bonds are established, and the third water molecule is hydrogen-bonded to O2.

For the complexes of Ba^{2+} , Sr^{2+} and Ca^{2+} , identification of the predominant isomer was easily made, as only the lowest energy isomer gave calculated spectra in suitable agreement with the experimental IRMPD spectra. For Mg^{2+} , however, multiple isomers provide spectral agreement and so no definitive conclusion on the structural assignment could be drawn.

The complexes examined in Chapters 2 and 3 were re-visited in Chapter 4 using a selection of d-block metal ions, along with Pb^{2+} , in place of the alkaline earth metals, where

some very interesting results were collected. These complexes, $[M(\text{Ura-H})(\text{Ura})]^+$ and $[M(\text{Ura-H})(\text{H}_2\text{O})_n]^+$ where $M = \text{Cu}^{2+}$, Zn^{2+} , and Pb^{2+} , and $n = 1 - 3$, were examined using IRMPD spectroscopy in the $1000 - 1900 \text{ cm}^{-1}$ mid-infrared region. The IR spectra generated for the lowest energy structures generally showed the best agreement with the experimental IRMPD spectra, however there were some instances where multiple isomers were in spectral agreement. For the dimeric complexes, the lowest energy structures are deprotonated at N3 of uracil with the metal bound by a bidentate electrostatic interaction with N3 and O4, and the second, neutral uracil being a keto-enol tautomer with proton transfer from N3 to O4, and an intramolecular hydrogen bond being formed by this enol and O2 of the neighbouring carbonyl. This configuration is consistent with the result of the group 2 metal complexes.

For hydrated monomeric species, a similar pattern of deprotonation is observed, with the exception of $[\text{Cu}(\text{Ura-H})(\text{H}_2\text{O})]^+$, where Cu is coordinated at the deprotonated N1 position. As this complex becomes doubly hydrated, the uracil is then deprotonated at N3, demonstrating a clear solvent effect on the preferred uracil tautomer in Cu^{2+} complexes. The singly hydrated Zn^{2+} complex also offers an interesting result. Although uracil deprotonates at N3, there is not a bidentate interaction – the metal coordination is to the O2 carbonyl only. The more interesting aspect of this complex is a proton transfer from the solvent transfers to the uracil, resulting in the complex resembling $[\text{Zn}(\text{Ura})(\text{OH})]^+$, with the uracil moiety being a neutral keto-enol tautomer. For the doubly and triply hydrated Zn species, metal coordination is monodentate to N3 only, and the solvent molecules remain intact. The water molecules are bound to Zn^{2+} and are positioned between the metal and the neighbouring carbonyl groups to facilitate hydrogen bonding.

In all complexes, any water molecules (or, in the case of Zn^{2+} , the hydroxy group) are bound to the metal ion and, for the most part, participate in hydrogen bonding with the neighbouring carbonyls, with the exception of $[\text{Cu}(\text{Ura-H})(\text{H}_2\text{O})]^+$ and $[\text{Zn}(\text{Ura})(\text{OH})]^+$ where no hydrogen bonding is observed. The experimental spectrum of $[\text{Zn}(\text{Ura-H})(\text{H}_2\text{O})_3]^+$ unfortunately did not contain enough spectral features to allow for any distinctions to be made between the calculated spectra. However, the calculated lowest energy isomer does follow logically with the same patterns of deprotonation and solvent coordination previously observed.

Finally, Chapter 5 expands the selection of d-block metals to include Co, Fe, Ni, Zn, Cu and Cd, and offers a first glimpse at an alternative solvent in the form of ammonia. These structures, $[\text{M}(\text{Ura-H})(\text{Ura})(\text{NH}_3)]^+$, were examined using IRMPD in the 1000 – 1900 cm^{-1} fingerprint region. Consistent with the other results, deprotonation occurs at the N3 position in all cases, and the other uracil displays hydrogen transfer from N3 to O4, with the Cu^{2+} complex once again offering an exception to the observed trend. As seen in all other dimeric complexes examined, this transferred hydrogen participates in an intramolecular hydrogen bond with a carbonyl group of the neighbouring uracil, which is confirmed through AIM analysis. For the complexes where this transfer occurs, the hydrogen bond is to the O2 position of this neighbouring uracil. No proton transfer occurs in the neutral uracil of the Cu^{2+} complex, resulting in the diketo form. While the metal ion is still bound to N3 and O4 of the deprotonated uracil, it interacts only with O2 of the neutral moiety. In this case, the intramolecular hydrogen bond is from the N3 hydrogen of the neutral uracil to the O2 carbonyl of the deprotonated uracil.

A new consideration for these d-block metals that isn't present for the group 2 metals is that of d-orbital splitting and spin multiplicity. In the cases where this is applicable, the metal is in the high spin configuration.

The ammonia molecule is bound directly to the metal ion in all lowest energy structures. For Fe^{2+} , Co^{2+} , Ni^{2+} , Zn^{2+} , and Cd^{2+} complexes, the metal ion is tetracoordinate with the uracil moieties, interacting with N3 and O2 of the neutral uracil and N3 and O4 of the deprotonated uracil. In the lowest energy Cu^{2+} structure, the interaction with uracil is tridentate with N3 and O4 of the deprotonated uracil and O4 of the neutral uracil. This deviation in complex configuration is potentially contributed to copper's tendency towards a Jahn-Teller distorted complex, and thus a preference for a square planar configuration.

6.2 Potential Future Work

Based on the insights provided by the current work, a number of new questions are raised offering multiple directions to take future work. First of all, there are many modifications and extensions to the current work that can reveal useful structural information using the same experimental and theoretical techniques. The exploration of a solvent effect has only really scratched the surface. The impact of water has been observed in complexes containing Cu^{2+} , but not elsewhere. By gradually increasing the degree of solvation in all of these complexes, the point at which uracil tautomerization occurs, if at all, can be determined. Being the universal solvent, water has been the primary solvent of interest in this research, along with a brief glimpse at the ammoniation of these complexes. There are other biological solvents which could be examined, including but not limited to hydrogen peroxide, methanol and formamide, to identify if a different solvent environment

will impact the tautomerization of uracil. In terms of metal variation, Cu^{2+} again led to deviations from the typical structural configurations. A wide range of metals are yet to be explored, and at varying charge, as all metals in this study were divalent. As uracil was the only nucleobase of interest, this same work could easily be adapted to include any of the others to identify the impacts of metal coordination and solvation. Finally, the complexes themselves could be expanded into trimers and tetramers, examining what tautomerization may occur, if any, in the additional uracil moieties.

These studies were carried out under the premise that altering the hydrogen bonding environment in uracil could lead to nucleobase mismatches, and ultimately genetic defects. Incorporating metal ions and microsolvation into a Ura-Ade complex (or any of the other Watson-Crick pairings) would presumably offer insight as to whether or not these pairings are altered or otherwise disrupted by the inclusion of a metal ion or solvent, as well as the degree of metalation or solvation that may be required to cause such a disruption. Of course, a DNA or RNA strand contains a countless number of these pairs, and so ideally these studies would ultimately expand beyond a single molecule or pair and on to a larger strand scale.

APPENDIX A – Chapter 2 Supplemental Information

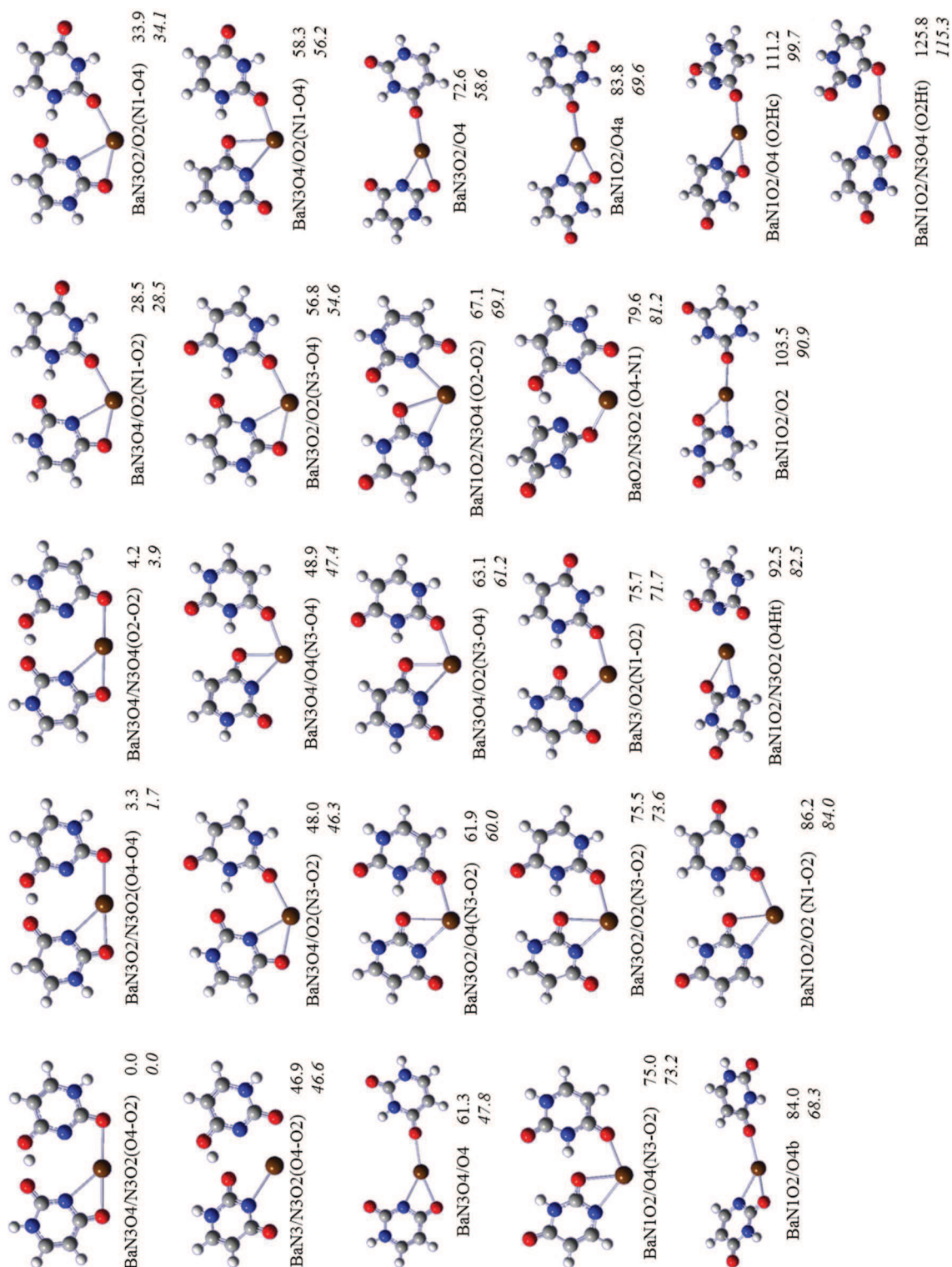


Figure A1. All structures found using calculation method 1 for $[\text{Ba}(\text{Ura-H})(\text{Ura})]^+$. The calculated relative enthalpies and Gibbs energies (italics) are also shown in kJ mol^{-1} at 298 K

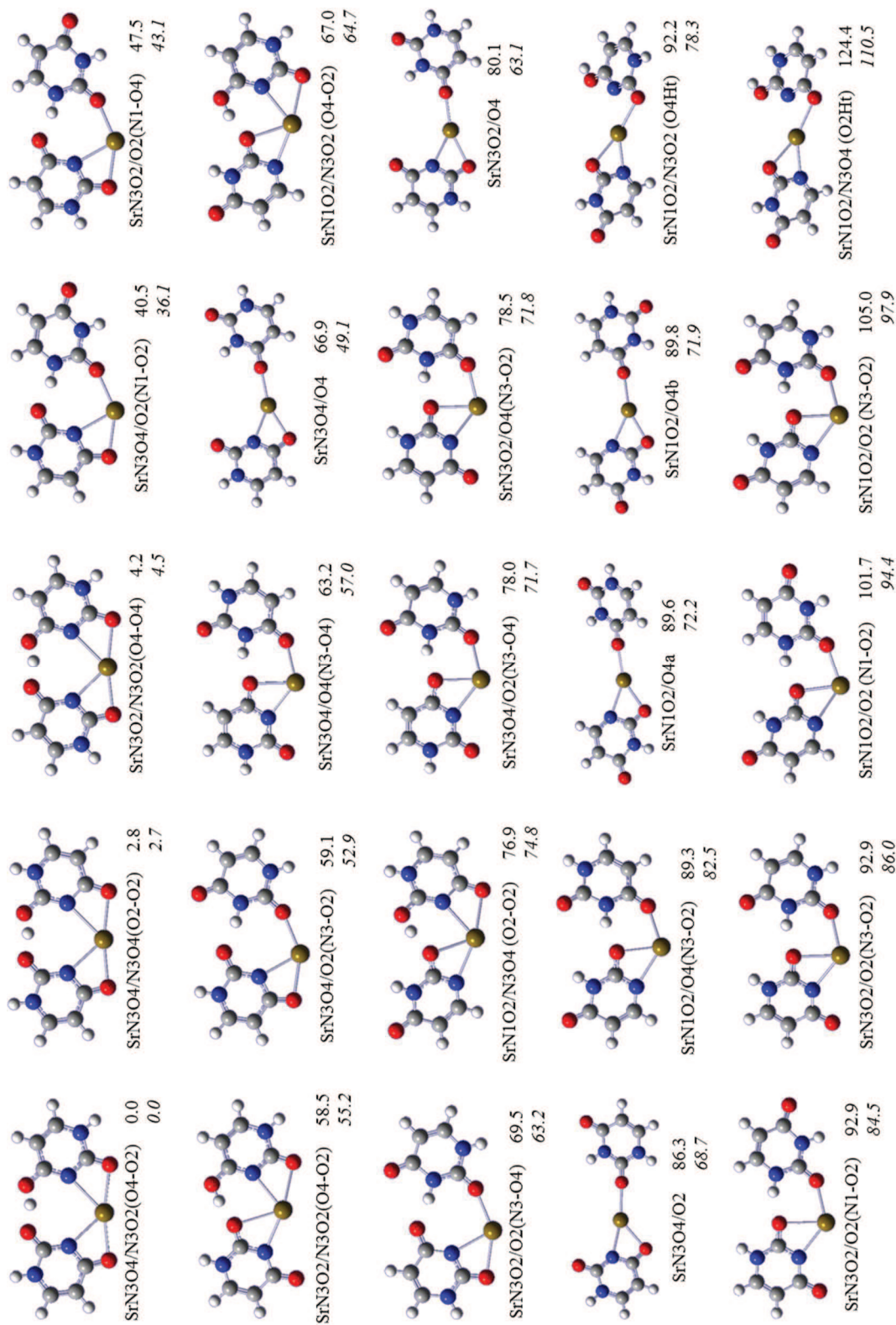


Figure A2. All structures found using calculation method 1 for $[\text{Sr}(\text{Ura-H})(\text{Ura})]^+$. The calculated relative enthalpies and Gibbs energies (italics) are also shown in kJ mol^{-1} at 298 K.

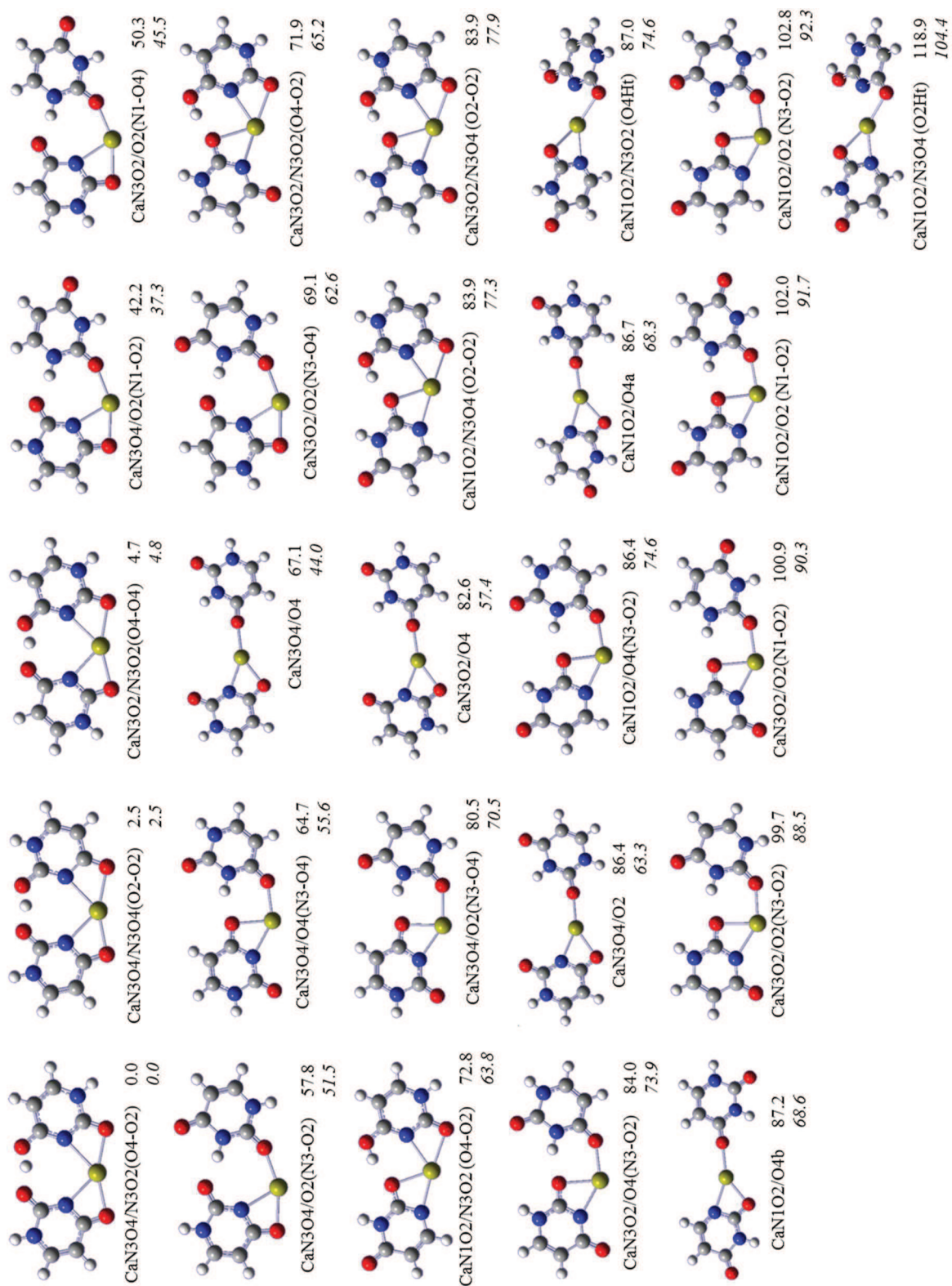


Figure A3. All structures found using calculation method 1 for $[\text{Ca}(\text{Ura-H})(\text{Ura})]^+$. The calculated relative enthalpies and Gibbs energies (italics) are also shown in kJ mol^{-1} at 298 K.

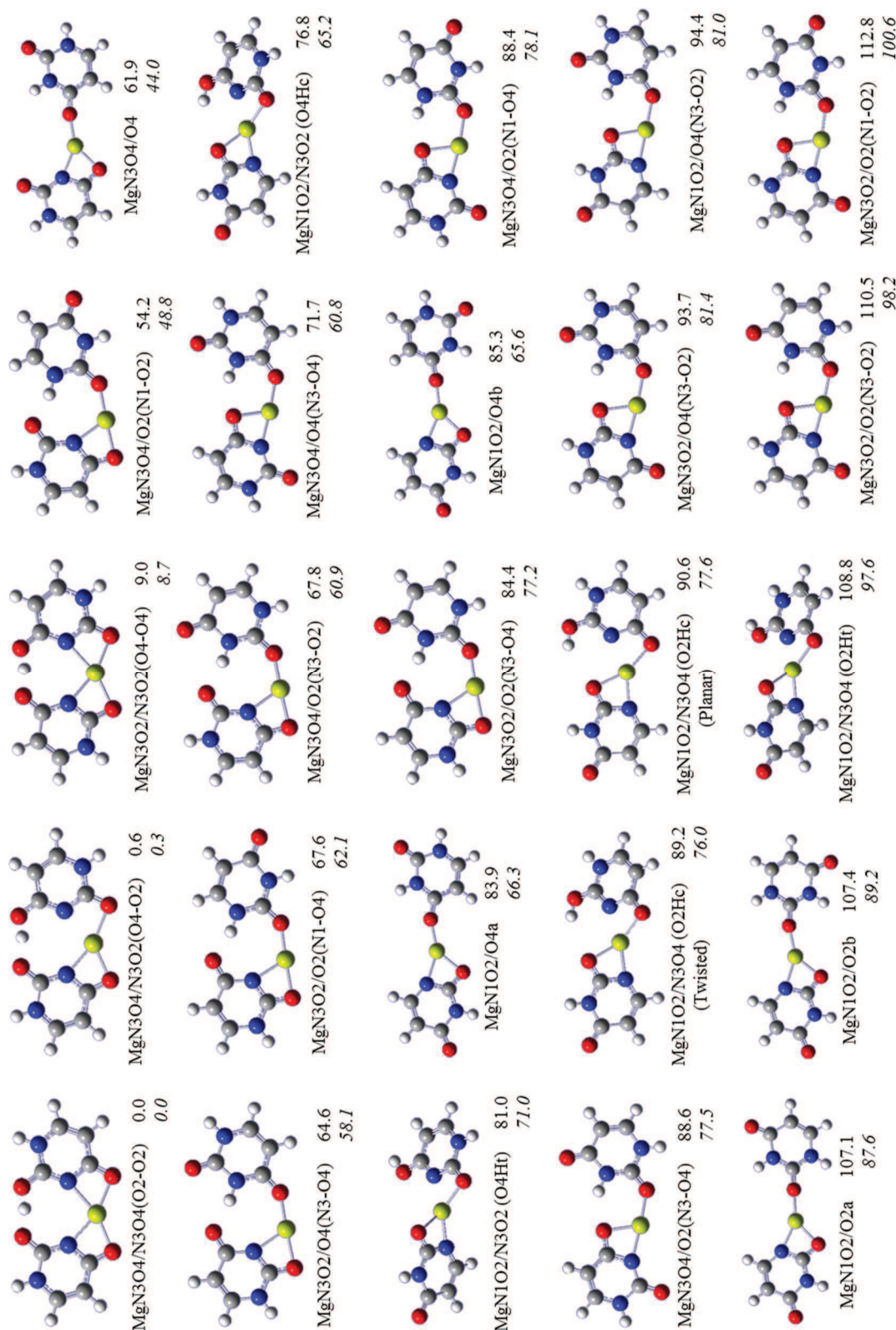


Figure A4. All structures found using calculation method 1 for $[\text{Mg}(\text{Ura-H})(\text{Ura})]^+$. The calculated relative enthalpies and Gibbs energies (italics) are also shown in kJ mol^{-1} at 298 K.

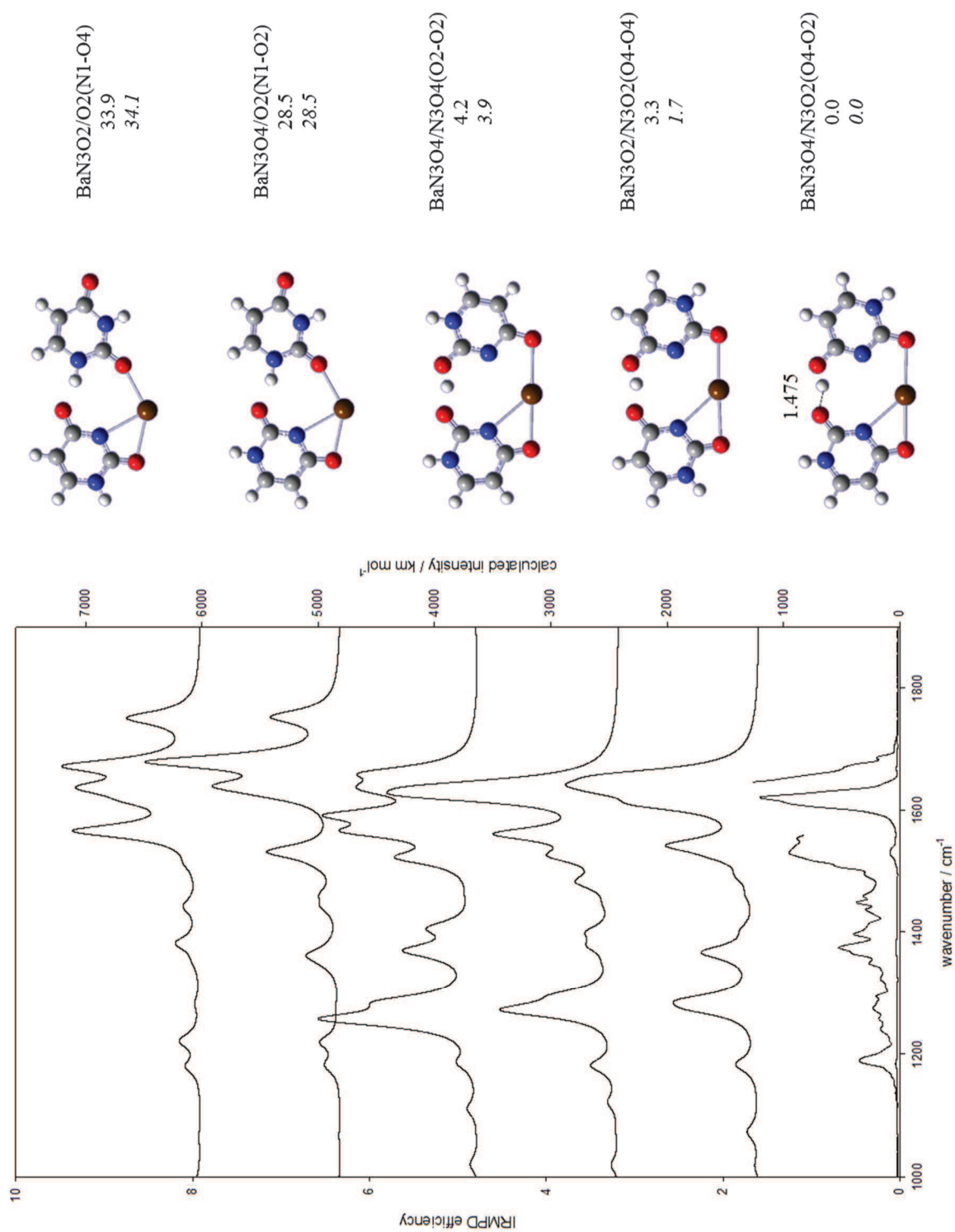


Figure A5. Experimental IRMPD spectrum (bottom) for $[\text{Ba}(\text{Ura-H})(\text{Ura})]^+$ compared with the B3LYP computed spectra using computational method 1 for the five lowest energy structures. The calculated relative enthalpies and Gibbs energies (*italics*) are also shown. Hydrogen bond distance is given for the lowest energy structure, in Angströms.

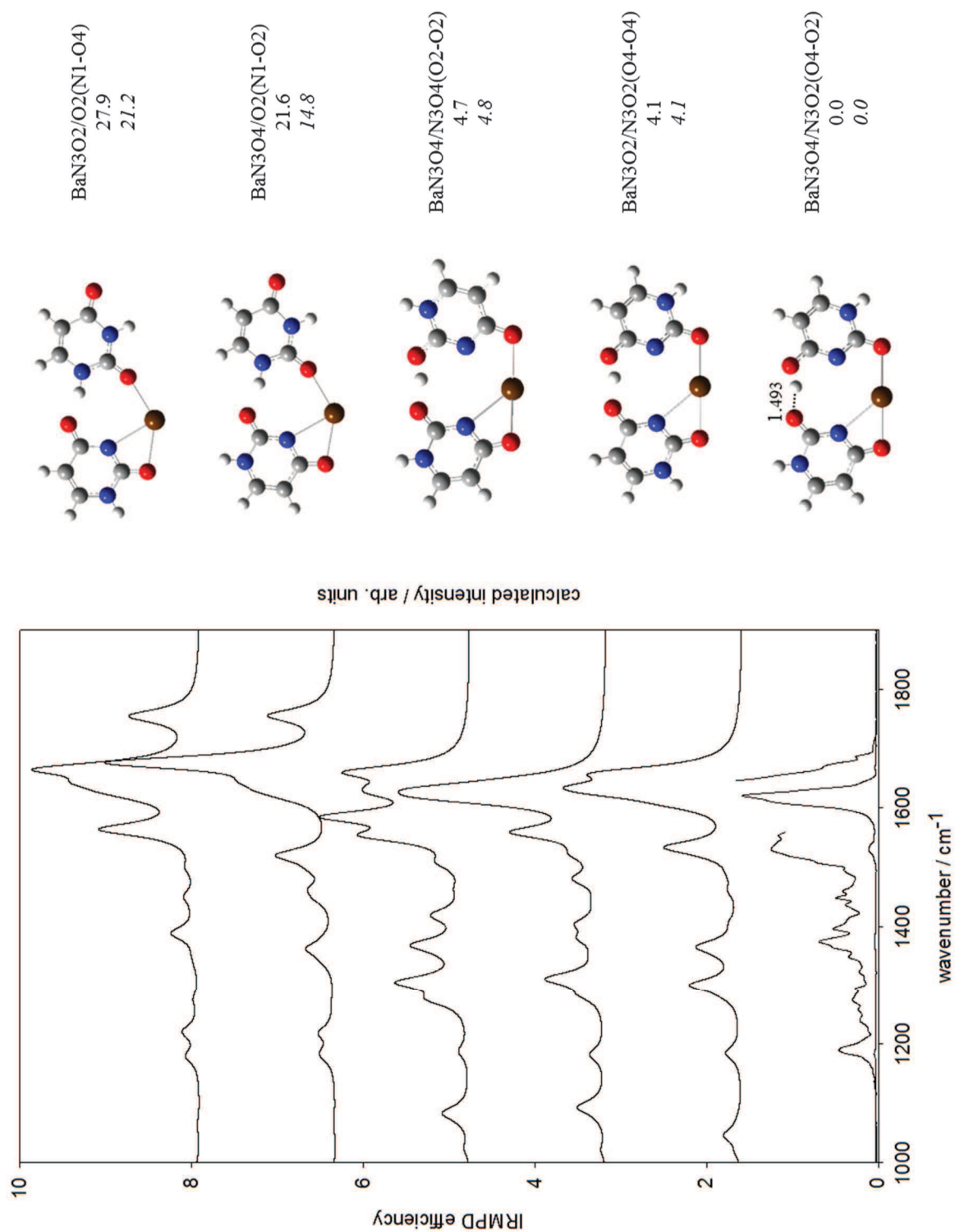


Figure A6. Experimental IRMPD spectrum (bottom) for [Ba(Ura-H)(Ura)]⁺ compared with the B3LYP computed spectra using computational method 2 for the five lowest energy structures. The calculated relative enthalpies and Gibbs energies (*italics*) are also shown. Hydrogen bond distance is given for the lowest energy structure, in Angströms.

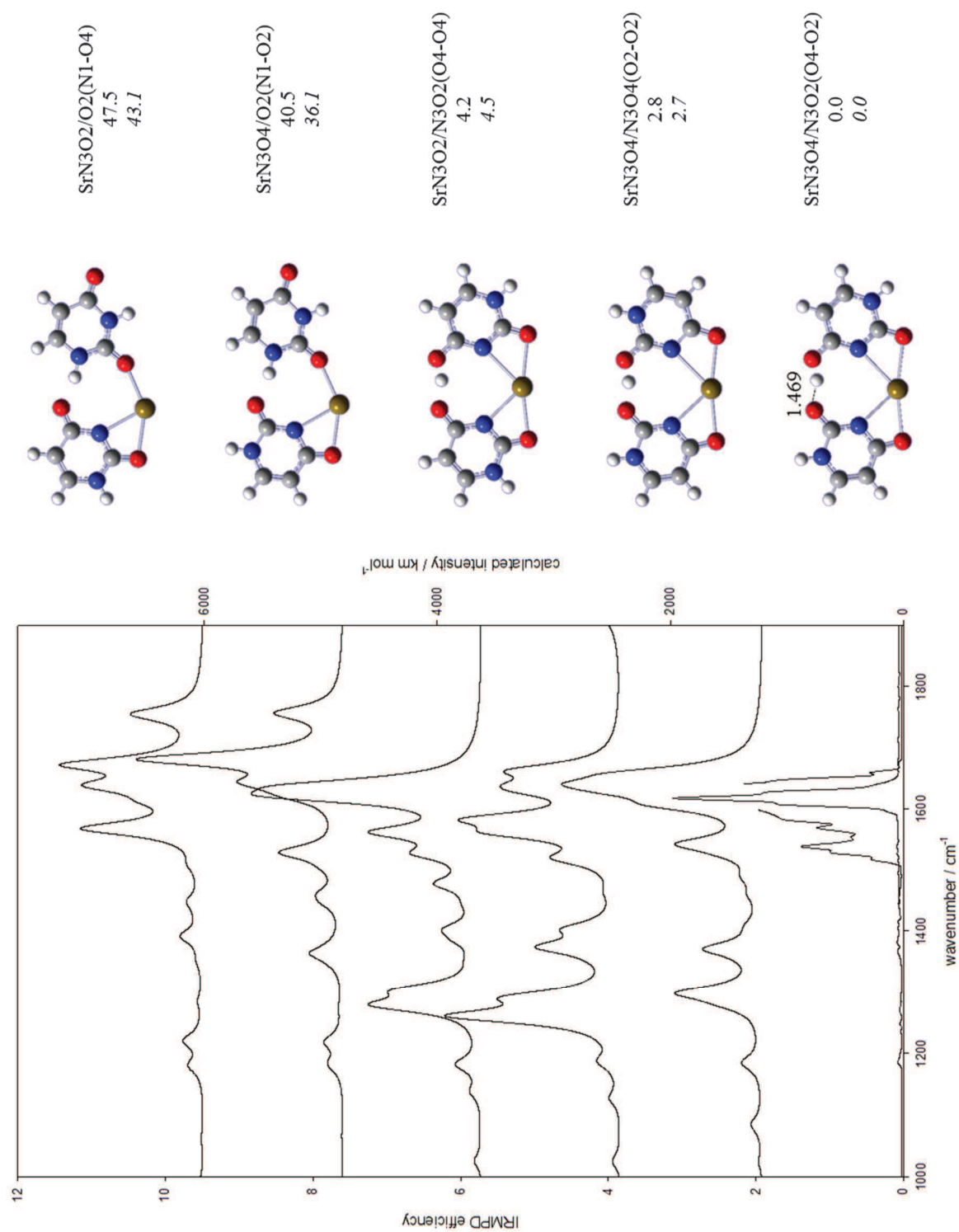


Figure A7. Experimental IRMPD spectrum (bottom) for [Sr(Ura-H)(Ura)]⁺ compared with the B3LYP computed spectra using computational method 1 for the five lowest energy structures. The calculated relative enthalpies and Gibbs energies (*italics*) are also shown. Hydrogen bond distance is given for the lowest energy structure, in Angströms.

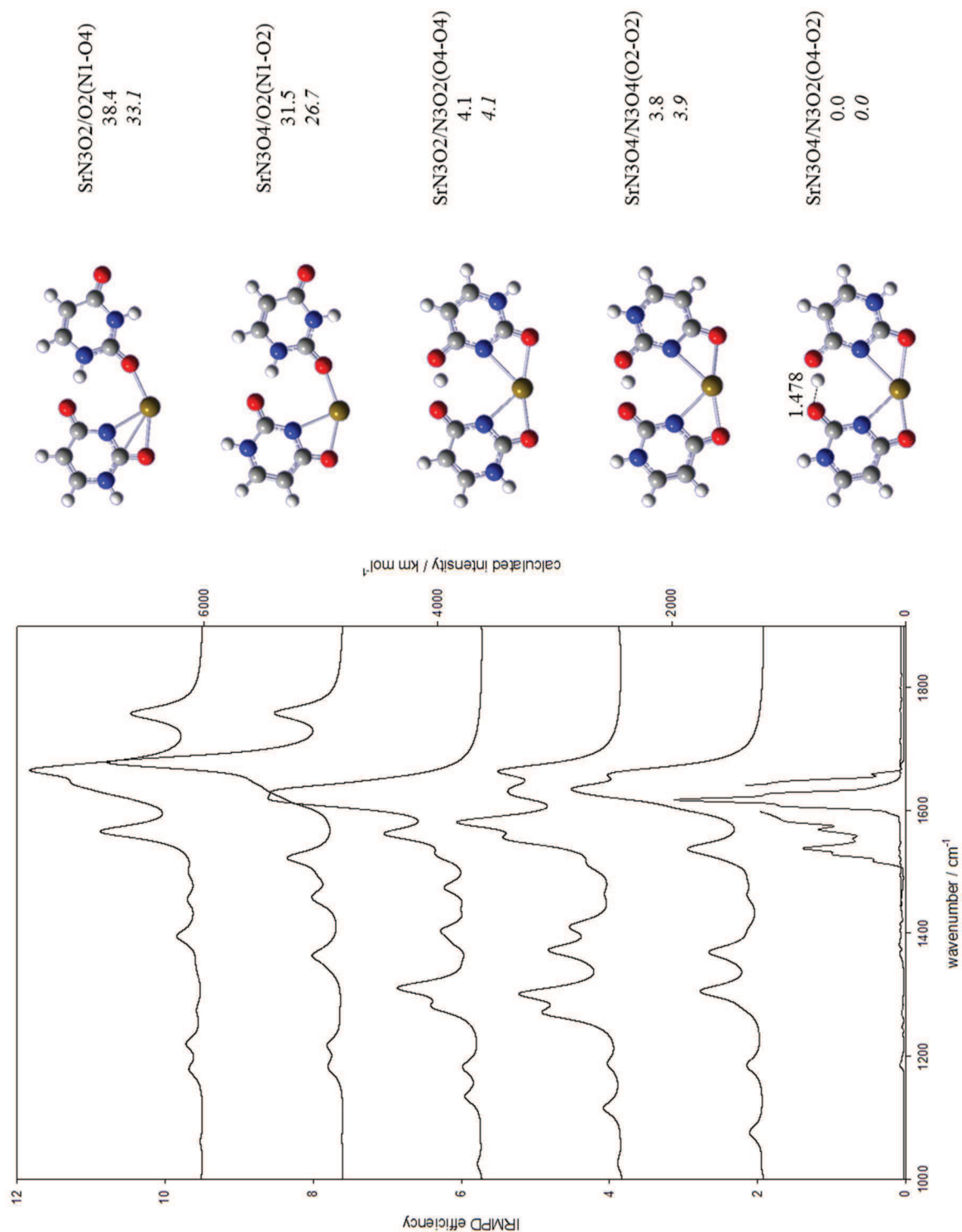


Figure A8. Experimental IRMPD spectrum (bottom) for $[\text{Sr}(\text{Ura-H})(\text{Ura})]^+$ compared with the B3LYP computed spectra using computational method 2 for the five lowest energy structures. The calculated relative enthalpies and Gibbs energies (italics) are also shown. Hydrogen bond distance is given for the lowest energy structure, in Angströms.

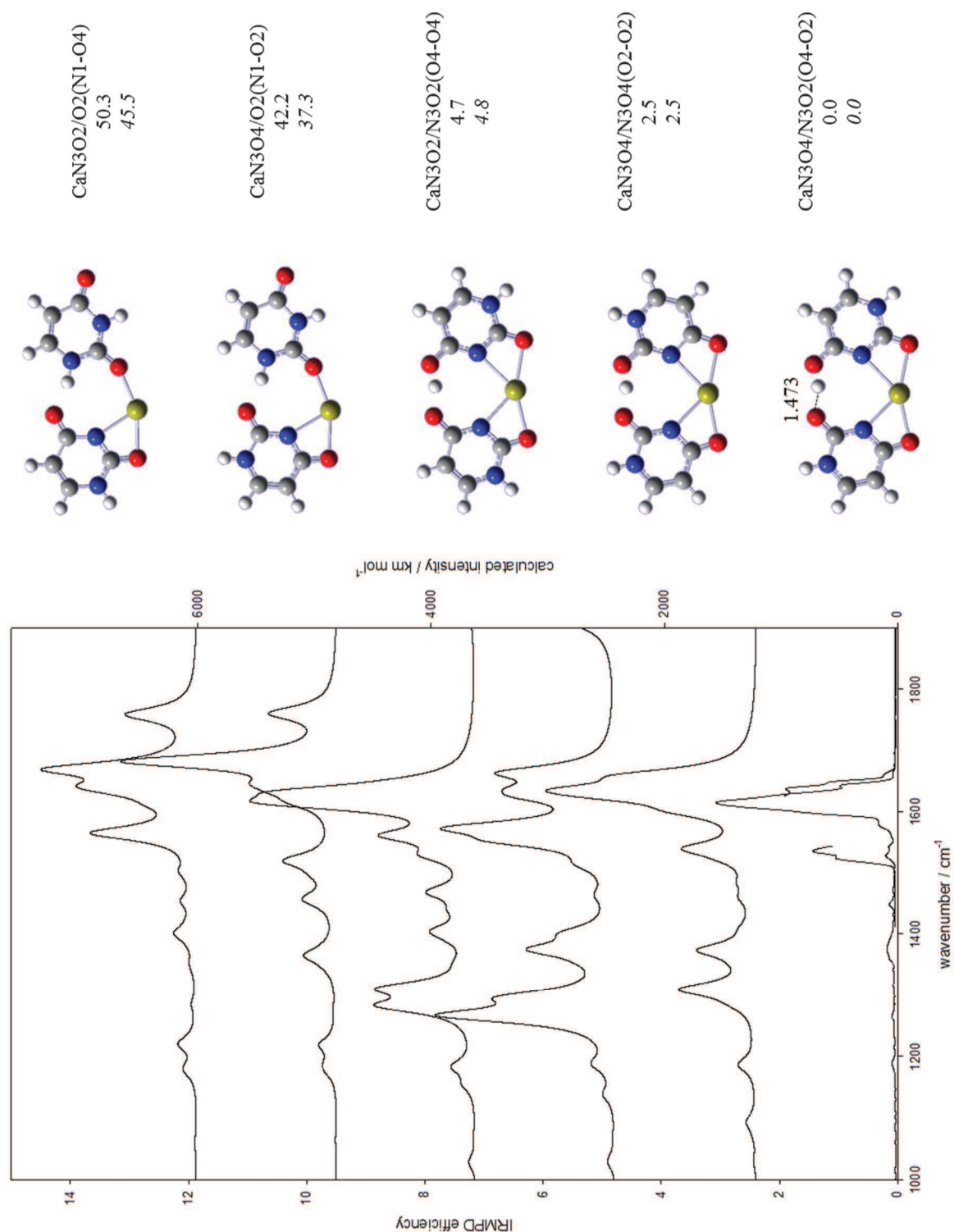


Figure A9. Experimental IRMPD spectrum (bottom) for $[\text{Ca}(\text{Ura-H})(\text{Ura})]^+$ compared with the B3LYP computed spectra using computational method 1 for the five lowest energy structures. The calculated relative enthalpies and Gibbs energies (italics) are also shown. Hydrogen bond distance is given for the lowest energy structure, in Angströms.

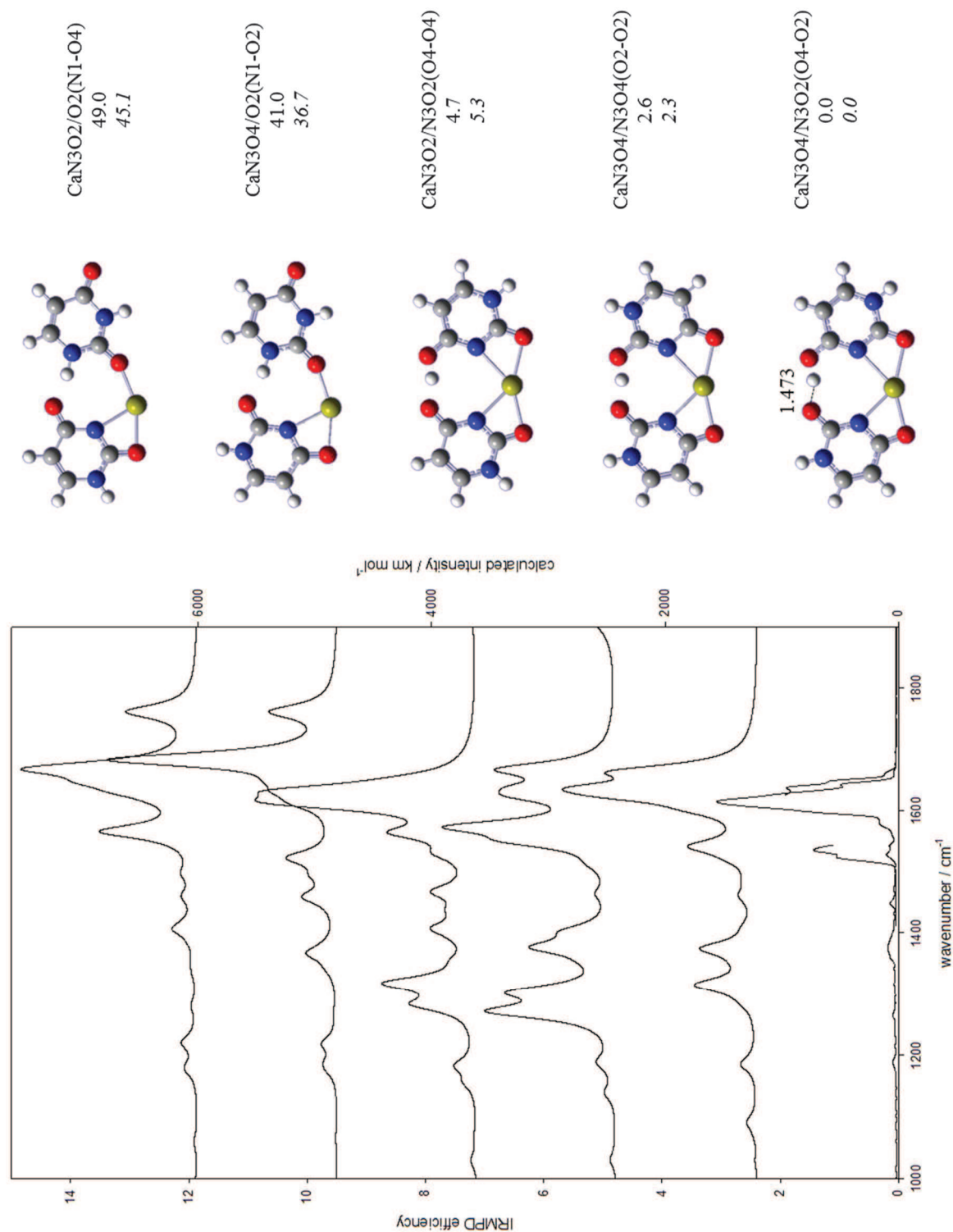


Figure A10. Experimental IRMPD spectrum (bottom) for $[\text{Ca}(\text{Ura-H})(\text{Ura})]^+$ compared with the B3LYP computed spectra using computational method 2 for the five lowest energy structures. The calculated relative enthalpies and Gibbs energies (italics) are also shown. Hydrogen bond distance is given for the lowest energy structure, in Angströms.

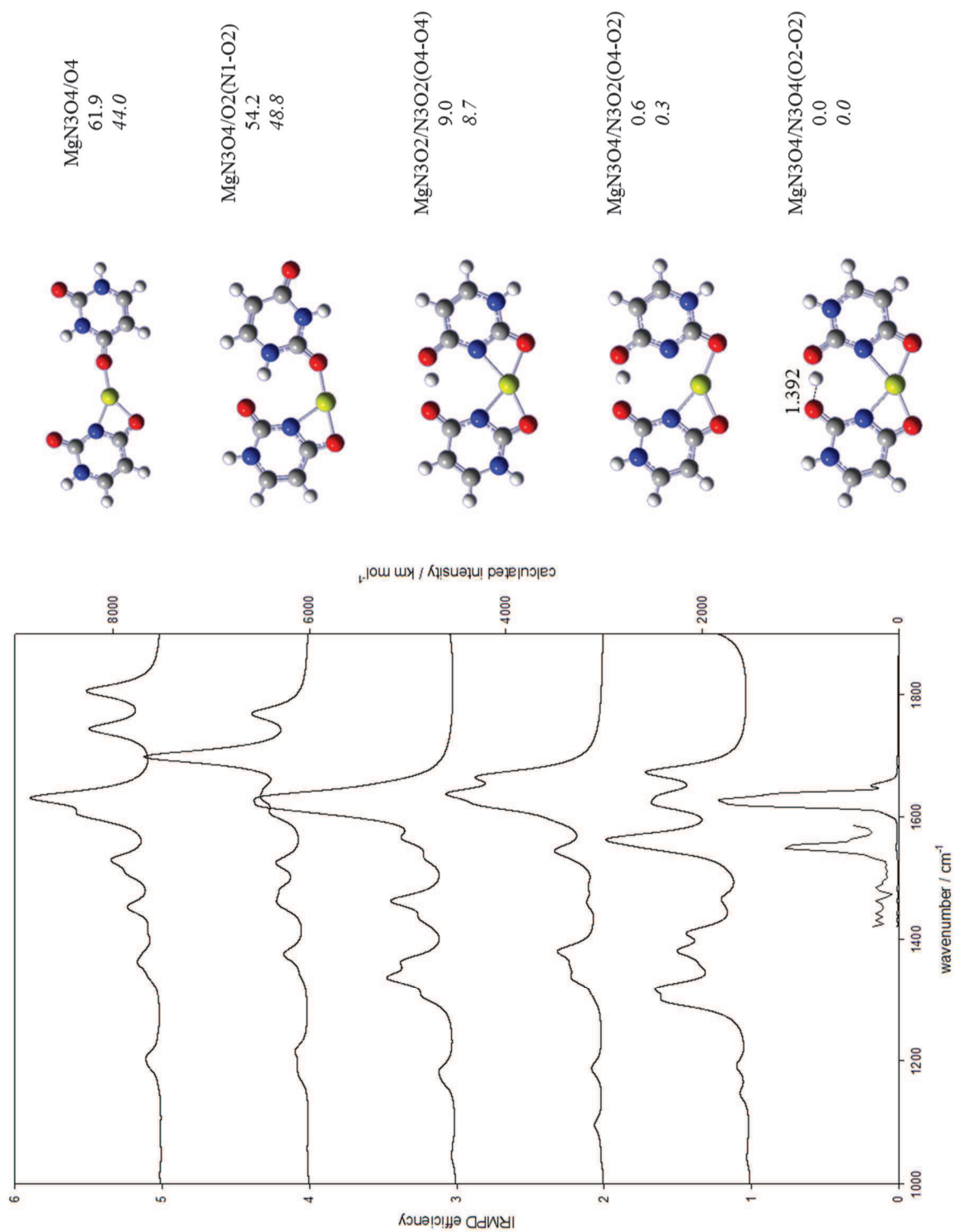
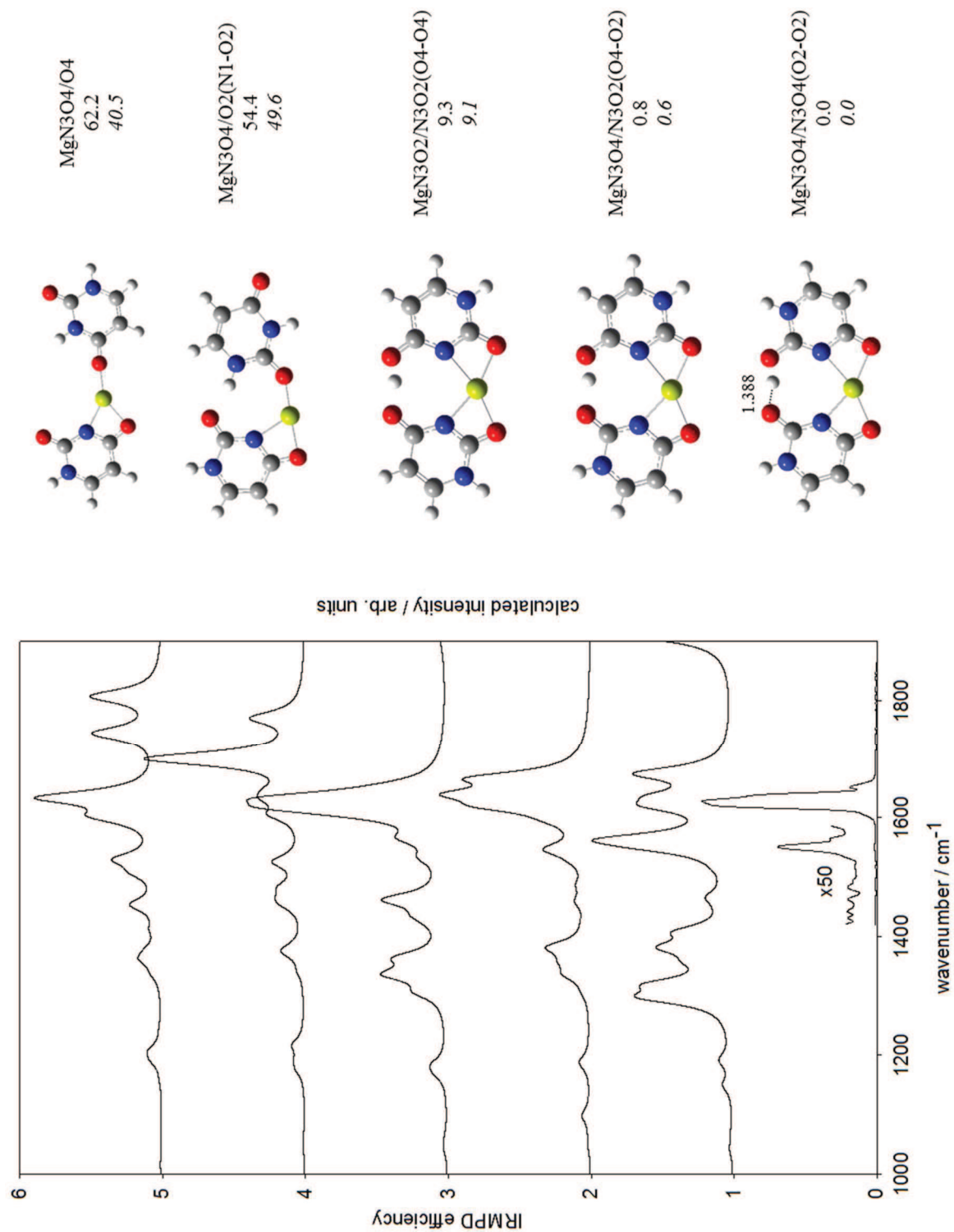


Figure A11. Experimental IRMPD spectrum (bottom) for $[\text{Mg}(\text{Ura-H})(\text{Ura})]^+$ compared with the B3LYP computed spectra using computational method 1 for the five lowest energy structures. The calculated relative enthalpies and Gibbs energies (italics) are also shown. Hydrogen bond distance is given for the lowest energy structure, in Angströms.



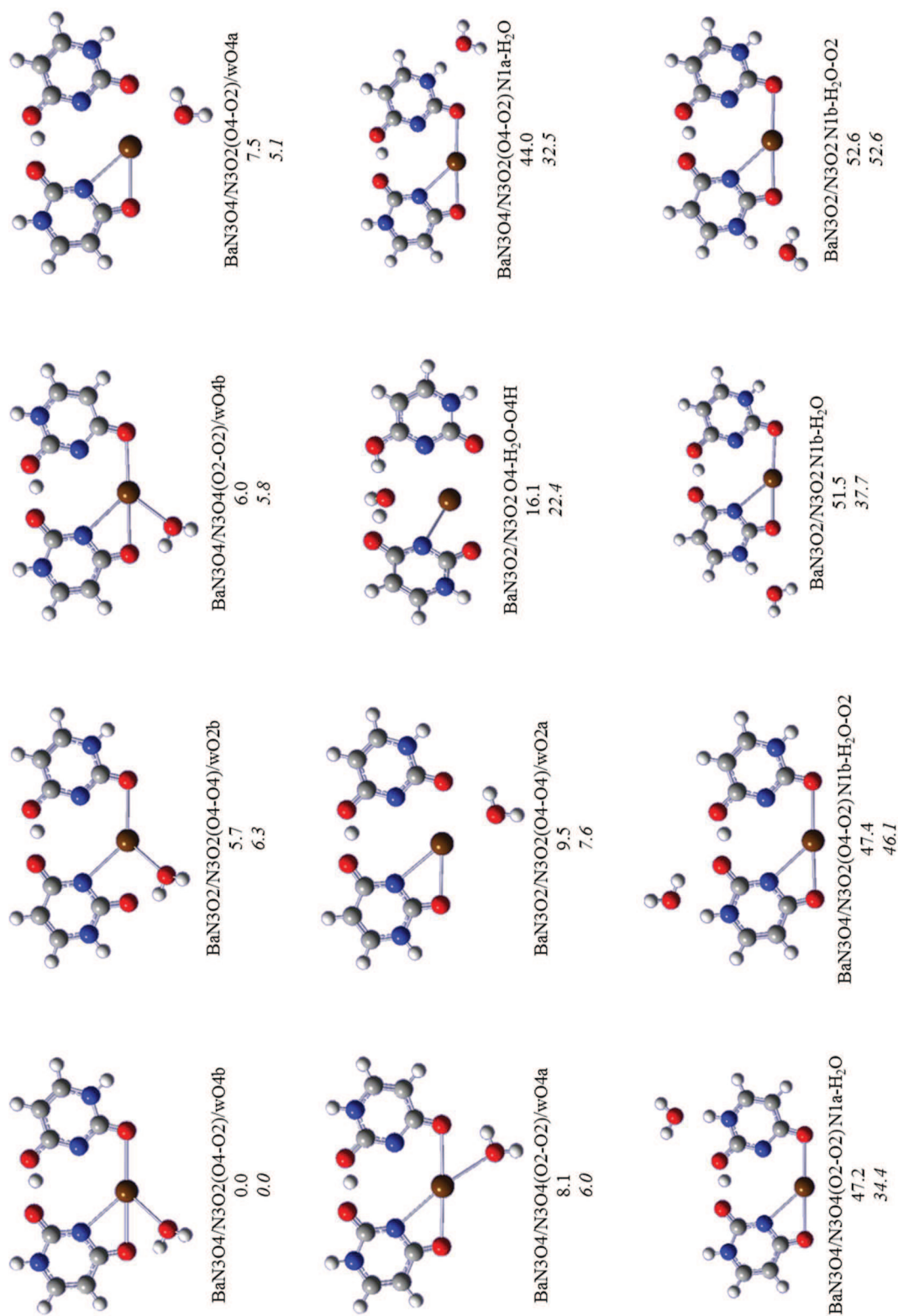


Figure A13. All structures found using calculation method 1 for $[\text{Ba}(\text{Ura-H})(\text{Ura})(\text{H}_2\text{O})]^+$. The calculated relative enthalpies and Gibbs energies (italics) are also shown in kJ mol^{-1} at 298 K.

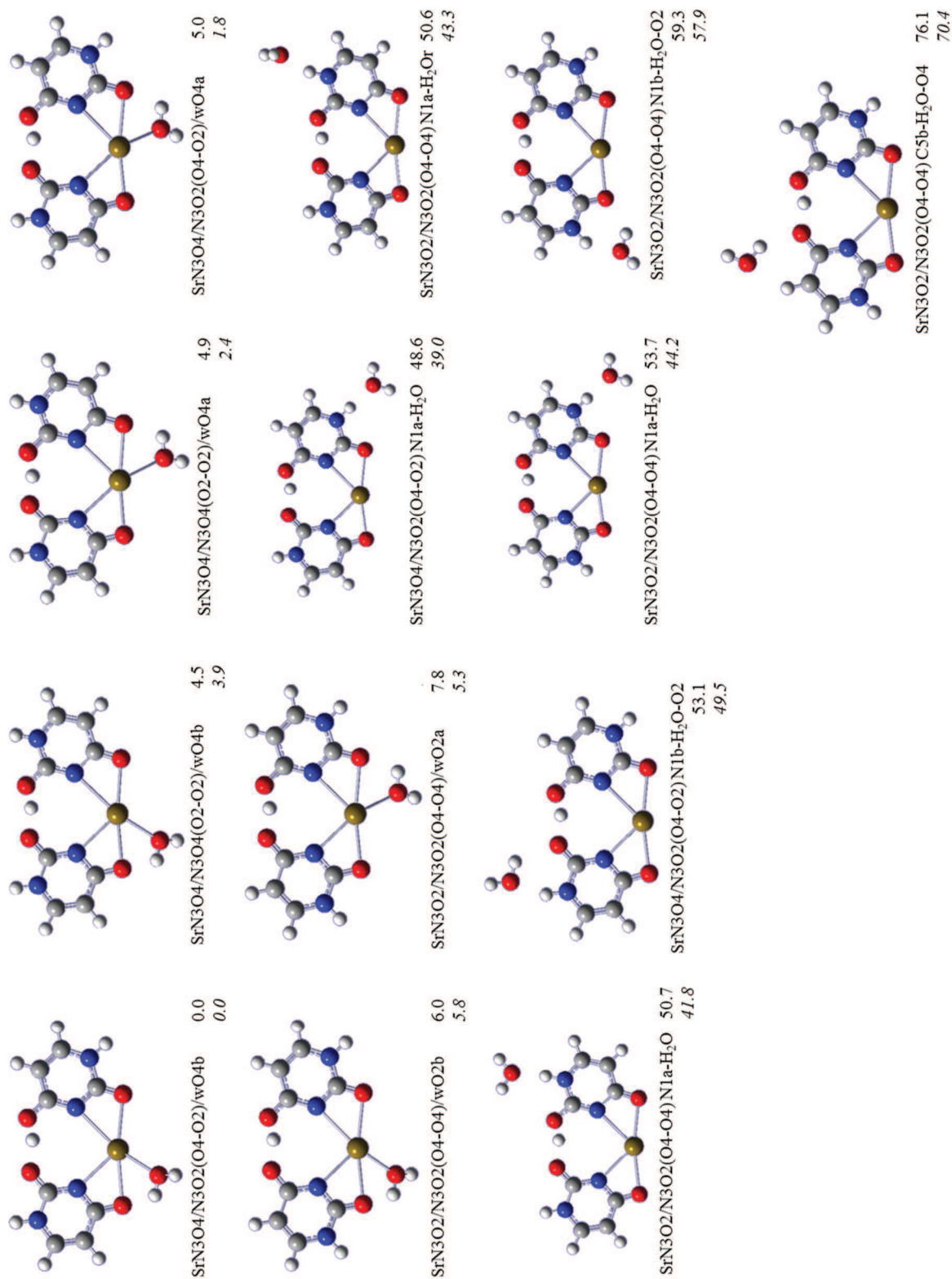


Figure A14. All structures found using calculation method 1 for $[\text{Sr}(\text{Ura-H})(\text{Ura})(\text{H}_2\text{O})]^+$. The calculated relative enthalpies and Gibbs energies (italics) are also shown in kJ mol^{-1} at 298 K.

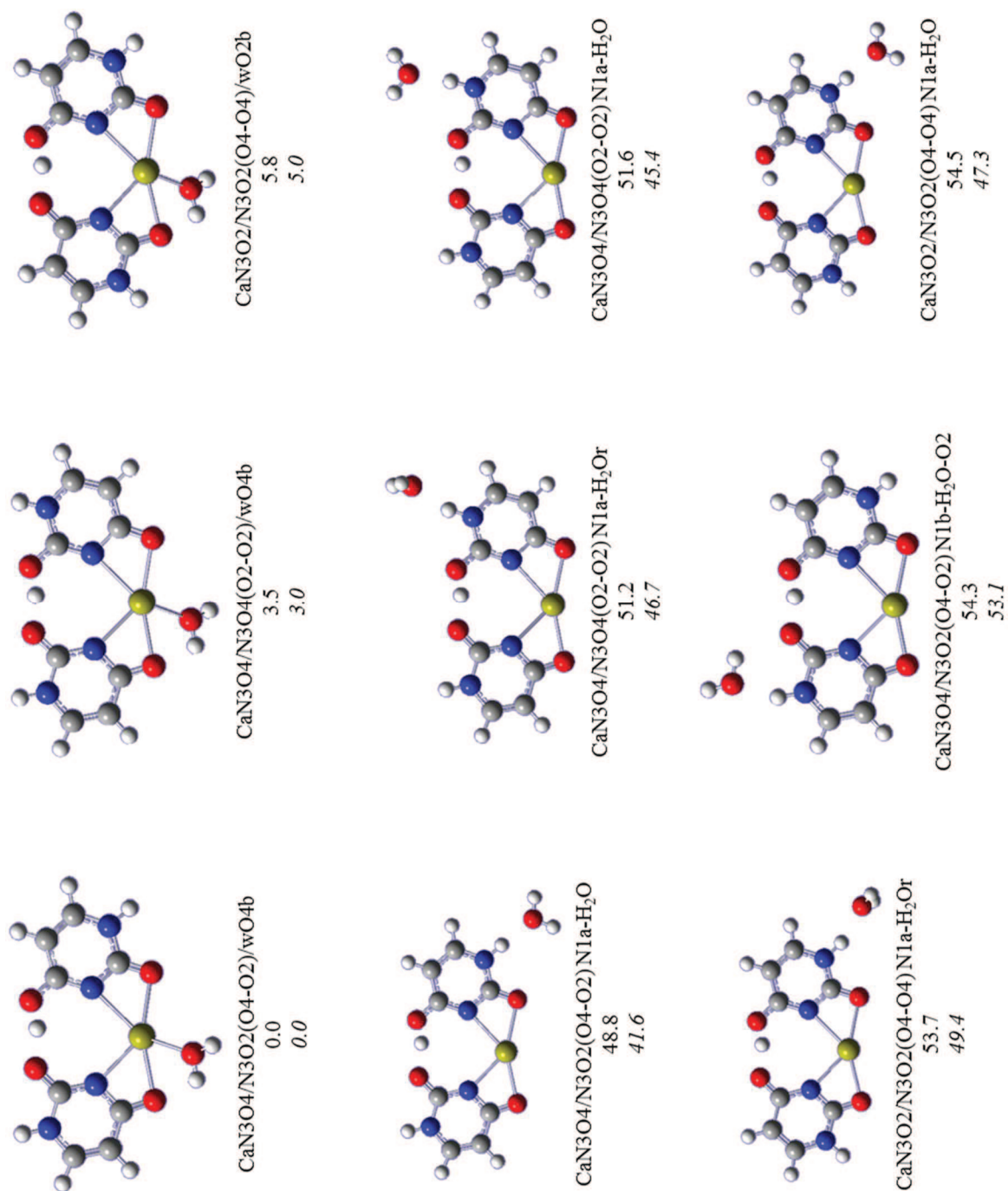


Figure A15. All structures found using calculation method 1 for $[\text{Ca}(\text{Ura-H})(\text{Ura})(\text{H}_2\text{O})]^+$. The calculated relative enthalpies and Gibbs energies (italics) are also shown in kJ mol^{-1} at 298 K.

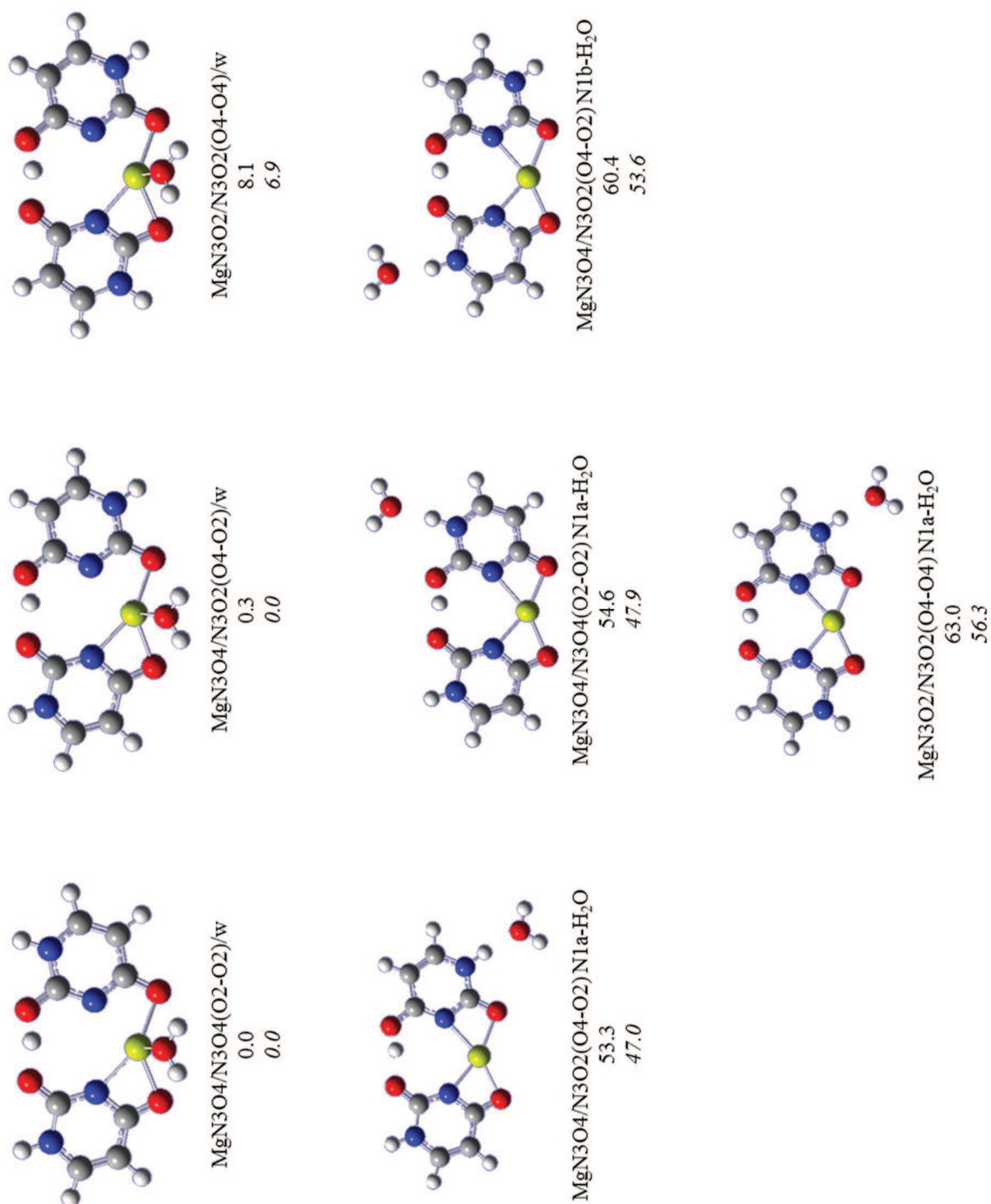
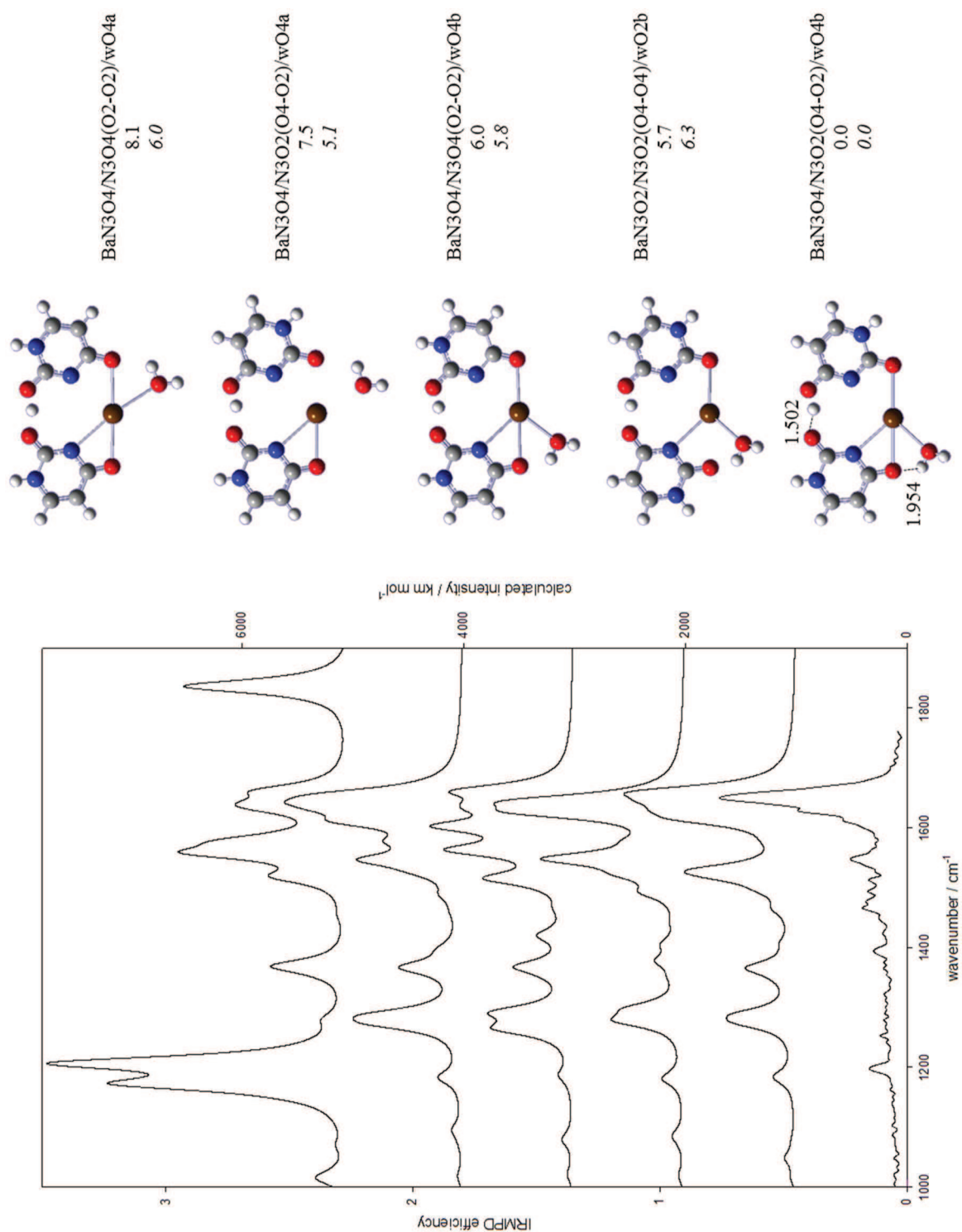


Figure A16. All structures found using calculation method 1 for $[\text{Mg}(\text{Ura-H})(\text{Ura})(\text{H}_2\text{O})]^+$. The calculated relative enthalpies and Gibbs energies (*italics*) are also shown in kJ mol^{-1} at 298 K.



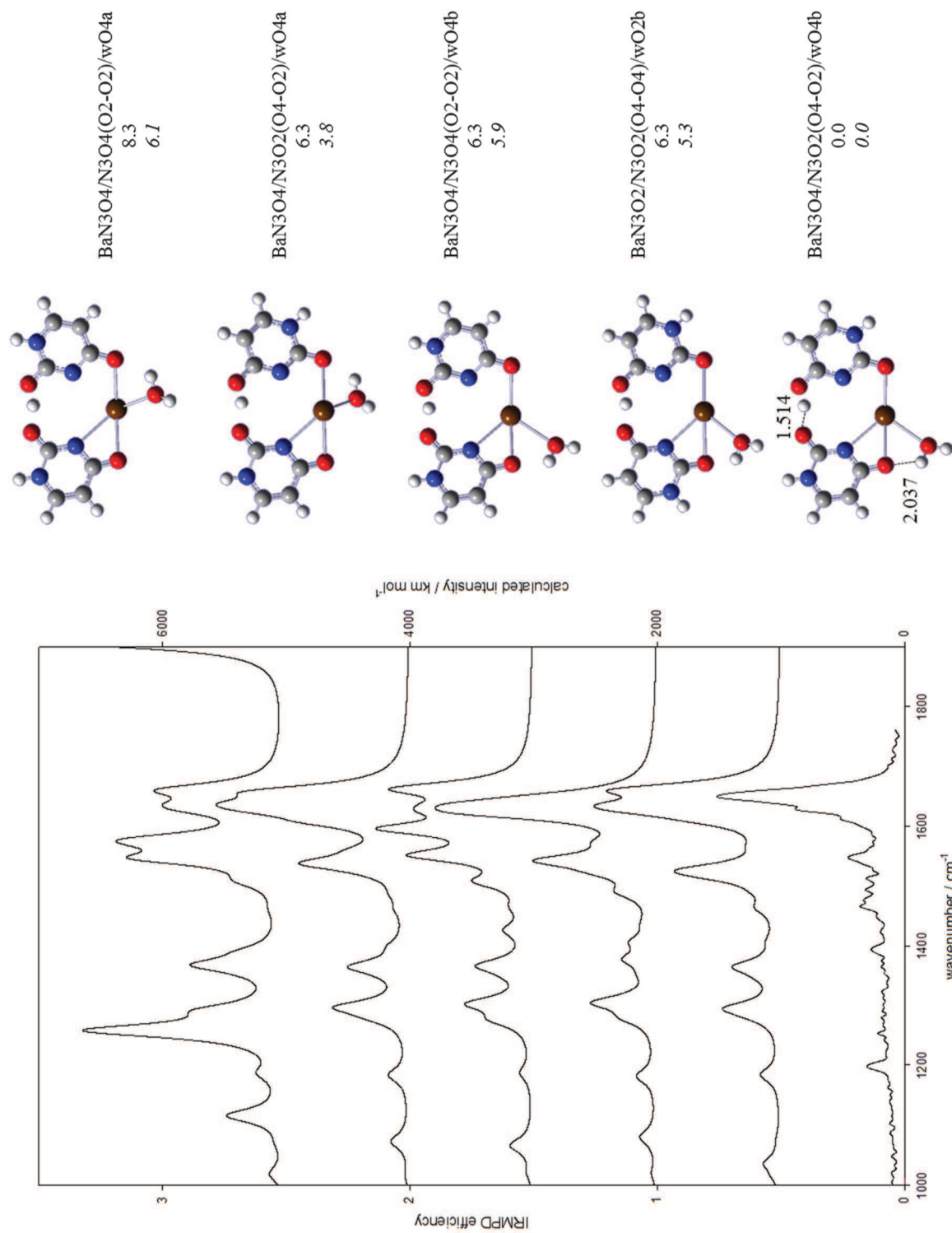


Figure A18. Experimental IRMPD spectrum (bottom) for $[\text{Ba}(\text{Ura-H})(\text{Ura})(\text{H}_2\text{O})]^+$ compared with the B3LYP computed spectra using computational method 2 for the five lowest energy structures. The calculated relative enthalpies and Gibbs energies (italics) are also shown. Hydrogen bond distances are given for the lowest energy structure, in Angströms.

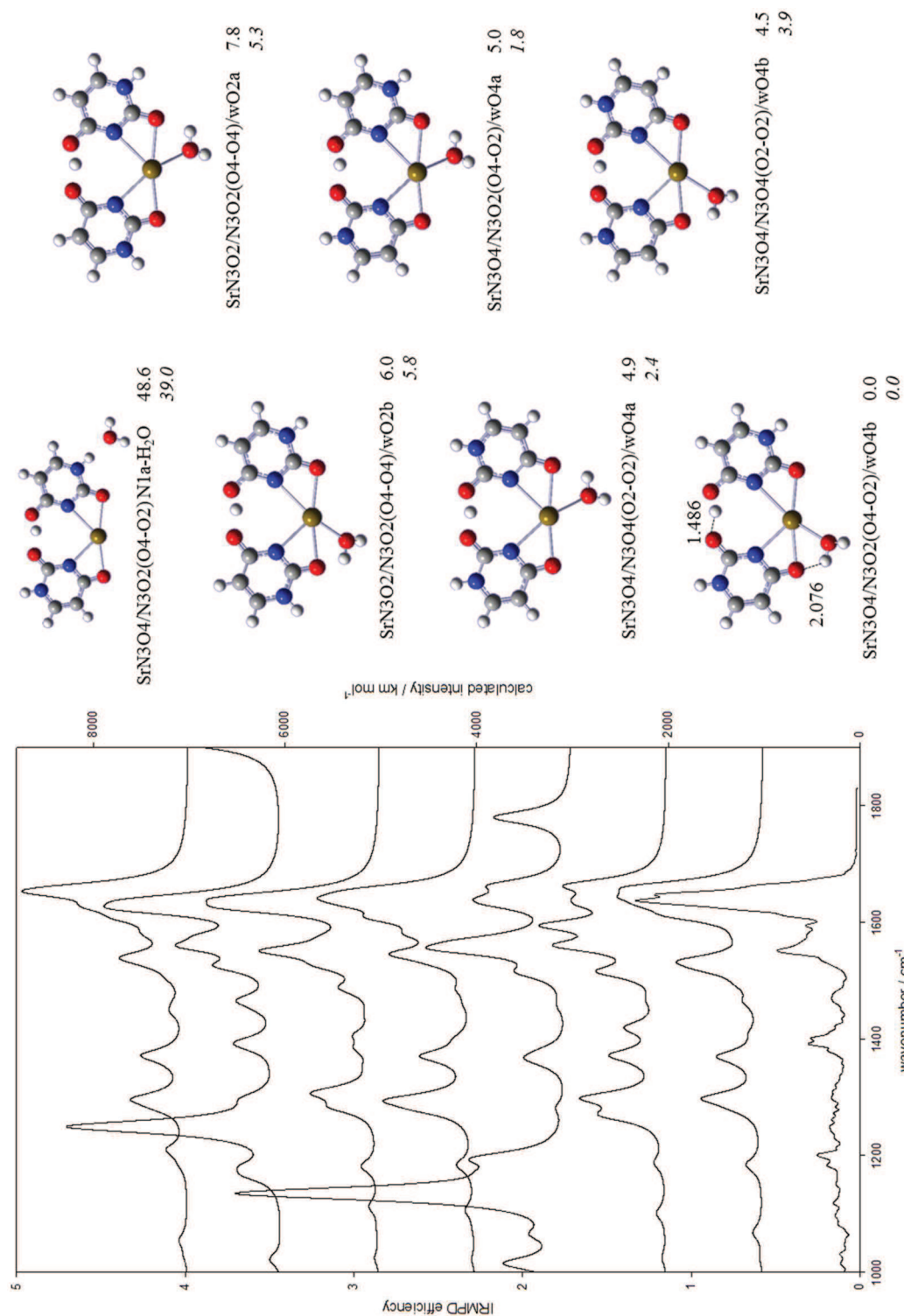


Figure A19. Experimental IRMPD spectrum (bottom) for $[\text{Sr}(\text{Ura-H})(\text{Ura})(\text{H}_2\text{O})]^+$ compared with the B3LYP computed spectra using computational method 1 for the five lowest energy structures. The calculated relative enthalpies and Gibbs energies (italics) are also shown. Hydrogen bond distances are given for the lowest energy structure, in Angströms.

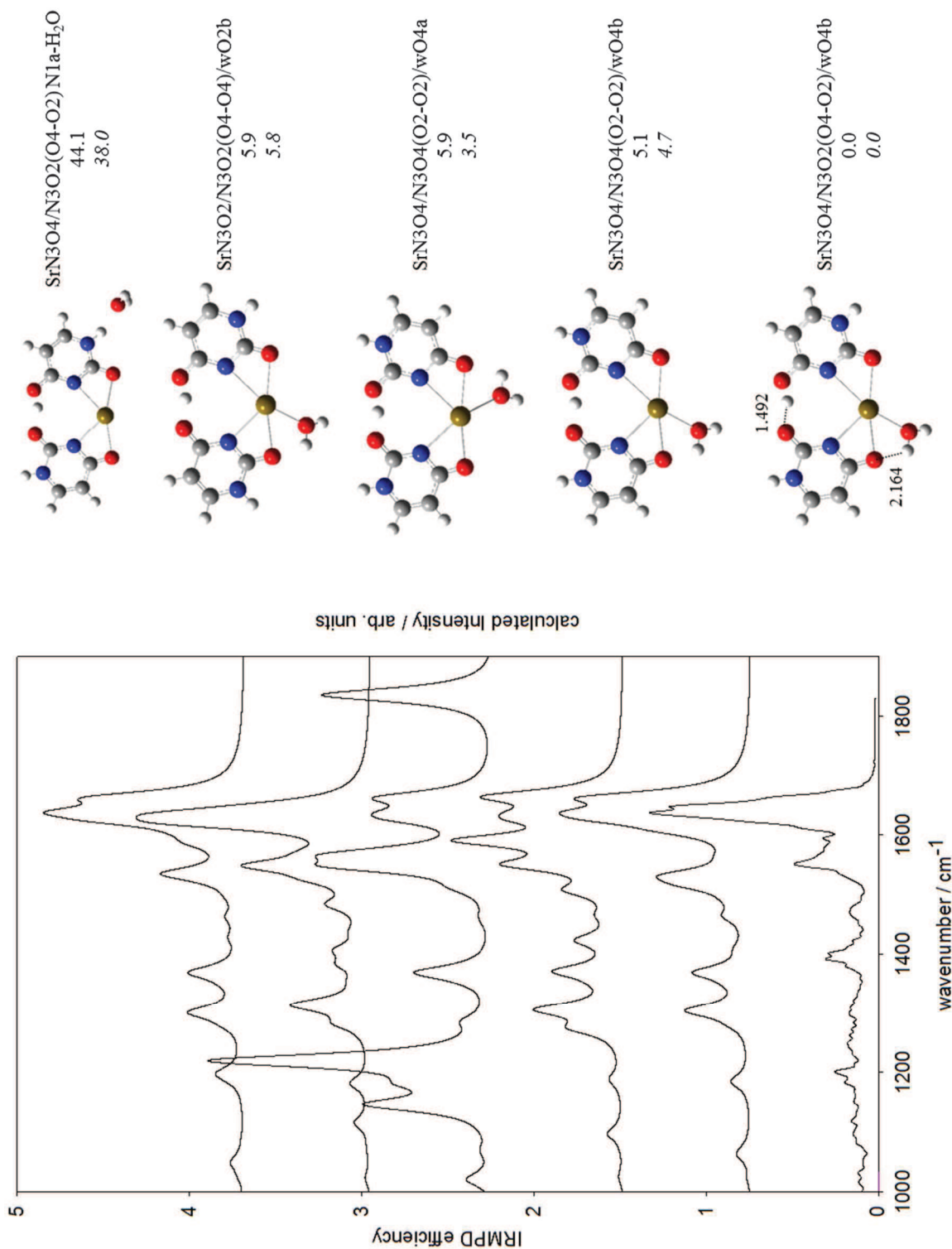


Figure A20. Experimental IRMPD spectrum (bottom) for $[\text{Sr}(\text{Ura-H})(\text{Ura})(\text{H}_2\text{O})]^+$ compared with the B3LYP computed spectra using computational method 2 for the five lowest energy structures. The calculated relative enthalpies and Gibbs energies (italics) are also shown. Hydrogen bond distances are given for the lowest energy structure, in Angströms.

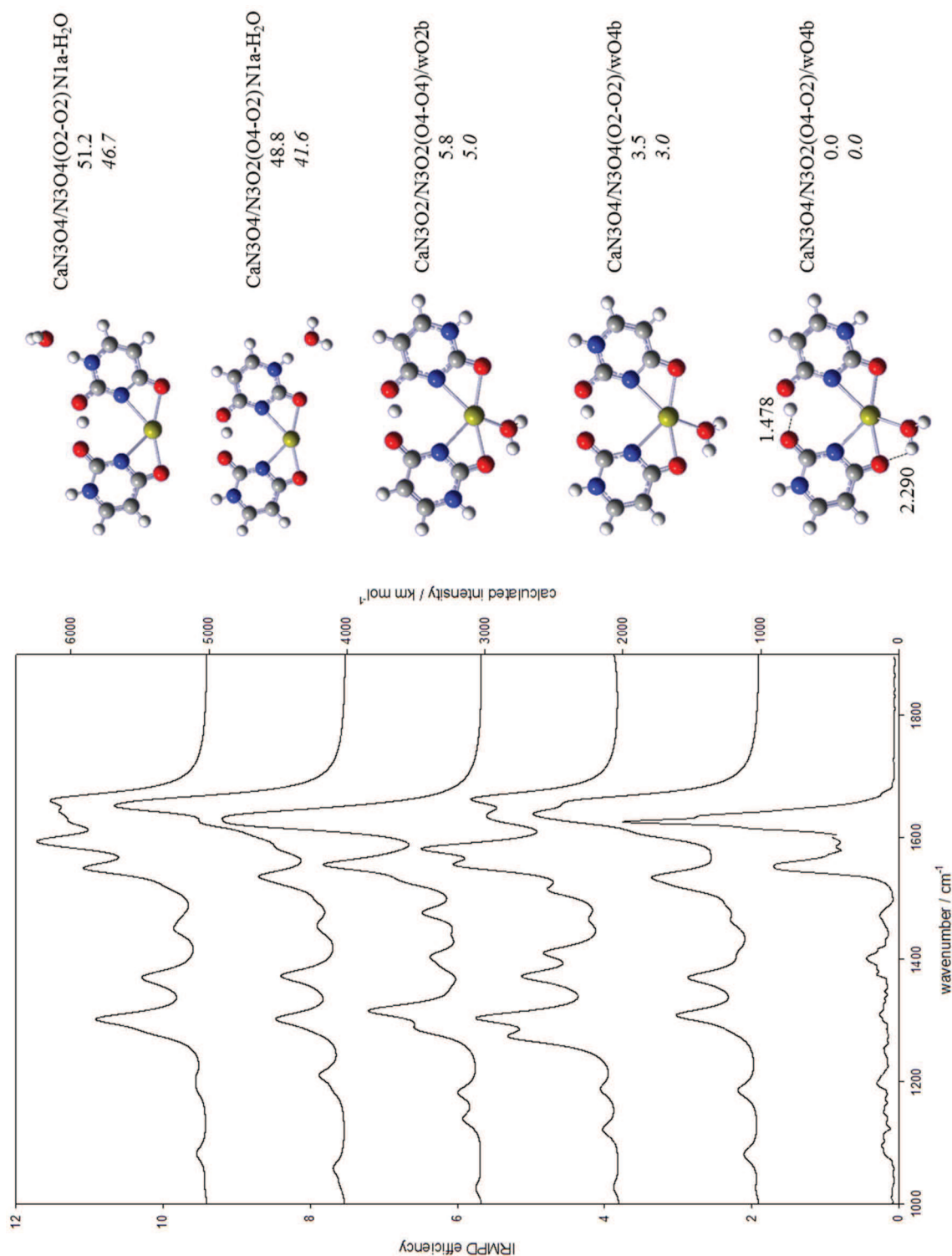


Figure A21. Experimental IRMPD spectrum (bottom) for $[\text{Ca}(\text{Ura-H})(\text{Ura})(\text{H}_2\text{O})]^+$ compared with the B3LYP computed spectra using computational method 1 for the five lowest energy structures. The calculated relative enthalpies and Gibbs energies (italics) are also shown. Hydrogen bond distances are given for the lowest energy structure, in Angströms.

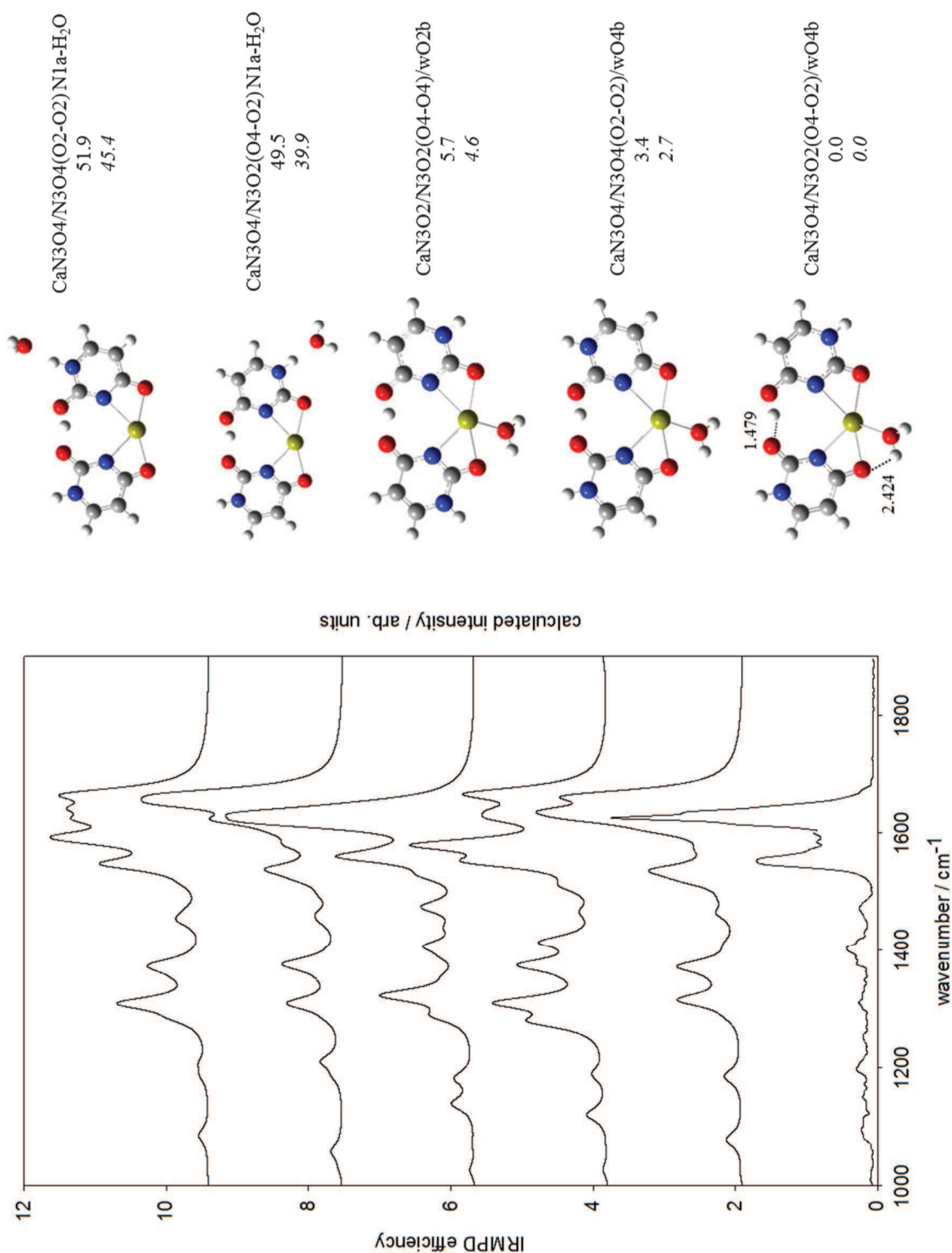


Figure A22. Experimental IRMPD spectrum (bottom) for $[\text{Ca}(\text{Ura-H})(\text{Ura})(\text{H}_2\text{O})]^+$ compared with the B3LYP computed spectra using computational method 2 for the five lowest energy structures. The calculated relative enthalpies and Gibbs energies (*italics*) are also shown. Hydrogen bond distances are given for the lowest energy structure, in Angströms.

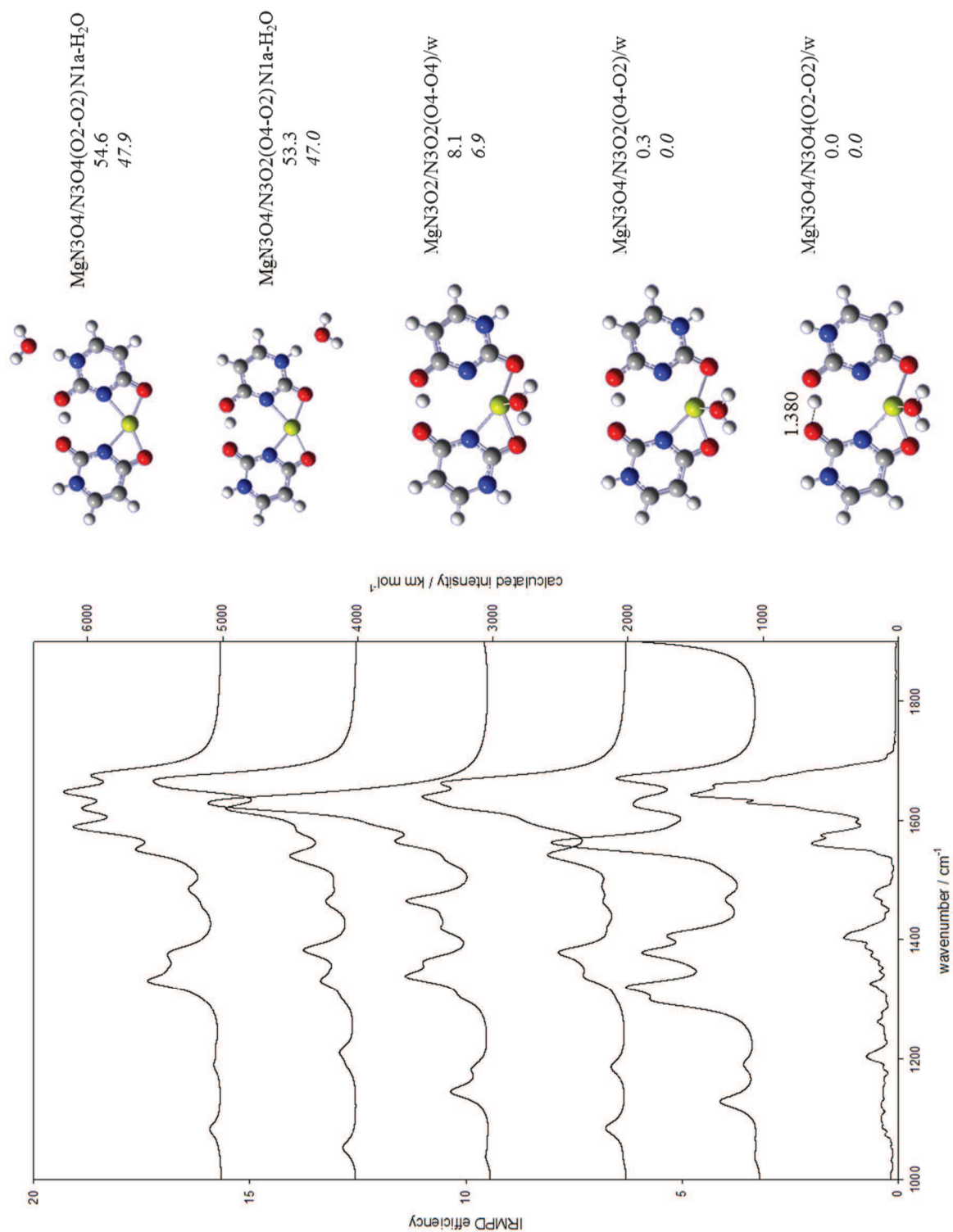


Figure A23. Experimental IRMPD spectrum (bottom) for $[\text{Mg}(\text{Ura-H})(\text{Ura})(\text{H}_2\text{O})]^+$ compared with the B3LYP computed spectra using computational method 1 for the five lowest energy structures. The calculated relative enthalpies and Gibbs energies (italics) are also shown. Hydrogen bond distances are given for the lowest energy structure, in Angströms.

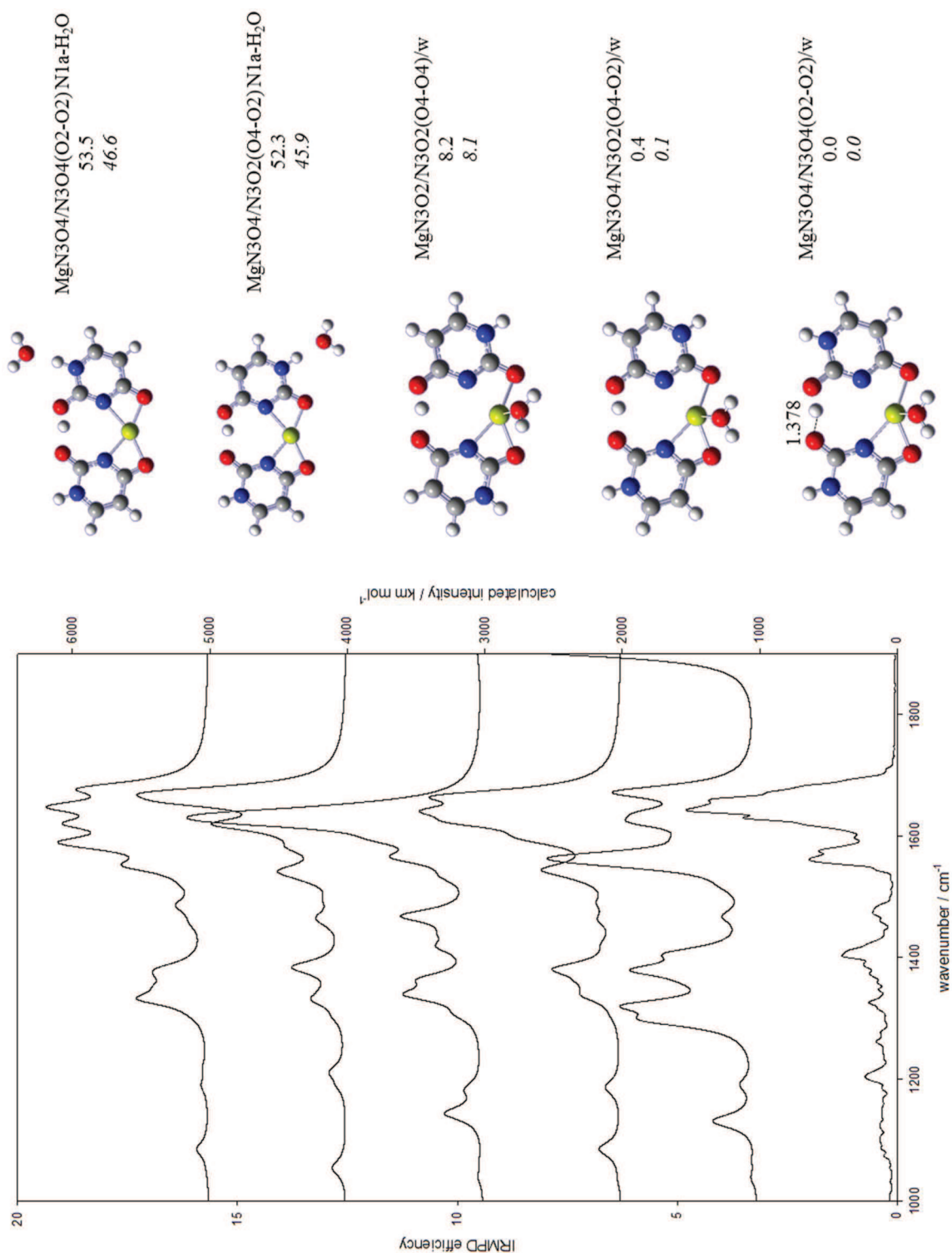


Figure A24. Experimental IRMPD spectrum (bottom) for $[\text{Mg}(\text{Ura-H})(\text{Ura})(\text{H}_2\text{O})]^+$ compared with the B3LYP computed spectra using computational method 2 for the five lowest energy structures. The calculated relative enthalpies and Gibbs energies (italics) are also shown. Hydrogen bond distances are given for the lowest energy structure, in Angströms.

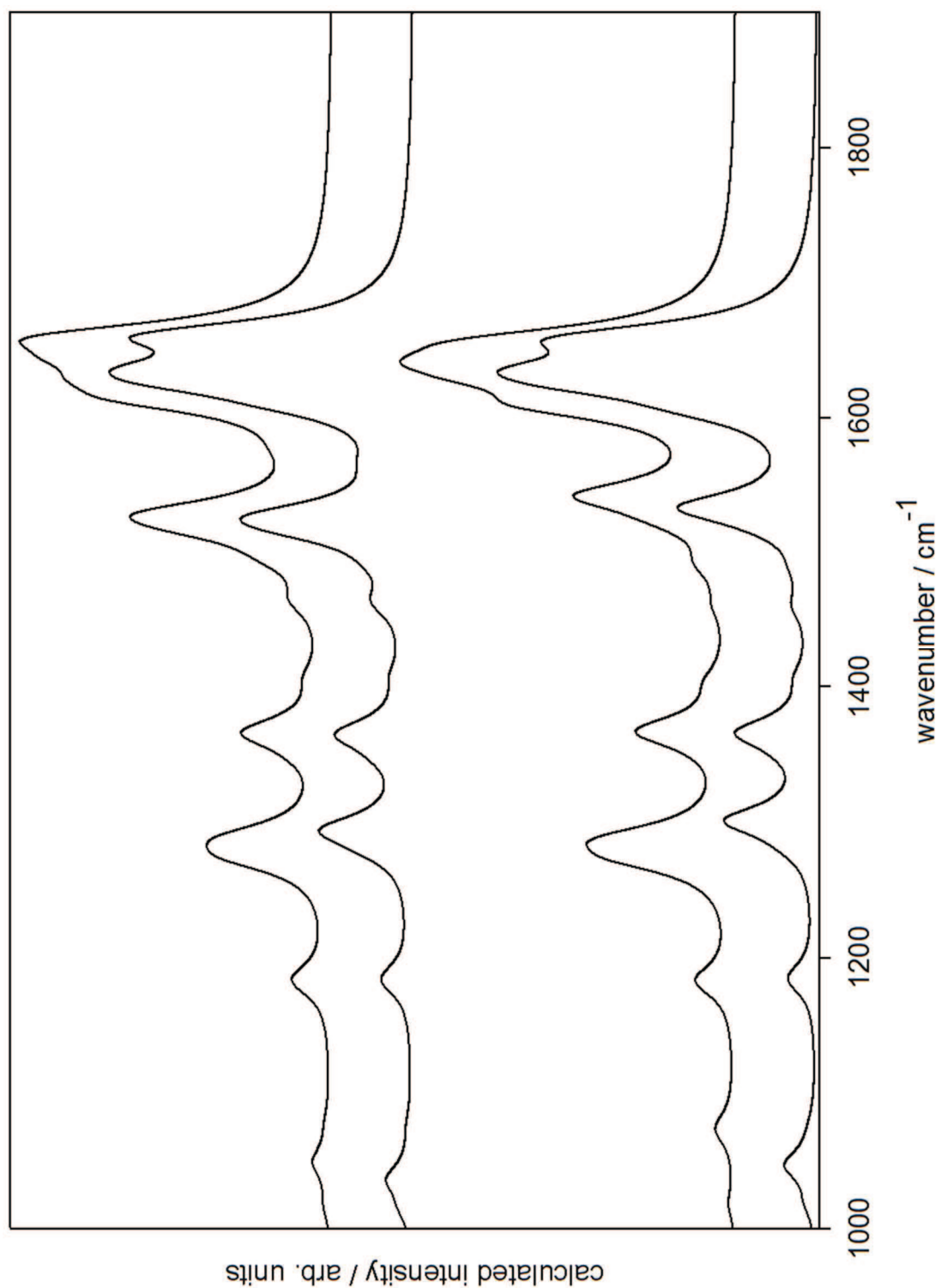


Figure A25. Comparison of calculated spectra for both calculation methods. The bottom pair of spectra corresponds to the calculated lowest energy structure of $[\text{Ba}(\text{Ura-H})(\text{Ura})]^+$ (Method 1 top; Method 2 bottom) and the top set of spectra corresponds to the calculated lowest energy structure of $[\text{Ba}(\text{Ura-H})(\text{Ura})(\text{H}_2\text{O})]^+$ (Method 1 top; Method 2 bottom).

Figure A26. Topological Analysis of uracil tautomers and lowest energy $[M(\text{Ura-H})(\text{Ura})]^+$, $[M(\text{Ura-H})(\text{Ura})(\text{H}_2\text{O})]^+$ structures.

Neutral uracil U1

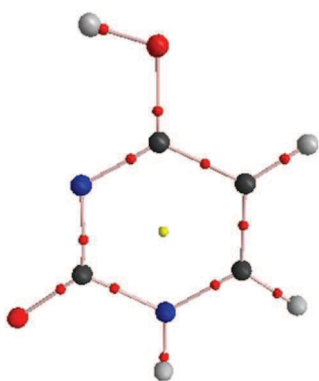
Electron densities ρ ($\text{e } \text{\AA}^{-3}$), Laplacian of the charge density $\nabla^2\rho$ ($\text{e } \text{\AA}^{-5}$) and ellipticity ε at the bond critical points, computed for geometries optimized at the B3LYP/6-31+G(d,p) level.



Bond	ρ	$\nabla^2\rho$	ε
N(1)-C(2)	0.308	-1.025	0.149
C(2)-N(3)	0.315	-1.068	0.165
C(2)-O(2)	0.413	-0.159	0.140
N(3)-C(4)	0.291	-0.906	0.078
C(4)-C(5)	0.284	-0.745	0.152
C(4)-O(4)	0.407	-0.068	0.107
C(5)-C(6)	0.336	-0.976	0.352
C(6)-N(1)	0.307	-0.835	0.049

Neutral uracil U2 (interacting with Mg, Ca, Sr, Ba in M-N3O4/N3O2 (O4-O2))

Electron densities ρ ($\text{e } \text{\AA}^{-3}$), Laplacian of the charge density $\nabla^2\rho$ ($\text{e } \text{\AA}^{-5}$) and ellipticity ε at the bond critical points, computed for geometries optimized at the B3LYP/6-31+G(d,p) level.



Bond	ρ	$\nabla^2\rho$	ε
N(1)-C(2)	0.285	-0.871	0.113
C(2)-N(3)	0.324	-1.104	0.115
C(2)-O(2)	0.412	-0.114	0.152
N(3)-C(4)	0.374	-1.289	0.182
C(4)-C(5)	0.298	-0.806	0.187
C(4)-O(4)	0.306	-0.427	0.003
C(5)-C(6)	0.331	-0.952	0.327
C(6)-N(1)	0.321	-0.853	0.067

Neutral uracil U3 (interacting with Mg in M-N3O4/N3O4 (O2-O2))

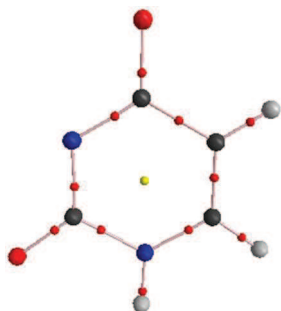
Electron densities ρ ($e \text{ \AA}^{-3}$), Laplacian of the charge density $\nabla^2\rho$ ($e \text{ \AA}^{-5}$) and ellipticity ε at the bond critical points, computed for geometries optimized at the B3LYP/6-31+G(d,p) level.



Bond	ρ	$\nabla^2\rho$	ε
N(1)-C(2)	0.388	-1.432	0.269
C(2)-N(3)	0.325	-1.057	0.201
C(2)-O(2)	0.305	-0.509	0.099
N(3)-C(4)	0.278	-0.815	0.063
C(4)-C(5)	0.292	-0.782	0.173
C(4)-O(4)	0.406	-0.109	0.109
C(5)-C(6)	0.33	-0.931	0.300
C(6)-N(1)	0.321	-1.071	0.041

Deprotonated uracil: dU (interacting with Mg, Ca, Sr, Ba in the complexes)

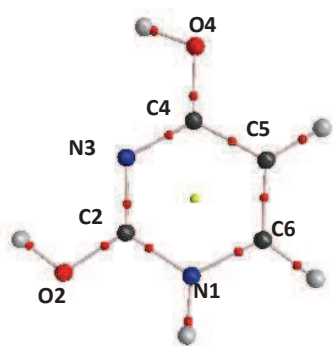
Electron densities ρ ($e \text{ \AA}^{-3}$), Laplacian of the charge density $\nabla^2\rho$ ($e \text{ \AA}^{-5}$) and ellipticity ε at the bond critical points, computed for geometries optimized at the B3LYP/6-31+G(d,p) level.



Bond	ρ	$\nabla^2\rho$	ε
N(1)-C(2)	0.277	-0.823	0.098
C(2)-N(3)	0.349	-1.223	0.172
C(2)-O(2)	0.389	-0.346	0.126
N(3)-C(4)	0.327	-1.116	0.107
C(4)-C(5)	0.272	-0.675	0.134
C(4)-O(4)	0.383	-0.245	0.081
C(5)-C(6)	0.336	-0.980	0.354
C(6)-N(1)	0.315	-0.901	0.096

Protonated uracil (u2_ha from Chapter 2, Ref. 65)

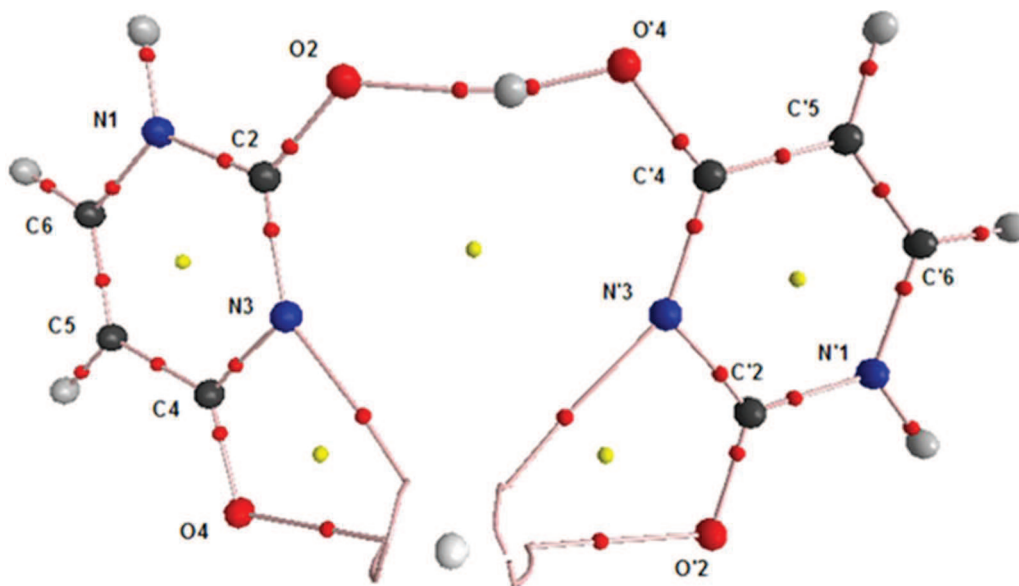
Electron densities ρ ($e \text{ \AA}^{-3}$), Laplacian of the charge density $\nabla^2\rho$ ($e \text{ \AA}^{-5}$) and ellipticity ε at the bond critical points, computed for geometries optimized at the B3LYP/6-31+G(d,p) level.



Bond	ρ	$\nabla^2\rho$	ε
N(1)-C(2)	0.333	-1.092	0.199
C(2)-N(3)	0.371	-1.364	0.197
C(2)-O(2)	0.304	-0.496	0.109
N(3)-C(4)	0.350	-1.245	0.111
C(4)-C(5)	0.303	-0.842	0.181
C(4)-O(4)	0.330	-0.354	0.031
C(5)-C(6)	0.332	-0.962	0.296
C(6)-N(1)	0.309	-0.710	0.020

M-N3O4/N3O2 (O4-O2) complex with Ba

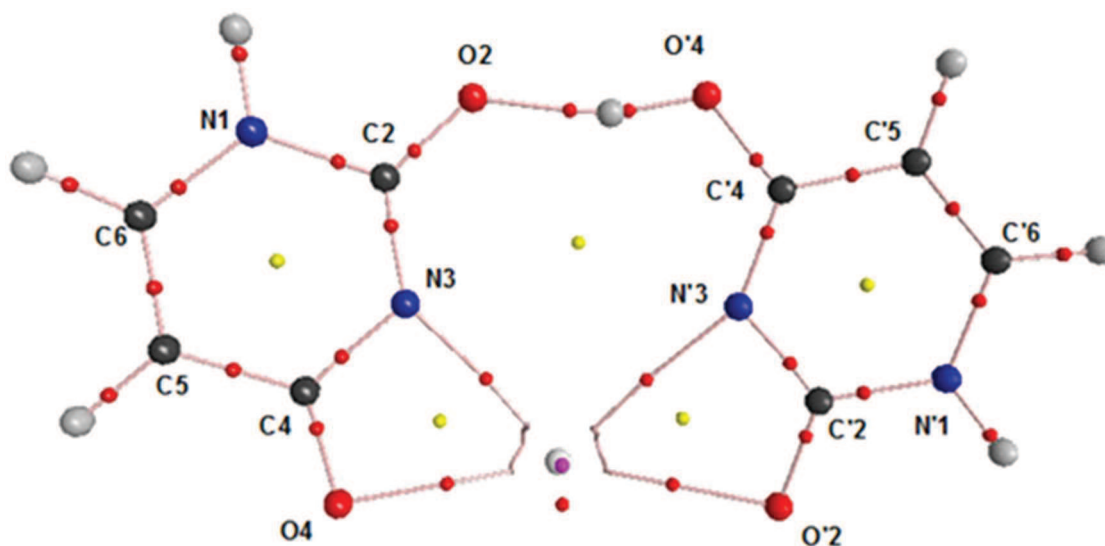
Electron densities ρ ($\text{e } \text{\AA}^{-3}$), Laplacian of the charge density $\nabla^2\rho$ ($\text{e } \text{\AA}^{-5}$) and ellipticity ε at the bond critical points, computed for geometries optimized at the B3LYP/6-31+G(d,p) level.



Bond	ρ	$\nabla^2\rho$	ε
N(1)-C(2)	0.309	-1.001	0.127
C(2)-N(3)	0.343	-1.235	0.154
C(2)-O(2)	0.381	-0.224	0.110
N(3)-C(4)	0.326	-1.128	0.086
C(4)-C(5)	0.294	-0.794	0.163
C(4)-O(4)	0.362	-0.272	0.038
C(5)-C(6)	0.334	-0.979	0.323
C(6)-N(1)	0.311	-0.761	0.029
Ba-N(3)	0.036	0.124	0.108
Ba-O(4)	0.041	0.149	0.100
N'(1)-C'(2)	0.315	-1.001	0.133
C'(2)-N'(3)	0.339	-1.213	0.147
C'(2)-O'(2)	0.378	-0.284	0.105
N'(3)-C'(4)	0.344	-1.185	0.111
C'(4)-C'(5)	0.297	-0.816	0.169
C'(4)-O'(4)	0.341	-0.256	0.030
C'(5)-C'(6)	0.335	-0.987	0.320
C'(6)-N'(1)	0.310	-0.731	0.022
Ba-N'(3)	0.023	0.079	0.042
Ba-O'(2)	0.035	0.131	0.094
O'(4)-H	0.280	-1.444	0.010
O(2)···H	0.072	0.160	0.023

M-N3O4/N3O2 (O4-O2) complex with Sr

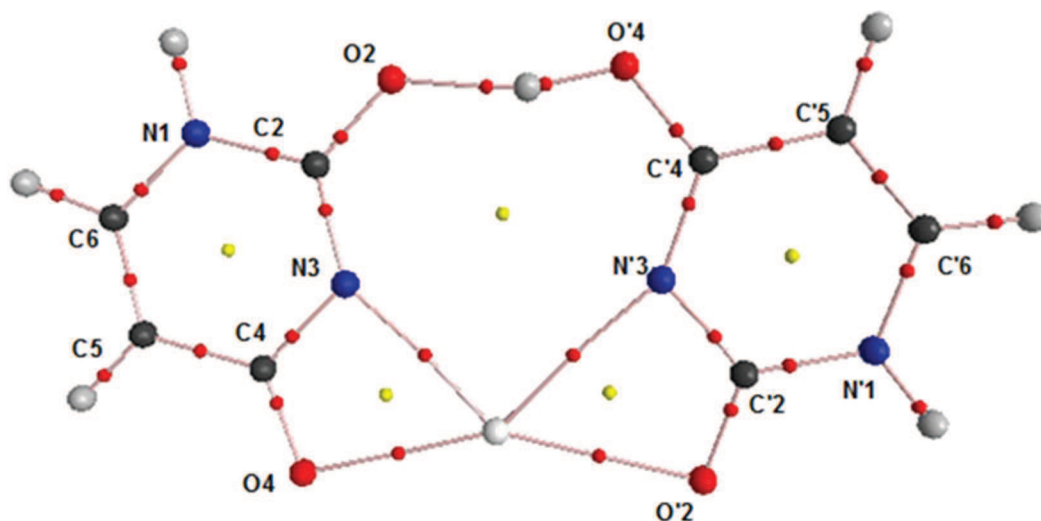
Electron densities ρ ($\text{e } \text{\AA}^{-3}$), Laplacian of the charge density $\nabla^2\rho$ ($\text{e } \text{\AA}^{-5}$) and ellipticity ε at the bond critical points, computed for geometries optimized at the B3LYP/6-31+G(d,p) level.



Bond	ρ	$\nabla^2\rho$	ε
N(1)-C(2)	0.310	-1.009	0.129
C(2)-N(3)	0.342	-1.233	0.152
C(2)-O(2)	0.382	-0.209	0.114
N(3)-C(4)	0.325	-1.122	0.084
C(4)-C(5)	0.294	-0.799	0.165
C(4)-O(4)	0.361	-0.288	0.036
C(5)-C(6)	0.333	-0.978	0.322
C(6)-N(1)	0.311	-0.758	0.026
Sr-N(3)	0.039	0.154	0.091
Sr-O(4)	0.043	0.179	0.073
N'(1)-C'(2)	0.318	-1.008	0.135
C'(2)-N'(3)	0.338	-1.209	0.147
C'(2)-O'(2)	0.377	-0.305	0.102
N'(3)-C'(4)	0.342	-1.180	0.107
C'(4)-C'(5)	0.297	-0.817	0.168
C'(4)-O'(4)	0.343	-0.241	0.032
C'(5)-C'(6)	0.335	-0.988	0.319
C'(6)-N'(1)	0.309	-0.730	0.019
Sr-N'(3)	0.027	0.103	0.037
Sr-O'(2)	0.037	0.155	0.058
O'(4)-H	0.275	-1.392	0.009
O(2)···H	0.076	0.156	0.014

M-N3O4/N3O2 (O4-O2) complex with Ca

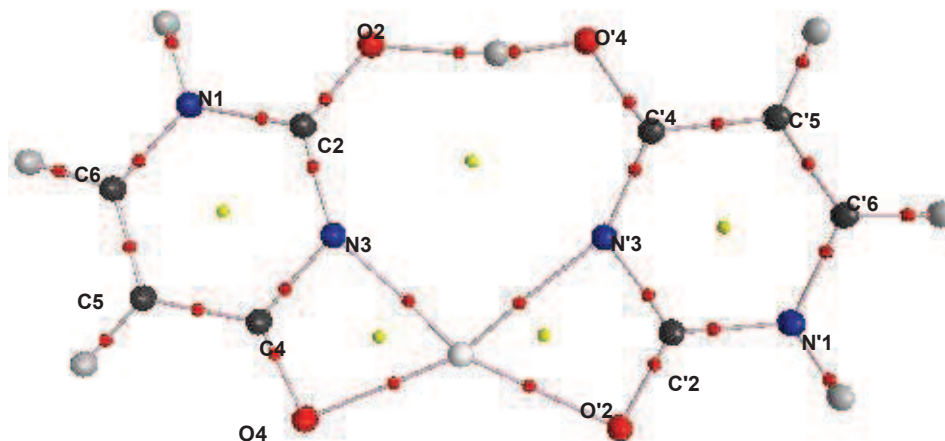
Electron densities ρ ($\text{e } \text{\AA}^{-3}$), Laplacian of the charge density $\nabla^2\rho$ ($\text{e } \text{\AA}^{-5}$) and ellipticity ε at the bond critical points, computed for geometries optimized at the B3LYP/6-31+G(d,p) level.



Bond	ρ	$\nabla^2\rho$	ε
N(1)-C(2)	0.311	-1.012	0.131
C(2)-N(3)	0.341	-1.228	0.149
C(2)-O(2)	0.383	-0.199	0.117
N(3)-C(4)	0.326	-1.124	0.082
C(4)-C(5)	0.296	-0.807	0.167
C(4)-O(4)	0.359	-0.305	0.031
C(5)-C(6)	0.333	-0.974	0.318
C(6)-N(1)	0.311	-0.756	0.024
Ca-N(3)	0.043	0.198	0.075
Ca-O(4)	0.048	0.233	0.053
N'(1)-C'(2)	0.320	-1.008	0.137
C'(2)-N'(3)	0.339	-1.216	0.146
C'(2)-O'(2)	0.375	-0.329	0.100
N'(3)-C'(4)	0.341	-1.169	0.102
C'(4)-C'(5)	0.297	-0.817	0.167
C'(4)-O'(4)	0.344	-0.235	0.034
C'(5)-C'(6)	0.335	-0.986	0.319
C'(6)-N'(1)	0.308	-0.724	0.016
Ca-N'(3)	0.031	0.137	0.019
Ca-O'(2)	0.042	0.202	0.030
O'(4)-H	0.272	-1.362	0.009
O(2)...H	0.077	0.151	0.013

M-N3O4/N3O2 (O4-O2) complex with Mg

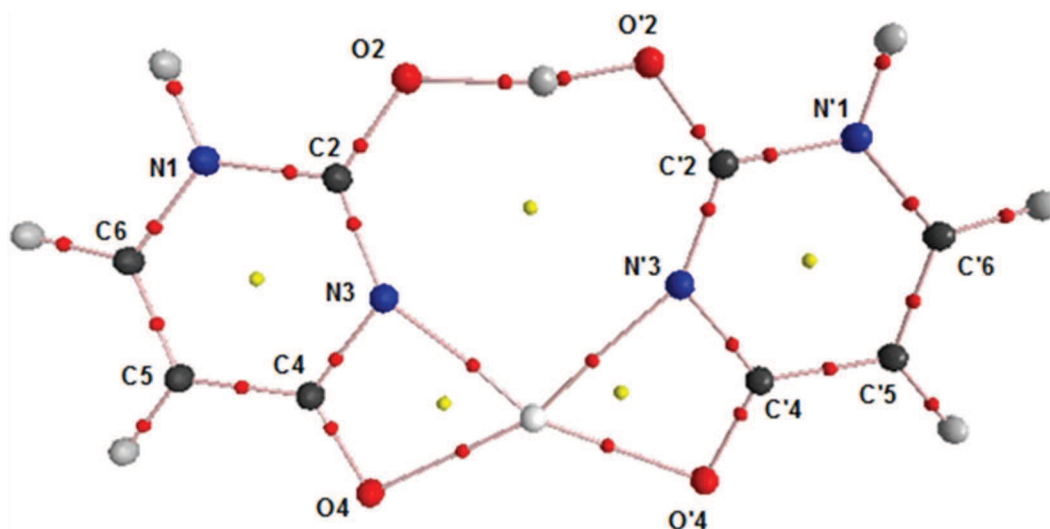
Electron densities ρ ($\text{e } \text{\AA}^{-3}$), Laplacian of the charge density $\nabla^2\rho$ ($\text{e } \text{\AA}^{-5}$) and ellipticity ε at the bond critical points, computed for geometries optimized at the B3LYP/6-31+G(d,p) level.



Bond	ρ	$\nabla^2\rho$	ε
N(1)-C(2)	0.311	-1.020	0.134
C(2)-N(3)	0.341	-1.222	0.148
C(2)-O(2)	0.384	-0.197	0.120
N(3)-C(4)	0.329	-1.130	0.076
C(4)-C(5)	0.298	-0.817	0.169
C(4)-O(4)	0.357	-0.346	0.028
C(5)-C(6)	0.331	-0.963	0.316
C(6)-N(1)	0.311	-0.757	0.021
Mg-N(3)	0.045	0.295	0.004
Mg-O(4)	0.048	0.326	0.013
N'(1)-C'(2)	0.326	-1.018	0.140
C'(2)-N'(3)	0.343	-1.237	0.144
C'(2)-O'(2)	0.372	-0.384	0.096
N'(3)-C'(4)	0.341	-1.153	0.097
C'(4)-C'(5)	0.297	-0.817	0.165
C'(4)-O'(4)	0.346	-0.239	0.039
C'(5)-C'(6)	0.334	-0.979	0.319
C'(6)-N'(1)	0.305	-0.722	0.013
Mg-N'(3)	0.034	0.202	0.106
Mg-O'(2)	0.044	0.300	0.012
O'(4)-H	0.271	-1.357	0.009
O(2)...H	0.075	0.147	0.016

M-N3O4/N3O4 (O2-O2) complex with Mg

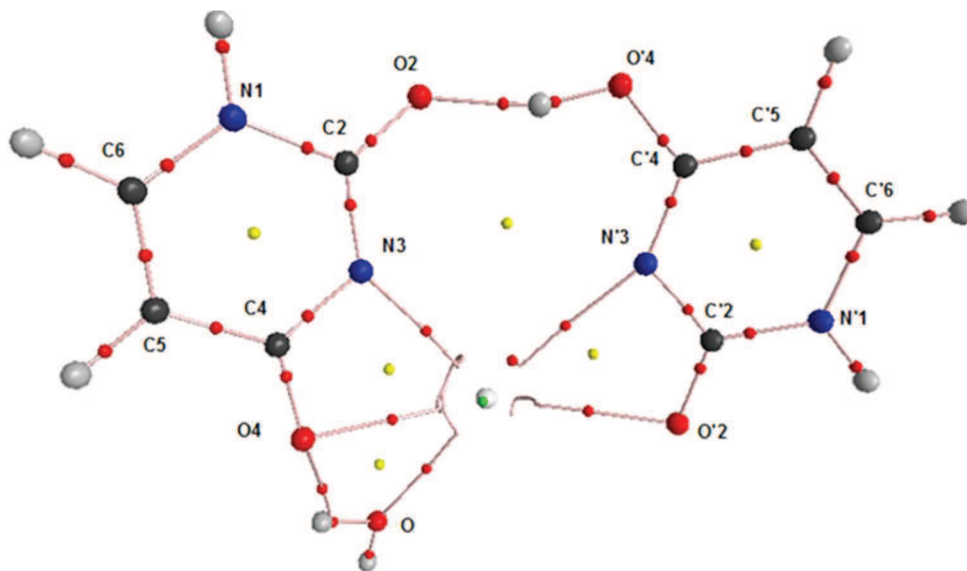
Electron densities ρ ($\text{e } \text{\AA}^{-3}$), Laplacian of the charge density $\nabla^2\rho$ ($\text{e } \text{\AA}^{-5}$) and ellipticity ε at the bond critical points, computed for geometries optimized at the B3LYP/6-31+G(d,p) level.



Bond	ρ	$\nabla^2\rho$	ε
N(1)-C(2)	0.314	-1.028	0.138
C(2)-N(3)	0.345	-1.238	0.155
C(2)-O(2)	0.379	-0.237	0.116
N(3)-C(4)	0.328	-1.126	0.074
C(4)-C(5)	0.297	-0.817	0.167
C(4)-O(4)	0.359	-0.334	0.031
C(5)-C(6)	0.331	-0.966	0.316
C(6)-N(1)	0.310	-0.749	0.019
Mg-N(3)	0.042	0.275	0.012
Mg-O(4)	0.047	0.322	0.014
N'(1)-C'(2)	0.325	-1.060	0.162
C'(2)-N'(3)	0.359	-1.279	0.182
C'(2)-O'(2)	0.355	-0.355	0.106
N'(3)-C'(4)	0.323	-1.105	0.065
C'(4)-C'(5)	0.297	-0.816	0.161
C'(4)-O'(4)	0.364	-0.289	0.042
C'(5)-C'(6)	0.333	-0.973	0.314
C'(6)-N'(1)	0.307	-0.713	0.013
Mg-N'(3)	0.035	0.215	0.095
Mg-O'(4)	0.046	0.318	0.019
O'(2)-H	0.239	-1.026	0.011
O(2)···H	0.099	+0.081	0.014

M-N3O4/N3O2(O4-O2)/wO4b complex with Ba

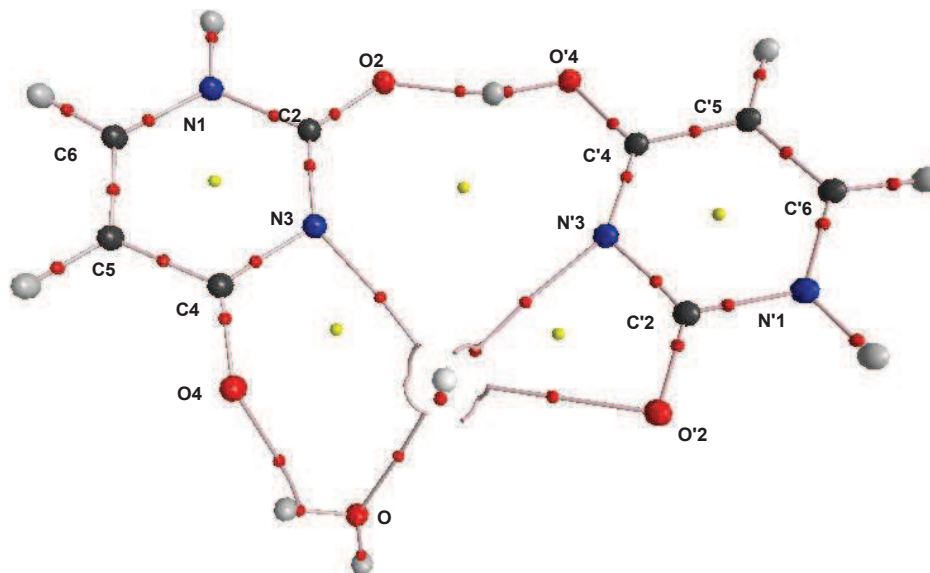
Electron densities ρ ($\text{e } \text{\AA}^{-3}$), Laplacian of the charge density $\nabla^2\rho$ ($\text{e } \text{\AA}^{-5}$) and ellipticity ε at the bond critical points, computed for geometries optimized at the B3LYP/6-31+G(d,p) level.



Bond	ρ	$\nabla^2\rho$	ε
N(1)-C(2)	0.308	-0.990	0.123
C(2)-N(3)	0.342	-1.235	0.153
C(2)-O(2)	0.382	-0.208	0.111
N(3)-C(4)	0.328	-1.141	0.090
C(4)-C(5)	0.293	-0.792	0.164
C(4)-O(4)	0.360	-0.250	0.034
C(5)-C(6)	0.333	-0.979	0.323
C(6)-N(1)	0.312	-0.761	0.031
Ba-N(3)	0.034	0.115	0.102
Ba-O(4)	0.034	0.121	0.090
N'(1)-C'(2)	0.313	-0.989	0.129
C'(2)-N'(3)	0.338	-1.212	0.145
C'(2)-O'(2)	0.379	-0.279	0.107
N'(3)-C'(4)	0.347	-1.191	0.113
C'(4)-C'(5)	0.297	-0.816	0.168
C'(4)-O'(4)	0.339	-0.262	0.027
C'(5)-C'(6)	0.335	-0.987	0.321
C'(6)-N'(1)	0.311	-0.731	0.025
Ba-N'(3)	0.020	0.071	0.020
Ba-O'(2)	0.033	0.124	0.078
O'(4)-H	0.280	-1.519	0.010
O(2)⋯H	0.067	0.164	0.021
O-Ba	0.026	0.106	0.149
O(4)⋯H	0.020	0.076	0.205

M-N3O4/N3O2(O4-O2)/wO4b complex with Sr

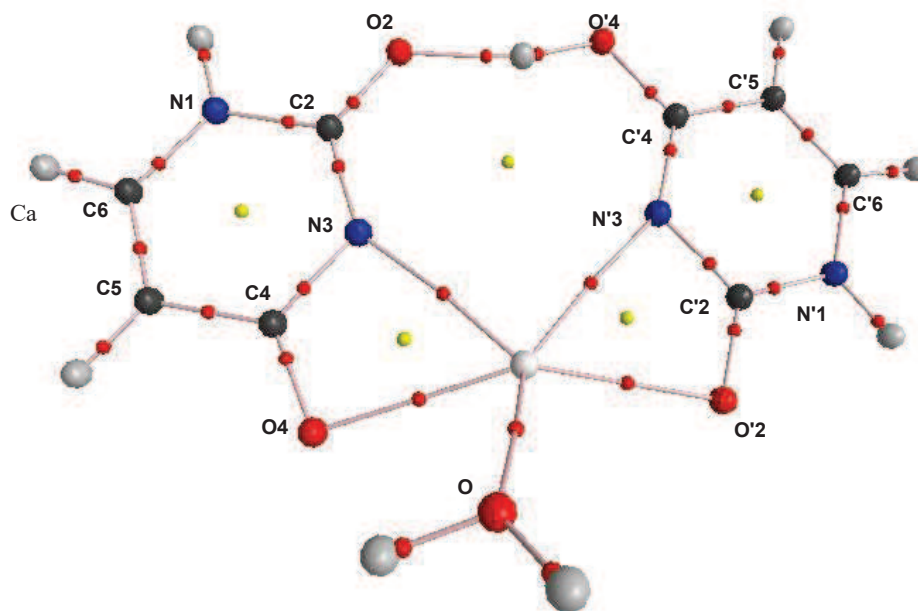
Electron densities ρ ($\text{e } \text{\AA}^{-3}$), Laplacian of the charge density $\nabla^2\rho$ ($\text{e } \text{\AA}^{-5}$) and ellipticity ε at the bond critical points, computed for geometries optimized at the B3LYP/6-31+G(d,p) level.



Bond	ρ	$\nabla^2\rho$	ε
N(1)-C(2)	0.309	-1.001	0.127
C(2)-N(3)	0.342	-1.235	0.153
C(2)-O(2)	0.382	-0.202	0.115
N(3)-C(4)	0.327	-1.134	0.088
C(4)-C(5)	0.294	-0.795	0.165
C(4)-O(4)	0.360	-0.283	0.034
C(5)-C(6)	0.333	-0.978	0.323
C(6)-N(1)	0.312	-0.760	0.029
Sr-N(3)	0.036	0.141	0.086
Sr-O(4)			
N'(1)-C'(2)	0.316	-1.002	0.132
C'(2)-N'(3)	0.338	-1.210	0.145
C'(2)-O'(2)	0.379	-0.290	0.104
N'(3)-C'(4)	0.344	-1.186	0.110
C'(4)-C'(5)	0.297	-0.816	0.168
C'(4)-O'(4)	0.341	-0.250	0.030
C'(5)-C'(6)	0.335	-0.987	0.320
C'(6)-N'(1)	0.310	-0.734	0.022
Sr-N'(3)	0.024	0.094	0.025
Sr-O'(2)	0.035	0.148	0.057
O'(4)-H	0.279	-1.447	0.009
O(2)⋯H	0.072	0.161	0.013
O-Sr	0.030	0.139	0.133
O(4)⋯H	0.016	0.064	0.419

M-N3O4/N3O2(O4-O2)/wO4b complex with Ca

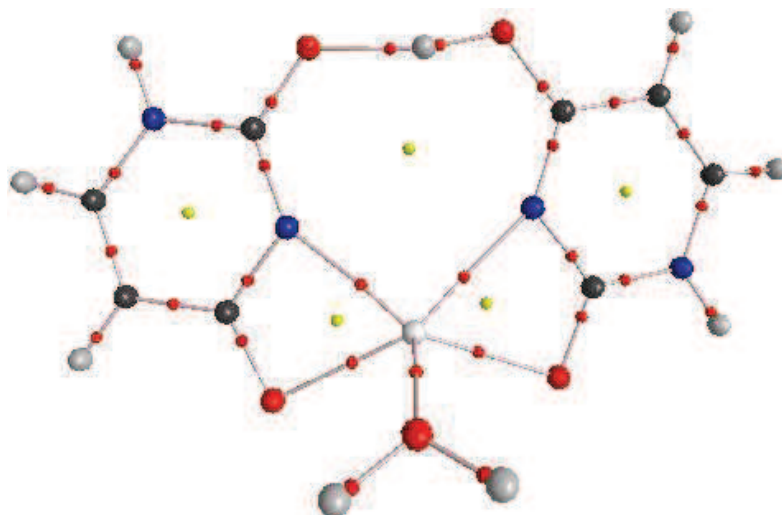
Electron densities ρ ($\text{e } \text{\AA}^{-3}$), Laplacian of the charge density $\nabla^2\rho$ ($\text{e } \text{\AA}^{-5}$) and ellipticity ε at the bond critical points, computed for geometries optimized at the B3LYP/6-31+G(d,p) level.



Bond	ρ	$\nabla^2\rho$	ε
N(1)-C(2)	0.309	-1.004	0.128
C(2)-N(3)	0.342	-1.235	0.152
C(2)-O(2)	0.382	-0.203	0.116
N(3)-C(4)	0.328	-1.134	0.086
C(4)-C(5)	0.295	-0.799	0.166
C(4)-O(4)	0.360	-0.295	0.032
C(5)-C(6)	0.333	-0.976	0.321
C(6)-N(1)	0.311	-0.759	0.028
Ca-N(3)	0.040	0.182	0.071
Ca-O(4)	0.042	0.199	0.045
N'(1)-C'(2)	0.318	-1.002	0.133
C'(2)-N'(3)	0.339	-1.217	0.145
C'(2)-O'(2)	0.377	-0.311	0.103
N'(3)-C'(4)	0.343	-1.177	0.107
C'(4)-C'(5)	0.297	-0.816	0.167
C'(4)-O'(4)	0.343	-0.246	0.032
C'(5)-C'(6)	0.335	-0.986	0.321
C'(6)-N'(1)	0.309	-0.729	0.021
Ca-N'(3)	0.028	0.124	0.017
Ca-O'(2)	0.039	0.190	0.041
O'(4)-H	0.275	-1.390	0.009
O(2)···H	0.076	0.155	0.015
O-Ca	0.034	0.181	0.130

M-N3O4/N3O2(O4-O2)/w complex with Mg

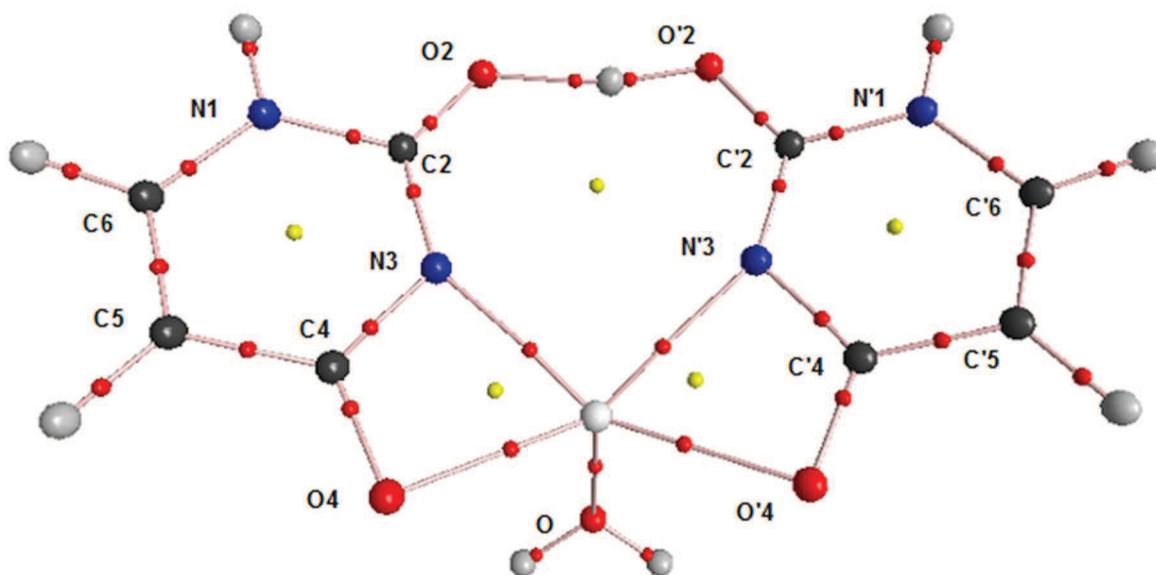
Electron densities ρ ($\text{e } \text{\AA}^{-3}$), Laplacian of the charge density $\nabla^2\rho$ ($\text{e } \text{\AA}^{-5}$) and ellipticity ε at the bond critical points, computed for geometries optimized at the B3LYP/6-31+G(d,p) level.



Bond	ρ	$\nabla^2\rho$	ε
N(1)-C(2)	0.310	-1.012	0.132
C(2)-N(3)	0.343	-1.234	0.154
C(2)-O(2)	0.383	-0.211	0.118
N(3)-C(4)	0.329	-1.134	0.080
C(4)-C(5)	0.296	-0.807	0.166
C(4)-O(4)	0.360	-0.323	0.034
C(5)-C(6)	0.332	-0.967	0.320
C(6)-N(1)	0.311	-0.761	0.026
Mg-N(3)	0.041	0.262	0.016
Mg-O(4)	0.042	0.276	0.011
N'(1)-C'(2)	0.322	-1.011	0.136
C'(2)-N'(3)	0.343	-1.237	0.145
C'(2)-O'(2)	0.375	-0.346	0.102
N'(3)-C'(4)	0.343	-1.165	0.104
C'(4)-C'(5)	0.296	-0.814	0.165
C'(4)-O'(4)	0.345	-0.248	0.037
C'(5)-C'(6)	0.334	-0.981	0.321
C'(6)-N'(1)	0.306	-0.728	0.018
Ca-N'(3)	0.029	0.170	0.154
Ca-O'(2)	0.039	0.258	0.002
O'(4)-H	0.270	-1.346	0.010
O(2)⋯H	0.077	0.147	0.020
O-Mg	0.035	0.263	0.073

M-N3O4/N3O4(O2-O2)/w complex with Mg

Electron densities ρ ($\text{e } \text{\AA}^{-3}$), Laplacian of the charge density $\nabla^2\rho$ ($\text{e } \text{\AA}^{-5}$) and ellipticity ε at the bond critical points, computed for geometries optimized at the B3LYP/6-31+G(d,p) level.



Bond	ρ	$\nabla^2\rho$	ε
N(1)-C(2)	0.313	-1.023	0.137
C(2)-N(3)	0.347	-1.249	0.161
C(2)-O(2)	0.377	-0.248	0.113
N(3)-C(4)	0.328	-1.128	0.076
C(4)-C(5)	0.296	-0.806	0.164
C(4)-O(4)	0.362	-0.305	0.038
C(5)-C(6)	0.332	-0.970	0.320
C(6)-N(1)	0.310	-0.753	0.024
Mg-N(3)	0.038	0.243	0.035
Mg-O(4)	0.042	0.274	0.008
N'(1)-C'(2)	0.323	-1.053	0.161
C'(2)-N'(3)	0.360	-1.287	0.188
C'(2)-O'(2)	0.355	-0.366	0.105
N'(3)-C'(4)	0.323	-1.108	0.067
C'(4)-C'(5)	0.295	-0.805	0.158
C'(4)-O'(4)	0.368	-0.257	0.049
C'(5)-C'(6)	0.333	-0.977	0.319
C'(6)-N'(1)	0.307	-0.718	0.018
Mg-N'(3)	0.031	0.185	0.135
Mg-O'(4)	0.041	0.273	0.004
O'(2)-H	0.238	-1.011	0.012
O(2)...H	0.102	0.073	0.017
O-Mg	0.035	0.261	0.070

Table A1. Comparison of relative enthalpies and Gibbs energies in kJ mol^{-1} at 298K for $[\text{M}(\text{Ura-H})(\text{Ura})]^+$ for both computational methods. Energetics when the def2-TZVPP basis set is applied to all atoms are given in *italics*.

M	Isomer	Method 1		Method 2	
		ΔH	ΔG	ΔH	ΔG
Ba^{2+}	N3O4/N3O2(O4-O2)	0.0	0.0	0.0	0.0
	N3O2/N3O2(O4-O4)	3.3	1.7	4.1	4.1
	N3O4/N3O4(O2-O2)	4.2	4.0	4.7	4.8
	N3O4/O2(N1-O2)	28.5	28.5	21.6	14.8
	N3O2/O2(N1-O4)	33.9	34.1	27.9	21.2
Sr^{2+}	N3O4/N3O2(O4-O2)	0.0	0.0	0.0	0.0
	N3O4/N3O4(O2-O2)	2.8	2.7	3.8	3.9
	N3O2/N3O2(O4-O4)	4.2	4.5	4.1	4.1
	N3O4/O2(N1-O2)	40.5	36.1	31.5	26.7
	N3O2/O2(N1-O4)	47.5	43.1	38.4	33.1
Ca^{2+}	N3O4/N3O2(O4-O2)	0.0	0.0	0.0	0.0
				<i>0.0</i>	<i>0.0</i>
	N3O4/N3O4(O2-O2)	2.5	2.5	2.6	2.3
				<i>3.0</i>	<i>3.0</i>
	N3O2/N3O2(O4-O4)	4.7	4.8	4.7	5.3
				<i>5.0</i>	<i>5.7</i>
Mg^{2+}	N3O4/O2(N1-O2)	42.2	37.3	41.0	36.7
	N3O2/O2(N1-O4)	50.3	45.5	49.0	45.1
	N3O4/N3O4(O2-O2)	0.0	0.0	0.0	0.0
	N3O4/N3O2(O4-O2)	0.6	0.3	0.8	0.6
	N3O2/N3O2(O4-O4)	9.0	8.7	9.3	9.1
	N3O4/O2(N1-O2)	54.2	48.8	54.4	49.6
	N3O4/O4	61.9	44.0	62.2	40.5

Table A2. Comparison of relative enthalpies and Gibbs energies in kJ mol^{-1} at 298K for $[\text{M}(\text{Ura-H})(\text{Ura})(\text{H}_2\text{O})]^+$ for both computational methods.

M	Isomer	Method 1		Method 2	
		ΔH	ΔG	ΔH	ΔG
Ba^{2+}	N3O4/N3O2(O4-O2)/wO4b	0.0	0.0	0.0	0.0
	N3O2/N3O2(O4-O4)/wO2b	5.7	6.3	6.3	5.3
	N3O4/N3O4(O2-O2)/wO4b	6.0	5.8	6.3	5.9
	N3O4/N3O2(O4-O2)/wO4a	7.5	5.1	6.3	3.8
	N3O4/N3O4(O2-O2)/wO4a	8.1	6.0	8.3	6.1
Sr^{2+}	N3O4/N3O2(O4-O2)/wO4b	0.0	0.0	0.0	0.0
	N3O4/N3O4(O2-O2)/wO4b	4.5	3.9	5.1	4.7
	N3O4/N3O4(O2-O2)/wO4a	4.9	2.4	5.9	3.5
	N3O4/N3O2(O4-O2)/wO4a	5.0	1.8	Optimizes to N3O4/N3O2(O4-O2)/wO4b	
	N3O2/N3O2(O4-O4)/wO2b	6.0	5.8	5.9	5.8
	N3O2/N3O2(O4-O4)/wO2a	7.8	5.3	Optimizes to N3O2/N3O2(O4-O4)/wO2b	
	N3O4/N3O2(O4-O2) N1a-H ₂ O	48.6	39.0	44.1	38.0
	N3O4/N3O2(O4-O2)/wO4b	0.0	0.0	0.0	0.0
Ca^{2+}	N3O4/N3O4(O2-O2)/wO4b	3.5	3.0	3.4	2.7
	N3O2/N3O2(O4-O4)/wO2b	5.8	5.0	5.7	4.6
	N3O4/N3O2(O4-O2) N1a-H ₂ O	48.8	41.6	49.5	39.9
	N3O4/N3O4(O2-O2) N1a-H ₂ Or	51.2	46.7	51.9	45.4
	N3O4/N3O4(O2-O2)/w	0.0	0.0	0.0	0.0
Mg^{2+}	N3O4/N3O2(O4-O2)/w	0.3	0.0	0.4	0.1
	N3O2/N3O2(O4-O4)/w	8.1	6.9	8.2	8.1
	N3O4/N3O2(O4-O2) N1a-H ₂ O	53.3	47.0	52.3	45.9
	N3O4/N3O4(O2-O2) N1a-H ₂ O	54.6	47.9	53.5	46.6
	N3O4/N3O4(O2-O2)/w	0.0	0.0	0.0	0.0

Table A3. Relative energies of the Mg-N3O4/N3O2(O4-O2) and Mg-N3O4/N3O4(O2-O2) at different levels of theory, in kJ mol^{-1} .

	B3LYPD3/6-31G+(d,p)				MP2/6-31+G(d,p)				MP2/6-311+G(3df,3pd)// MP2/6-31+G(d,p)			
	$\Delta\text{E}_{\text{el}}$	$\Delta\text{E}(0\text{K})$	$\Delta\text{H}^{\text{a}}$	$\Delta\text{G}^{\text{a}}$	$\Delta\text{E}_{\text{el}}$	$\Delta\text{E}(0\text{K})$	$\Delta\text{H}^{\text{a}}$	$\Delta\text{G}^{\text{a}}$	$\Delta\text{E}_{\text{el}}$	$\Delta\text{E}(0\text{K})$	$\Delta\text{H}^{\text{a}}$	$\Delta\text{G}^{\text{a}}$
i	0.0	1.5	1.6	1.3	0.0	0.7	0.7	0.5	0.0	0.6	0.7	0.5
ii	1.1	0.0	0.0	0.0	2.0	0.0	0.0	0.0	2.0	0.0	0.0	0.0

i: Mg-N3O4/N3O2(O4-O2)

ii: Mg-N3O4/N3O4(O2-O2)

a: 298 K

APPENDIX B – Chapter 3 Supplemental Information

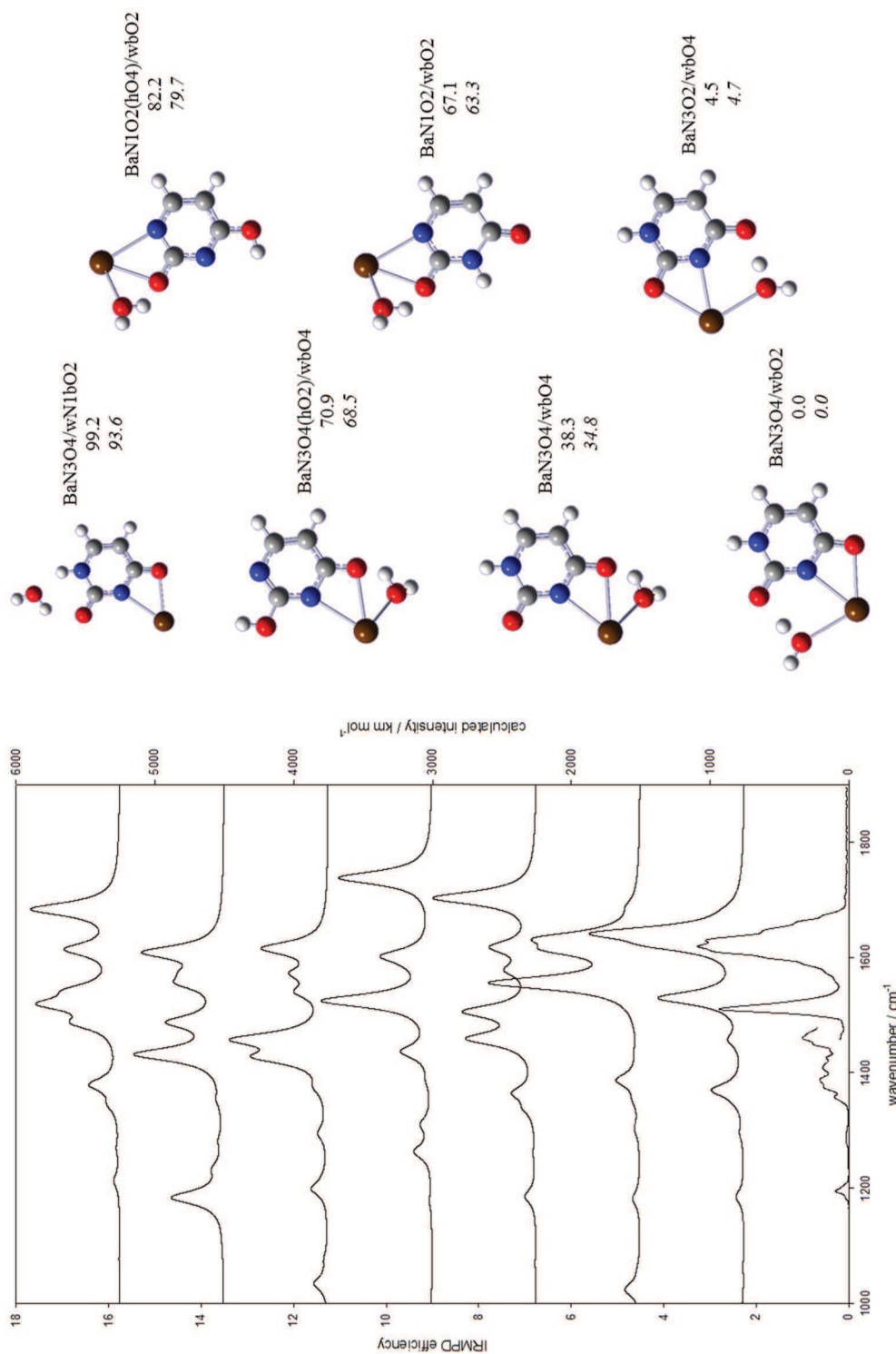


Figure B1. Experimental IRMPD spectrum (bottom) for $[\text{Ba}(\text{Ura-H})(\text{H}_2\text{O})]^+$ compared with the B3LYP computed spectra using computational method 1 for the seven lowest energy structures. Calculated relative enthalpies and Gibbs free energies (italics) at 298 K are also shown in kJ mol^{-1} .

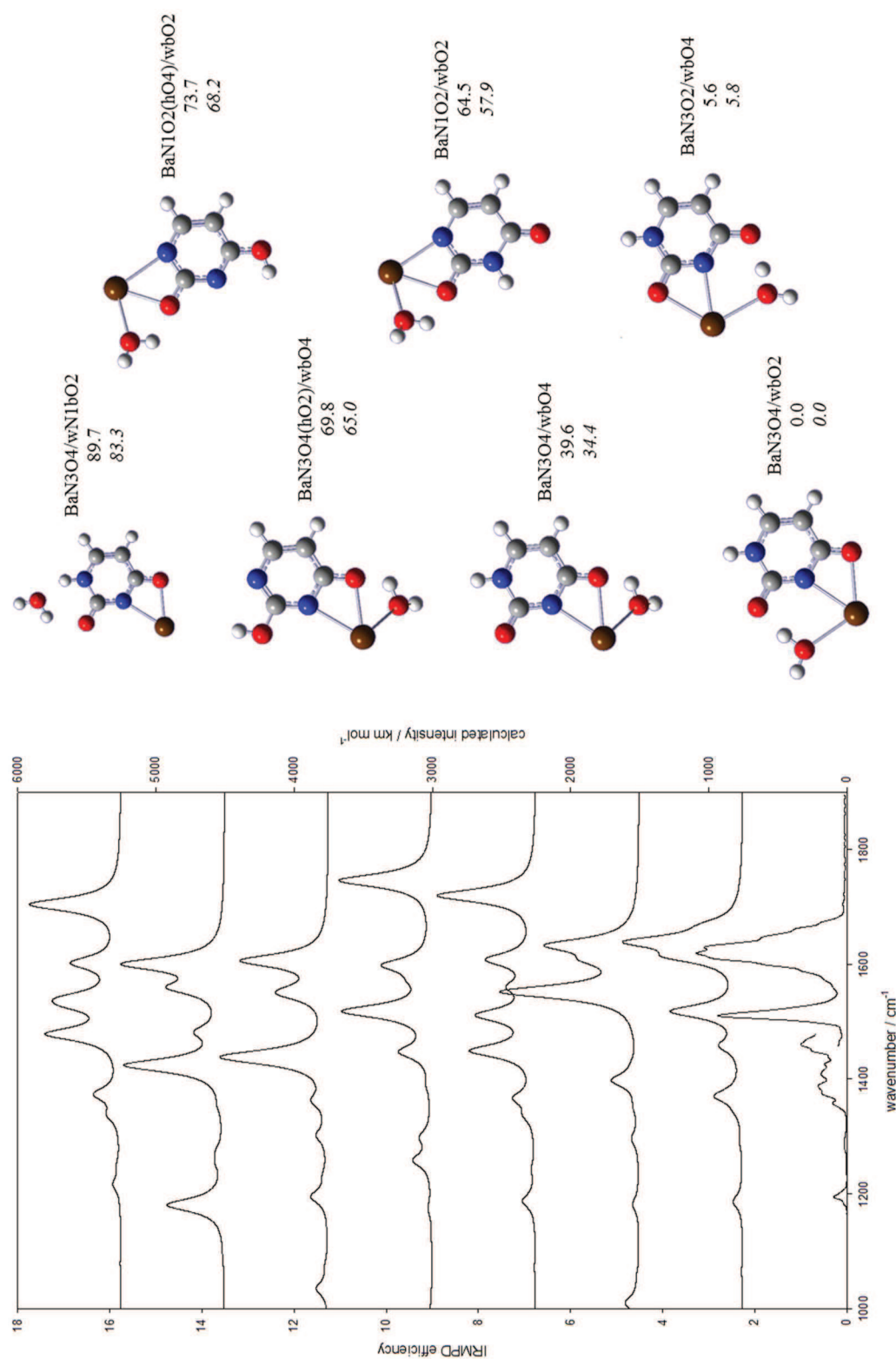


Figure B2. Experimental IRMPD spectrum (bottom) for $[\text{Ba}(\text{Ura-H})(\text{H}_2\text{O})]^+$ compared with the B3LYP computed spectra using computational method 2 for the seven lowest energy structures. Calculated relative enthalpies and Gibbs free energies (*italics*) at 298 K are also shown in kJ mol^{-1} .

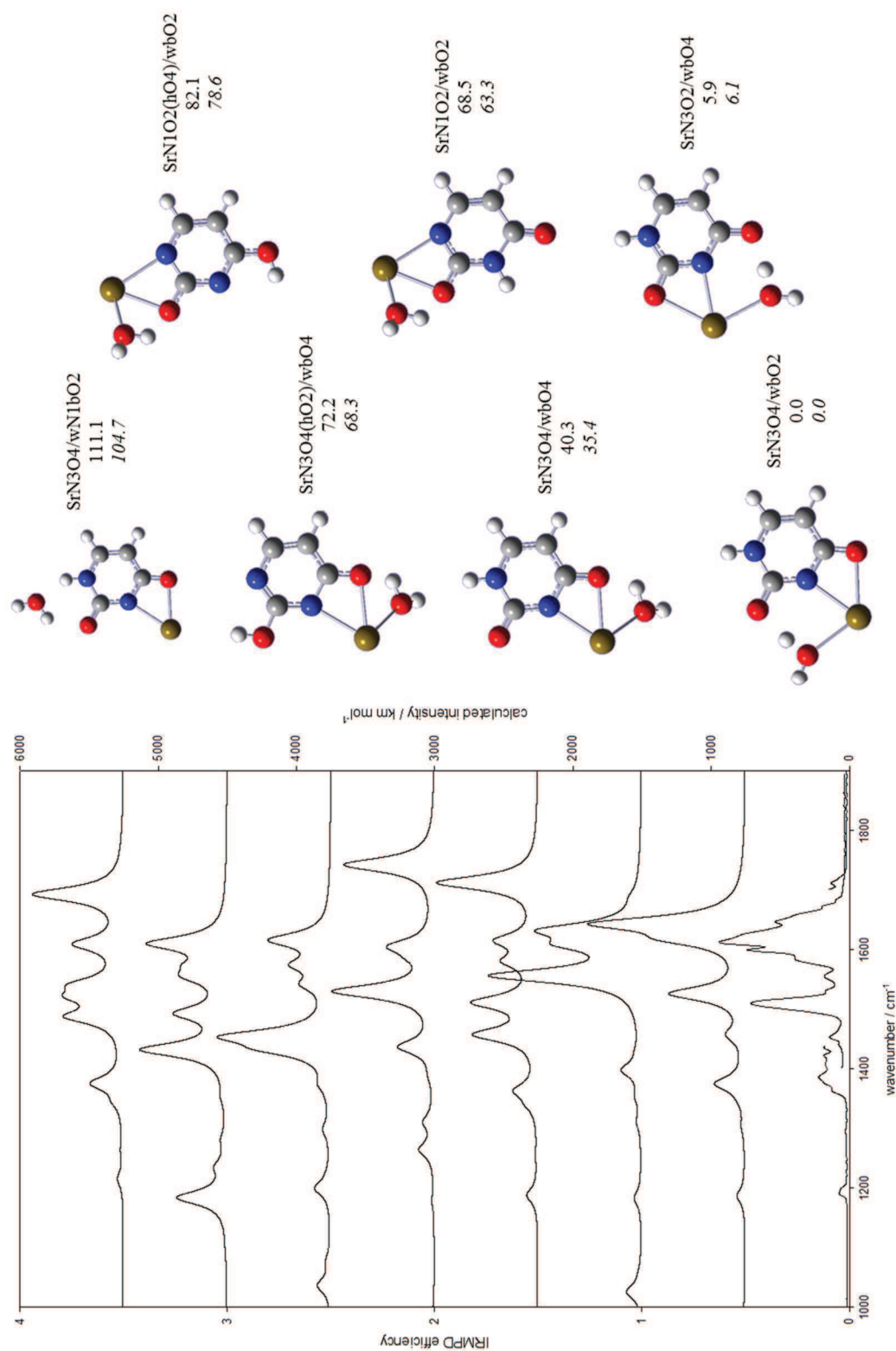


Figure B3. Experimental IRMPD spectrum (bottom) for $[\text{Sr}(\text{Ura-H})(\text{H}_2\text{O})]^+$ compared with the B3LYP computed spectra using computational method 1 for the seven lowest energy structures. Calculated relative enthalpies and Gibbs free energies (italics) at 298 K are also shown in kJ mol^{-1} .

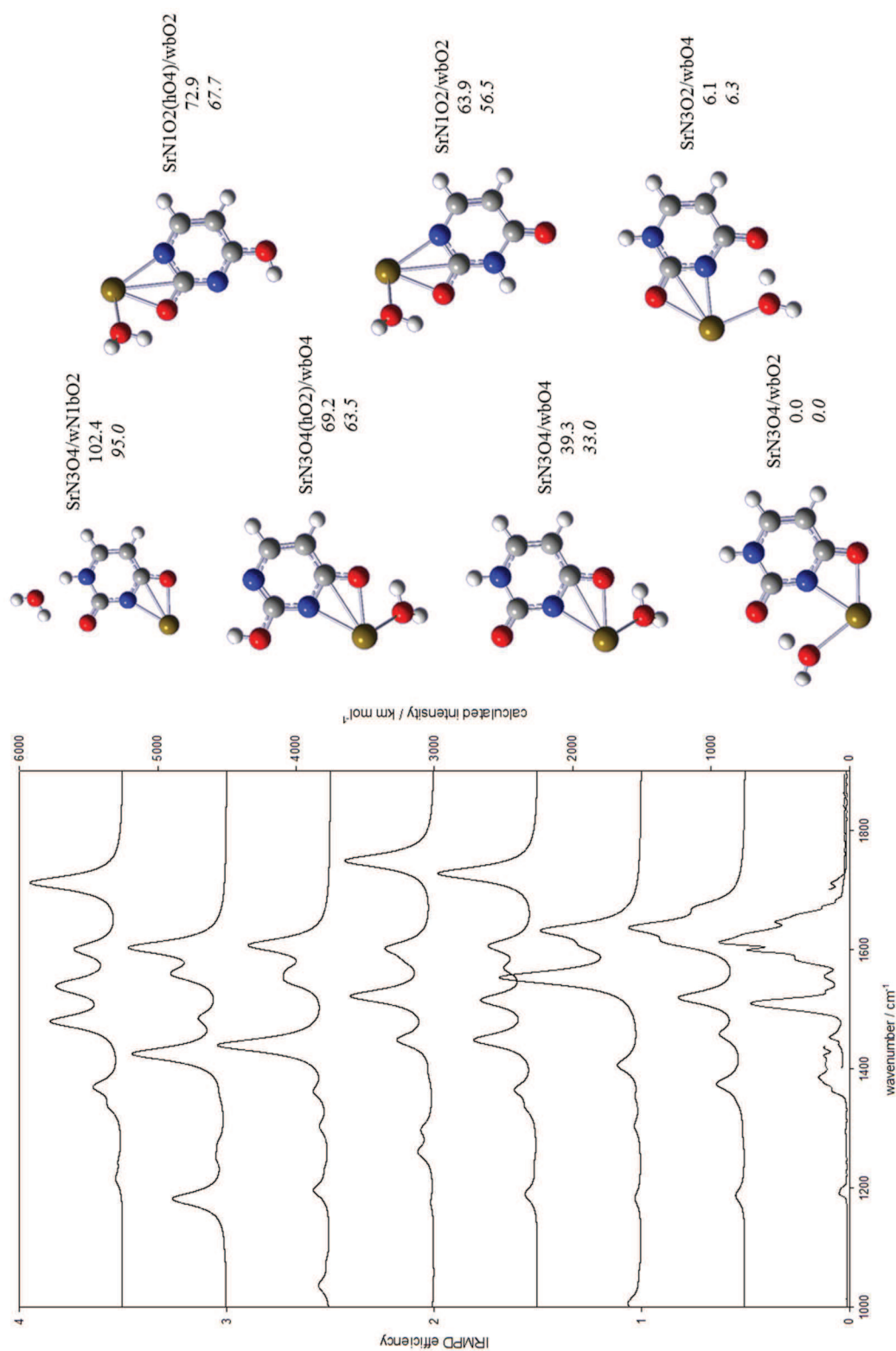


Figure B4. Experimental IRMPD spectrum (bottom) for $[\text{Sr}(\text{Ura-H})(\text{H}_2\text{O})]^+$ compared with the B3LYP computed spectra using computational method 2 for the seven lowest energy structures. Calculated relative enthalpies and Gibbs free energies (italics) at 298 K are also shown in kJ mol^{-1} .

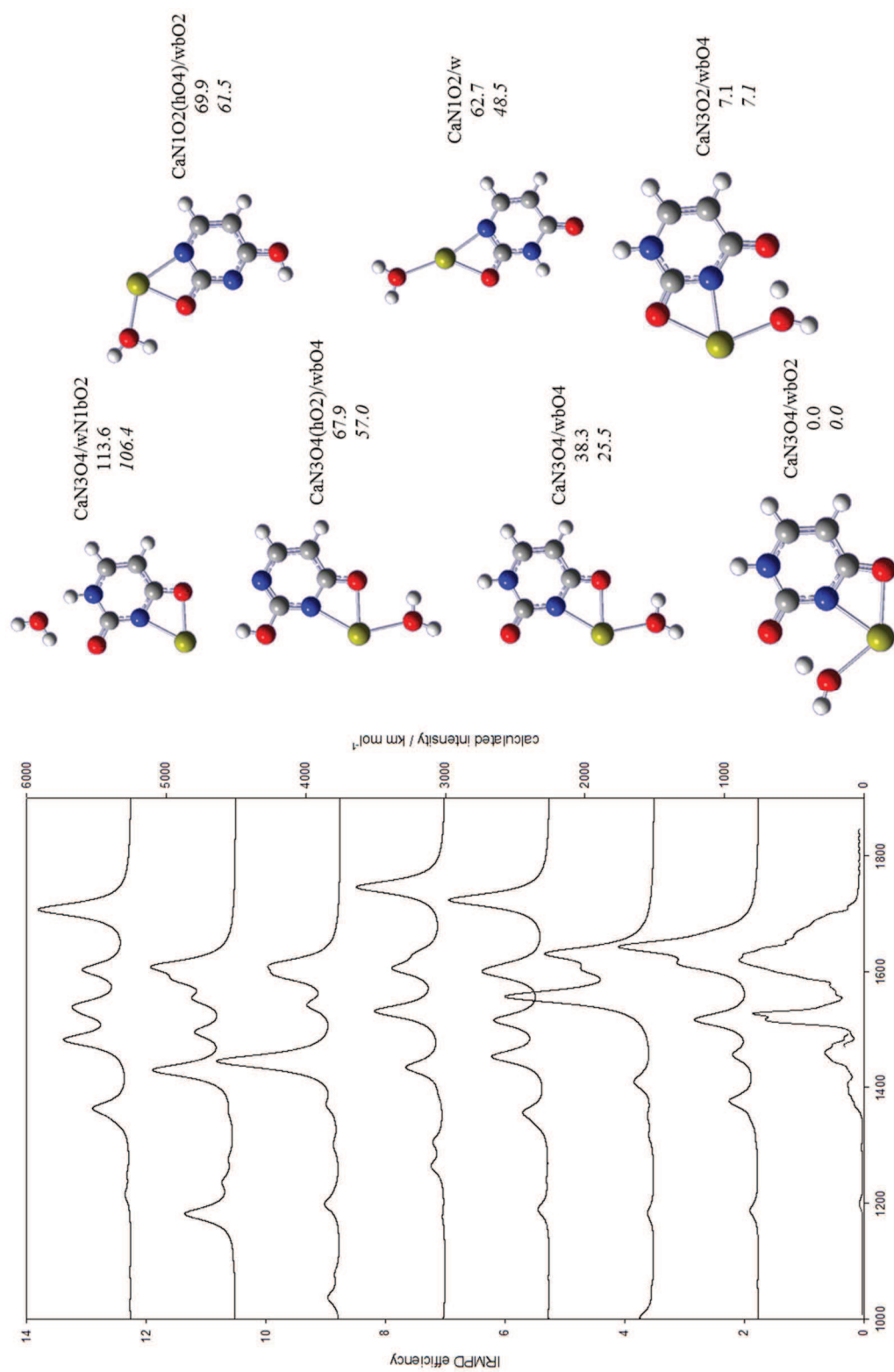


Figure B5. Experimental IRMPD spectrum (bottom) for $[\text{Ca}(\text{Ura-H})(\text{H}_2\text{O})]^+$ compared with the B3LYP computed spectra using computational method 1 for the seven lowest energy structures. Calculated relative enthalpies and Gibbs free energies (italics) at 298 K are also shown in kJ mol^{-1} .

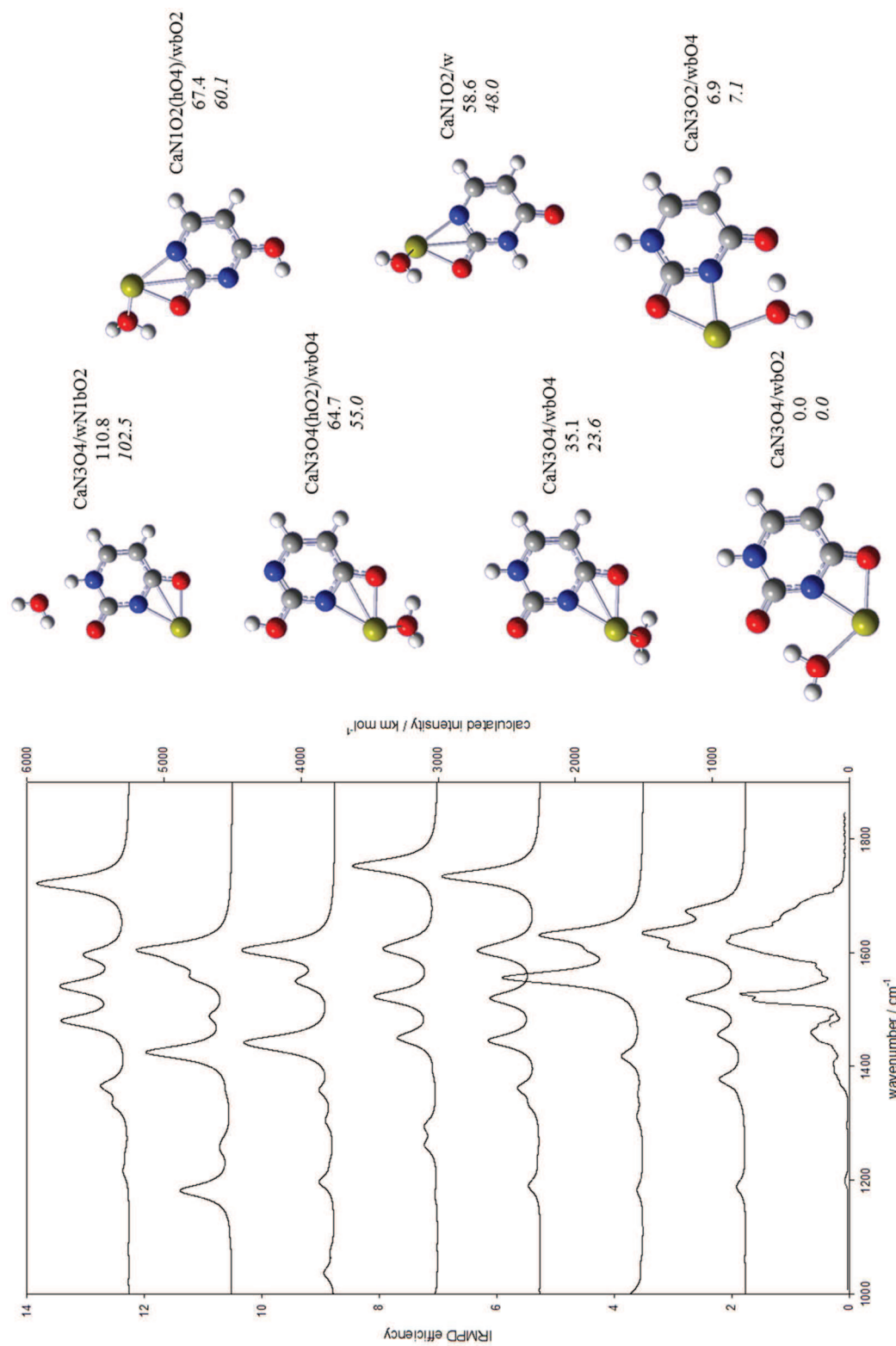


Figure B6. Experimental IRMPD spectrum (bottom) for $[\text{Ca}(\text{Ura-H})(\text{H}_2\text{O})]^+$ compared with the B3LYP computed spectra using computational method 2 for the seven lowest energy structures. Calculated relative enthalpies and Gibbs free energies (italics) at 298 K are also shown in kJ mol^{-1} .

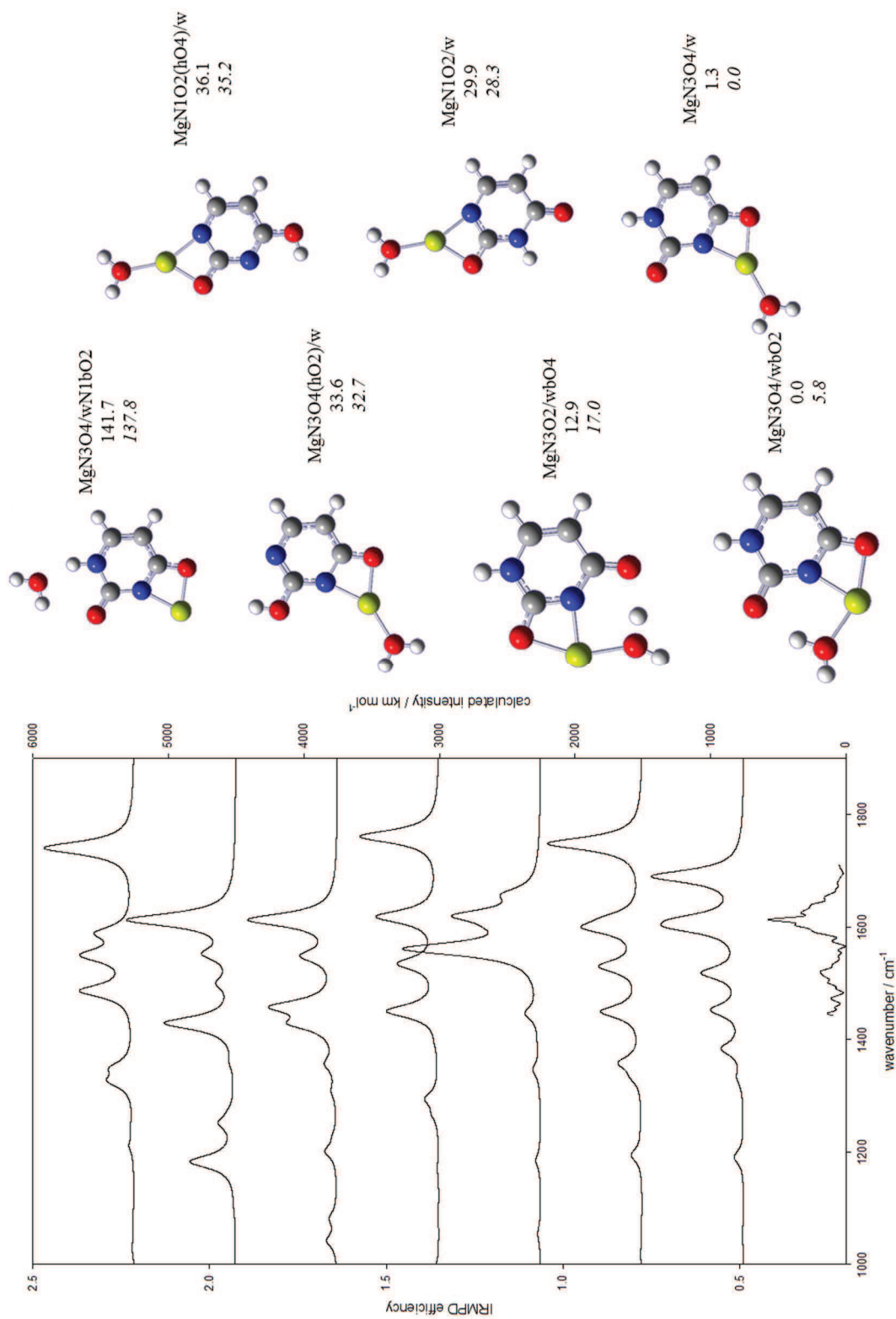


Figure B7. Experimental IRMPD spectrum (bottom) for $[\text{Mg}(\text{Ura-H})(\text{H}_2\text{O})]^+$ compared with the B3LYP computed spectra using computational method 1 for the seven lowest energy structures. Calculated relative enthalpies and Gibbs free energies (italics) at 298 K are also shown in kJ mol^{-1} .

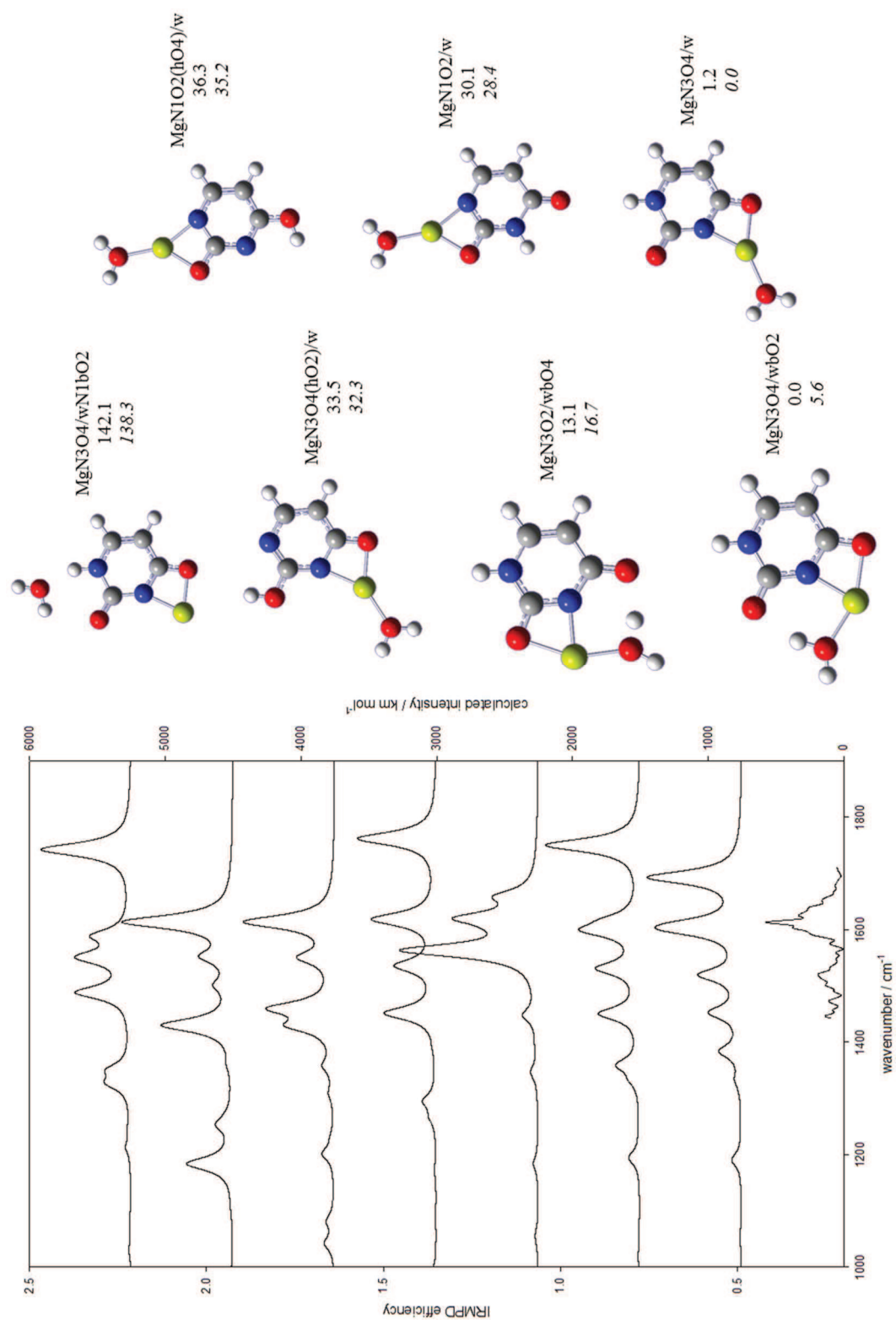


Figure B8. Experimental IRMPD spectrum (bottom) for $[\text{Mg}(\text{Ura-H})(\text{H}_2\text{O})]^+$ compared with the B3LYP computed spectra using computational method 2 for the seven lowest energy structures. Calculated relative enthalpies and Gibbs free energies (italics) at 298 K are also shown in kJ mol^{-1} .

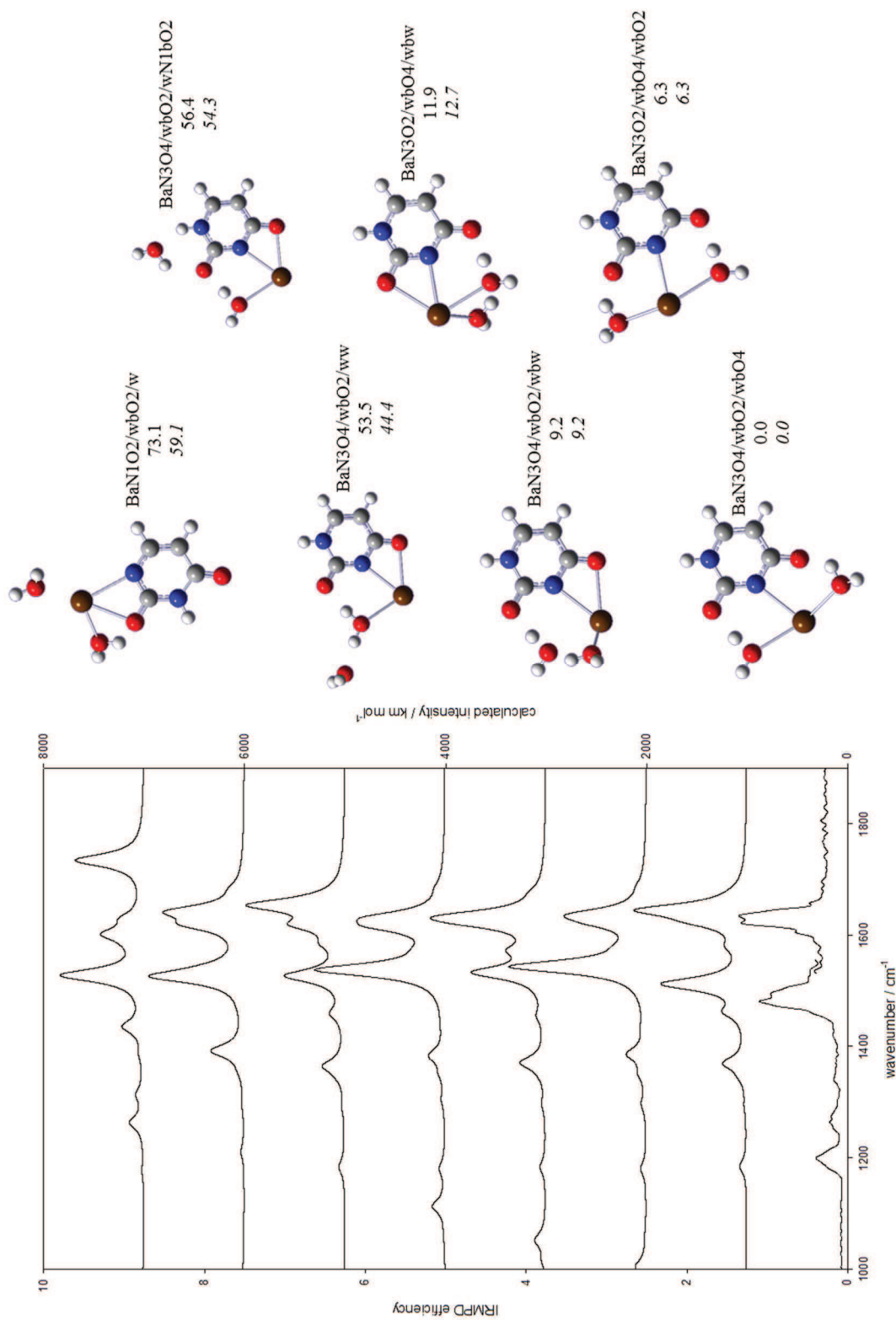


Figure B9. Experimental IRMPD spectrum (bottom) for $[\text{Ba}(\text{Ura-H})(\text{H}_2\text{O})_2]^+$ compared with the B3LYP computed spectra using computational method 1 for the seven lowest energy structures. Calculated relative enthalpies and Gibbs free energies (italics) at 298 K are also shown in kJ mol^{-1} .

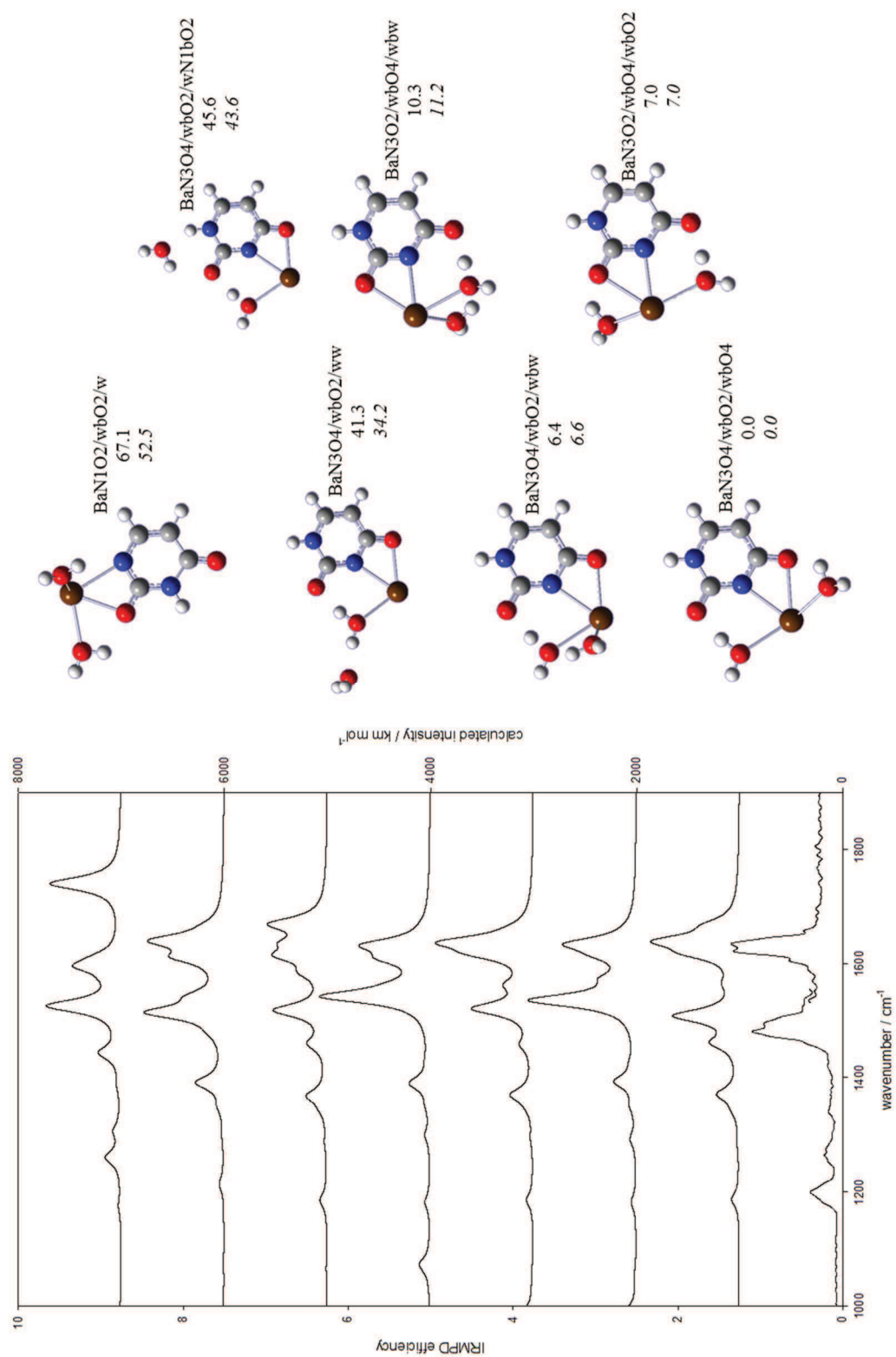


Figure B10. Experimental IRMPD spectrum (bottom) for $[\text{Ba}(\text{Ura-H})(\text{H}_2\text{O})_2]^+$ compared with the B3LYP computed spectra using computational method 2 for the seven lowest energy structures. Calculated relative enthalpies and Gibbs free energies (in italics) at 298 K are also shown in kJ mol^{-1} .

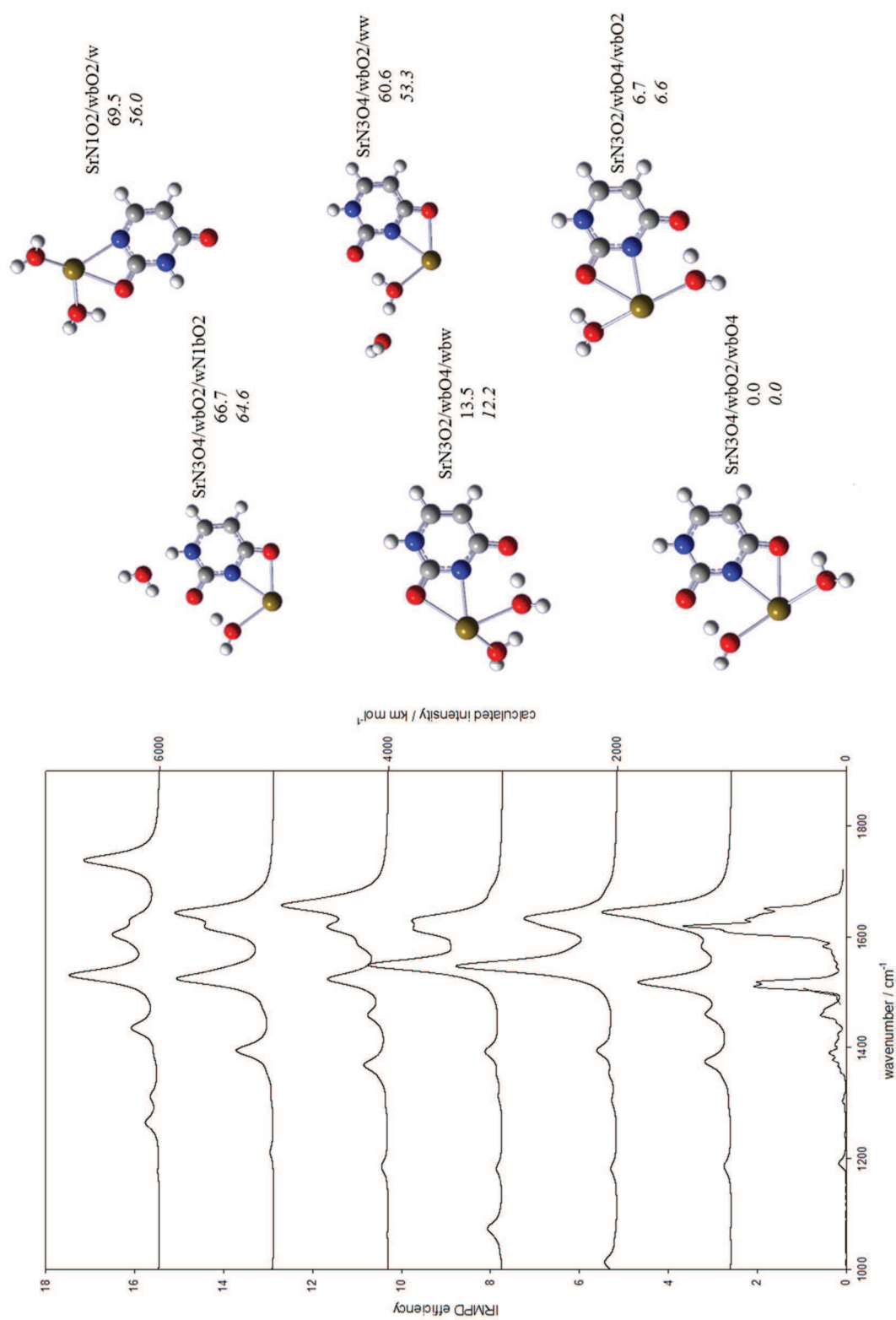


Figure B11. Experimental IRMPD spectrum (bottom) for $[\text{Sr}(\text{Ura-H})(\text{H}_2\text{O})_2]^+$ compared with the B3LYP computed spectra using computational method 1 for the six lowest energy structures. Calculated relative enthalpies and Gibbs free energies (italics) at 298 K are also shown in kJ mol^{-1} .

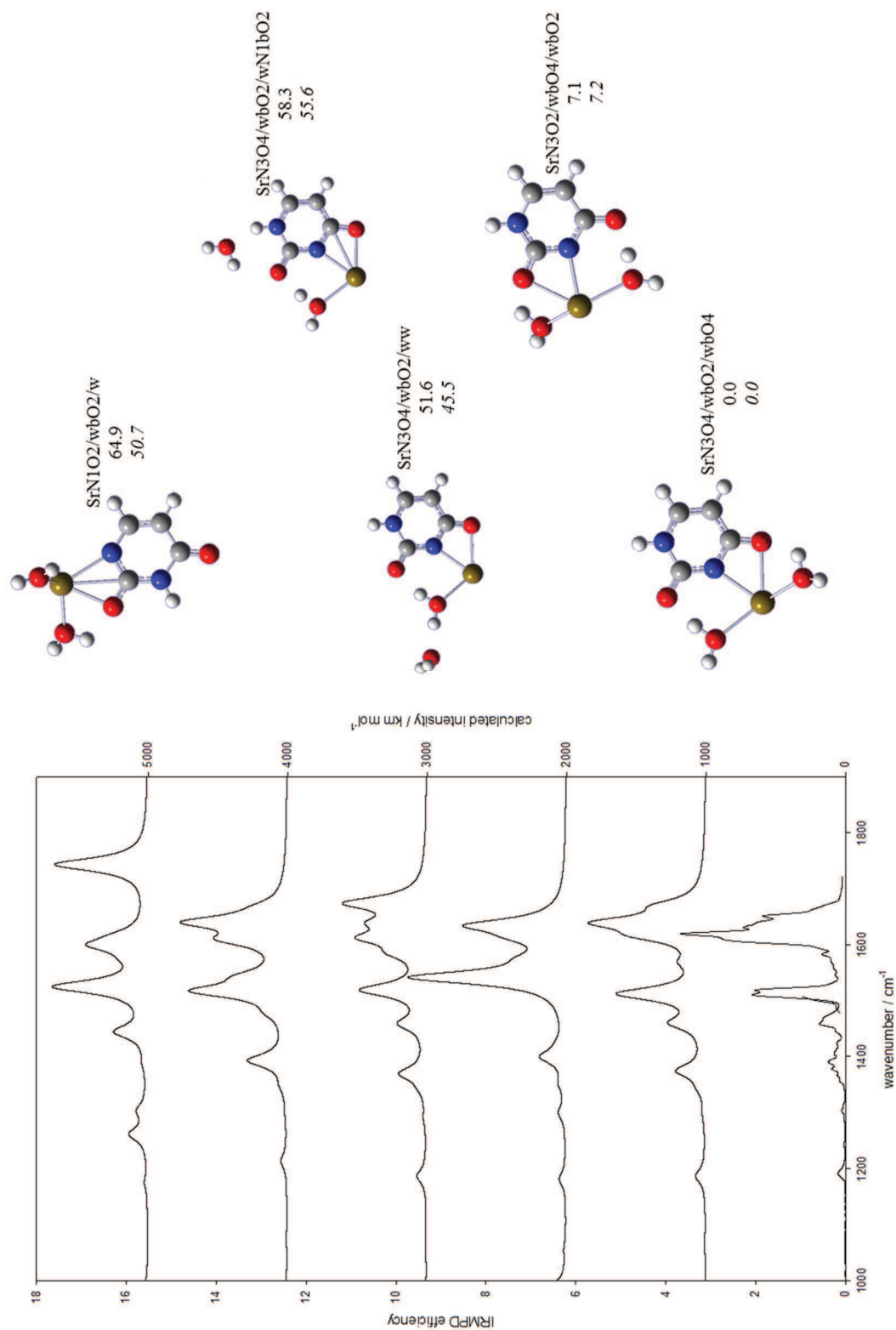


Figure B12. Experimental IRMPD spectrum (bottom) for $[\text{Sr}(\text{Ura-H})(\text{H}_2\text{O})_2]^+$ compared with the B3LYP computed spectra using computational method 2 for the five lowest energy structures. Calculated relative enthalpies and Gibbs free energies (in italics) at 298 K are also shown in kJ mol^{-1} .

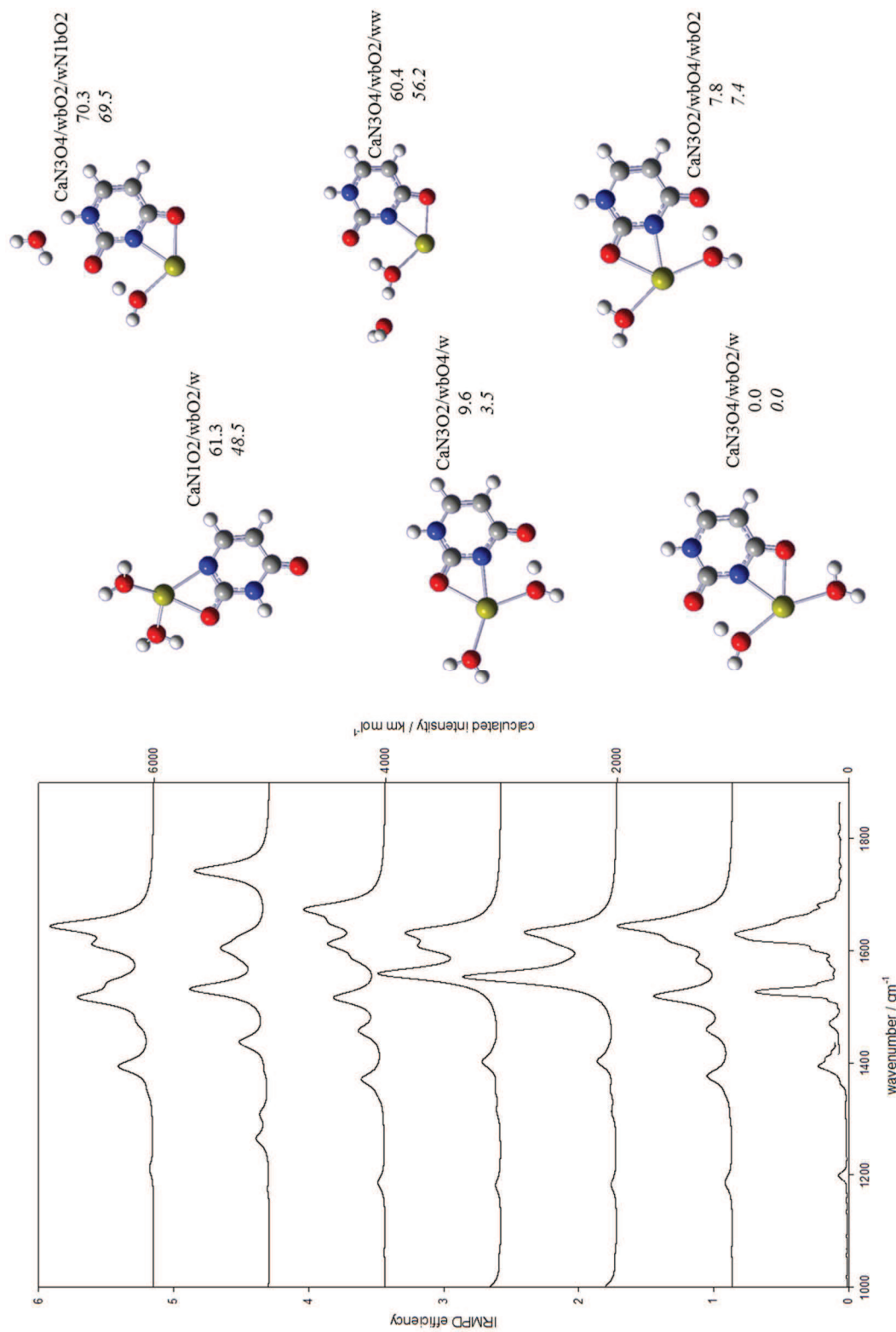


Figure B13. Experimental IRMPD spectrum (bottom) for $[\text{Ca}(\text{Ura-H})(\text{H}_2\text{O})_2]^+$ compared with the B3LYP computed spectra using computational method 1 for the six lowest energy structures. Calculated relative enthalpies and Gibbs free energies (italics) at 298 K are also shown in kJ mol^{-1} .

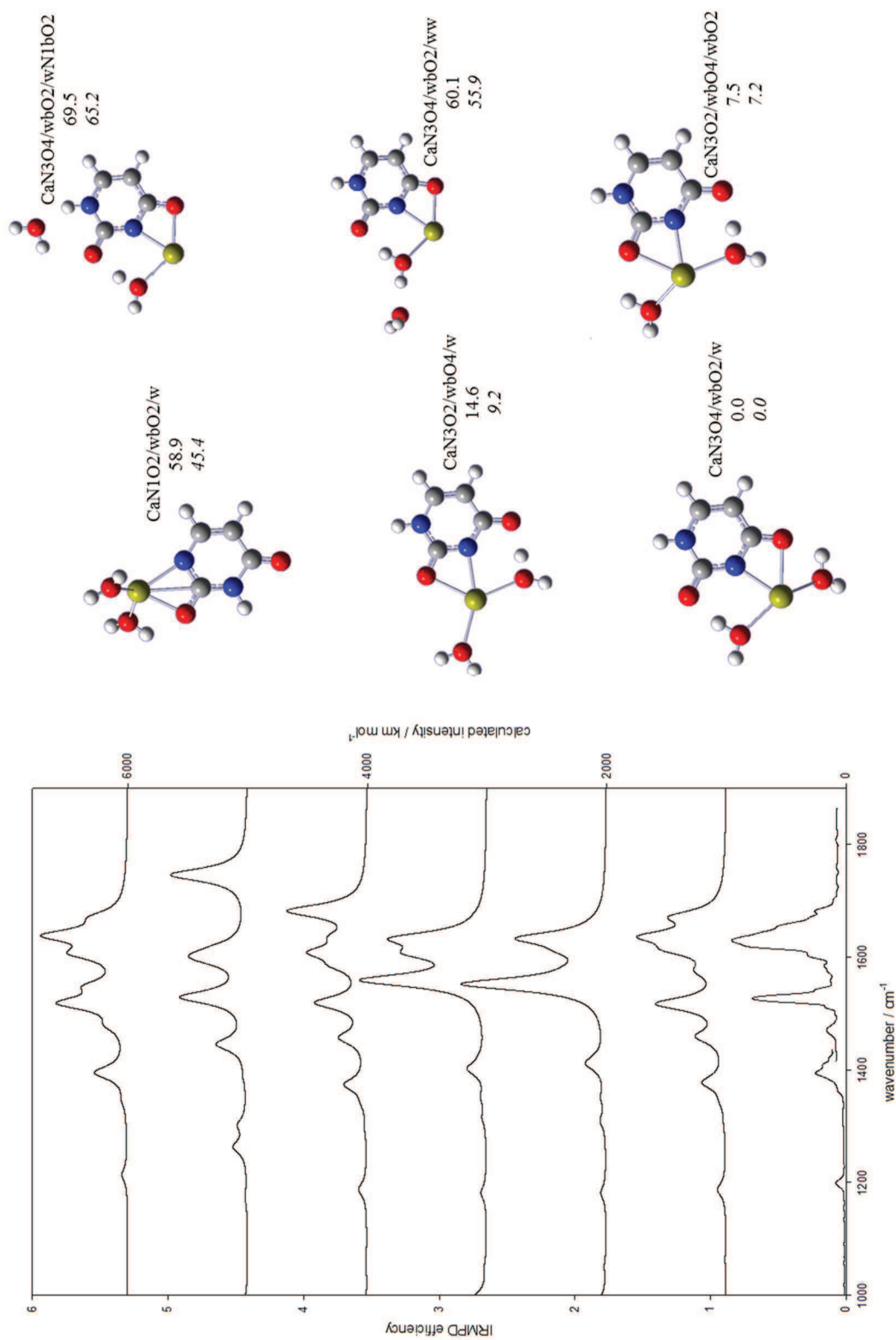


Figure B14. Experimental IRMPD spectrum (bottom) for $[\text{Ca}(\text{Ura-H})(\text{H}_2\text{O})_2]^+$ compared with the B3LYP computed spectra using computational method 2 for the six lowest energy structures. Calculated relative enthalpies and Gibbs free energies (italics) at 298 K are also shown in kJ mol^{-1} .

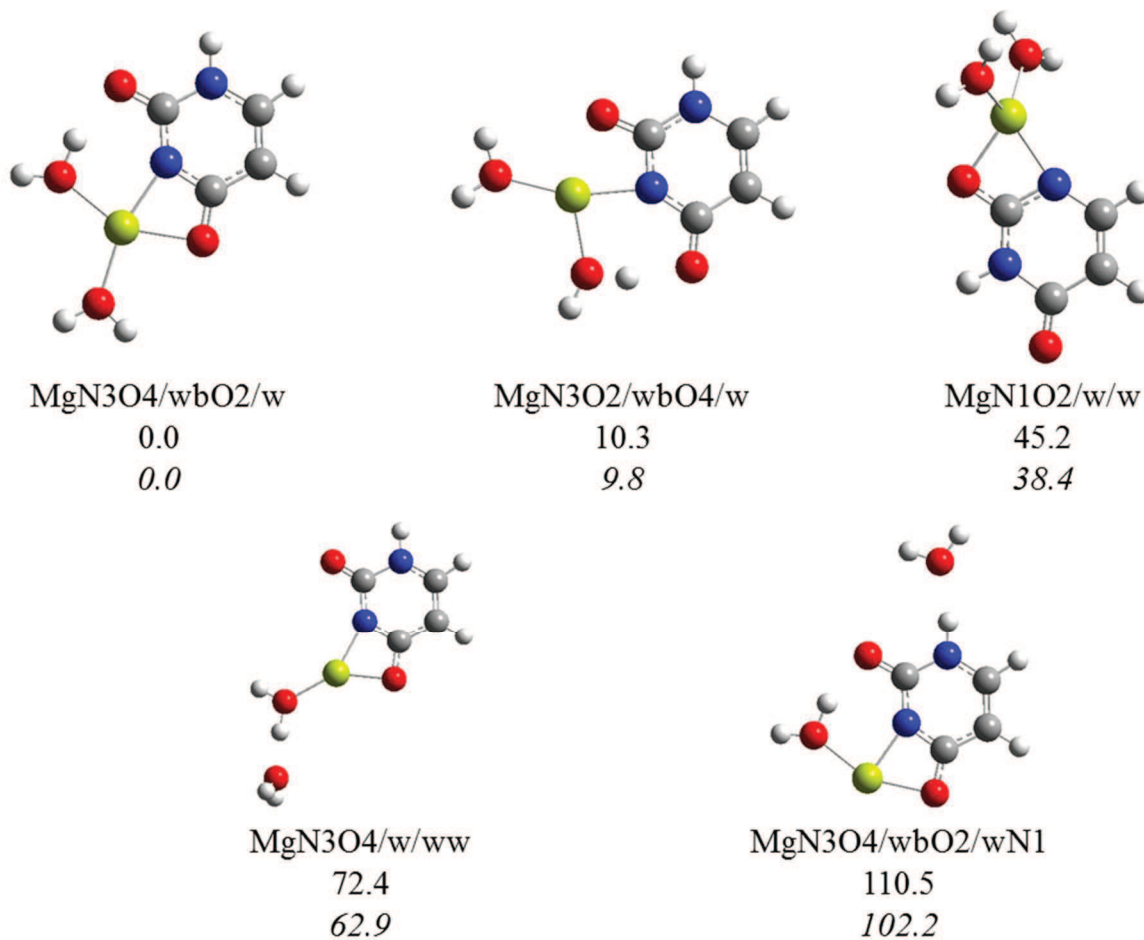


Figure B15. All structures found using calculation method 1 for $[\text{Mg}(\text{Ura-H})(\text{H}_2\text{O})_2]^+$. The calculated relative enthalpies and Gibbs free energies (italics) at 298 K are also shown in kJ mol^{-1} .

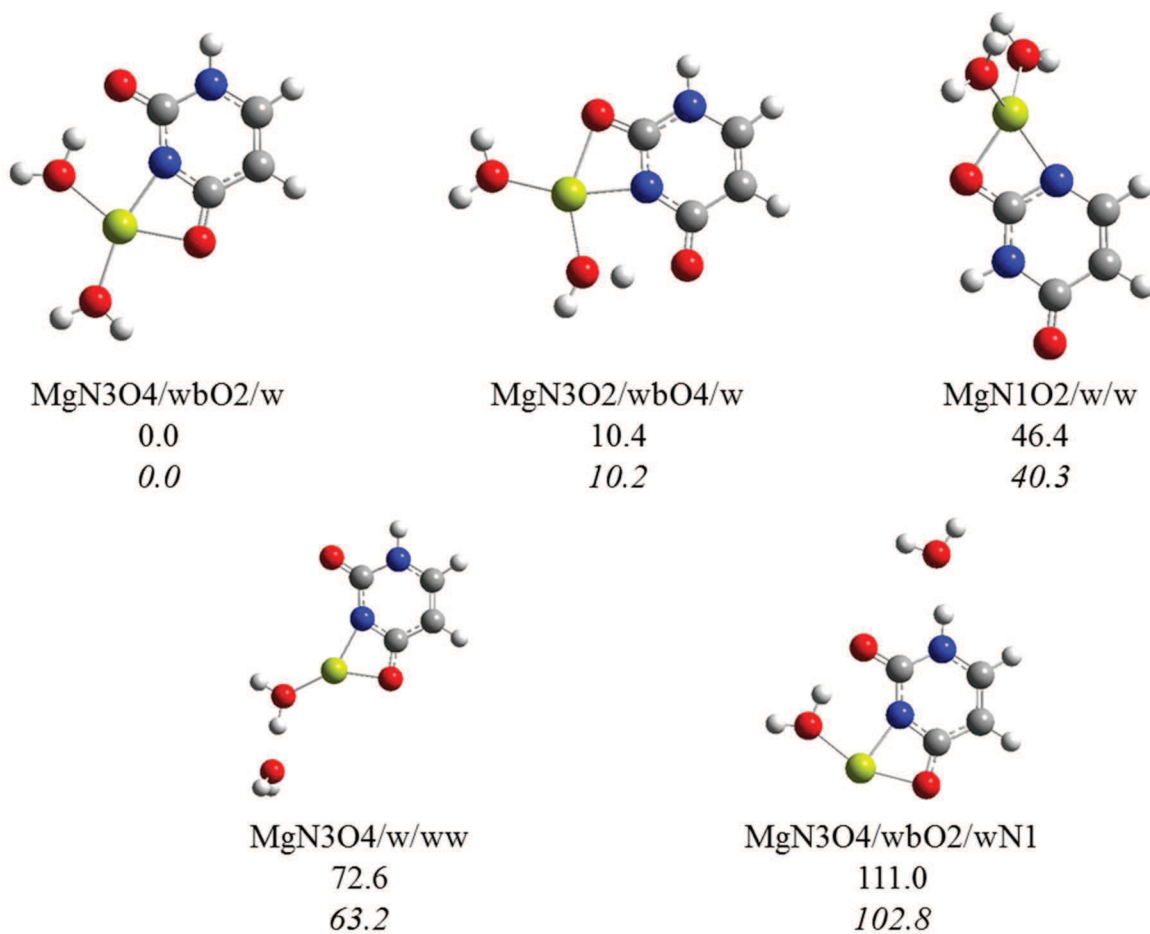


Figure B16. All structures found using calculation method 2 for $[\text{Mg}(\text{Ura-H})(\text{H}_2\text{O})_2]^+$. The calculated relative enthalpies and Gibbs free energies (italics) at 298 K are also shown in kJ mol^{-1} .

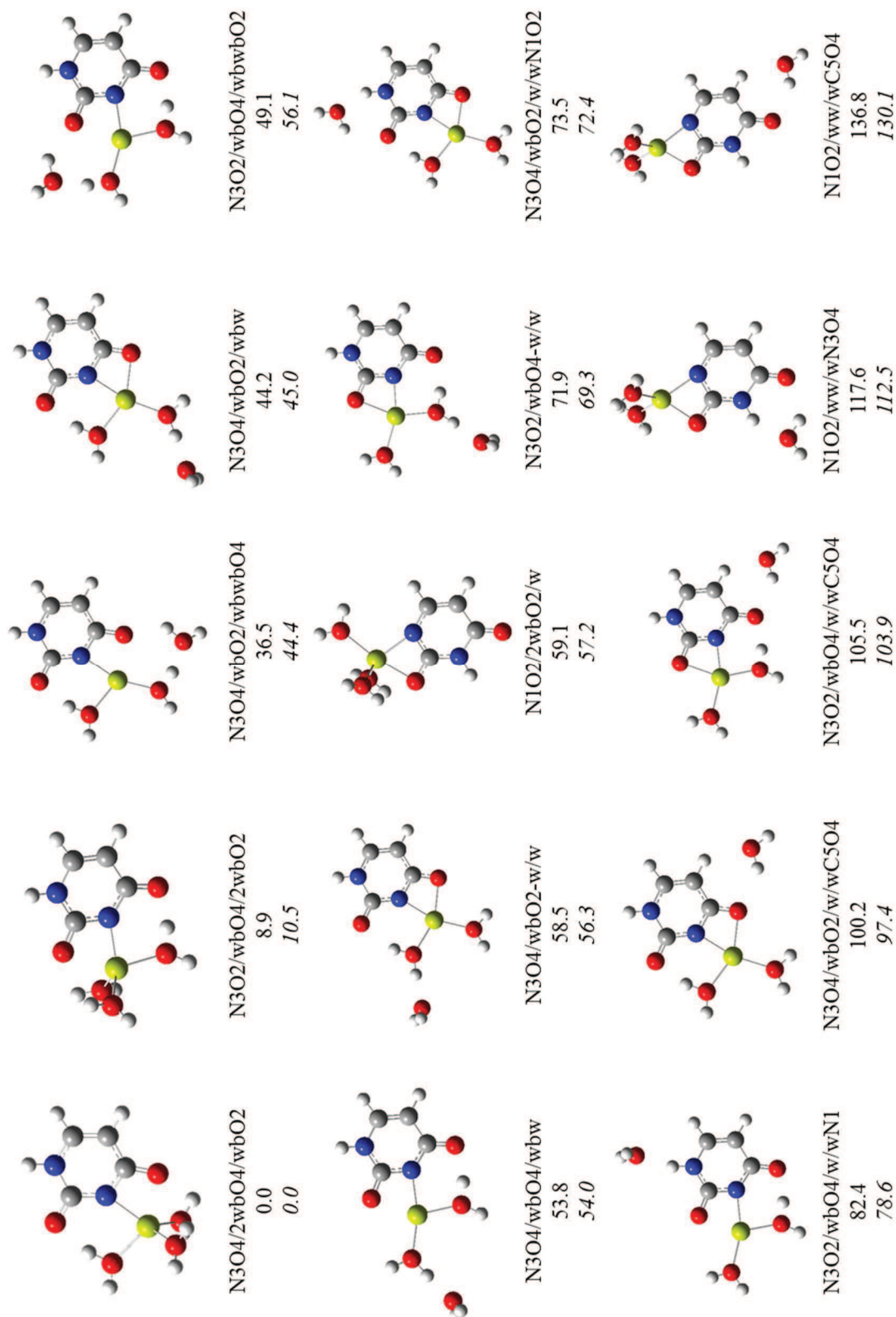


Figure B17. All structures found using calculation method 1 for $[\text{Mg}(\text{Ura-H})(\text{H}_2\text{O})_3]^+$. The calculated relative enthalpies and Gibbs free energies (italics) at 298 K are also shown in kJ mol^{-1} .

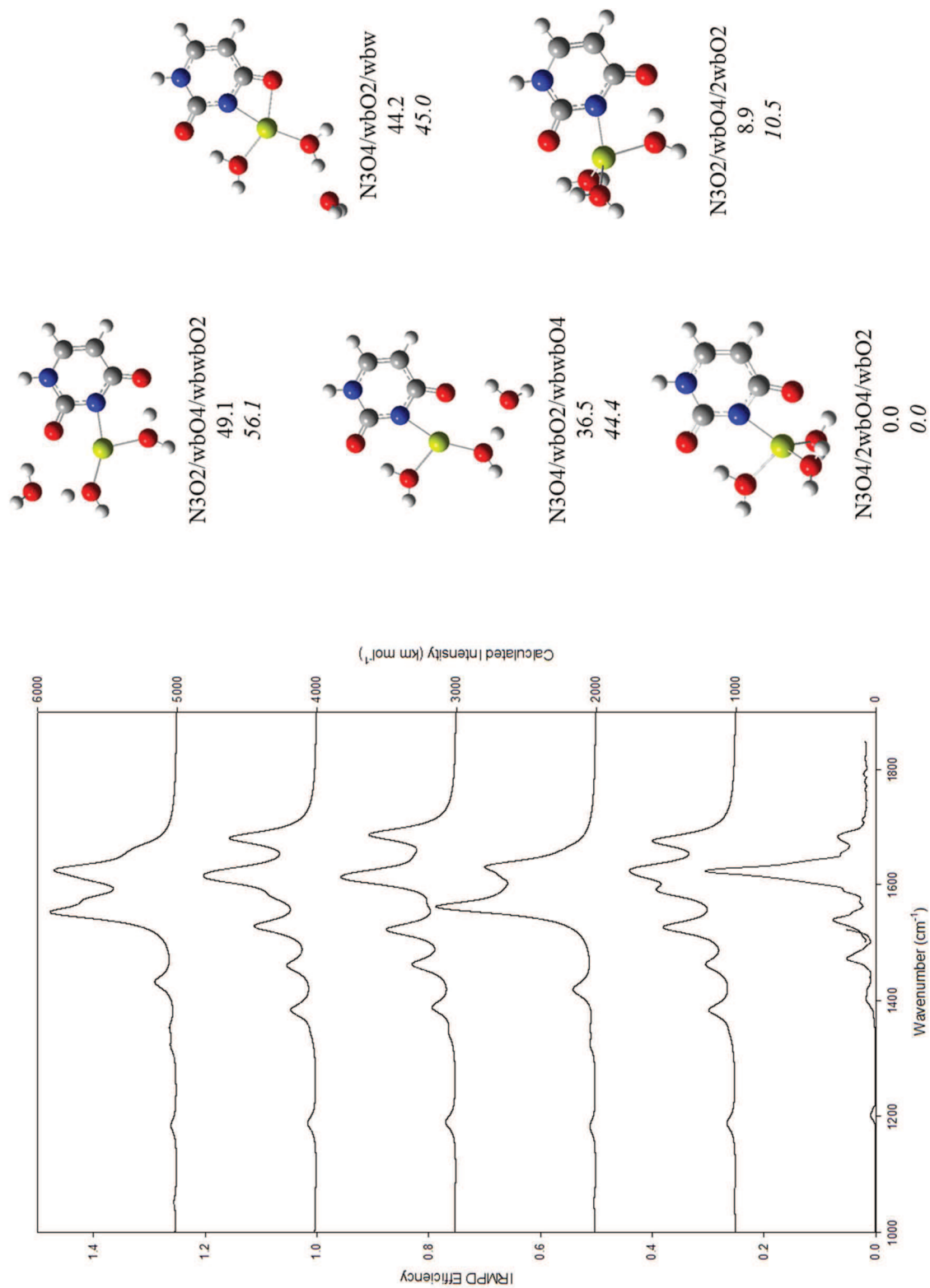


Figure B18. Experimental IRMPD spectrum (bottom) for $[\text{Mg}(\text{Ura-H})(\text{H}_2\text{O})_3]^+$ compared with the B3LYP computed spectra using computational method 1 for the five lowest energy structures. Calculated relative enthalpies and Gibbs free energies (italics) at 298 K are also shown in kJ mol^{-1} .

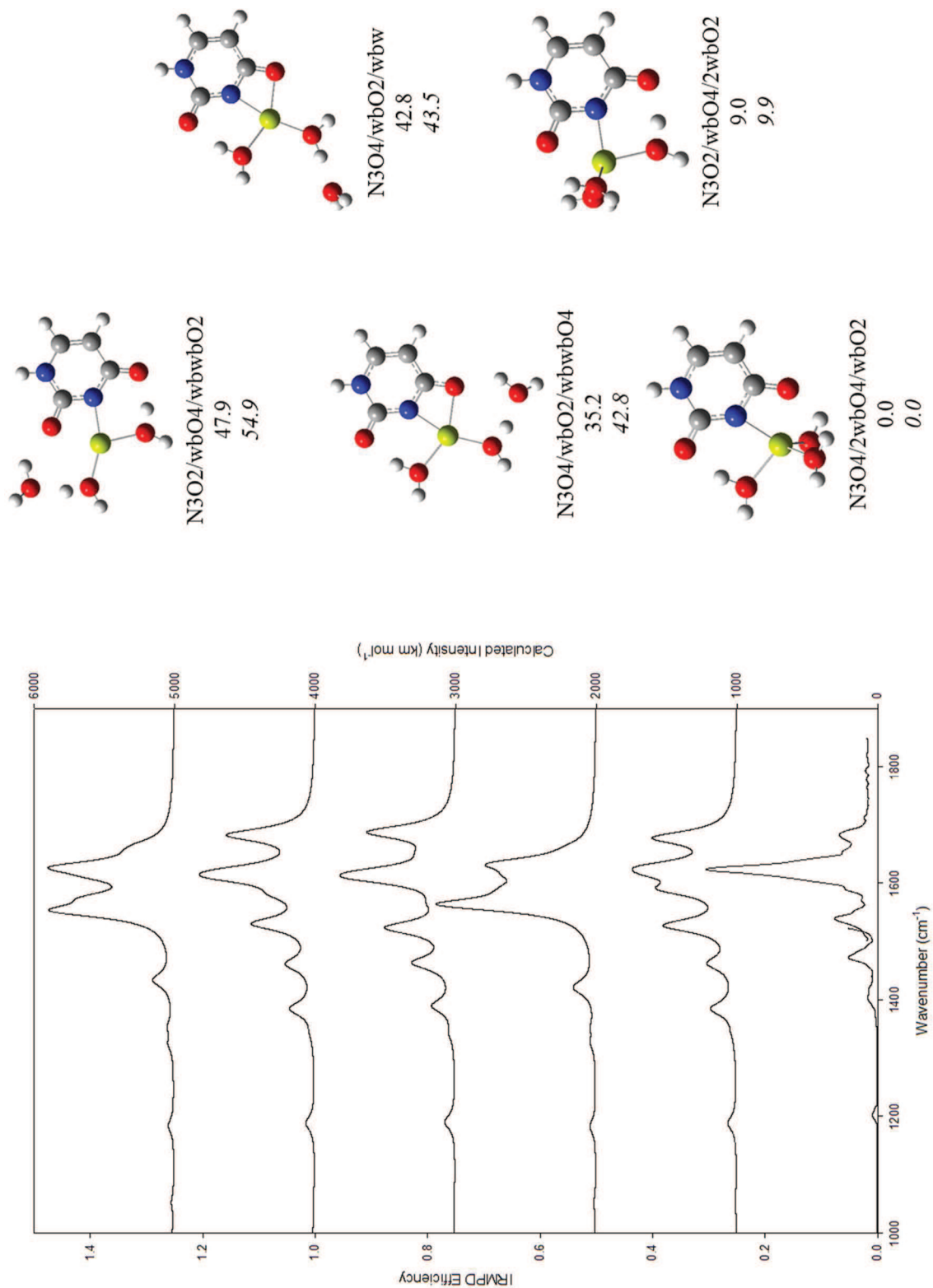
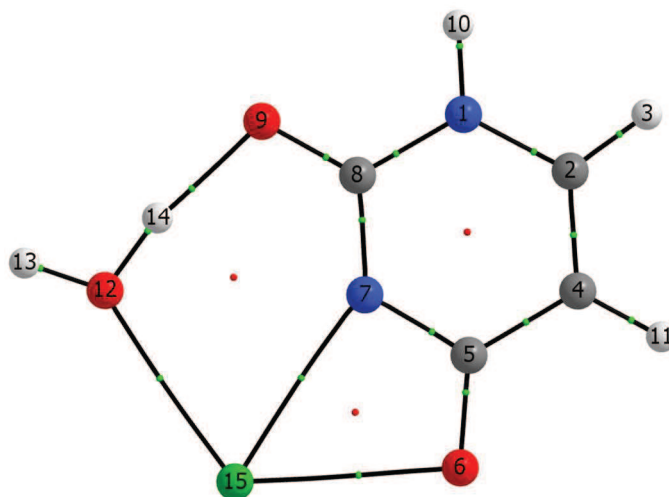


Figure B19. Experimental IRMPD spectrum (bottom) for $[\text{Mg}(\text{Ura-H})(\text{H}_2\text{O})_3]^+$ compared with the B3LYP computed spectra using computational method 2 for the five lowest energy structures. Calculated relative enthalpies and Gibbs free energies (italics) at 298 K are also shown in kJ mol^{-1} .

FIGURE B20.

M-N3O4/wbO2 complex with Ba

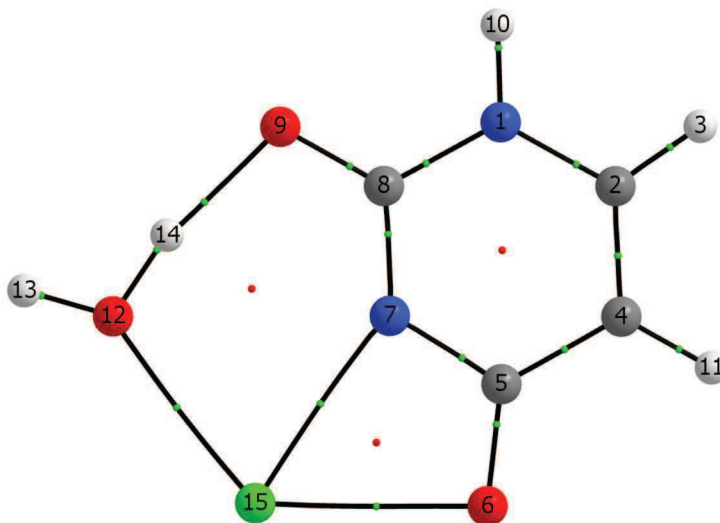
Electron densities ρ ($\text{e } \text{\AA}^{-3}$), Laplacian of the charge density $\nabla^2\rho$ ($\text{e } \text{\AA}^{-5}$) and ellipticity ε at the bond critical points, computed for geometries optimized at the B3LYP/6-31+G(d,p) level.



Bond	ρ	$\nabla^2\rho$	ε
N7 - C8	0.338	-1.207	0.140
N1 - C2	0.311	-0.766	0.026
C2 - C4	0.332	-0.967	0.321
C2 - H3	0.293	-1.132	0.020
C5 - N7	0.329	-1.128	0.082
C4 - C5	0.295	-0.802	0.168
C4 - H11	0.287	-1.064	0.030
C5 - O6	0.359	-0.307	0.033
N1 - C8	0.309	-1.003	0.125
N7 - Ba15	0.046	0.153	0.126
C8 - O9	0.388	-0.200	0.127
N1 - H10	0.341	-1.853	0.038
O9 - H14	0.055	0.139	0.037
O12 - H14	0.299	-1.631	0.020
O12 - H13	0.357	-2.077	0.019
O6 - Ba15	0.045	0.161	0.071
O12 - Ba15	0.035	0.147	0.140

M-N3O4/wbO2 complex with Sr

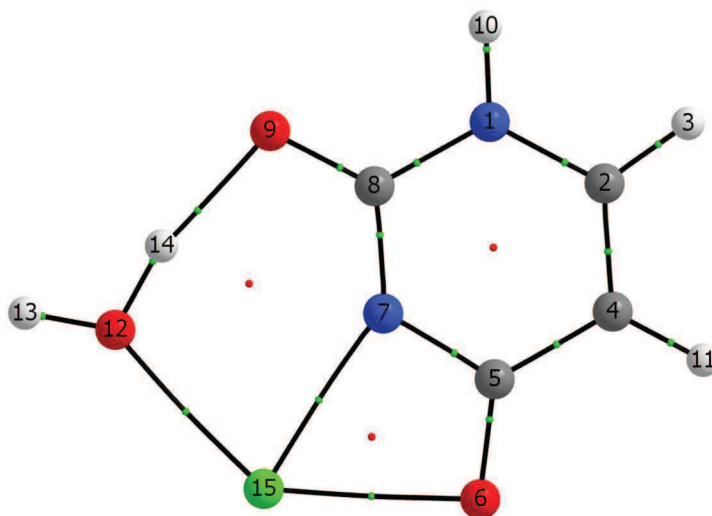
Electron densities ρ ($\text{e } \text{\AA}^{-3}$), Laplacian of the charge density $\nabla^2\rho$ ($\text{e } \text{\AA}^{-5}$) and ellipticity ε at the bond critical points, computed for geometries optimized at the B3LYP/6-31+G(d,p) level.



Bond	ρ	$\nabla^2\rho$	ε
N1 - C2	0.310	-0.767	0.024
C2 - C4	0.331	-0.963	0.319
C2 - H3	0.293	-1.136	0.020
C5 - N7	0.330	-1.122	0.078
C4 - C5	0.295	-0.805	0.169
C4 - H11	0.287	-1.067	0.030
C5 - O6	0.357	-0.323	0.031
N7 - C8	0.338	-1.203	0.138
N1 - C8	0.310	-1.008	0.127
N1 - H10	0.341	-1.852	0.038
C8 - O9	0.389	-0.195	0.128
N7 - Sr15	0.049	0.184	0.120
O9 - H14	0.053	0.133	0.037
O12 - H14	0.298	-1.632	0.020
O12 - H13	0.356	-2.086	0.019
O6 - Sr15	0.044	0.176	0.061
O12 - Sr15	0.037	0.169	0.125

M-N3O4/wbO2 complex with Ca

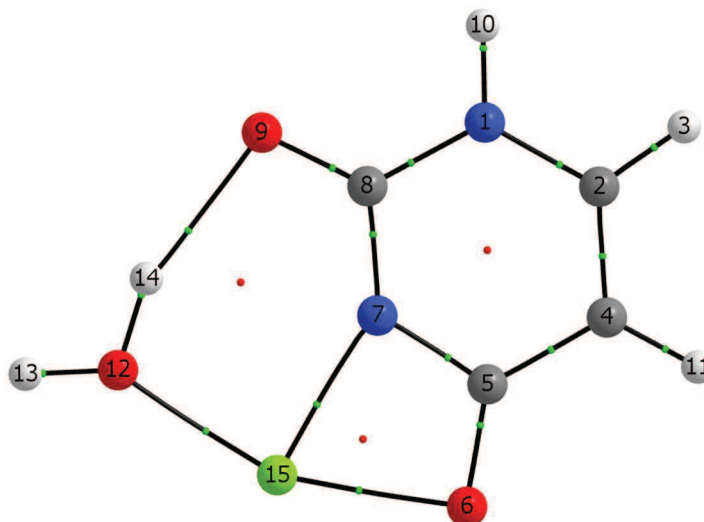
Electron densities ρ ($\text{e } \text{\AA}^{-3}$), Laplacian of the charge density $\nabla^2\rho$ ($\text{e } \text{\AA}^{-5}$) and ellipticity ε at the bond critical points, computed for geometries optimized at the B3LYP/6-31+G(d,p) level.



Bond	ρ	$\nabla^2\rho$	ε
N1 - C2	0.311	-0.827	0.038
C2 - H3	0.293	-1.135	0.021
C2 - C4	0.329	-0.941	0.321
C5 - N7	0.332	-1.144	0.087
C4 - C5	0.296	-0.799	0.174
C4 - H11	0.287	-1.067	0.032
C5 - O6	0.357	-0.435	0.031
N7 - C8	0.339	-1.209	0.141
N1 - C8	0.310	-1.024	0.136
N1 - H10	0.341	-1.855	0.039
C8 - O9	0.393	-0.301	0.132
N7 - Ca15	0.051	0.275	0.119
O9 - H14	0.049	0.122	0.037
O12 - H13	0.356	-2.096	0.019
O12 - H14	0.299	-1.656	0.020
O6 - Ca15	0.045	0.246	0.058
O12 - Ca15	0.038	0.222	0.113

M-N3O4/wbO2 complex with Mg

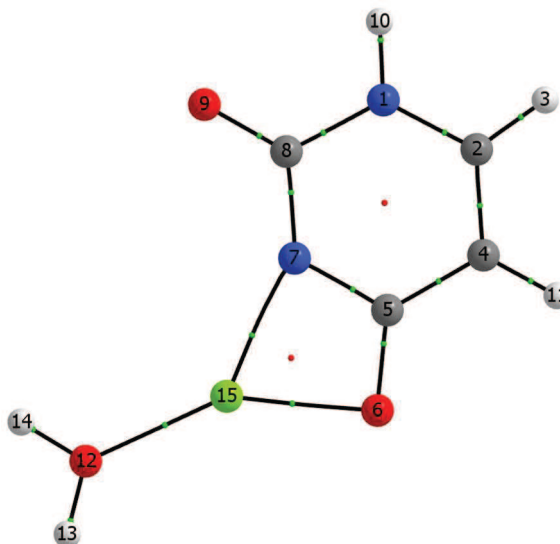
Electron densities ρ ($e \text{ \AA}^{-3}$), Laplacian of the charge density $\nabla^2\rho$ ($e \text{ \AA}^{-5}$) and ellipticity ε at the bond critical points, computed for geometries optimized at the B3LYP/6-31+G(d,p) level.



Bond	ρ	$\nabla^2\rho$	ε
N1 - C2	0.312	-0.835	0.036
C2 - H3	0.294	-1.146	0.019
C2 - C4	0.326	-0.924	0.313
C5 - N7	0.336	-1.153	0.088
C4 - C5	0.298	-0.809	0.183
C5 - O6	0.349	-0.493	0.023
N7 - C8	0.335	-1.182	0.135
N1 - C8	0.308	-1.017	0.138
N1 - H10	0.340	-1.856	0.038
C8 - O9	0.400	-0.267	0.142
C4 - H11	0.287	-1.077	0.033
N7 - Mg15	0.054	0.402	0.058
O12 - Mg15	0.042	0.330	0.063
O9 - H14	0.026	0.061	0.024
O12 - H13	0.353	-2.140	0.021
O12 - H14	0.312	-1.849	0.021
O6 - Mg15	0.047	0.328	0.013

M-N3O4/w complex with Mg

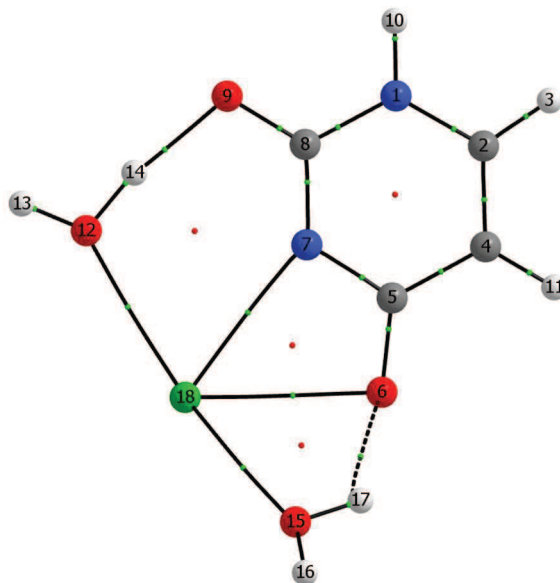
Electron densities ρ ($\text{e } \text{\AA}^{-3}$), Laplacian of the charge density $\nabla^2\rho$ ($\text{e } \text{\AA}^{-5}$) and ellipticity ε at the bond critical points, computed for geometries optimized at the B3LYP/6-31+G(d,p) level.



Bond	ρ	$\nabla^2\rho$	ε
N1 - C2	0.320	-0.844	0.038
C2 - C4	0.327	-0.936	0.307
C2 - H3	0.293	-1.140	0.017
C5 - N7	0.329	-1.129	0.105
C4 - C5	0.301	-0.824	0.195
C4 - H11	0.287	-1.069	0.036
C5 - O6	0.345	-0.497	0.013
N7 - C8	0.318	-1.084	0.130
N1 - C8	0.297	-0.956	0.131
N1 - H10	0.341	-1.857	0.038
C8 - O9	0.415	-0.110	0.153
N7 - Mg15	0.052	0.373	0.039
O6 - Mg15	0.054	0.418	0.032
O12 - Mg15	0.042	0.331	0.100
O12 - H13	0.348	-2.143	0.023
O12 - H14	0.346	-2.136	0.023

M-N3O4/wbO2/wbO4 complex with Ba

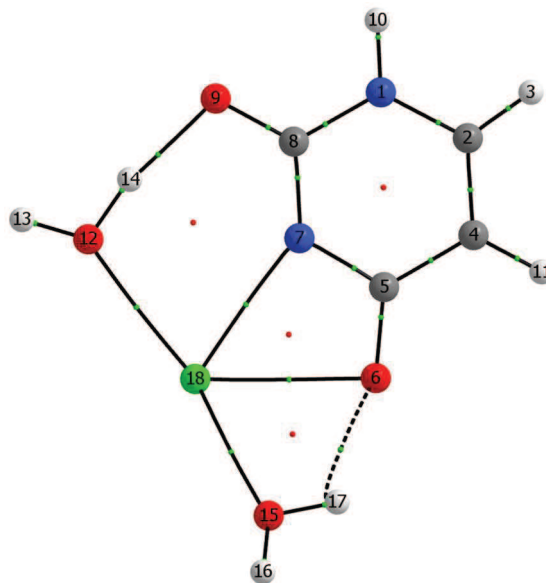
Electron densities ρ ($\text{e } \text{\AA}^{-3}$), Laplacian of the charge density $\nabla^2\rho$ ($\text{e } \text{\AA}^{-5}$) and ellipticity ε at the bond critical points, computed for geometries optimized at the B3LYP/6-31+G(d,p) level.



Bond	ρ	$\nabla^2\rho$	ε
C5 - N7	0.331	-1.137	0.087
N1 - C2	0.312	-0.767	0.028
C2 - C4	0.332	-0.969	0.322
C2 - H3	0.293	-1.129	0.020
C4 - C5	0.294	-0.797	0.168
C5 - O6	0.357	-0.300	0.029
N7 - C8	0.338	-1.210	0.142
N1 - C8	0.308	-0.996	0.123
N1 - H10	0.341	-1.853	0.038
N7 - Ba18	0.042	0.142	0.120
C8 - O9	0.388	-0.197	0.126
C4 - H11	0.286	-1.058	0.031
O9 - H14	0.054	0.139	0.038
O12 - H13	0.358	-2.076	0.019
O12 - H14	0.302	-1.664	0.020
O6 - H17	0.021	0.073	0.227
O15 - H16	0.357	-2.111	0.022
O6 - Ba18	0.036	0.129	0.053
O15 - H17	0.344	-2.065	0.022
O12 - Ba18	0.033	0.140	0.154
O15 - Ba18	0.029	0.123	0.159

M-N3O4/wbO2/wbO4 complex with Sr

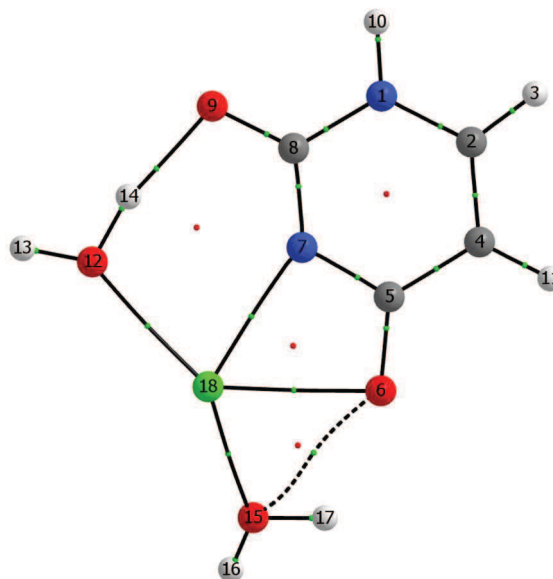
Electron densities ρ ($\text{e } \text{\AA}^{-3}$), Laplacian of the charge density $\nabla^2\rho$ ($\text{e } \text{\AA}^{-5}$) and ellipticity ε at the bond critical points, computed for geometries optimized at the B3LYP/6-31+G(d,p) level.



Bond	ρ	$\nabla^2\rho$	ε
N1 - C2	0.311	-0.769	0.027
C2 - C4	0.331	-0.965	0.321
C2 - H3	0.293	-1.132	0.020
C5 - N7	0.331	-1.132	0.083
C4 - C5	0.295	-0.800	0.168
C4 - H11	0.287	-1.061	0.030
C5 - O6	0.357	-0.309	0.030
N7 - C8	0.338	-1.210	0.140
N1 - C8	0.308	-1.000	0.124
N7 - Sr18	0.045	0.171	0.113
C8 - O9	0.389	-0.196	0.127
N1 - H10	0.341	-1.852	0.038
O9 - H14	0.052	0.133	0.038
O12 - H14	0.301	-1.658	0.020
O12 - H13	0.357	-2.086	0.019
O6 - Sr18	0.036	0.142	0.040
O6 - H17	0.017	0.063	0.423
O15 - H17	0.345	-2.084	0.022
O15 - H16	0.356	-2.120	0.023
O12 - Sr18	0.035	0.162	0.137
O15 - Sr18	0.031	0.146	0.138

M-N3O4/wbO2/wbO4 complex with Ca

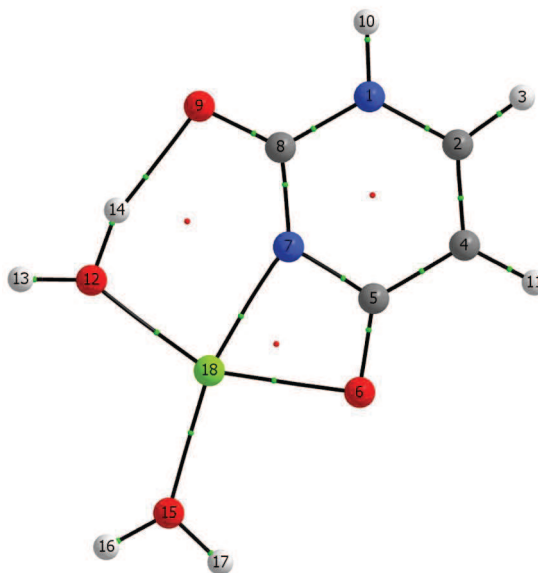
Electron densities ρ ($\text{e } \text{\AA}^{-3}$), Laplacian of the charge density $\nabla^2\rho$ ($\text{e } \text{\AA}^{-5}$) and ellipticity ε at the bond critical points, computed for geometries optimized at the B3LYP/6-31+G(d,p) level.



Bond	ρ	$\nabla^2\rho$	ε
N1 - C2	0.311	-0.830	0.041
C2 - C4	0.330	-0.944	0.323
C2 - H3	0.293	-1.131	0.021
C5 - N7	0.333	-1.152	0.091
C4 - C5	0.295	-0.793	0.172
C4 - H11	0.287	-1.061	0.032
C5 - O6	0.358	-0.415	0.033
N7 - C8	0.340	-1.214	0.144
N1 - C8	0.309	-1.017	0.134
N1 - H10	0.341	-1.855	0.039
C8 - O9	0.392	-0.307	0.131
N7 - Ca18	0.047	0.250	0.112
O9 - H14	0.048	0.122	0.038
O12 - H14	0.301	-1.675	0.020
O12 - H13	0.357	-2.096	0.019
O6 - Ca18	0.039	0.199	0.042
O6 - O15	0.013	0.051	4.668
O15 - Ca18	0.034	0.194	0.125
O15 - H17	0.347	-2.105	0.022
O15 - H16	0.356	-2.132	0.023
O12 - Ca18	0.037	0.211	0.117

M-N3O4/wbO2/w complex with Mg

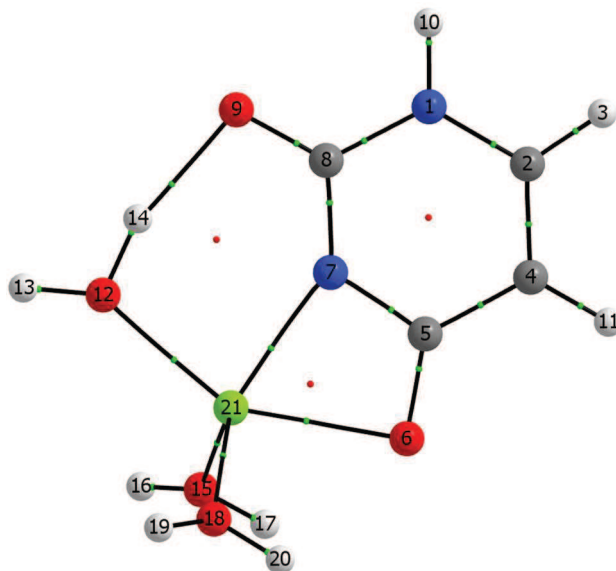
Electron densities ρ ($\text{e } \text{\AA}^{-3}$), Laplacian of the charge density $\nabla^2\rho$ ($\text{e } \text{\AA}^{-5}$) and ellipticity ε at the bond critical points, computed for geometries optimized at the B3LYP/6-31+G(d,p) level.



Bond	ρ	$\nabla^2\rho$	ε
N1 - C2	0.311	-0.836	0.039
C2 - C4	0.328	-0.932	0.320
C2 - H3	0.293	-1.138	0.020
C5 - N7	0.335	-1.152	0.085
C4 - C5	0.296	-0.800	0.175
C4 - H11	0.287	-1.069	0.033
C5 - O6	0.356	-0.449	0.032
N7 - C8	0.339	-1.205	0.142
N1 - C8	0.308	-1.020	0.137
N1 - H10	0.341	-1.855	0.038
C8 - O9	0.396	-0.298	0.137
N7 - Mg18	0.051	0.367	0.053
O12 - Mg18	0.038	0.292	0.059
O9 - H14	0.036	0.089	0.035
O12 - H13	0.356	-2.124	0.021
O12 - H14	0.308	-1.774	0.021
O6 - Mg18	0.040	0.261	0.015
O15 - Mg18	0.040	0.313	0.100
O15 - H16	0.352	-2.151	0.023
O15 - H17	0.349	-2.138	0.023

M-N3O4/2wbO4/wbO2 complex with Mg

Electron densities ρ ($\text{e } \text{\AA}^{-3}$), Laplacian of the charge density $\nabla^2\rho$ ($\text{e } \text{\AA}^{-5}$) and ellipticity ε at the bond critical points, computed for geometries optimized at the B3LYP/6-31+G(d,p) level.



Bond	ρ	$\nabla^2\rho$	ε
N1 - C2	0.311	-0.836	0.043
C2 - C4	0.329	-0.938	0.325
C2 - H3	0.293	-1.131	0.021
C5 - N7	0.334	-1.151	0.089
C4 - C5	0.294	-0.789	0.170
C4 - H11	0.287	-1.061	0.033
C5 - O6	0.360	-0.423	0.039
N7 - C8	0.340	-1.217	0.147
N1 - C8	0.308	-1.016	0.136
N1 - H10	0.341	-1.855	0.039
C8 - O9	0.394	-0.314	0.134
N7 - Mg21	0.048	0.339	0.032
O12 - Mg21	0.035	0.259	0.037
O9 - H14	0.039	0.100	0.038
O12 - H14	0.308	-1.765	0.021
O12 - H13	0.358	-2.115	0.022
O15 - H16	0.355	-2.146	0.024
O15 - Mg21	0.036	0.275	0.080
O15 - H17	0.352	-2.136	0.024
O6 - Mg21	0.033	0.201	0.086
O18 - Mg21	0.036	0.275	0.080
O18 - H19	0.355	-2.146	0.024
O18 - H20	0.352	-2.136	0.024

Table B1. Comparison of relative enthalpies and Gibbs energies in kJ mol⁻¹ at 298K for [M(Ura-H)(H₂O)]⁺ for both computational methods.

M	Isomer	Method 1		Method 2	
		$\Delta_{\text{rel}}\text{H}$	$\Delta_{\text{rel}}\text{G}$	$\Delta_{\text{rel}}\text{H}$	$\Delta_{\text{rel}}\text{G}$
Ba ²⁺	N3O4/wbO2	0.0	0.0	0.0	0.0
	N3O2/wbO4	4.5	4.7	5.6	5.8
	N3O4/wbO4	38.3	34.8	39.6	34.4
	N1O2/wbO2	67.1	63.3	64.5	57.9
	N3O4(hO2)/wbO4	70.9	68.5	69.8	65.0
	N1O2(hO4)/wbO2	82.2	79.7	73.7	68.2
	N3O4/wN1bO2	99.2	93.6	89.7	83.3
Sr ²⁺	N3O4/wbO2	0.0	0.0	0.0	0.0
	N3O2/wbO4	5.9	6.1	6.1	6.3
	N3O4/wbO4	40.3	35.4	39.3	33.0
	N1O2/wbO2	68.5	63.3	63.9	56.5
	N3O4(hO2)/wbO4	72.2	68.3	69.2	63.5
	N1O2(hO4)/wbO2	82.1	78.6	72.9	67.7
	N3O4/wN1bO2	111.1	104.7	102.4	95.0
Ca ²⁺	N3O4/wbO2	0.0	0.0	0.0	0.0
	N3O2/wbO4	7.1	7.1	6.9	7.1
	N3O4/wbO4	38.3	25.5	35.1	23.6
	N1O2/w	62.7	48.5	58.6	48.0
	N3O4(hO2)/wbO4	67.9	57.0	64.7	55.0
	N1O2(hO4)/wbO2	69.9	61.5	67.4	60.1
	N3O4/wN1bO2	113.6	106.4	110.8	102.5
Mg ²⁺	N3O4/wbO2	0.0	5.8	0.0	5.6
	N3O4/w	1.3	0.0	1.2	0.0
	N3O2/wbO4	12.9	17.0	13.1	16.7
	N1O2/w	29.9	28.3	30.1	28.4
	N3O4(hO2)/w	33.6	32.7	33.5	32.3
	N1O2(hO4)/w	36.1	35.2	36.3	35.2
	N3O4/wN1bO2	141.7	137.8	142.1	138.3

Table B2. Comparison of relative enthalpies and Gibbs energies in kJ mol⁻¹ at 298K for [M(Ura-H)(H₂O)₂]⁺ for both computational methods.

M	Isomer	Method 1		Method 2	
		Δ_{relH}	Δ_{relG}	Δ_{relH}	Δ_{relG}
Ba ²⁺	N3O4/wbO2/wbO4	0.0	0.0	0.0	0.0
	N3O2/wbO4/wbO2	6.3	6.3	7.0	7.0
	N3O4/wbO2/wbw	9.2	9.2	6.4	6.6
	N3O2/wbO4/wbw	11.9	12.7	10.3	11.2
	N3O4/wbO2/ww	53.5	44.4	41.3	34.2
	N3O4/wbO2/wN1bO2	56.4	54.3	45.6	43.6
	N1O2/wbO2/w	73.1	59.1	67.1	52.5
Sr ²⁺	N3O4/wbO2/wbO4	0.0	0.0	0.0	0.0
	N3O2/wbO4/wbO2	6.7	6.6	7.1	7.2
	N3O2/wbO4/wbw	13.5	12.2	Optimizes to N3O2/wbO4/wbO2	
	N3O4/wbO2/ww	60.6	53.3	51.6	45.5
	N3O4/wbO2/wN1bO2	66.7	64.6	58.3	55.6
	N1O2/wbO2/w	69.5	56.0	64.9	50.7
	N3O4/wbO2/w	0.0	0.0	0.0	0.0
Ca ²⁺	N3O2/wbO4/wbO2	7.8	7.4	7.5	7.2
	N3O2/wbO4/w	9.6	3.5	14.6	9.2
	N3O4/wbO2/ww	60.4	56.2	60.1	55.9
	N1O2/wbO2/w	61.3	48.5	58.9	45.4
	N3O4/wbO2/wN1bO2	70.3	69.5	69.5	65.2
	MgN3O4/wbO2/w	0.0	0.0	0.0	0.0
Mg ²⁺	MgN3O2/wbO4/w	10.3	9.8	10.4	10.2
	MgN1O2/w/w	45.2	38.4	46.4	40.3
	MgN3O4/w/ww	72.4	62.9	72.6	63.2
	MgN3O4/wbO2/wN1	110.5	102.2	111.0	102.8

Table B3. Comparison of relative enthalpies and Gibbs energies in kJ mol⁻¹ at 298K for [Mg(Ura-H)(H₂O)₃]⁺ for both computational methods.

Isomer	Method 1		Method 2	
	Δ_{relH}	Δ_{relG}	Δ_{relH}	Δ_{relG}
N3O4/2wbO4/wbO2	0.0	0.0	0.0	0.0
N3O2/wbO4/2wbO2	8.9	10.5	9.0	9.9
N3O4/wbO2/wbwbO4	36.5	44.4	35.2	42.8
N3O4/wbO2/wbw	44.2	45.0	42.8	43.5
N3O2/wbO4/wbwbO2	49.1	56.1	47.9	54.9

APPENDIX C – Chapter 4 Supplemental Information

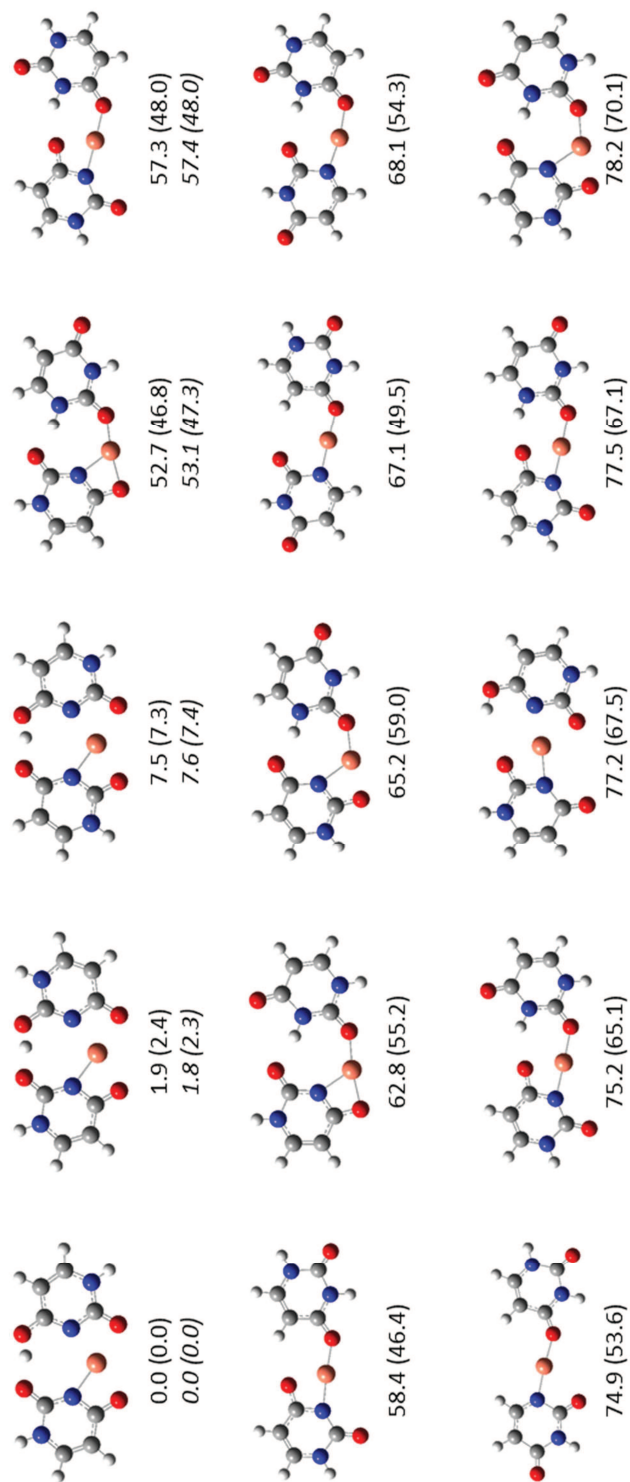


Figure C1a. All structures found using calculation method 1 for $[\text{Cu}(\text{Ura-H})(\text{Ura})]^+$. The calculated relative enthalpies and Gibbs energies (parenthesis) are also shown in $\text{kJ}\cdot\text{mol}^{-1}$ at 298 K, with a comparison to method 2 (italics) for the five lowest energy isomers.

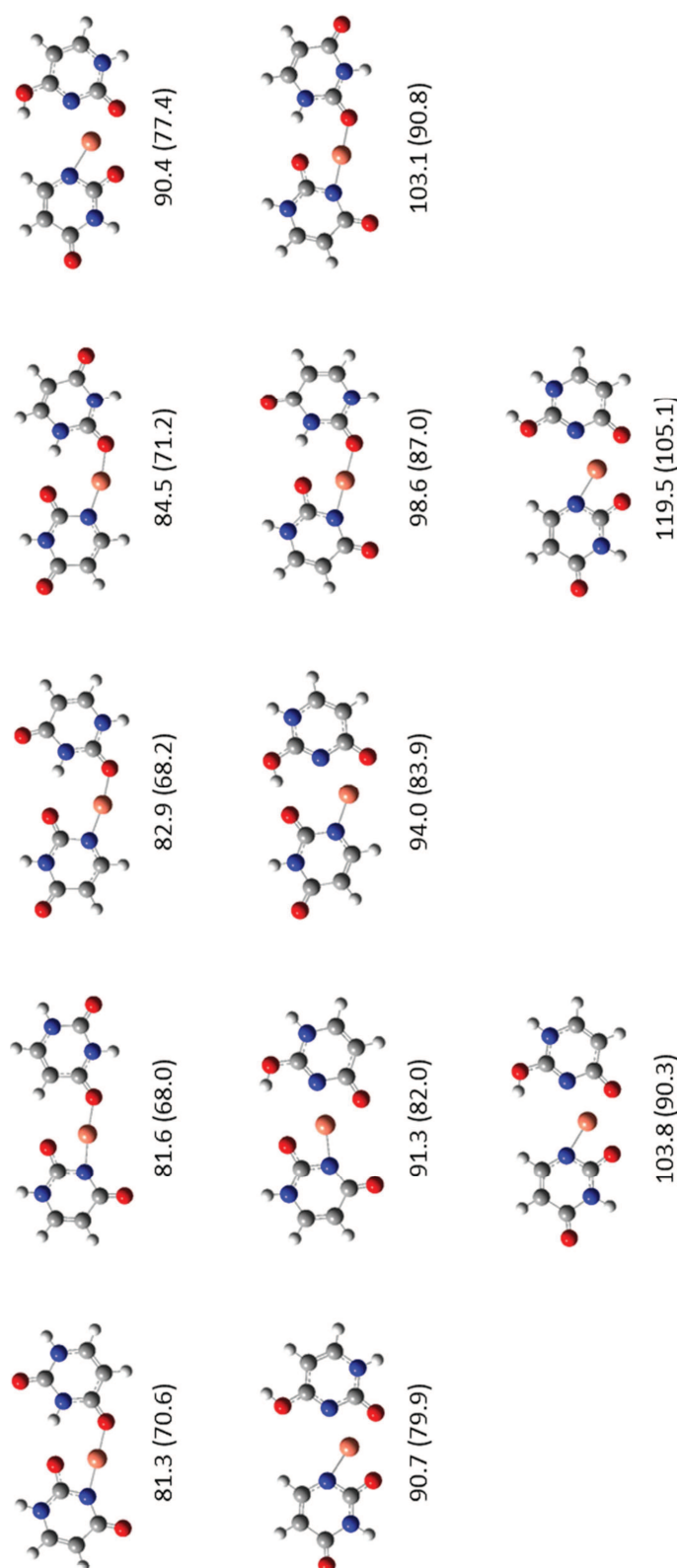


Figure C1b. All structures found using calculation method 1 for $[\text{Cu}(\text{Ura-H})(\text{Ura})]^+$. The calculated relative enthalpies and Gibbs energies (parenthesis) are also shown in $\text{kJ}\cdot\text{mol}^{-1}$ at 298 K.

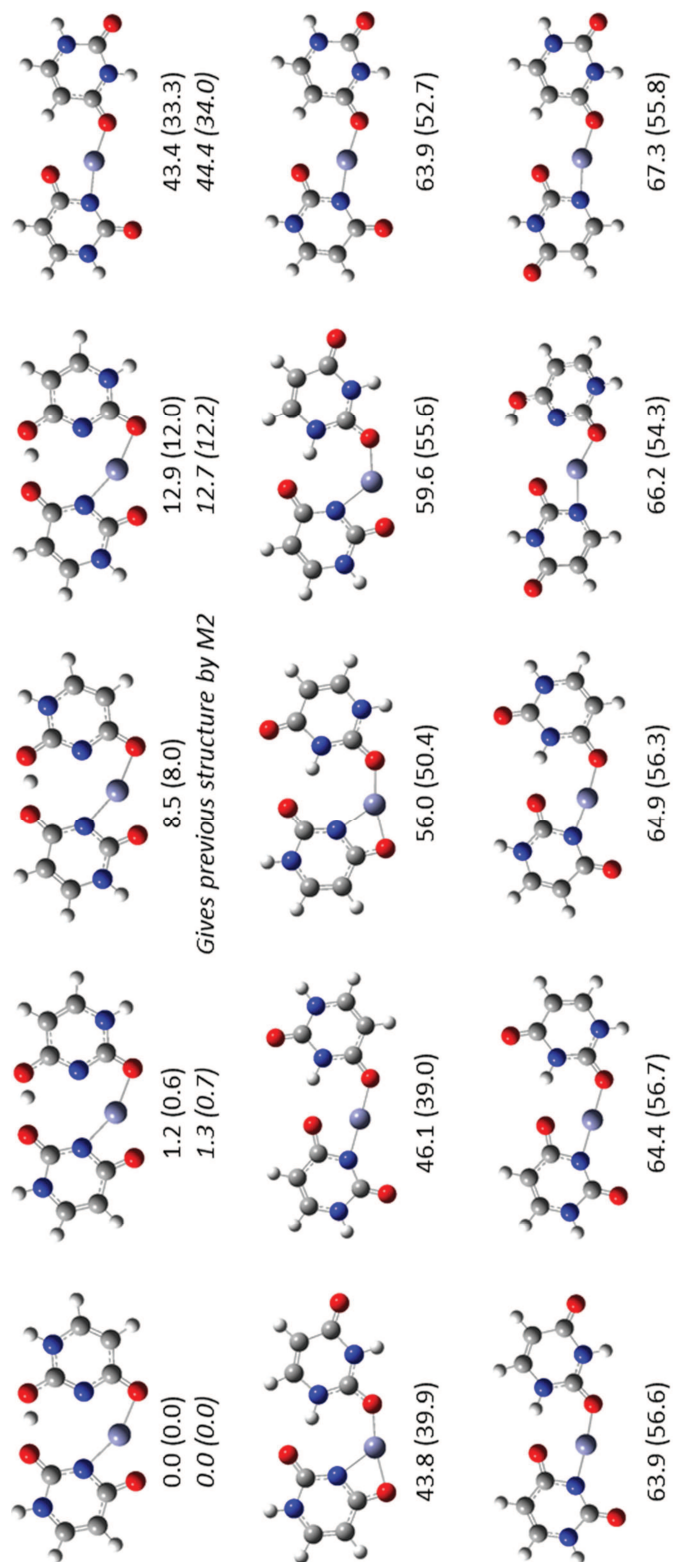


Figure C2a. All structures found using calculation method 1 for $[\text{Zn}(\text{Ura-H})(\text{Ura})]^+$. The calculated relative enthalpies and Gibbs energies (parenthesis) are also shown in $\text{kJ}\cdot\text{mol}^{-1}$ at 298 K, with a comparison to method 2 (*italics*) for the five lowest energy isomers.

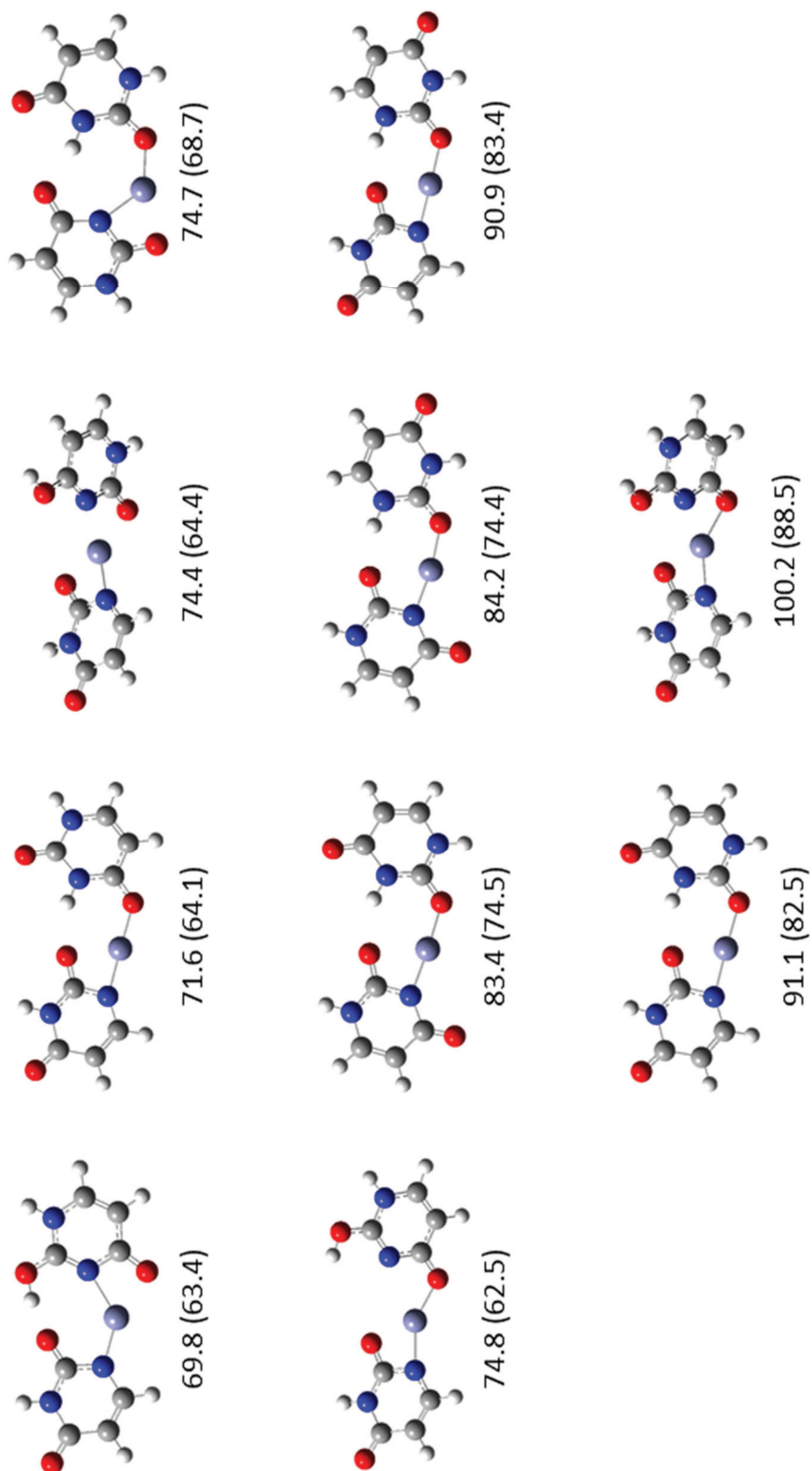


Figure C2b. All structures found using calculation method 1 for $[\text{Zn}(\text{Ura-H})(\text{Ura})]^+$. The calculated relative enthalpies and Gibbs energies (parenthesis) are also shown in $\text{kJ}\cdot\text{mol}^{-1}$ at 298 K.

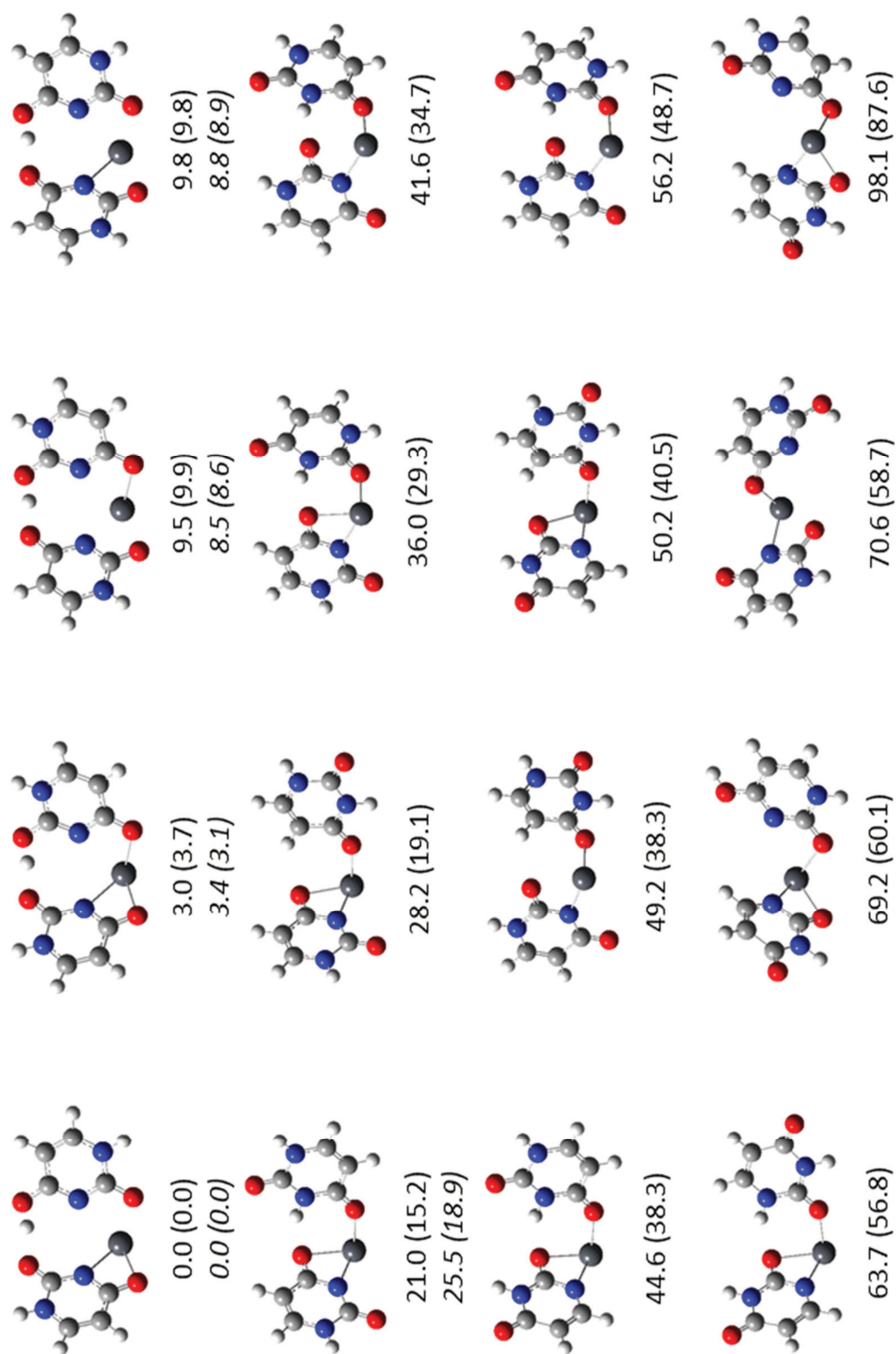


Figure C3. All structures found using calculation method 1 for $[\text{Pb}(\text{Ura-H})(\text{Ura})]^+$. The calculated relative enthalpies and Gibbs energies (parenthesis) are also shown in $\text{kJ}\cdot\text{mol}^{-1}$ at 298 K, with a comparison to method 2 (*italics*) for the five lowest energy isomers.

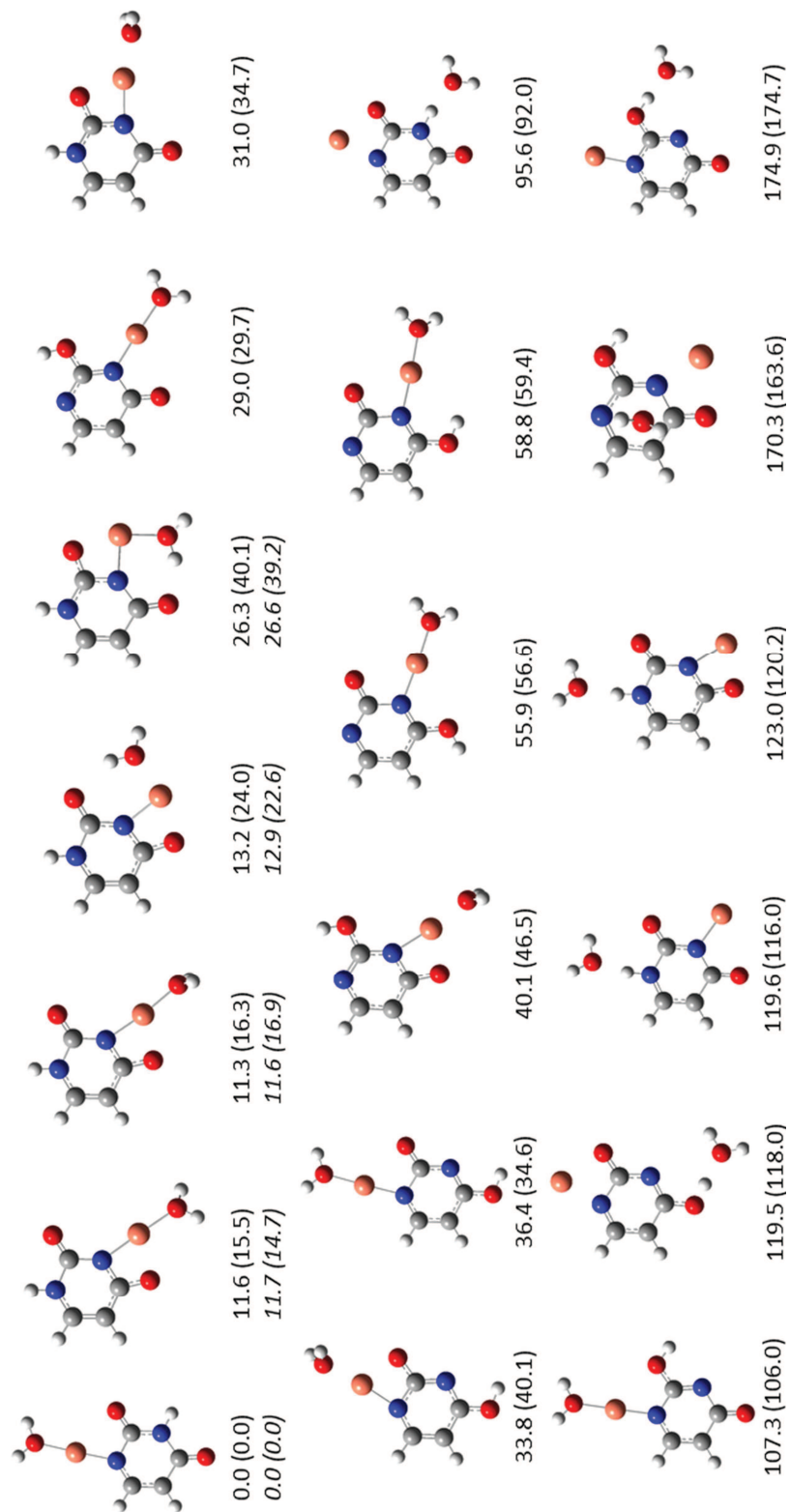


Figure C4. All structures found using calculation method 1 for $[\text{Cu}(\text{Ura-H})(\text{H}_2\text{O})]^+$. The calculated relative enthalpies and Gibbs energies (parenthesis) are also shown in $\text{kJ}\cdot\text{mol}^{-1}$ at 298 K, with a comparison to method 2 (italics) for the five lowest energy isomers.

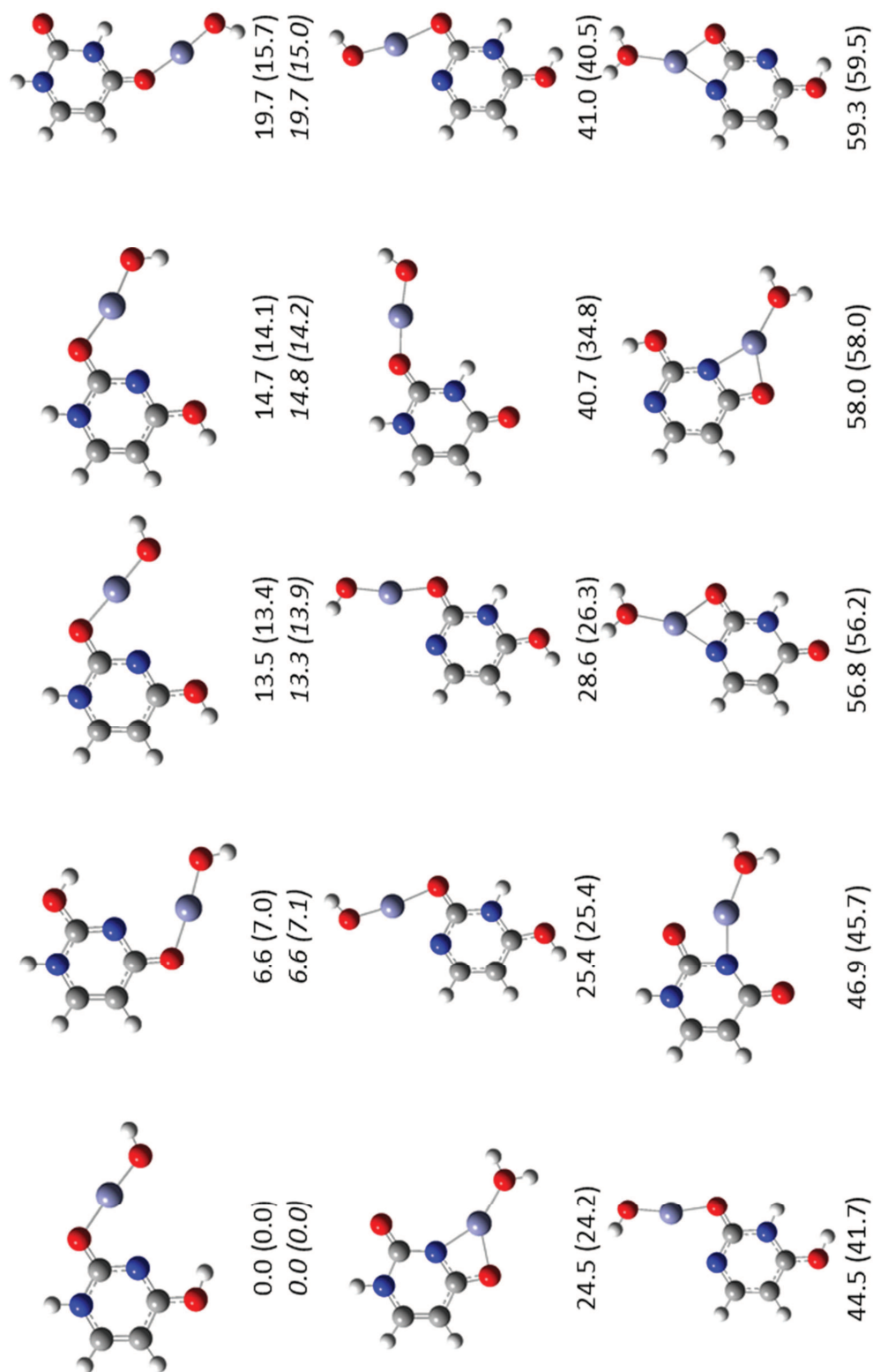


Figure C5a. All structures found using calculation method 1 for $[\text{Zn}(\text{Ura-H})(\text{H}_2\text{O})]^+$. The calculated relative enthalpies and Gibbs energies (parenthesis) are also shown in $\text{kJ}\cdot\text{mol}^{-1}$ at 298 K, with a comparison to method 2 (*italics*) for the five lowest energy isomers.

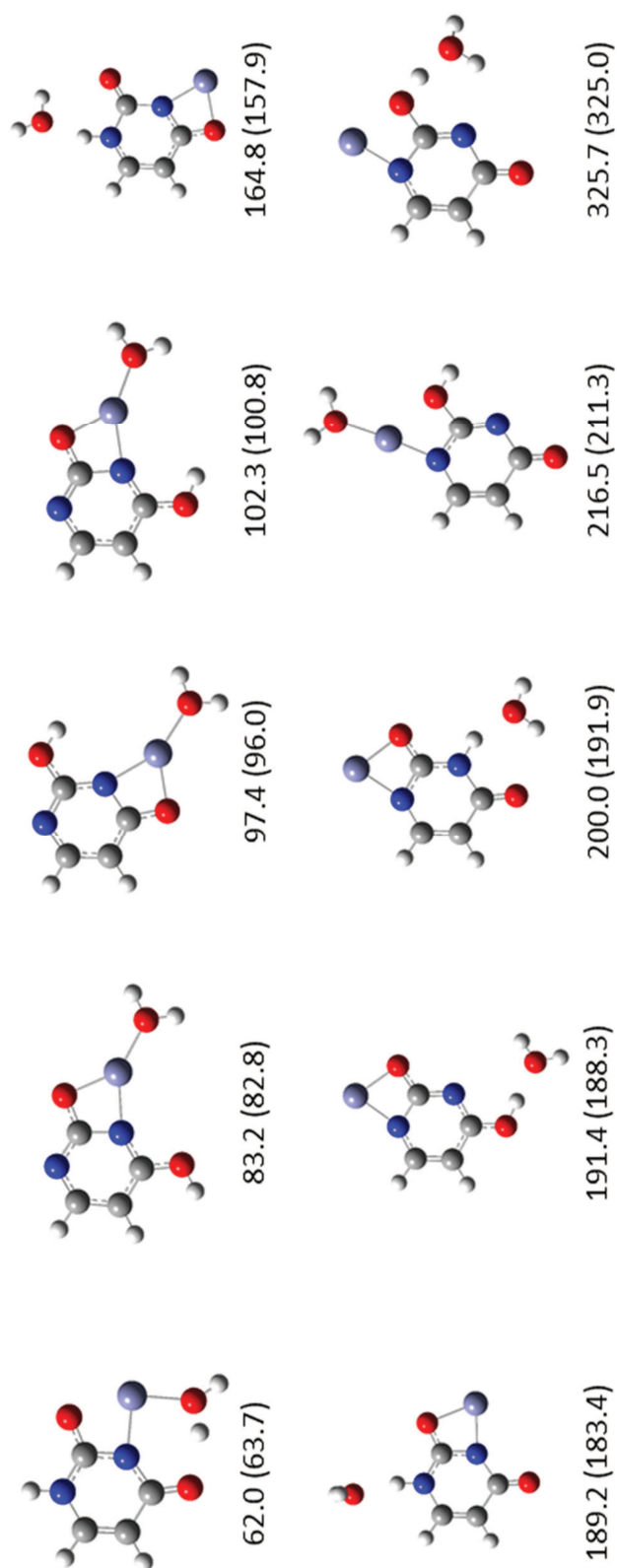


Figure C5b. All structures found using calculation method 1 for $[\text{Zn}(\text{Ura-H})(\text{H}_2\text{O})]^+$. The calculated relative enthalpies and Gibbs energies (parenthesis) are also shown in $\text{kJ}\cdot\text{mol}^{-1}$ at 298 K.

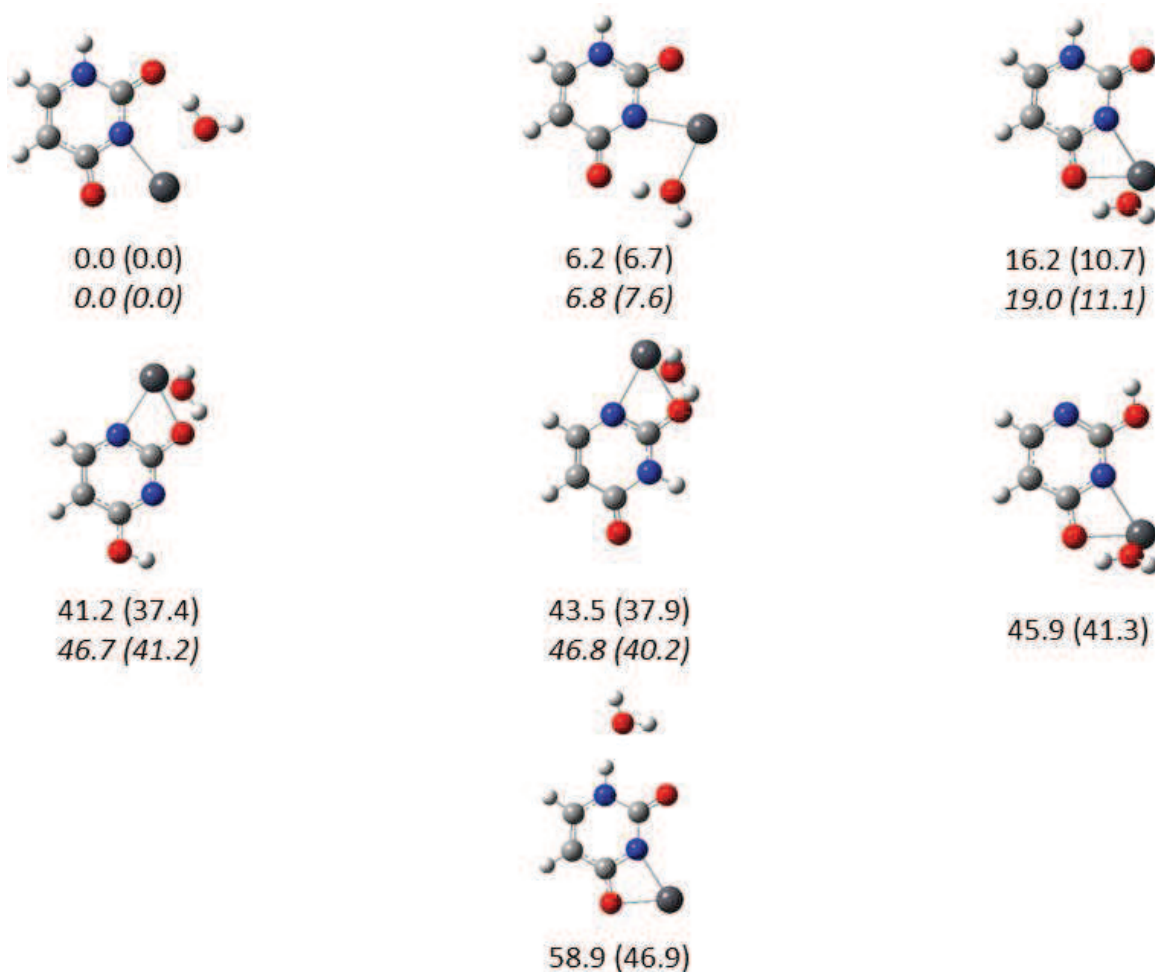


Figure C6. All structures found using calculation method 1 for $[\text{Pb}(\text{Ura-H})(\text{H}_2\text{O})]^+$. The calculated relative enthalpies and Gibbs energies (parenthesis) are also shown in $\text{kJ}\cdot\text{mol}^{-1}$ at 298 K, with a comparison to method 2 (*italics*) for the five lowest energy isomers.

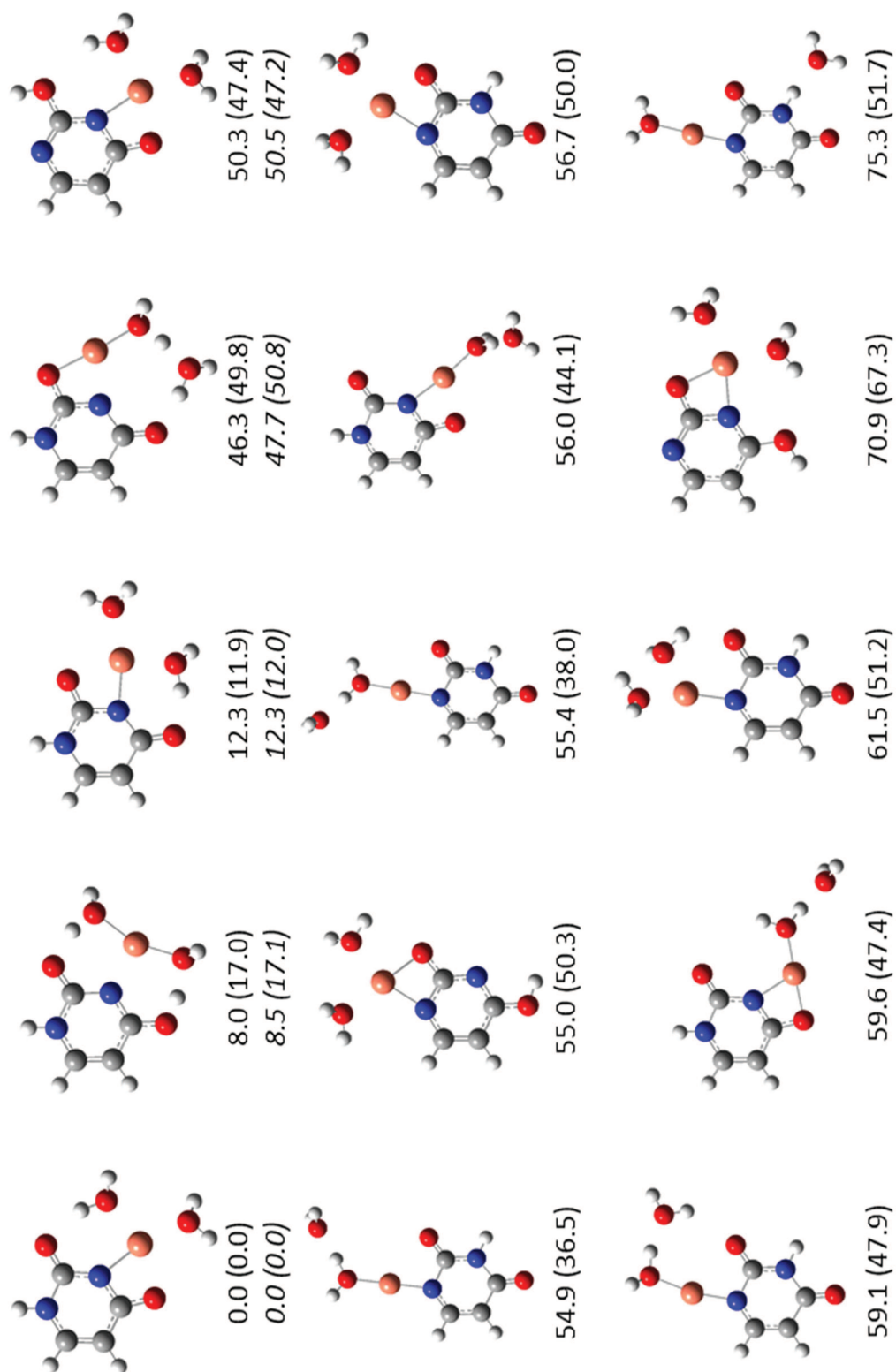


Figure C7a. All structures found using calculation method 1 for $[\text{Cu}(\text{Ura-H})(\text{H}_2\text{O})_2]^+$. The calculated relative enthalpies and Gibbs energies (parenthesis) are also shown in $\text{kJ}\cdot\text{mol}^{-1}$ at 298 K, with a comparison to method 2 (*italics*) for the five lowest energy isomers.

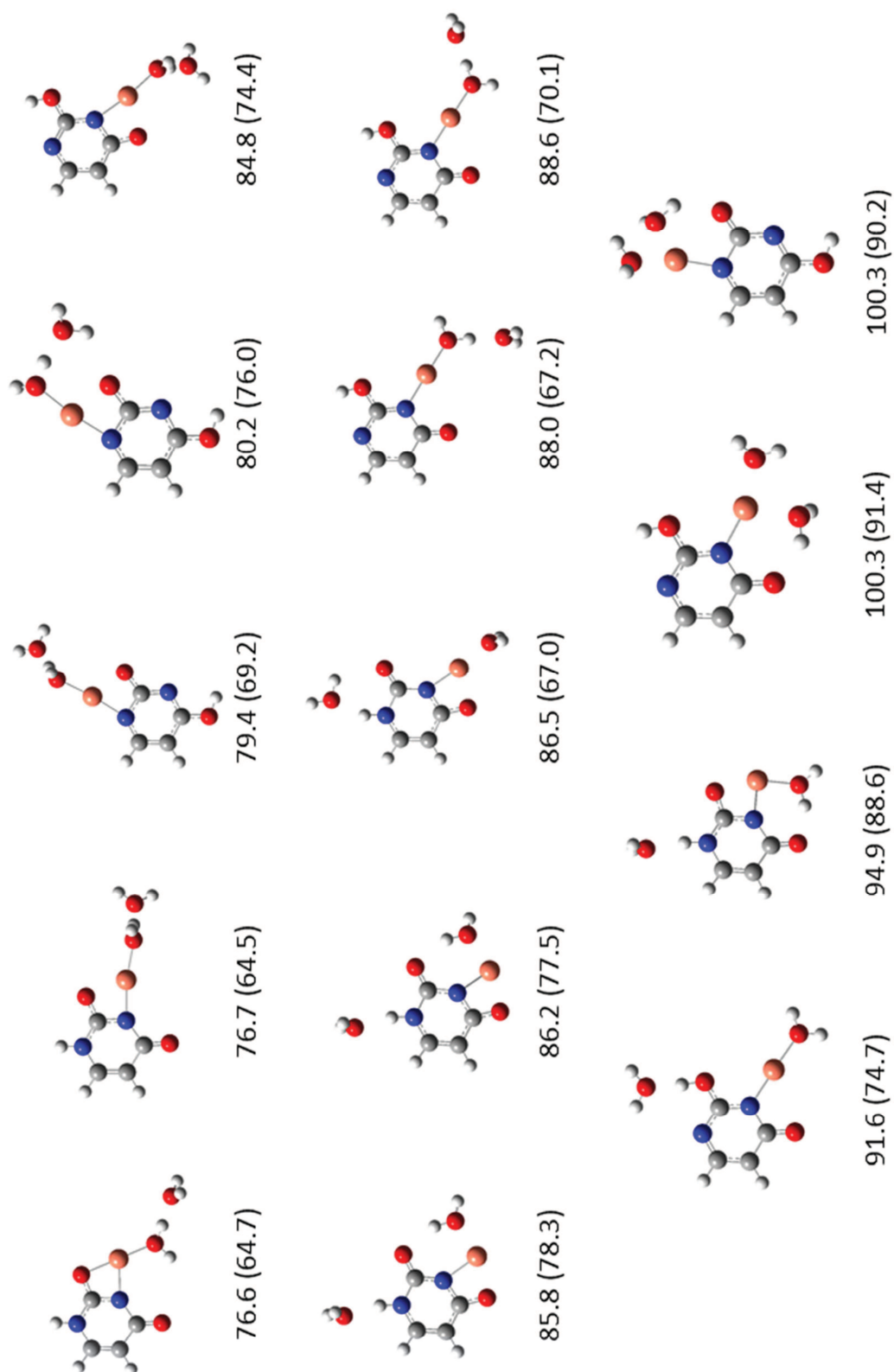


Figure C7b. All structures found using calculation method 1 for $[\text{Cu}(\text{Ura-H})(\text{H}_2\text{O})_2]^+$. The calculated relative enthalpies and Gibbs energies (parenthesis) are also shown in $\text{kJ}\cdot\text{mol}^{-1}$ at 298 K.

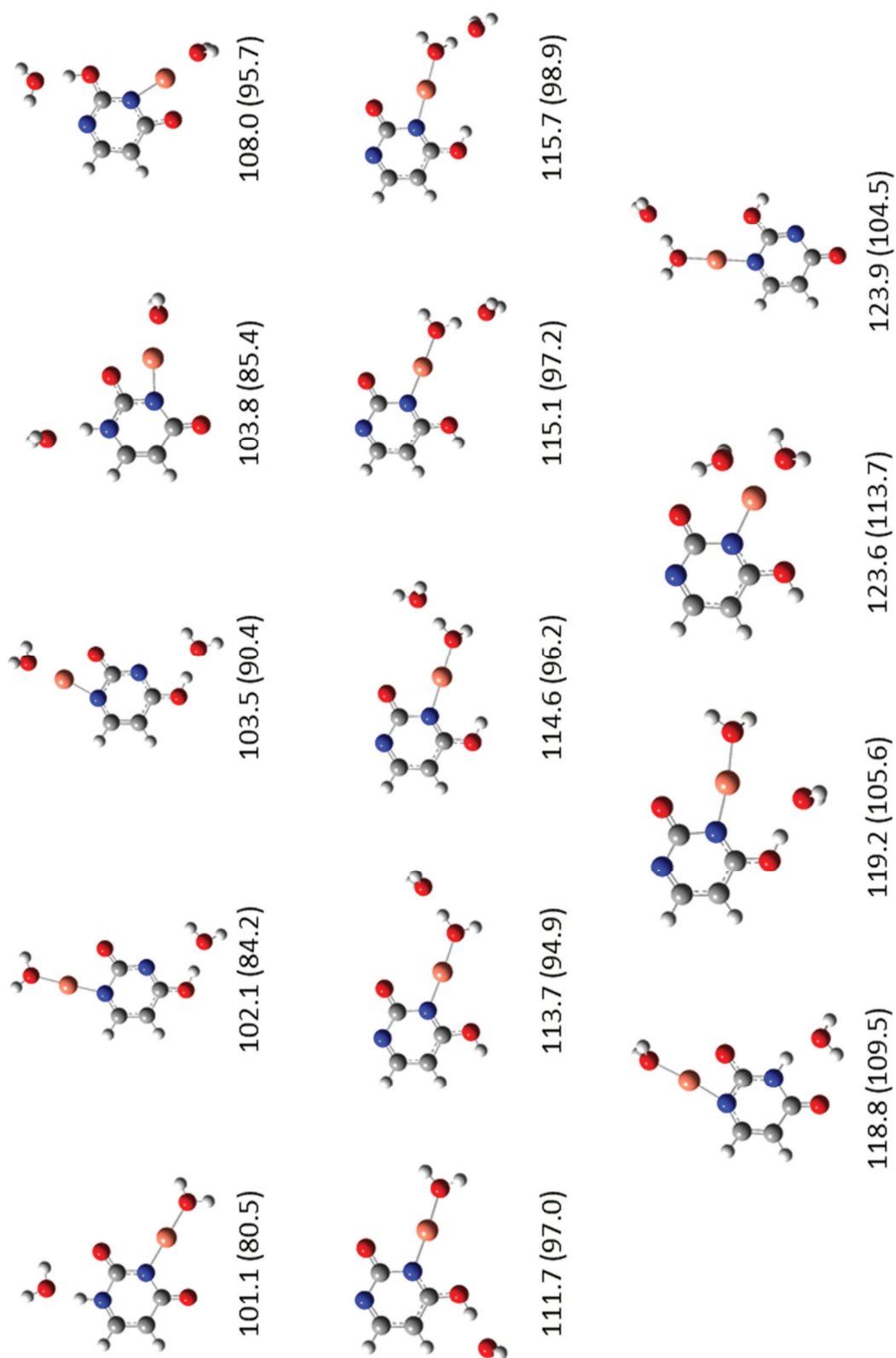


Figure C7c. All structures found using calculation method 1 for $[\text{Cu}(\text{Ura-H})(\text{H}_2\text{O})_2]^+$. The calculated relative enthalpies and Gibbs energies (parenthesis) are also shown in $\text{kJ}\cdot\text{mol}^{-1}$ at 298 K.

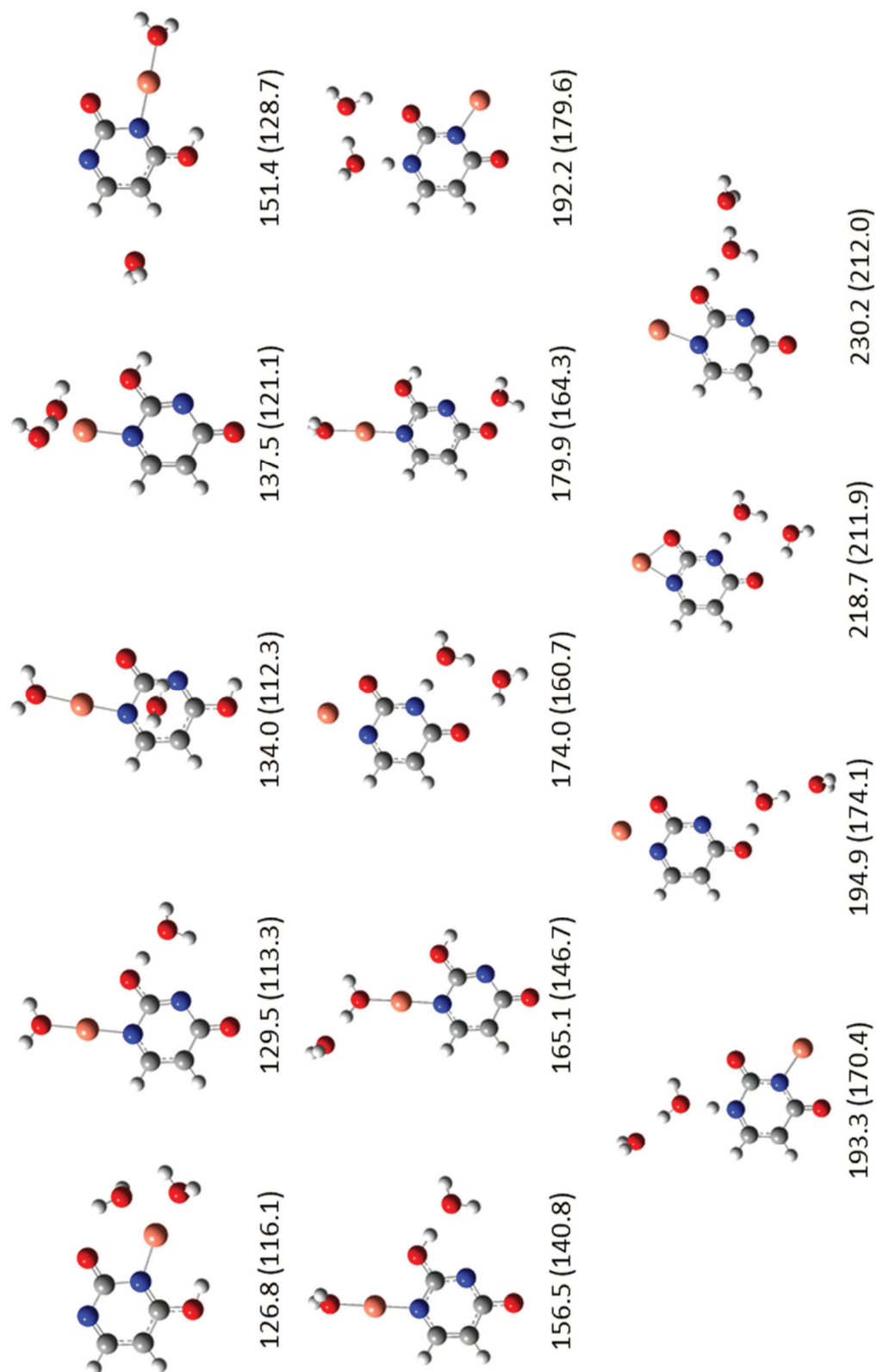


Figure C7d. All structures found using calculation method 1 for $[\text{Cu}(\text{Ura-H})(\text{H}_2\text{O})_2]^+$. The calculated relative enthalpies and Gibbs energies (parenthesis) are also shown in $\text{kJ}\cdot\text{mol}^{-1}$ at 298 K.

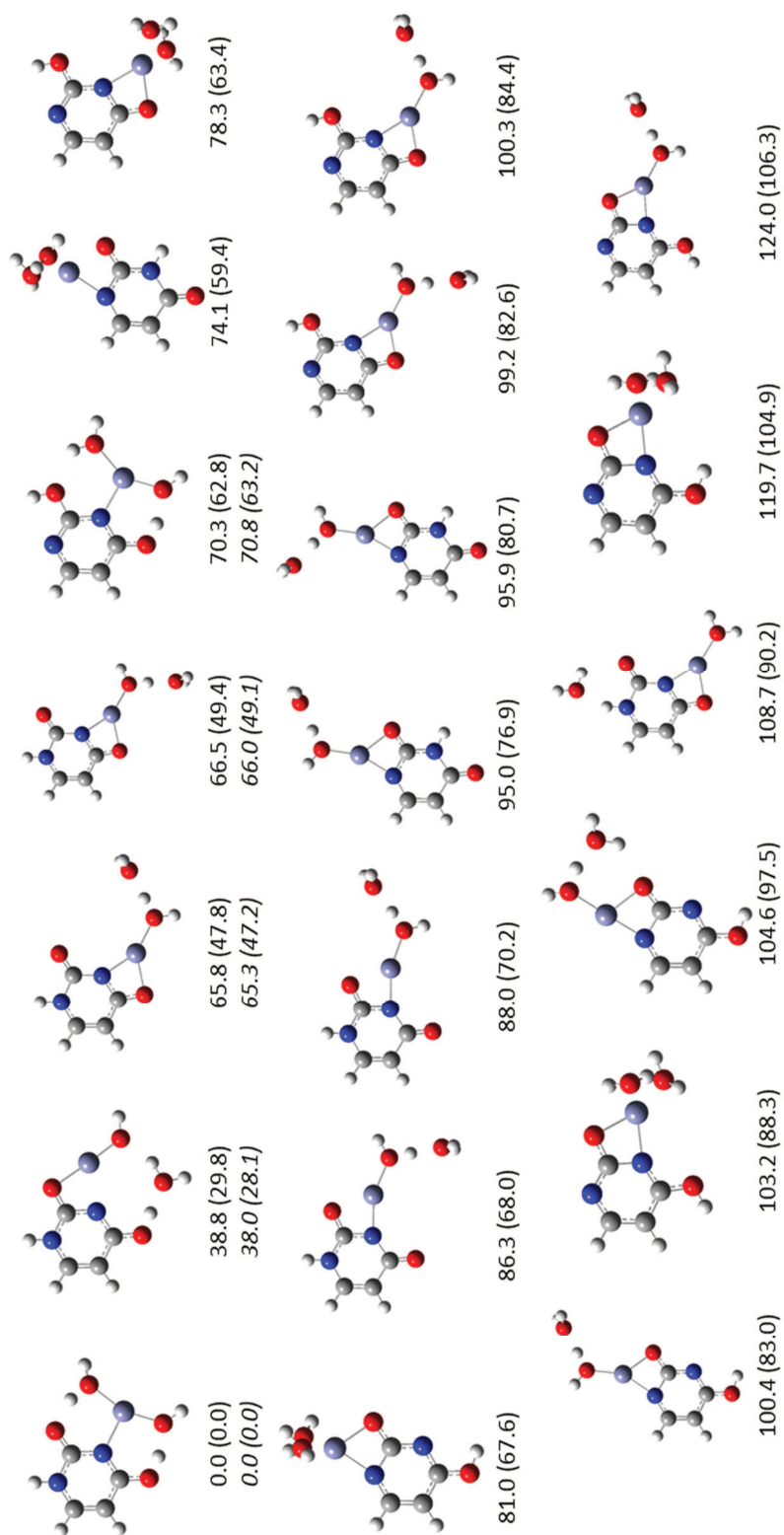


Figure C8a. All structures found using calculation method 1 for $[\text{Zn}(\text{Ura-H})(\text{H}_2\text{O})_2]^+$. The calculated relative enthalpies and Gibbs energies (parenthesis) are also shown in $\text{kJ}\cdot\text{mol}^{-1}$ at 298 K, with a comparison to method 2 (*italics*) for the five lowest energy isomers.

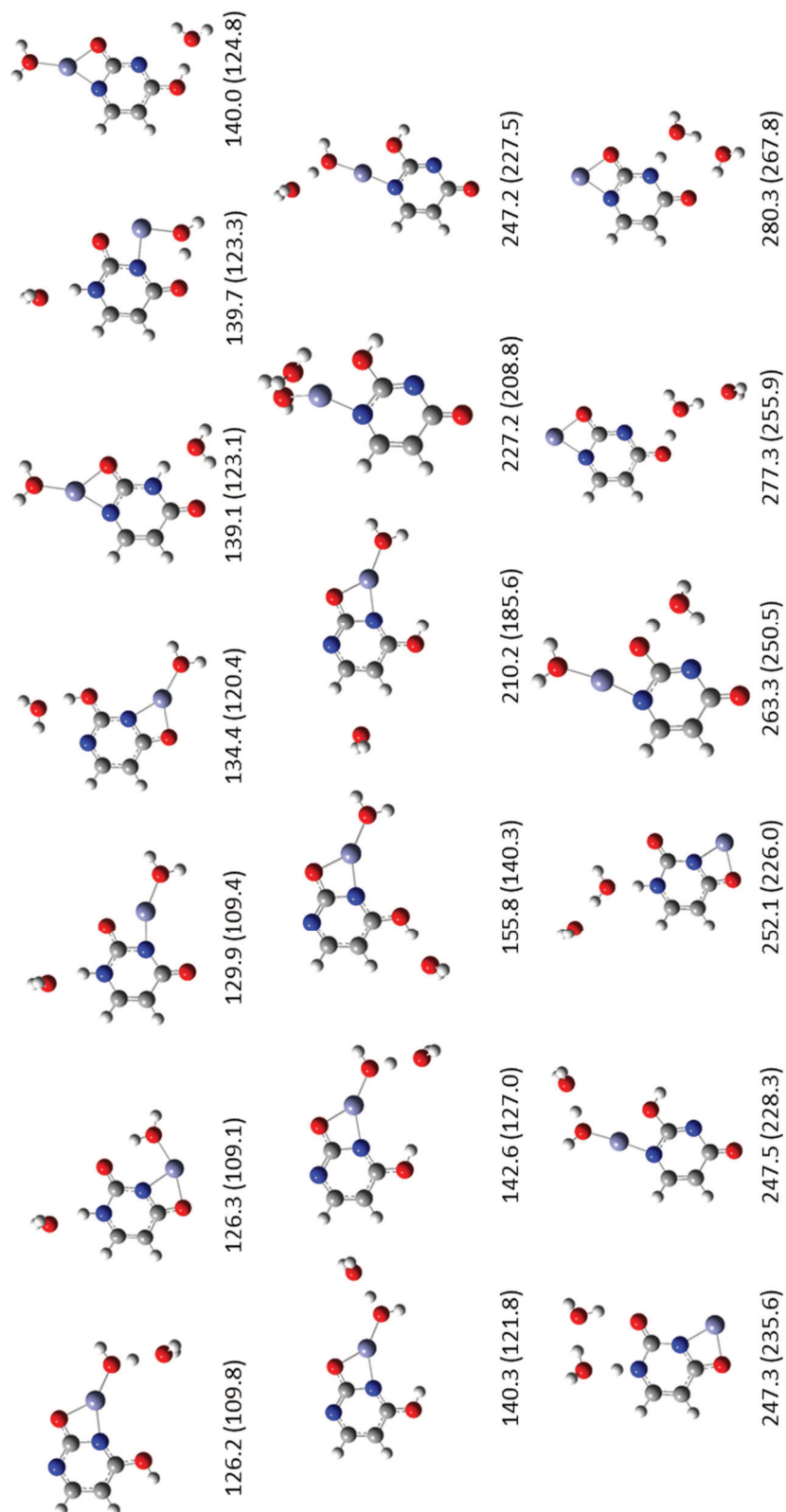


Figure C8b. All structures found using calculation method 1 for $[\text{Zn}(\text{Ura-H})(\text{H}_2\text{O})_2]^+$. The calculated relative enthalpies and Gibbs energies (parenthesis) are also shown in $\text{kJ}\cdot\text{mol}^{-1}$ at 298 K.

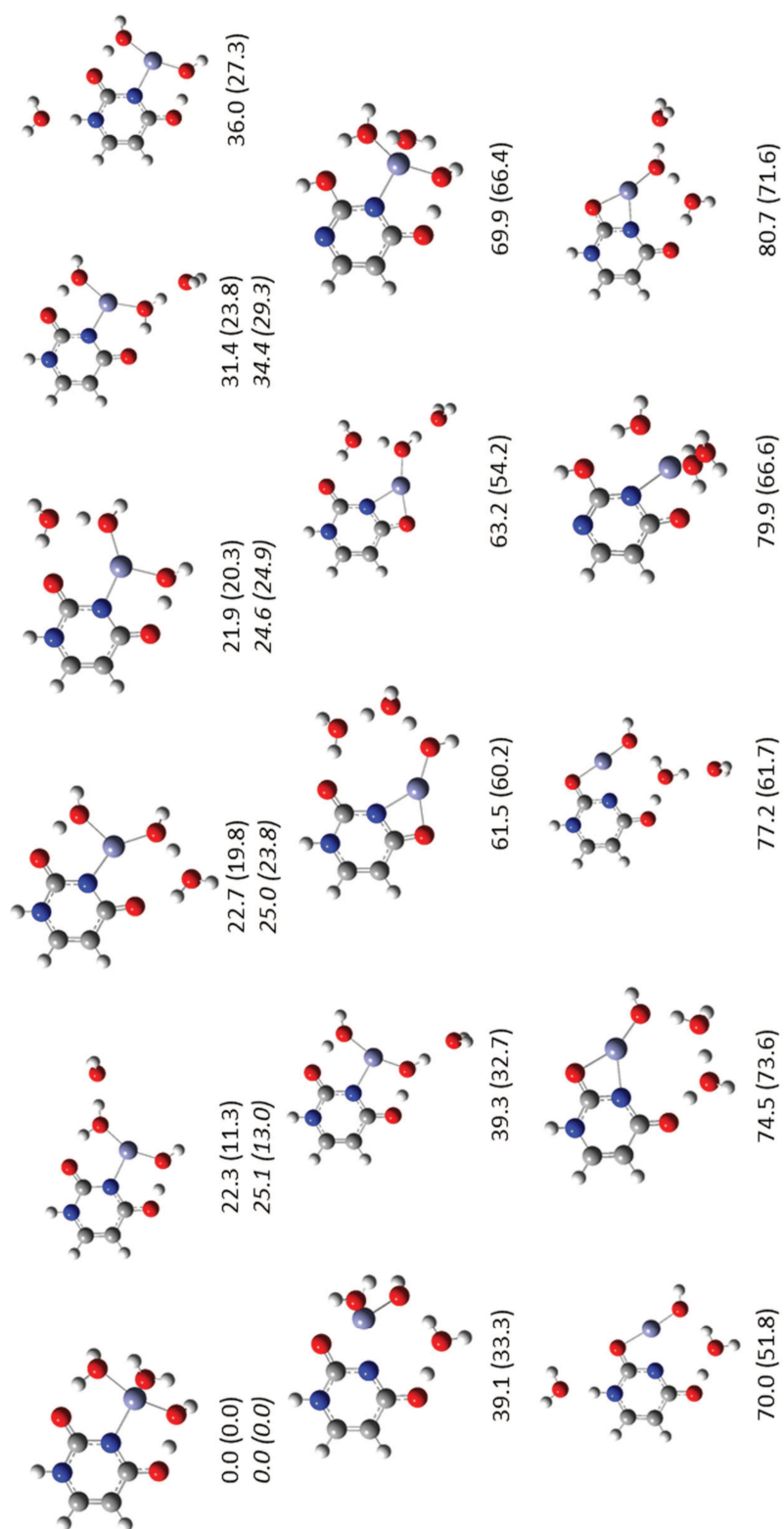


Figure C9a. All structures found using calculation method 1 for $[\text{Zn}(\text{Ura-H})(\text{H}_2\text{O})_3]^+$. The calculated relative enthalpies and Gibbs energies (parenthesis) are also shown in $\text{kJ}\cdot\text{mol}^{-1}$ at 298 K, with a comparison to method 2 (*italics*) for the five lowest energy isomers.

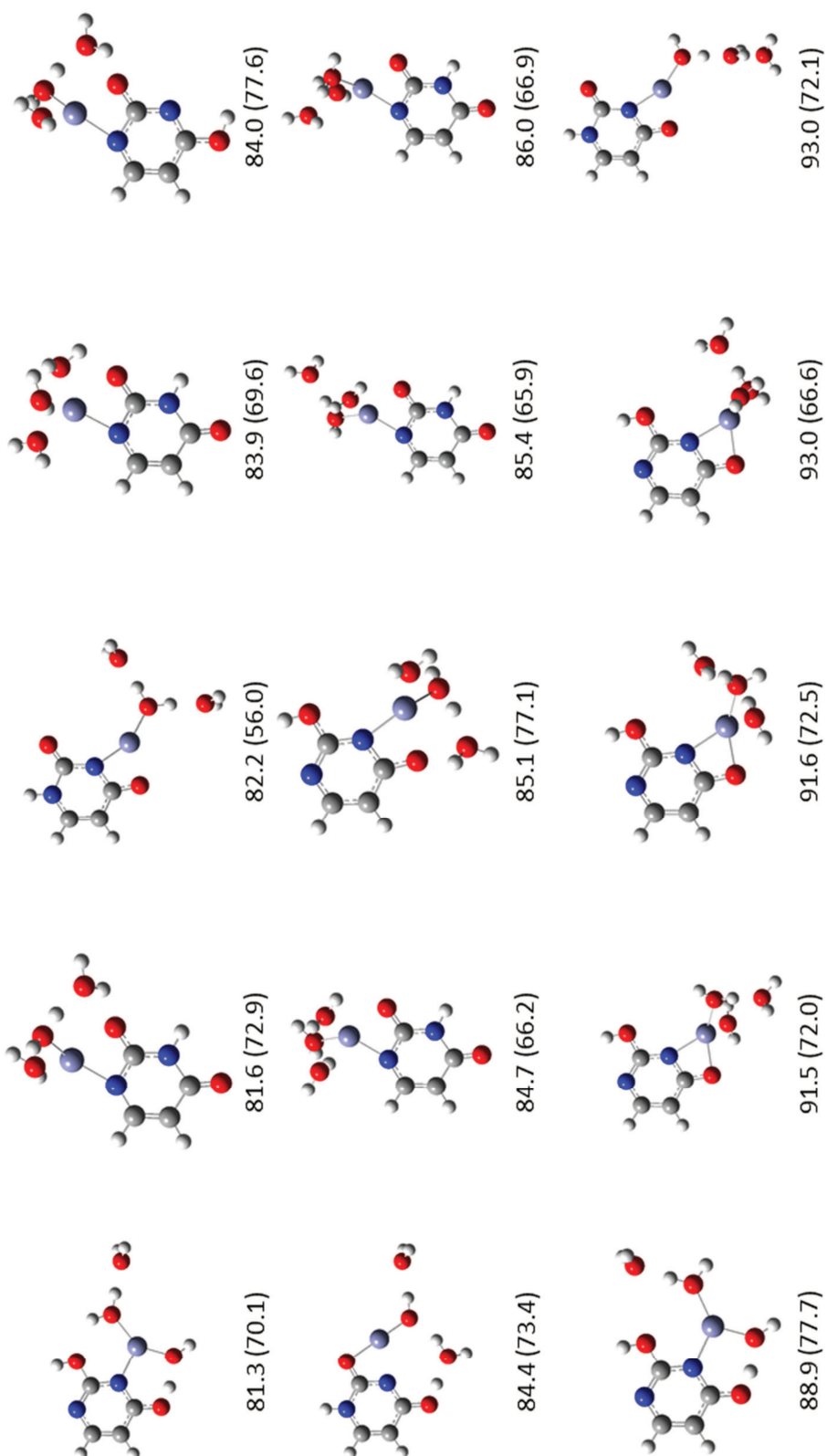


Figure C9b. All structures found using calculation method 1 for $[\text{Zn}(\text{Ura-H})(\text{H}_2\text{O})_3]^+$. The calculated relative enthalpies and Gibbs energies (parenthesis) are also shown in $\text{kJ}\cdot\text{mol}^{-1}$ at 298 K.

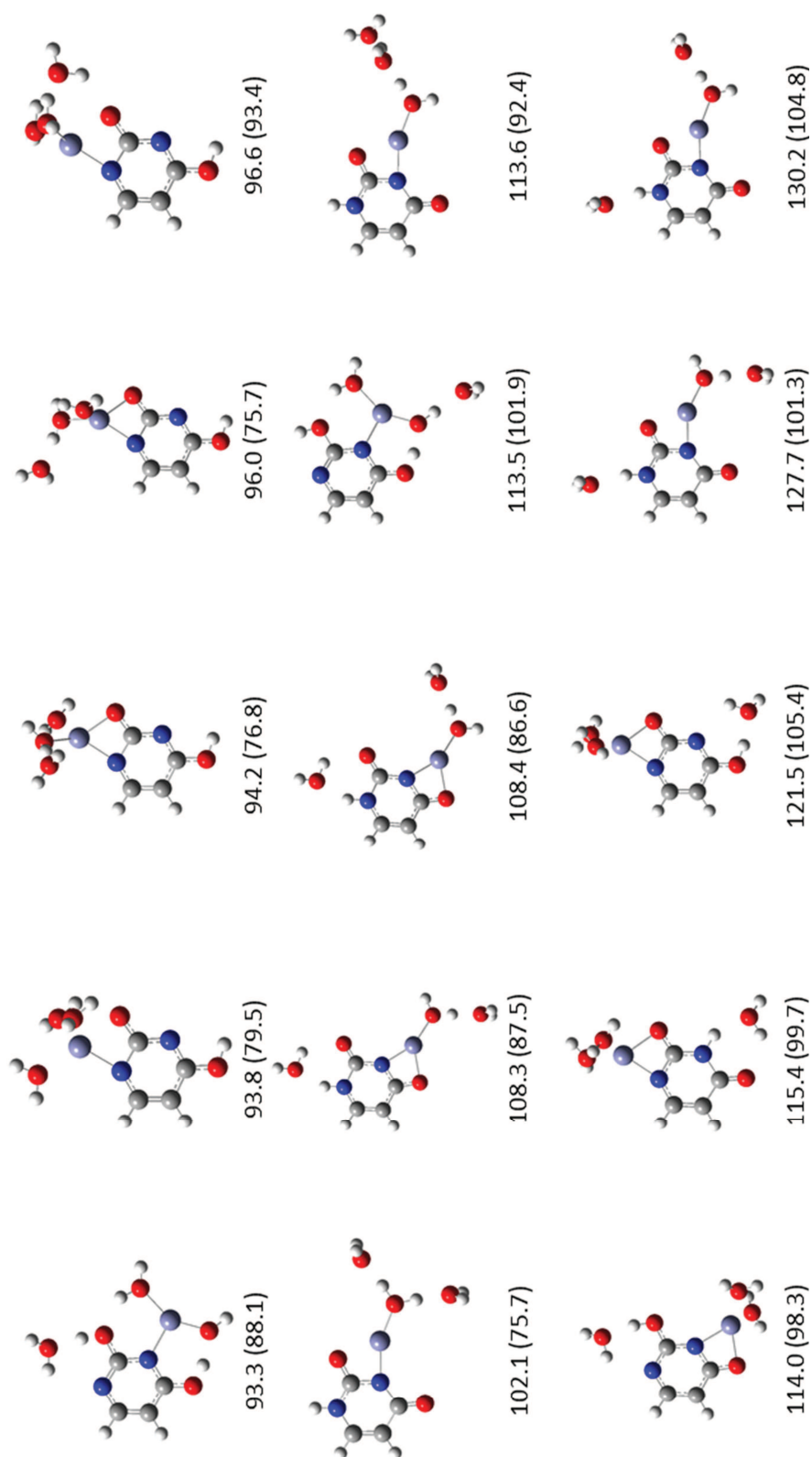


Figure C9c. All structures found using calculation method 1 for $[\text{Zn}(\text{Ura-H})(\text{H}_2\text{O})_3]^+$. The calculated relative enthalpies and Gibbs energies (parenthesis) are also shown in $\text{kJ}\cdot\text{mol}^{-1}$ at 298 K.

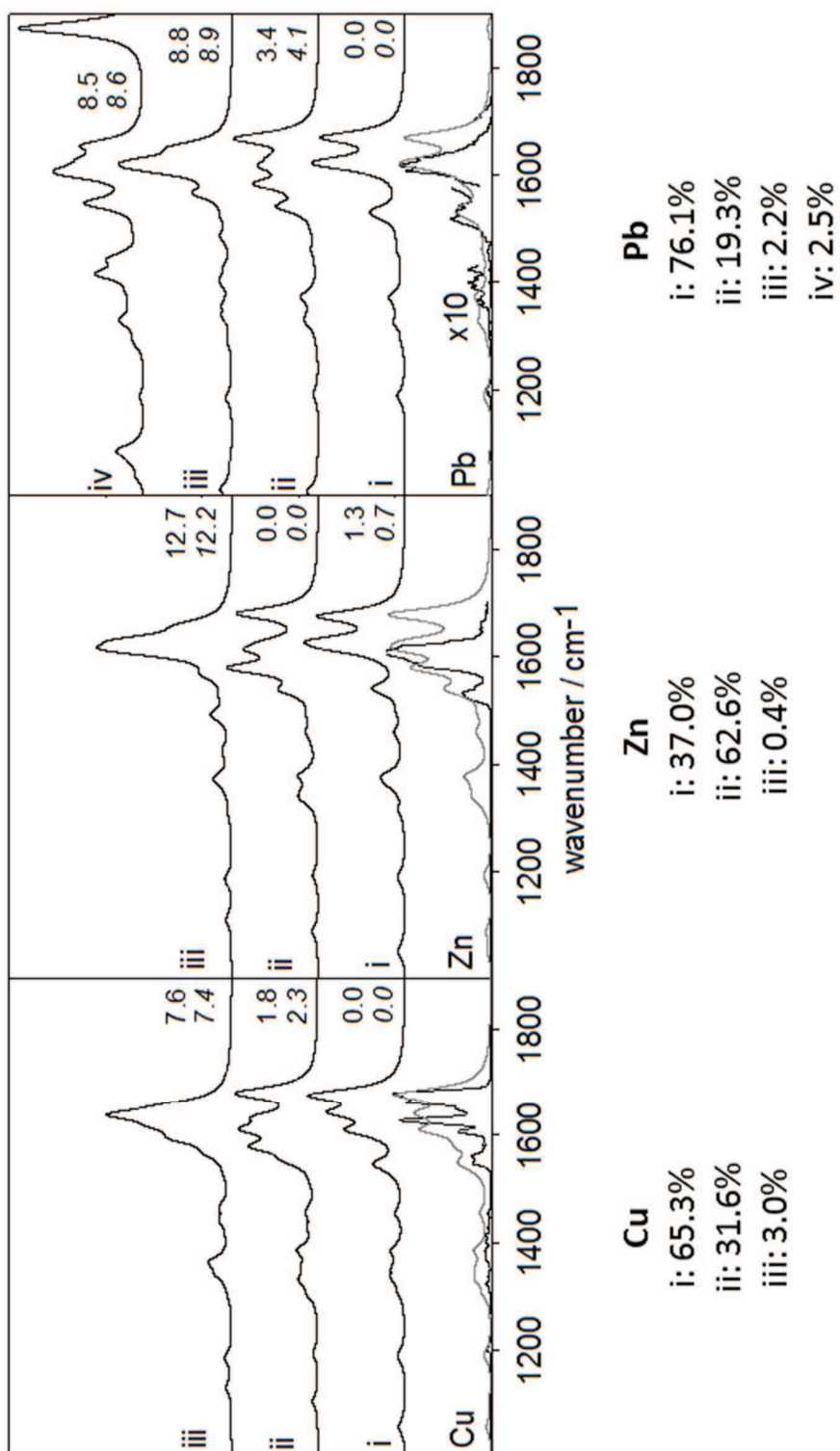


Figure C10. Experimental IRMPD spectrum (bottom) for $[M(\text{Ura-H})(\text{Ura})]^+$ compared with the B3LYP computed spectra using computational method 2 for the lowest energy structures. The calculated relative enthalpies and 298 K Gibbs energies (italics) are also shown. Boltzmann distribution spectra (grey) is overlaid on the experimental spectra. Composition of each isomer in the total mixture is indicated beneath each spectra.

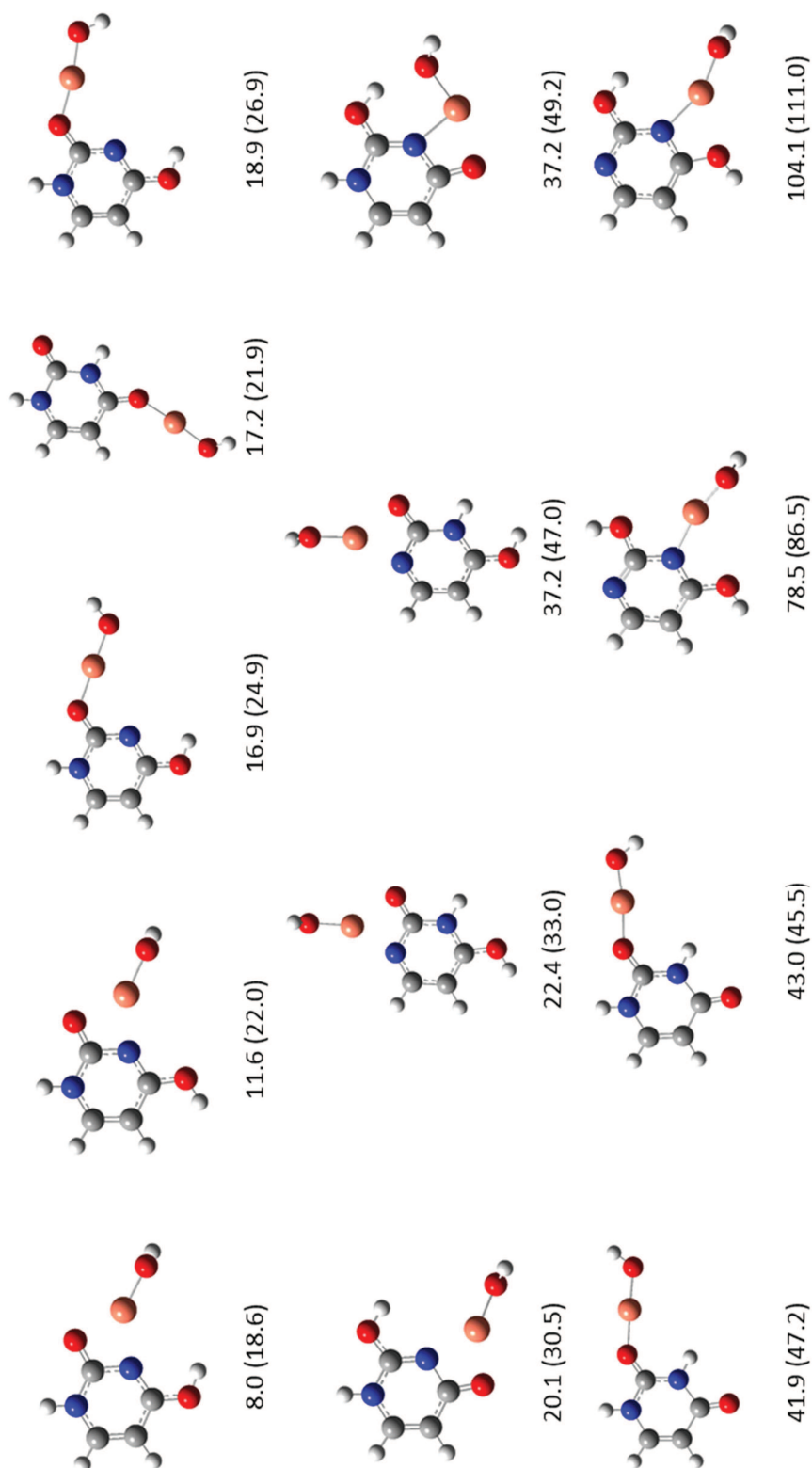


Figure C11. All structures found using calculation method 1 for $[\text{Cu}(\text{Ura})(\text{OH})]^+$. The calculated relative enthalpies and Gibbs energies (parenthesis) are also shown in $\text{kJ}\cdot\text{mol}^{-1}$ at 298 K, and are relative to structure 1-i(Cu).

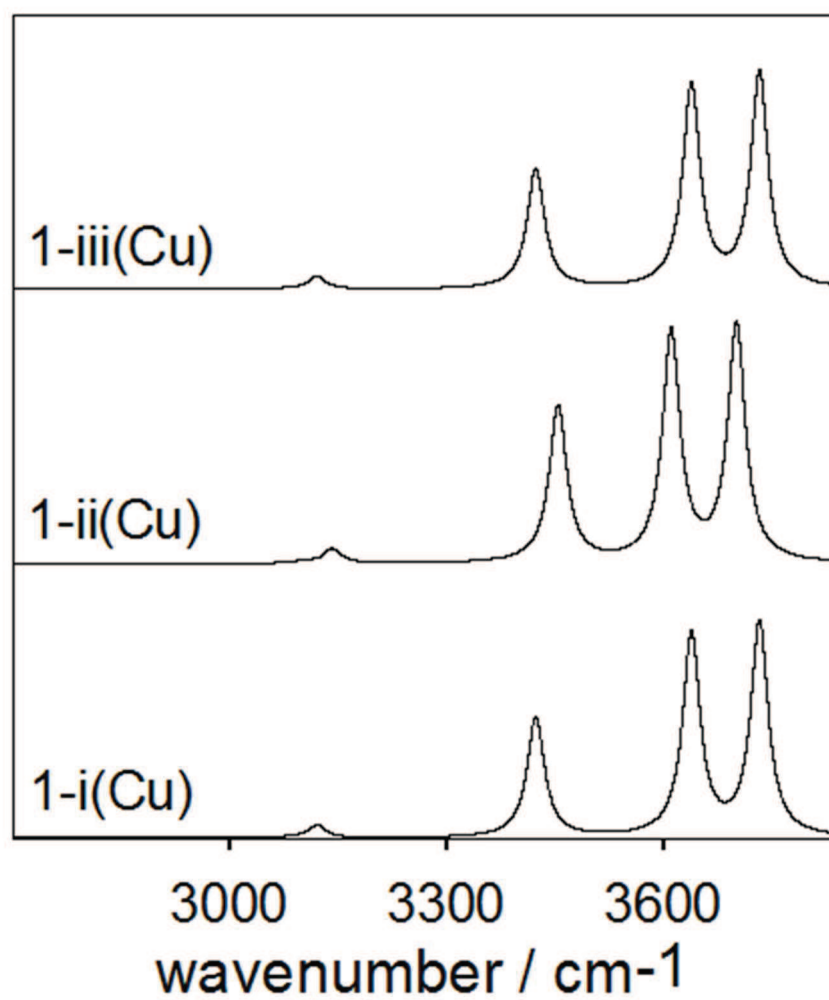


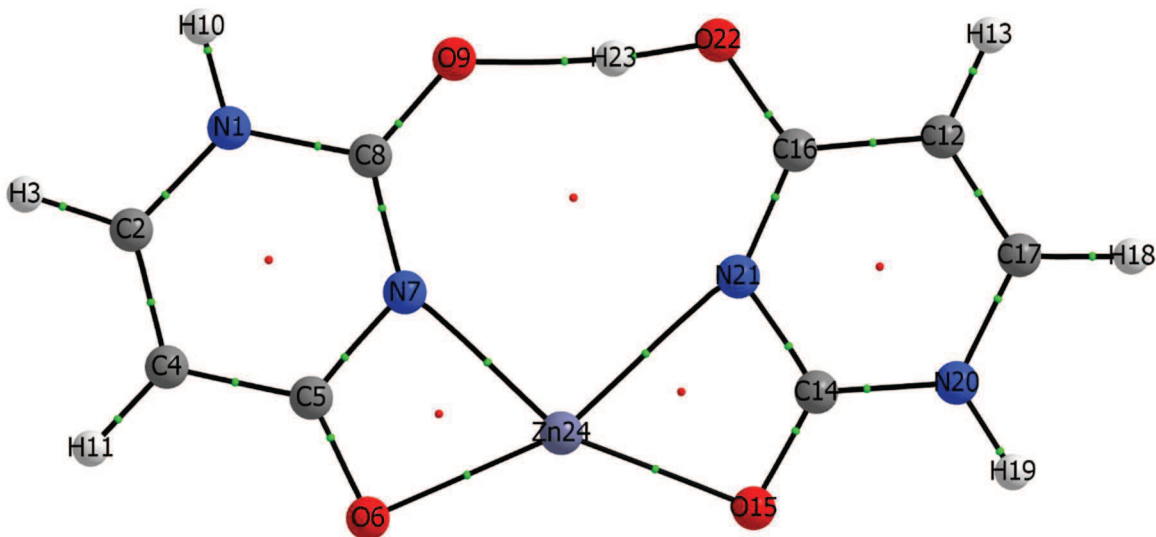
Figure C12. Comparison of the calculated spectra by method 2 of three lowest energy isomers of $[\text{Cu}(\text{Ura-H})(\text{H}_2\text{O})]^+$ in the O-H/N-H stretching region.

[Cu(Ura-H)(Ura)]⁺ Structure i

Bond	ρ	$\nabla^2\rho$	ε
N1 - Cu12	0.086	0.268	0.027
N1 - C2	0.339	-1.208	0.145
C2 - N3	0.328	-1.088	0.160
N3 - C4	0.306	-0.783	0.026
N3 - H9	0.339	-1.855	0.036
C4 - H5	0.294	-1.156	0.022
N1 - C8	0.341	-1.156	0.119
C4 - C6	0.333	-0.959	0.322
C6 - C8	0.296	-0.806	0.173
C6 - H7	0.288	-1.089	0.028
C8 - O10	0.347	-0.329	0.048
C2 - O11	0.382	-0.443	0.129
O11 - Cu12	0.069	0.243	0.046
O20 - H22	0.068	0.150	0.018
Cu12 - N13	0.105	0.329	0.046
Cu12 - O14	0.079	0.264	0.041
O14 - C15	0.362	-0.433	0.058
N13 - C15	0.331	-1.120	0.080
C15 - C24	0.299	-0.816	0.175
C16 - H17	0.294	-1.144	0.021
C16 - C24	0.329	-0.939	0.317
C16 - N23	0.310	-0.818	0.035

[Zn(Ura-H)(Ura)]⁺ Structure i

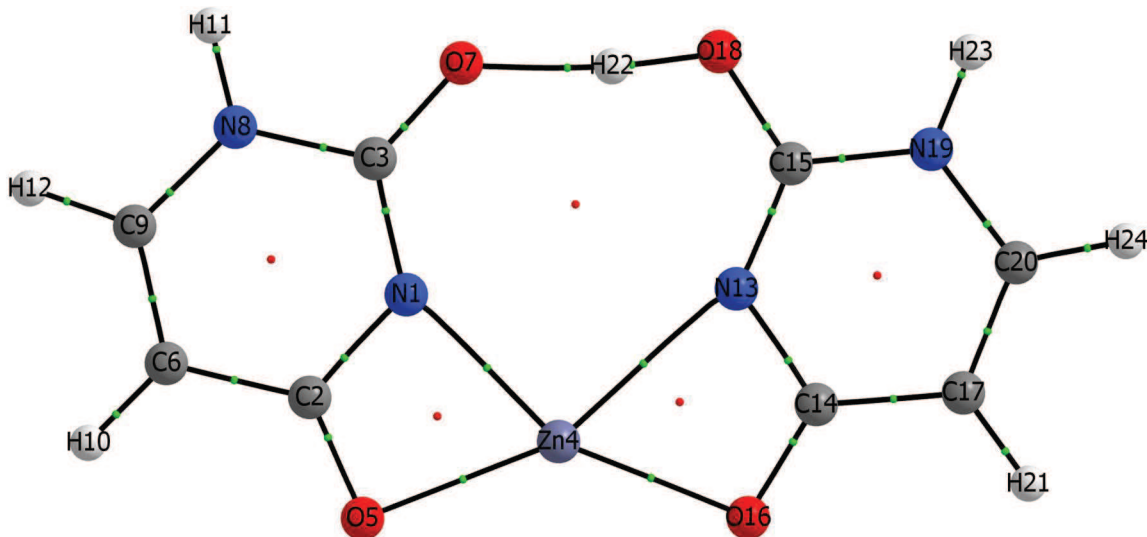
Electron densities ρ ($e \text{ \AA}^{-3}$), Laplacian of the charge density $\nabla^2\rho$ ($e \text{ \AA}^{-5}$) and ellipticity ε at the bond critical points, computed for geometries optimized at the B3LYP/6-31+G(d,p) level.



Bond	ρ	$\nabla^2\rho$	ε
N7 - C8	0.337	-1.200	0.160
N1 - C2	0.312	-0.820	0.035
C2 - H3	0.293	-1.141	0.020
C5 - N7	0.330	-1.138	0.089
C2 - C4	0.330	-0.945	0.318
N7 - Zn24	0.084	0.241	0.054
C4 - H11	0.287	-1.076	0.032
C4 - C5	0.297	-0.809	0.174
C5 - O6	0.361	-0.416	0.042
N1 - C8	0.310	-1.033	0.149
C8 - O9	0.390	-0.286	0.128
N1 - H10	0.340	-1.856	0.038
C16 - N21	0.346	-1.209	0.111
C12 - C16	0.296	-0.807	0.168
C12 - H13	0.288	-1.088	0.026
N21 - Zn24	0.045	0.167	0.061
C17 - H18	0.294	-1.154	0.023
C12 - C17	0.333	-0.962	0.319
O15 - Zn24	0.084	0.301	0.029
C14 - N21	0.351	-1.275	0.160
C17 - N20	0.305	-0.774	0.029
C14 - O15	0.368	-0.502	0.105

[Zn(Ura-H)(Ura)]⁺ Structure ii

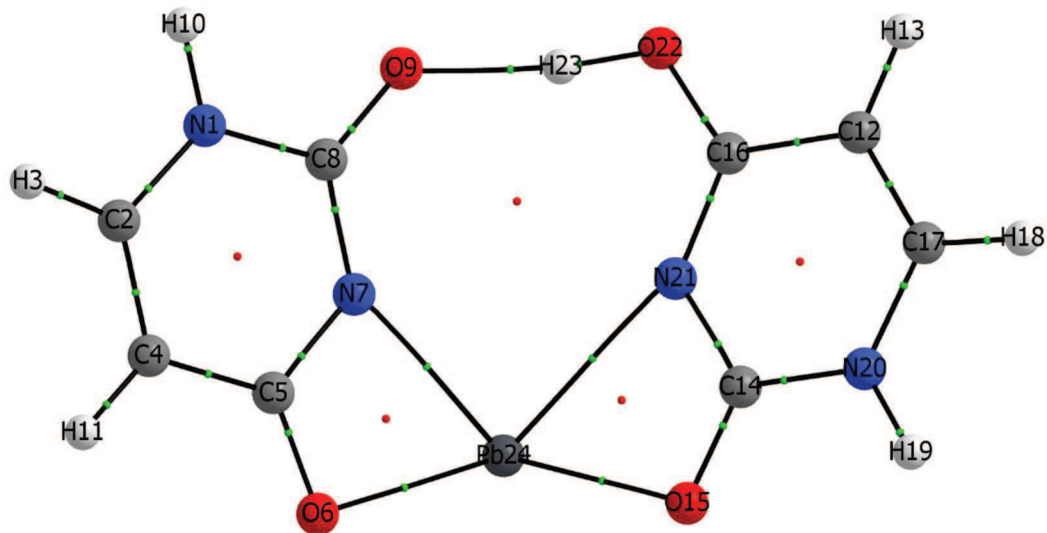
Electron densities ρ (e Å⁻³), Laplacian of the charge density $\nabla^2\rho$ (e Å⁻⁵) and ellipticity ε at the bond critical points, computed for geometries optimized at the B3LYP/6-31+G(d,p) level.



Bond	ρ	$\nabla^2\rho$	ε
N1 - Zn4	0.079	0.232	0.049
N1 - C2	0.330	-1.138	0.088
C2 - C6	0.297	-0.809	0.172
N1 - C3	0.341	-1.217	0.165
C3 - N8	0.312	-1.043	0.152
C2 - O5	0.362	-0.409	0.044
Zn4 - O5	0.077	0.264	0.023
C6 - H10	0.288	-1.077	0.031
C9 - H12	0.293	-1.142	0.020
C3 - O7	0.386	-0.312	0.125
N8 - C9	0.312	-0.814	0.034
C6 - C9	0.330	-0.947	0.318
N8 - H11	0.340	-1.856	0.038
Zn4 - N13	0.046	0.171	0.053
C14 - O16	0.360	-0.388	0.046
N13 - C14	0.333	-1.156	0.082
C14 - C17	0.297	-0.806	0.165
O7 - H22	0.079	0.141	0.014
O18 - H22	0.265	-1.302	0.012
N13 - C15	0.363	-1.327	0.193
C15 - N19	0.326	-1.101	0.177
Zn4 - O16	0.088	0.310	0.031

[Pb(Ura-H)(Ura)]⁺ Structure i

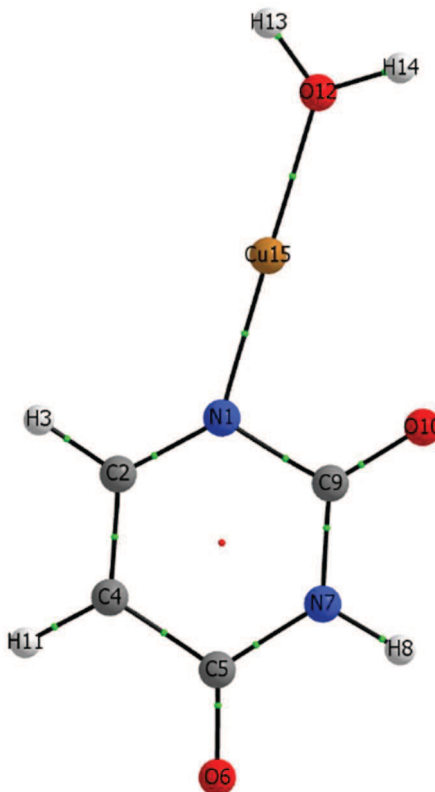
Electron densities ρ (e Å⁻³), Laplacian of the charge density $\nabla^2\rho$ (e Å⁻⁵) and ellipticity ε at the bond critical points, computed for geometries optimized at the B3LYP/6-31+G(d,p) level.



Bond	ρ	$\nabla^2\rho$	ε
N1 - C2	0.311	-0.756	0.023
N7 - C8	0.336	-1.181	0.151
C2 - H3	0.293	-1.138	0.019
C5 - N7	0.329	-1.108	0.082
C2 - C4	0.332	-0.967	0.319
C4 - C5	0.296	-0.812	0.168
N7 - Pb24	0.062	0.213	0.072
C5 - O6	0.360	-0.279	0.043
N1 - C8	0.309	-1.014	0.136
C8 - O9	0.388	-0.180	0.118
N1 - H10	0.341	-1.853	0.038
C4 - H11	0.287	-1.073	0.030
C16 - N21	0.345	-1.149	0.110
C12 - C16	0.298	-0.823	0.172
C12 - H13	0.288	-1.084	0.026
N21 - Pb24	0.033	0.108	0.017
C12 - C17	0.333	-0.978	0.315
C14 - N21	0.343	-1.239	0.151
C17 - N20	0.309	-0.723	0.019
C14 - O15	0.376	-0.296	0.114
C14 - N20	0.319	-1.014	0.138
C17 - H18	0.294	-1.150	0.020

[Cu(Ura-H)(H₂O)]⁺ Structure 1-i(Cu)

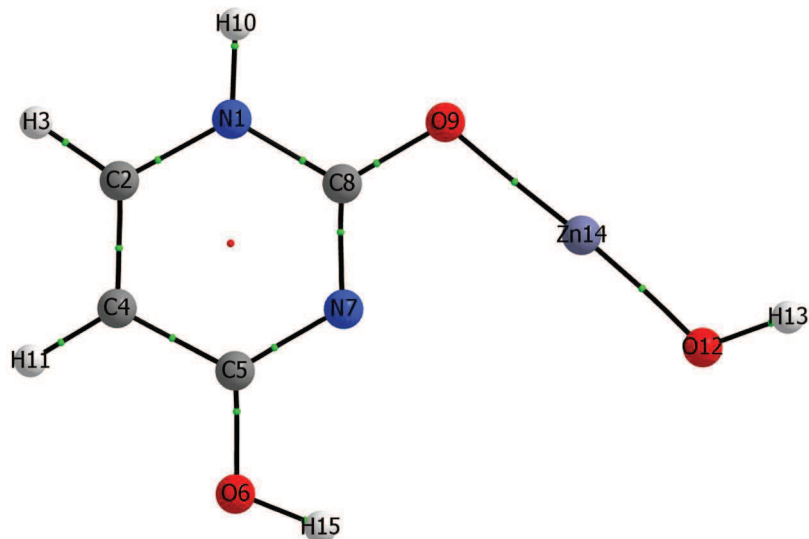
Electron densities ρ (e Å⁻³), Laplacian of the charge density $\nabla^2\rho$ (e Å⁻⁵) and ellipticity ε at the bond critical points, computed for geometries optimized at the B3LYP/6-31+G(d,p) level.



Bond	ρ	$\nabla^2\rho$	ε
N1 - C9	0.293	-0.911	0.081
N1 - C2	0.341	-0.877	0.083
C2 - H3	0.294	-1.146	0.018
C2 - C4	0.315	-0.878	0.176
C4 - C5	0.284	-0.751	0.114
C4 - H11	0.291	-1.133	0.009
C5 - O6	0.412	0.003	0.120
C5 - N7	0.297	-0.944	0.091
N7 - C9	0.324	-1.104	0.166
N7 - H8	0.335	-1.833	0.036
C9 - O10	0.411	-0.087	0.145
N1 - Cu15	0.110	0.415	0.077
O12 - Cu15	0.087	0.434	0.017
O12 - H13	0.353	-2.165	0.026
O12 - H14	0.352	-2.162	0.026

[Zn(Ura-H)(H₂O)]⁺ Structure 1-i(Zn)

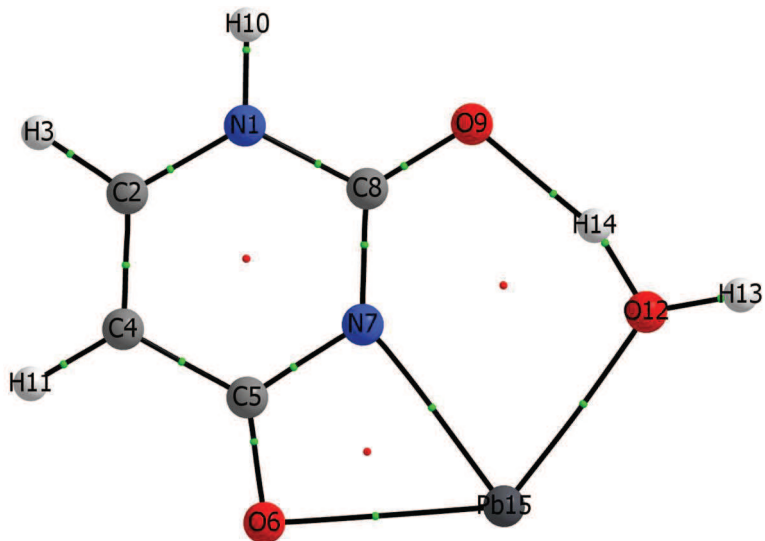
Electron densities ρ (e Å⁻³), Laplacian of the charge density $\nabla^2\rho$ (e Å⁻⁵) and ellipticity ε at the bond critical points, computed for geometries optimized at the B3LYP/6-31+G(d,p) level.



Bond	ρ	$\nabla^2\rho$	ε
N1 - C2	0.309	-0.752	0.024
C2 - H3	0.294	-1.166	0.021
N7 - C8	0.354	-1.292	0.169
C2 - C4	0.332	-0.961	0.303
C5 - N7	0.353	-1.244	0.128
C4 - C5	0.301	-0.833	0.181
C5 - O6	0.328	-0.361	0.025
N1 - C8	0.327	-1.073	0.170
N1 - H10	0.338	-1.859	0.034
C8 - O9	0.359	-0.469	0.104
C4 - H11	0.288	-1.098	0.024
O12 - Zn14	0.146	0.642	0.055
O9 - Zn14	0.106	0.425	0.048
O12 - H13	0.356	-2.025	0.010
O6 - H15	0.351	-2.117	0.014

[Pb(Ura-H)(H₂O)]⁺ Structure 1-i(Pb)

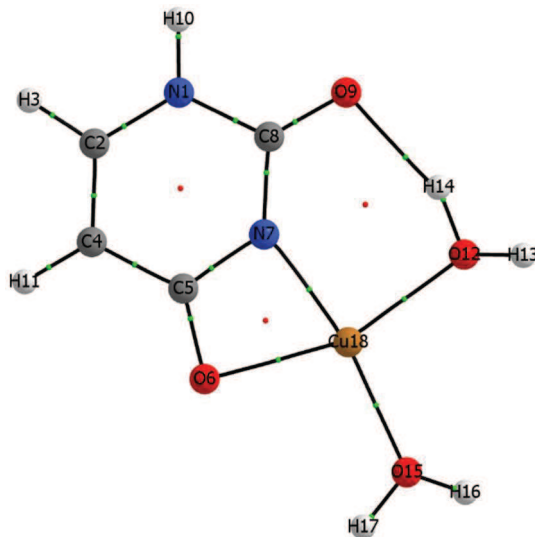
Electron densities ρ (e Å⁻³), Laplacian of the charge density $\nabla^2\rho$ (e Å⁻⁵) and ellipticity ε at the bond critical points, computed for geometries optimized at the B3LYP/6-31+G(d,p) level.



Bond	ρ	$\nabla^2\rho$	ε
N1 - C2	0.292	-0.714	0.035
C2 - C4	0.312	-0.780	0.213
C2 - H3	0.273	-0.892	0.007
C5 - N7	0.301	-0.815	0.038
C4 - C5	0.278	-0.614	0.115
C4 - H11	0.269	-0.856	0.025
C5 - O6	0.349	-0.648	0.007
N7 - Pb15	0.074	0.259	0.114
N7 - C8	0.307	-0.828	0.090
N1 - C8	0.291	-0.761	0.091
C8 - O9	0.377	-0.575	0.061
N1 - H10	0.318	-1.525	0.035
O9 - H14	0.058	0.183	0.019
O12 - H14	0.283	-1.251	0.020
O12 - Pb15	0.050	0.210	0.102
O12 - H13	0.332	-1.612	0.018
O6 - Pb15	0.054	0.194	0.022

[Cu(Ura-H)(H₂O)₂]⁺ Structure 2-i

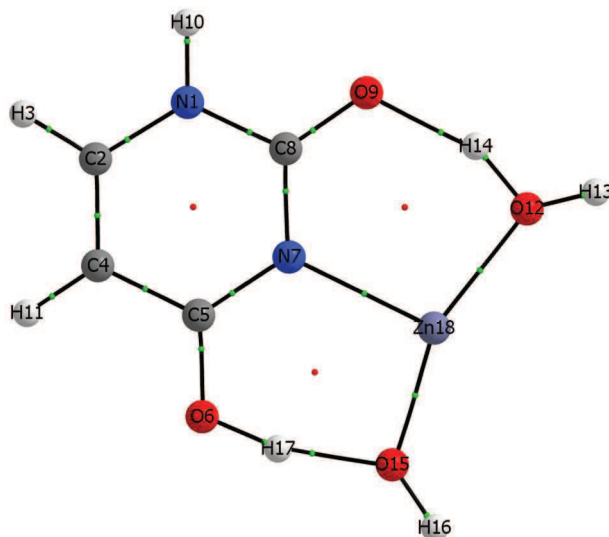
Electron densities ρ (e Å⁻³), Laplacian of the charge density $\nabla^2\rho$ (e Å⁻⁵) and ellipticity ε at the bond critical points, computed for geometries optimized at the B3LYP/6-31+G(d,p) level.



Bond	ρ	$\nabla^2\rho$	ε
N1 - C2	0.312	-0.830	0.037
C2 - C4	0.326	-0.924	0.313
C2 - H3	0.294	-1.147	0.019
C5 - N7	0.338	-1.118	0.086
C4 - C5	0.300	-0.820	0.184
C4 - H11	0.287	-1.075	0.032
C5 - O6	0.354	-0.467	0.048
N7 - C8	0.330	-1.131	0.146
N1 - C8	0.307	-1.019	0.148
N1 - H10	0.340	-1.855	0.038
N7 - Cu18	0.115	0.358	0.065
C8 - O9	0.402	-0.254	0.146
O9 - H14	0.033	0.087	0.029
O12 - H13	0.355	-2.116	0.021
O12 - H14	0.319	-1.884	0.021
O6 - Cu18	0.074	0.230	0.037
O15 - Cu18	0.076	0.364	0.036
O12 - Cu18	0.072	0.301	0.041
O15 - H16	0.353	-2.150	0.024
O15 - H17	0.351	-2.151	0.024

[Zn(Ura-H)(H₂O)₂]⁺ Structure 2-ii

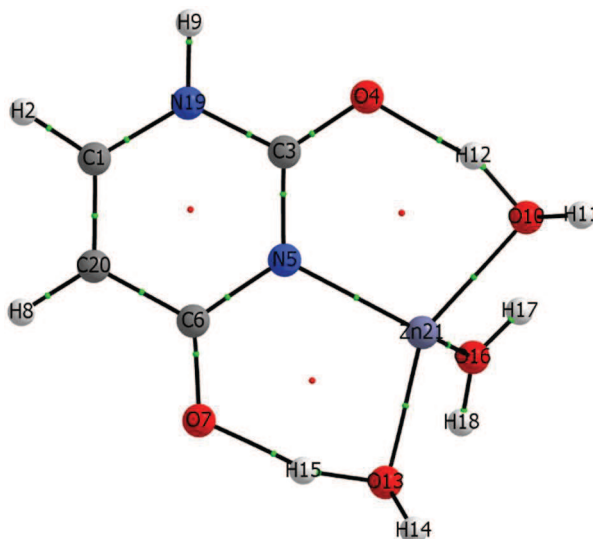
Electron densities ρ (e Å⁻³), Laplacian of the charge density $\nabla^2\rho$ (e Å⁻⁵) and ellipticity ε at the bond critical points, computed for geometries optimized at the B3LYP/6-31+G(d,p) level.



Bond	ρ	$\nabla^2\rho$	ε
N1 - C2	0.313	-0.791	0.023
C2 - H3	0.294	-1.155	0.019
C2 - C4	0.334	-0.969	0.312
N7 - C8	0.324	-1.116	0.150
C5 - N7	0.332	-1.155	0.120
C4 - C5	0.300	-0.830	0.184
C4 - H11	0.288	-1.088	0.030
C5 - O6	0.345	-0.347	0.045
N1 - C8	0.318	-1.071	0.157
N1 - H10	0.340	-1.860	0.037
C8 - O9	0.391	-0.293	0.132
N7 - Zn18	0.082	0.242	0.053
O9 - H14	0.067	0.157	0.014
O12 - Zn18	0.093	0.385	0.052
O12 - H13	0.352	-2.133	0.019
O12 - H14	0.288	-1.547	0.018
O15 - H17	0.079	0.158	0.027
O15 - Zn18	0.122	0.538	0.037
O15 - H16	0.356	-2.075	0.011
O6 - H17	0.276	-1.387	0.010

[Zn(Ura-H)(H₂O)₃]⁺ Structure 3-i

Electron densities ρ (e Å⁻³), Laplacian of the charge density $\nabla^2\rho$ (e Å⁻⁵) and ellipticity ε at the bond critical points, computed for geometries optimized at the B3LYP/6-31+G(d,p) level.



Bond	ρ	$\nabla^2\rho$	ε
C1 - H2	0.293	-1.136	0.023
C3 - N5	0.331	-1.154	0.165
C1 - N19	0.308	-0.798	0.030
C3 - N19	0.320	-1.079	0.157
C3 - O4	0.385	-0.352	0.120
C1 - C20	0.336	-0.978	0.331
N5 - C6	0.312	-1.042	0.091
N5 - Zn21	0.093	0.264	0.062
C6 - C20	0.292	-0.782	0.162
H8 - C20	0.288	-1.075	0.030
C6 - O7	0.376	-0.249	0.070
H9 - N19	0.341	-1.858	0.040
O4 - H12	0.069	0.155	0.010
O10 - H11	0.355	-2.104	0.017
O10 - H12	0.286	-1.498	0.018
O7 - H15	0.086	0.133	0.009
O13 - H14	0.355	-2.093	0.016
O13 - H15	0.265	-1.255	0.018
O16 - Zn21	0.064	0.275	0.100
O16 - H17	0.354	-2.147	0.025
O16 - H18	0.353	-2.147	0.025
O10 - Zn21	0.080	0.320	0.037
O13 - Zn21	0.084	0.334	0.035

APPENDIX D – Chapter 5 Supplemental Information

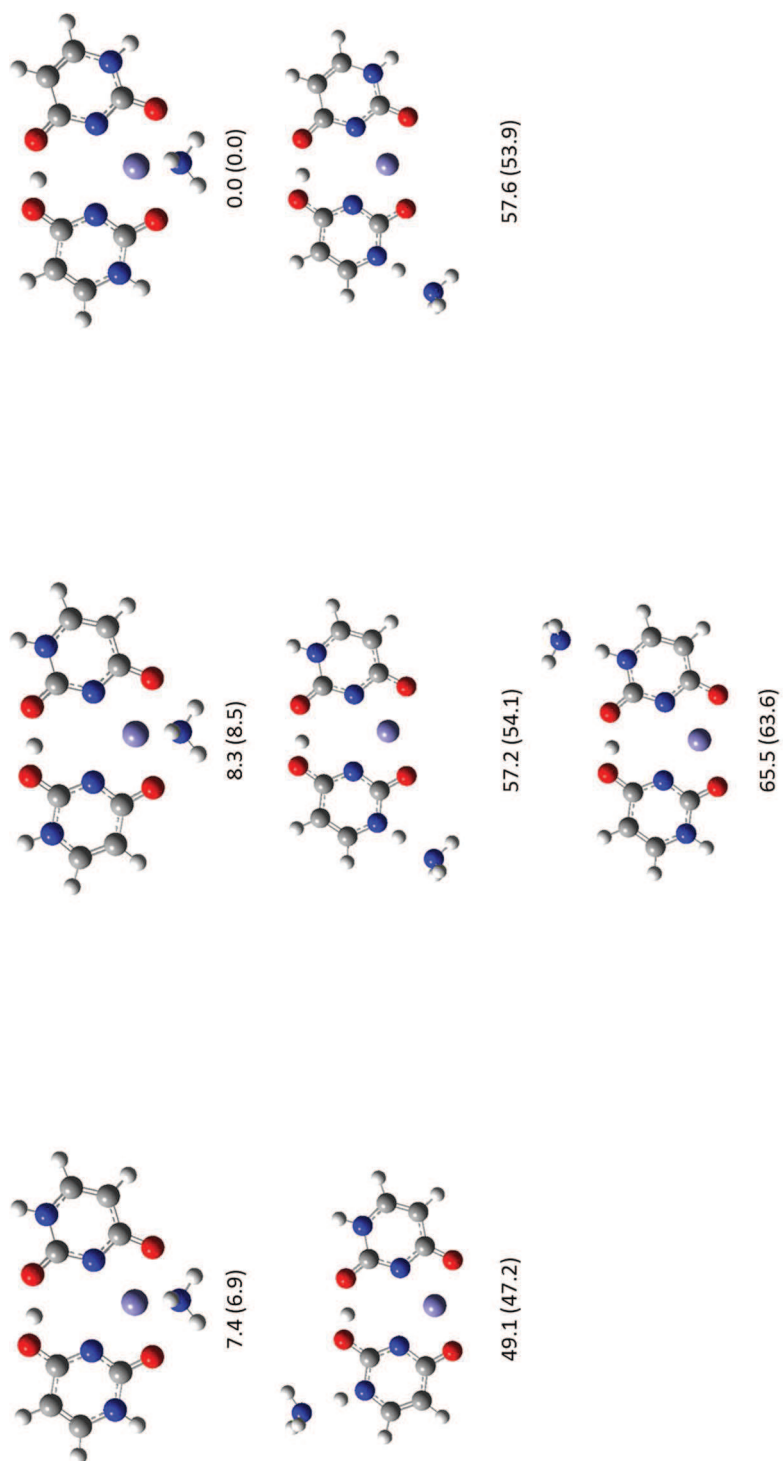


Figure D1. All structures found using calculation method 1 for $[\text{Fe}(\text{Ura-H})(\text{Ura})(\text{NH}_3)]^+$. The calculated relative enthalpies and Gibbs energies (parentheses) are also shown in kJ mol⁻¹ at 298 K.

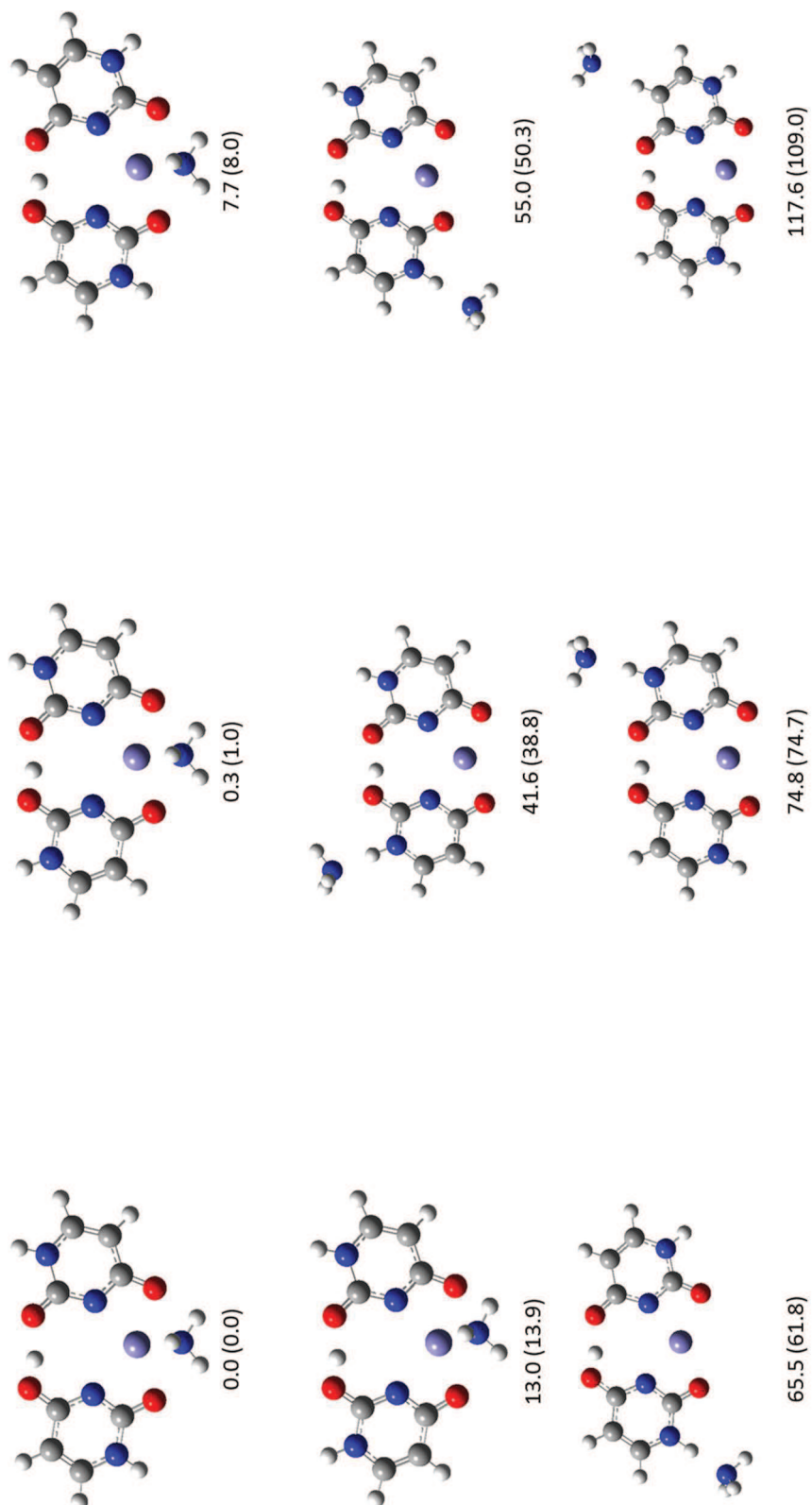


Figure D2. All structures found using calculation method 2 for $[\text{Fe}(\text{Ura-H})(\text{Ura})(\text{NH}_3)]^+$. The calculated relative enthalpies and Gibbs energies (parentheses) are also shown in kJ mol^{-1} at 298 K.

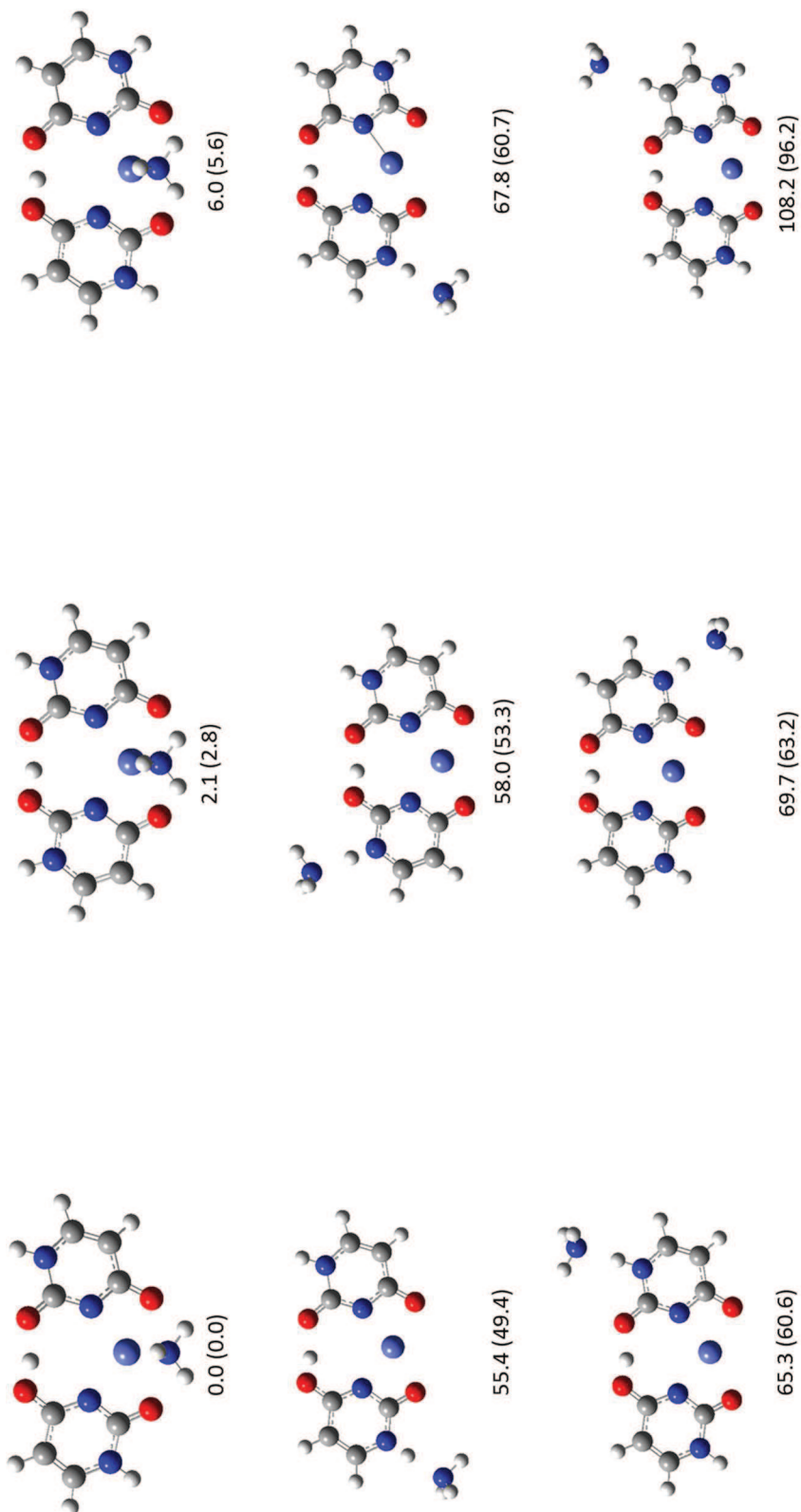


Figure D3. All structures found using calculation method 1 for $[\text{Co}(\text{Ura-H})(\text{Ura})(\text{NH}_3)]^+$. The calculated relative enthalpies and Gibbs energies (parentheses) are also shown in kJ mol^{-1} at 298 K.

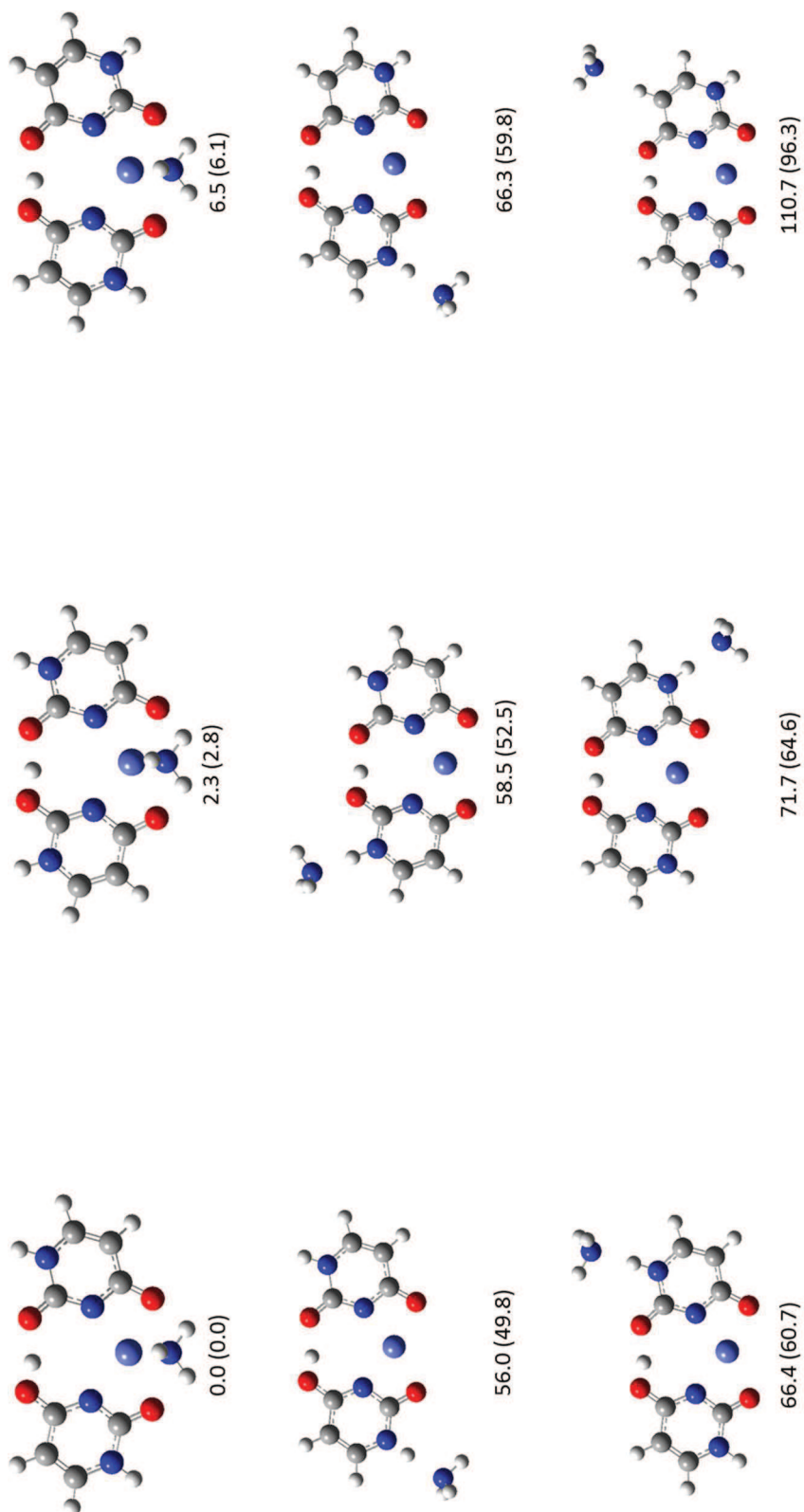


Figure D4. All structures found using calculation method 2 for $[\text{Co}(\text{Ura-H})(\text{Ura})(\text{NH}_3)]^+$. The calculated relative enthalpies and Gibbs energies (parentheses) are also shown in kJ mol^{-1} at 298 K.

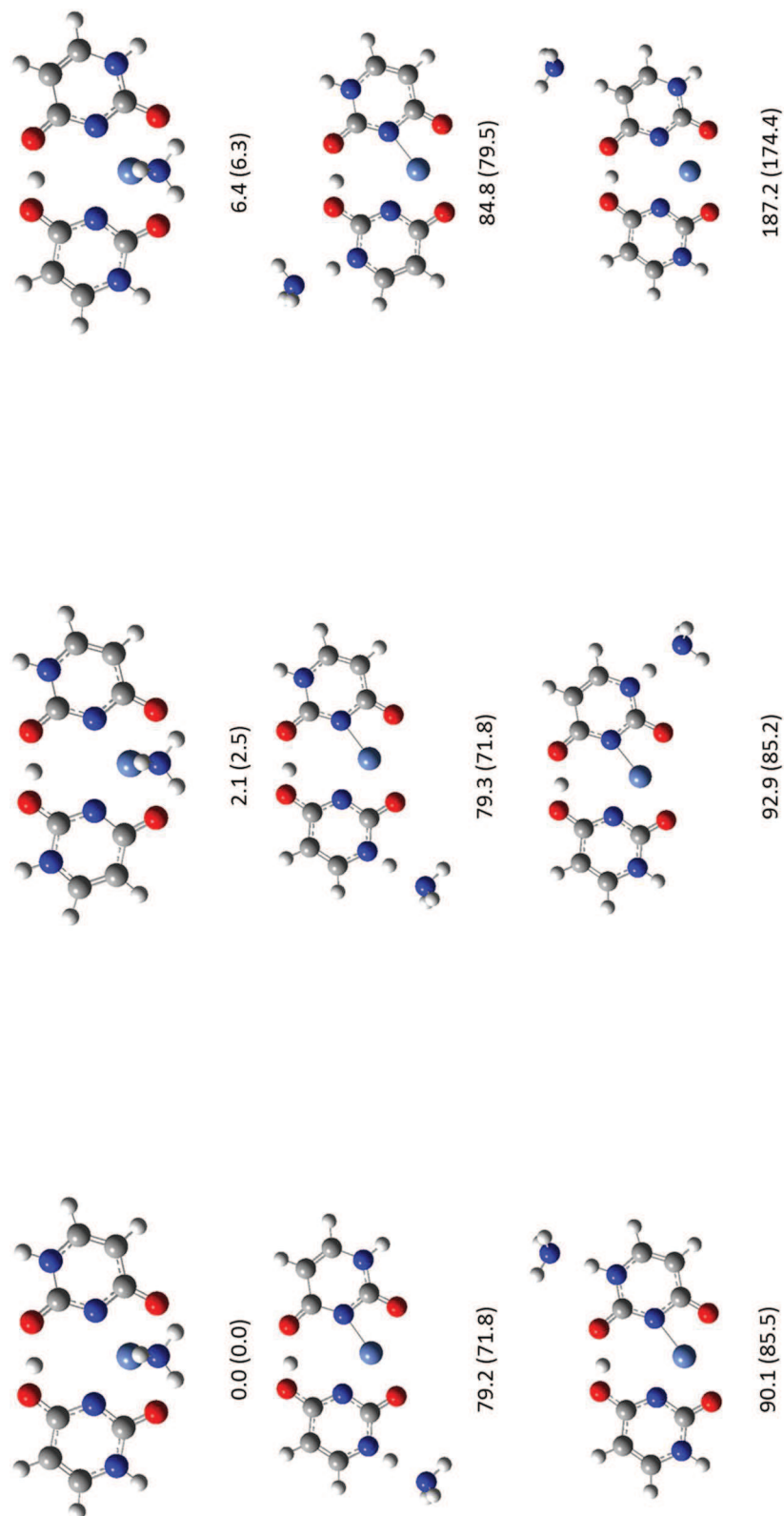


Figure D5. All structures found using calculation method 1 for $[\text{Ni}(\text{Ura-H})(\text{Ura})(\text{NH}_3)]^+$. The calculated relative enthalpies and Gibbs energies (parentheses) are also shown in kJ mol^{-1} at 298 K.

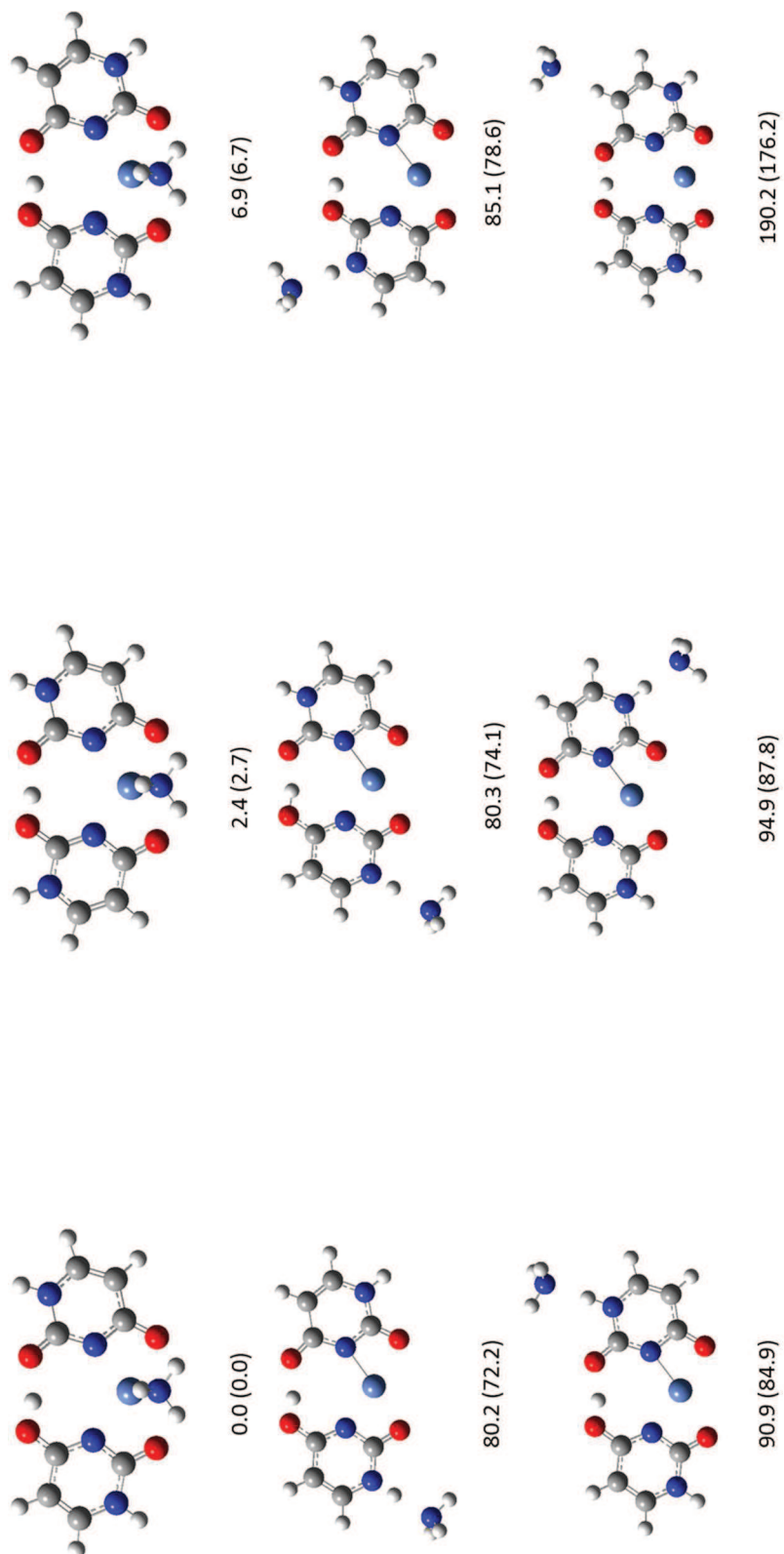


Figure D6. All structures found using calculation method 2 for $[\text{Ni}(\text{Ura-H})(\text{Ura})(\text{NH}_3)]^+$. The calculated relative enthalpies and Gibbs energies (parentheses) are also shown in kJ mol^{-1} at 298 K.

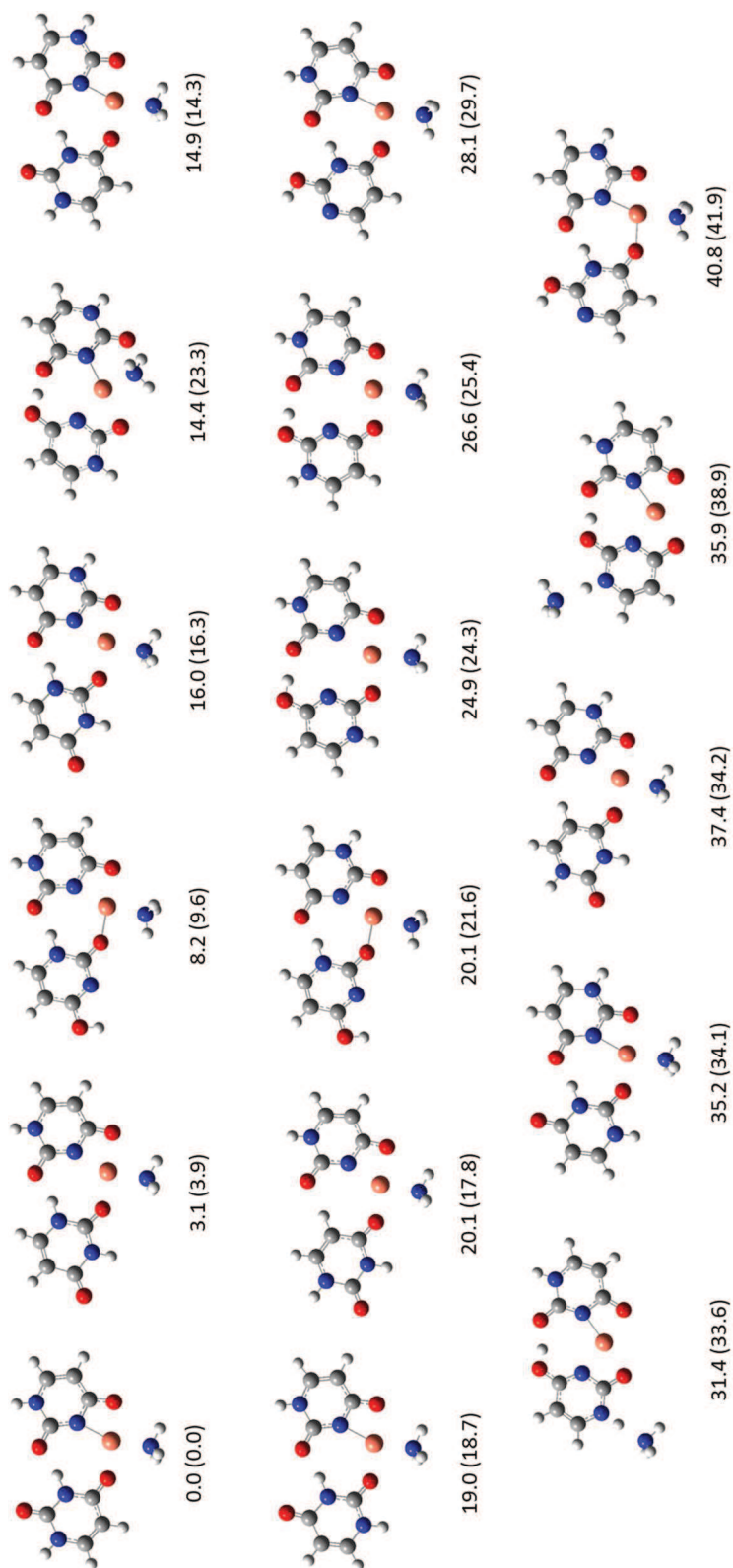


Figure D7a. All structures found using calculation method 1 for $[\text{Cu}(\text{Ura-H})(\text{Ura})(\text{NH}_3)]^+$. The calculated relative enthalpies and Gibbs energies (parentheses) are also shown in kJ mol^{-1} at 298 K.

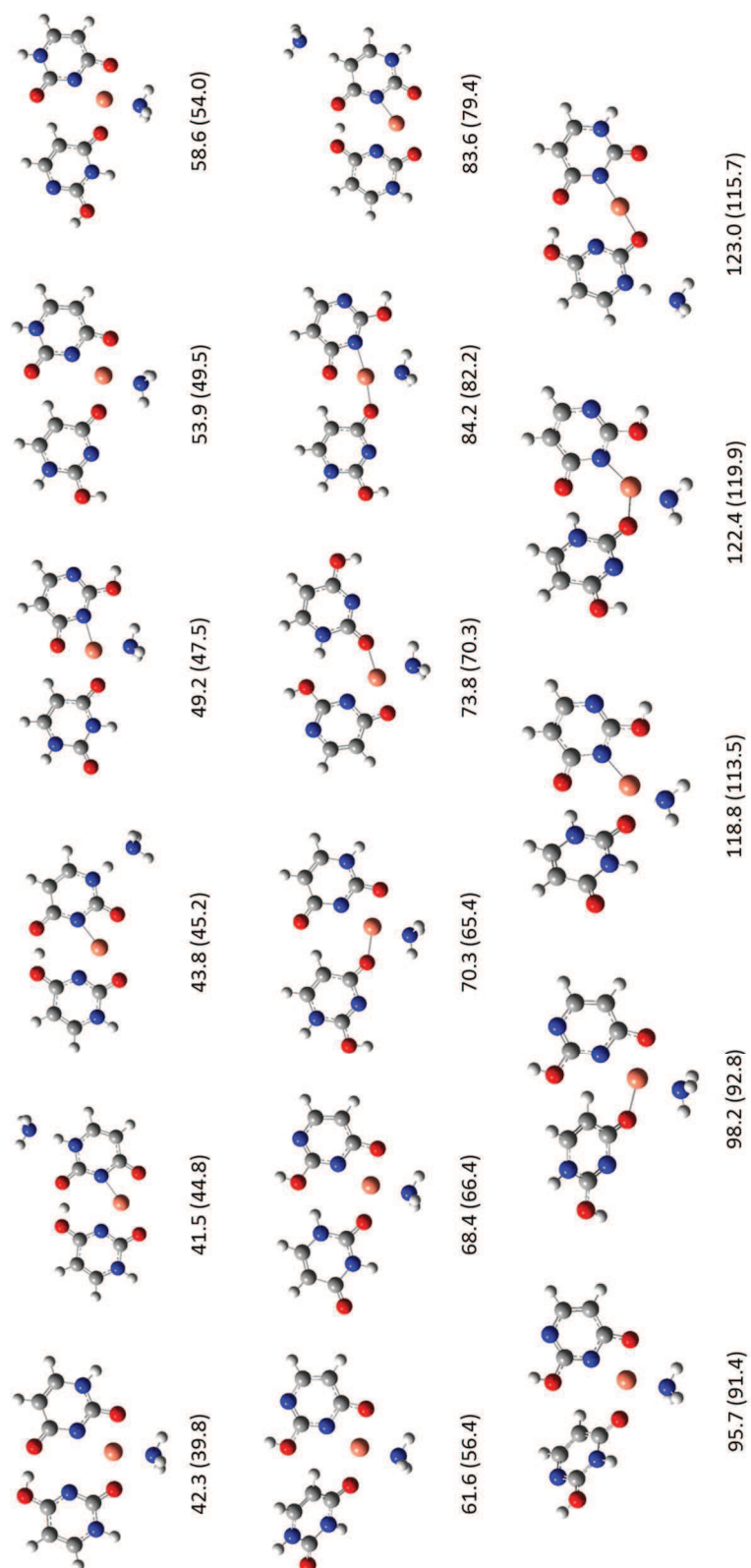


Figure D7b. All structures found using calculation method 1 for $[\text{Cu}(\text{Ura-H})(\text{Ura})(\text{NH}_3)]^+$. The calculated relative enthalpies and Gibbs energies (parentheses) are also shown in kJ mol^{-1} at 298 K.

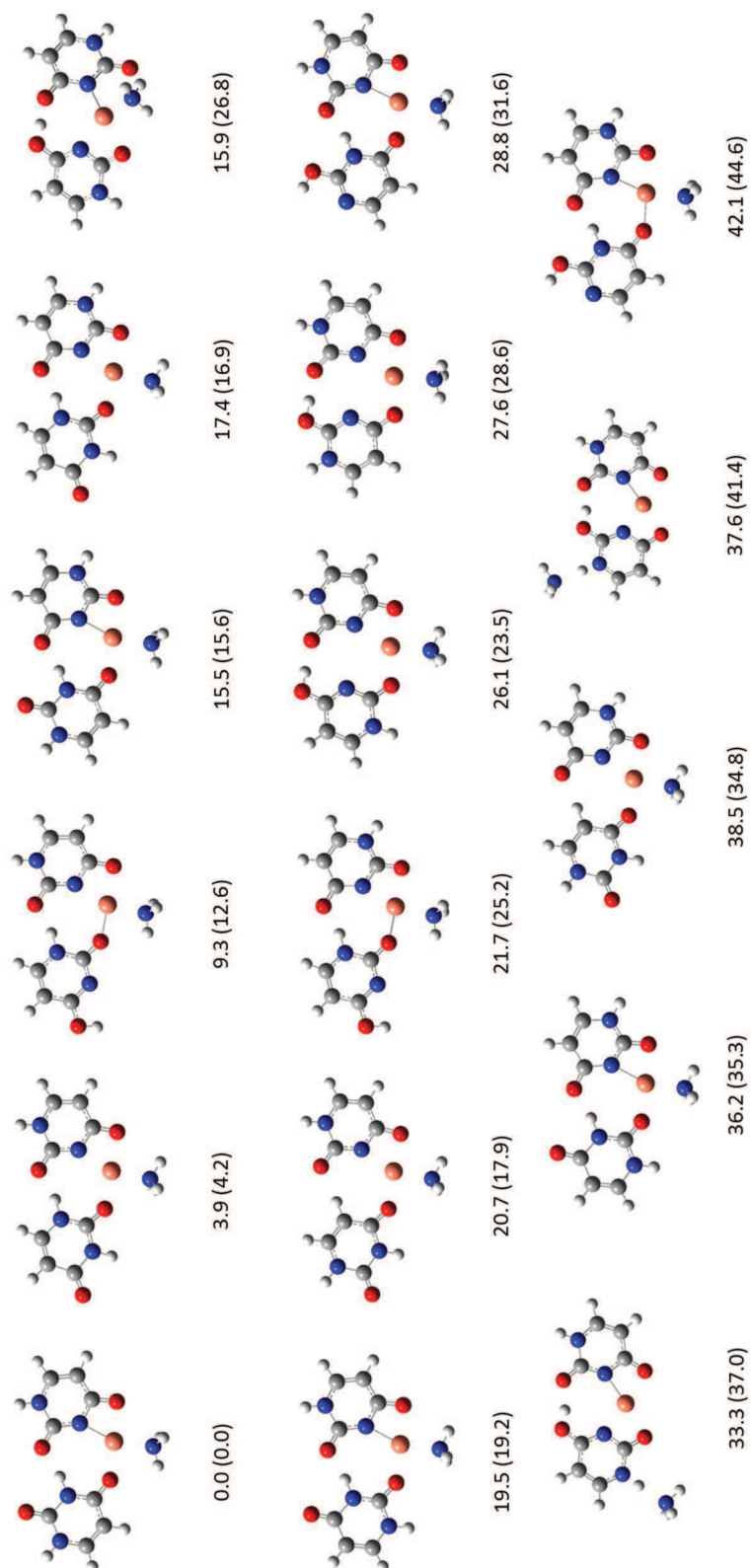


Figure D8a. All structures found using calculation method 2 for $[\text{Cu}(\text{Ura-H})(\text{Ura})(\text{NH}_3)]^+$. The calculated relative enthalpies and Gibbs energies (parentheses) are also shown in kJ mol^{-1} at 298 K.

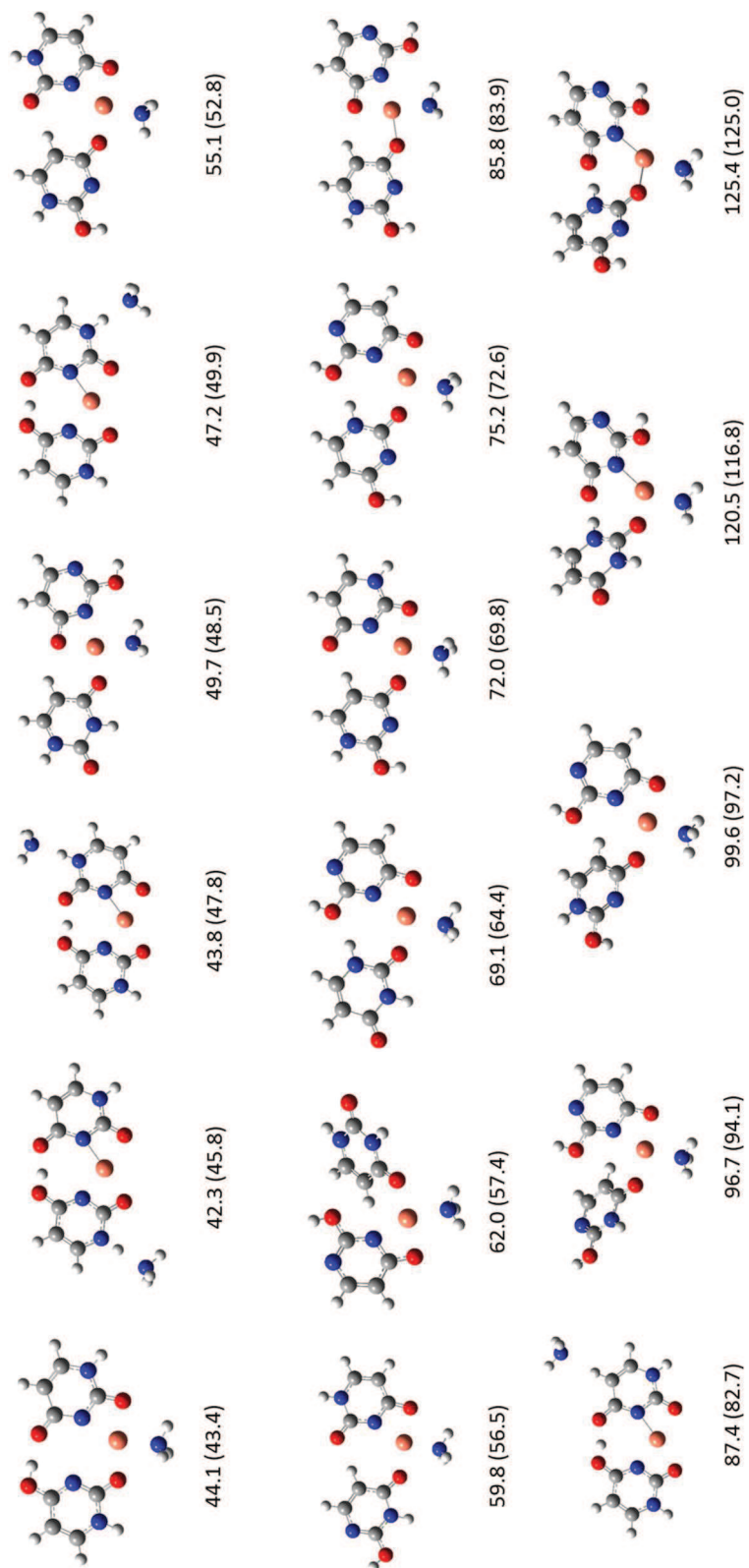


Figure D8b. All structures found using calculation method 2 for $[\text{Cu}(\text{Ura-H})(\text{Ura})(\text{NH}_3)]^+$. The calculated relative enthalpies and Gibbs energies (parentheses) are also shown in kJ mol^{-1} at 298 K.

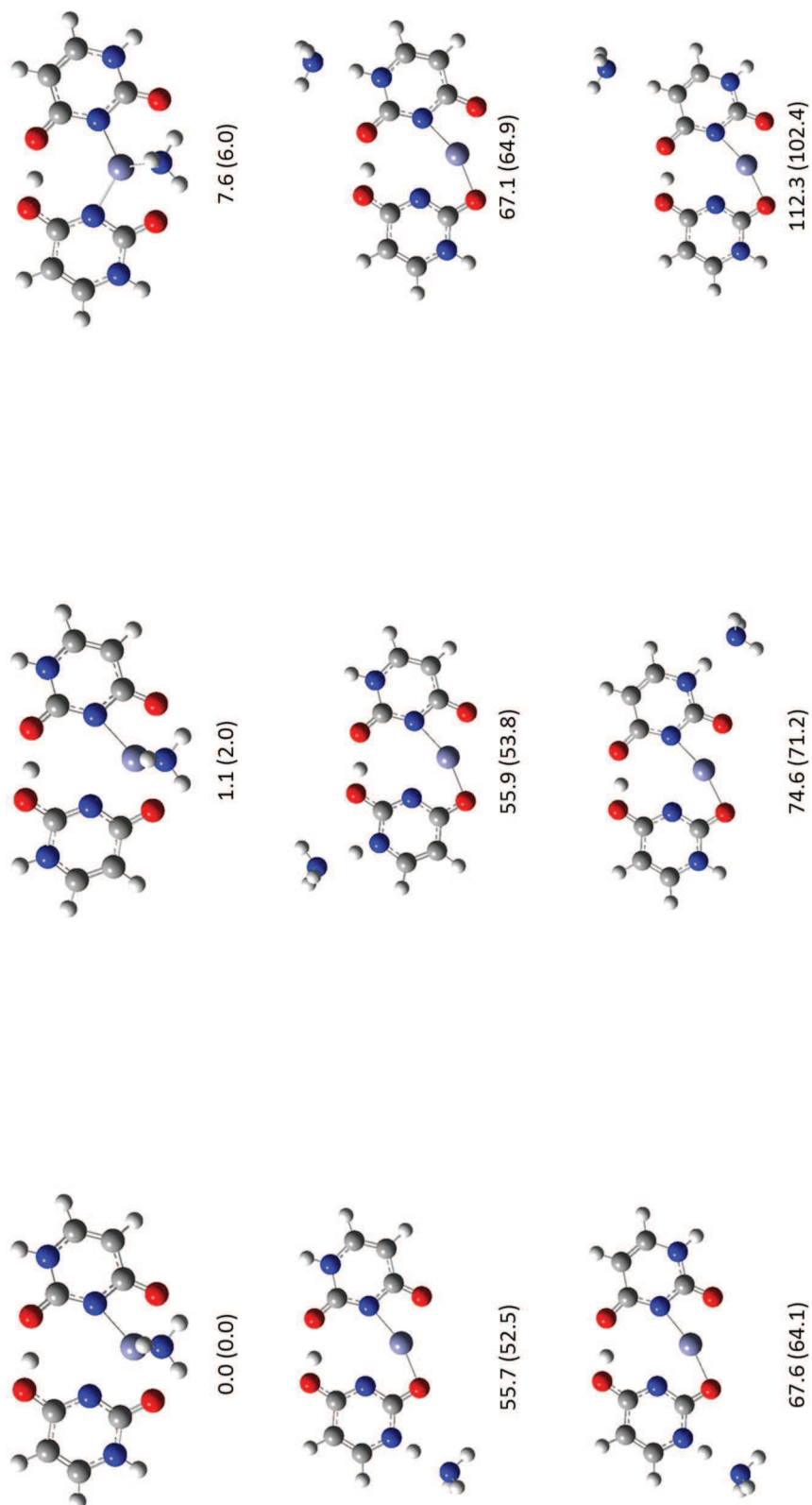


Figure D9. All structures found using calculation method 1 for $[\text{Zn}(\text{Ura-H})(\text{Ura})(\text{NH}_3)]^+$. The calculated relative enthalpies and Gibbs energies (parentheses) are also shown in kJ mol^{-1} at 298 K.

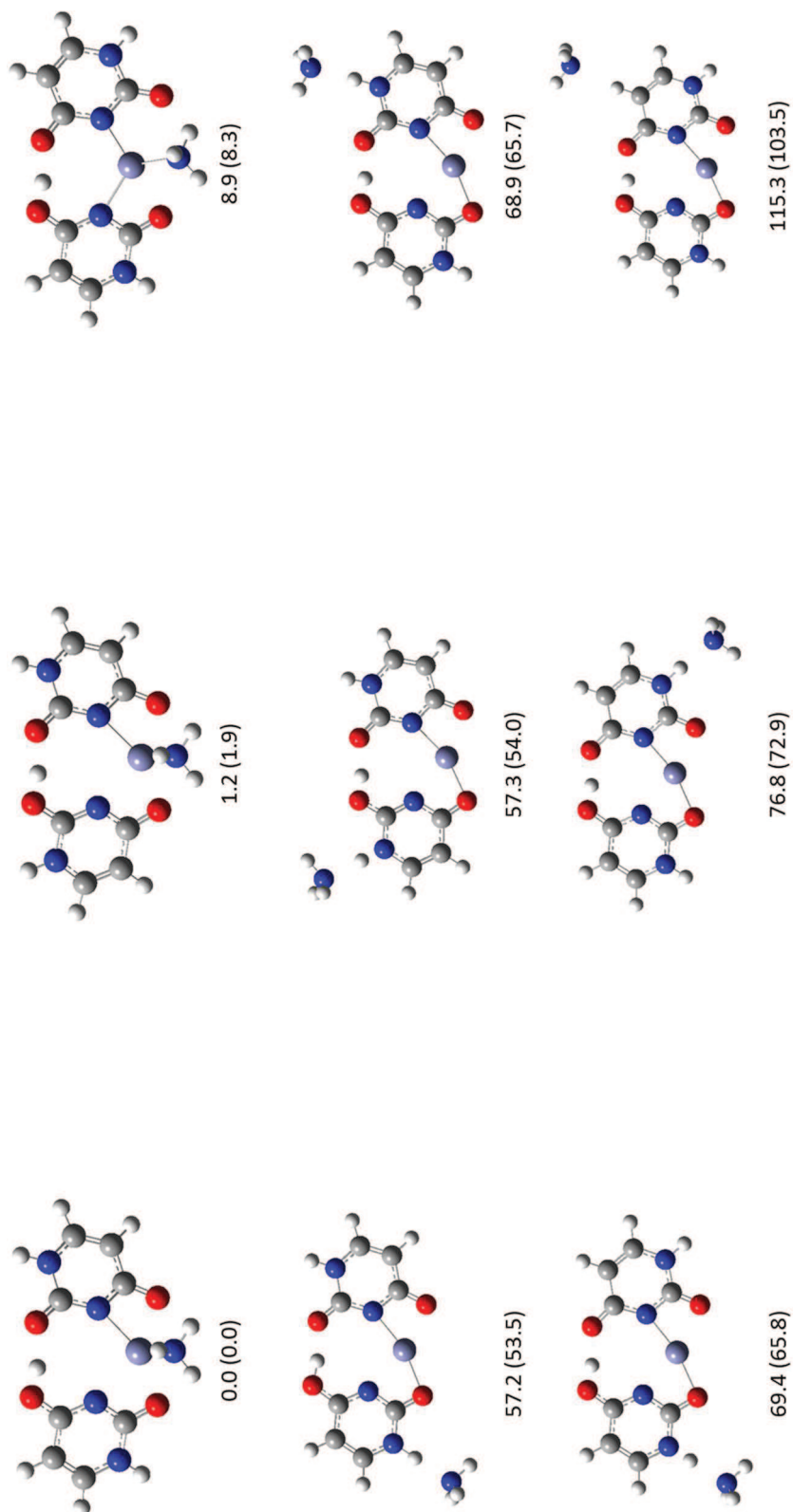


Figure D10. All structures found using calculation method 2 for $[\text{Zn}(\text{Ura-H})(\text{Ura})(\text{NH}_3)]^+$. The calculated relative enthalpies and Gibbs energies (parentheses) are also shown in kJ mol^{-1} at 298 K.

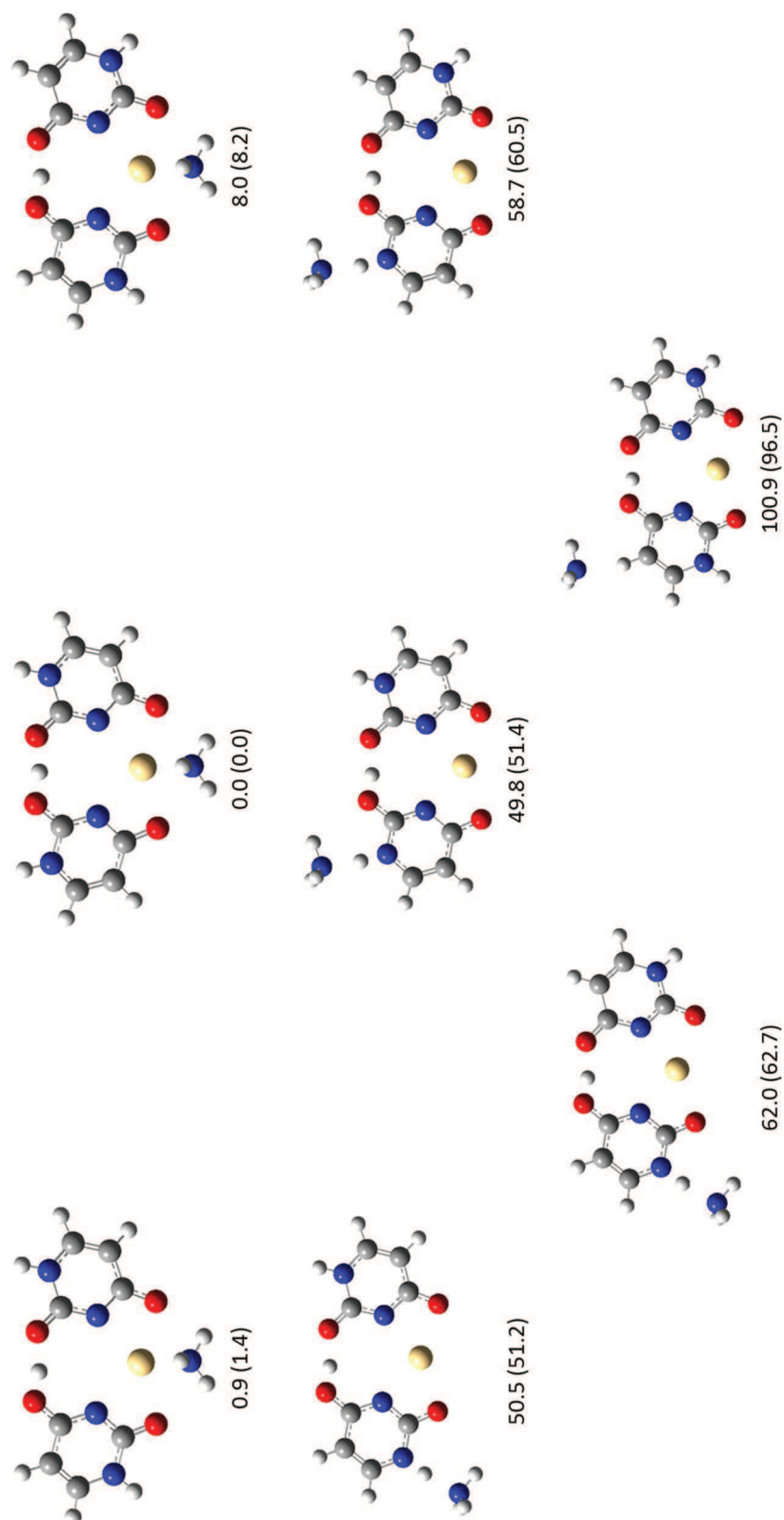


Figure D11. All structures found using calculation method 1 for $[\text{Cd}(\text{Ura-H})(\text{Ura})(\text{NH}_3)]^+$. The calculated relative enthalpies and Gibbs energies (parentheses) are also shown in kJ mol⁻¹ at 298 K.

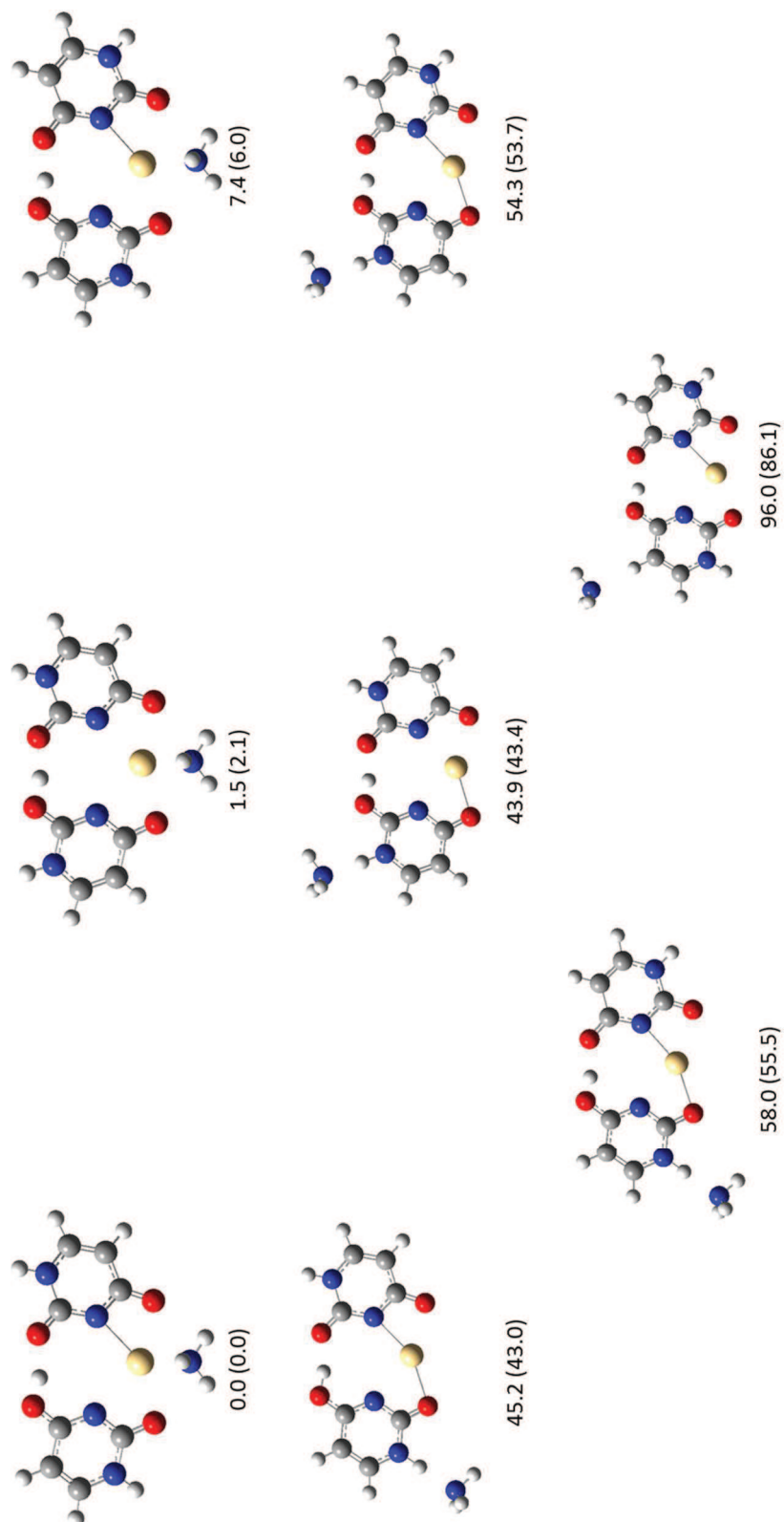


Figure D12. All structures found using calculation method 2 for $[\text{Cd}(\text{Ura-H})(\text{Ura})(\text{NH}_3)]^+$. The calculated relative enthalpies and Gibbs energies (parentheses) are also shown in kJ mol^{-1} at 298 K.

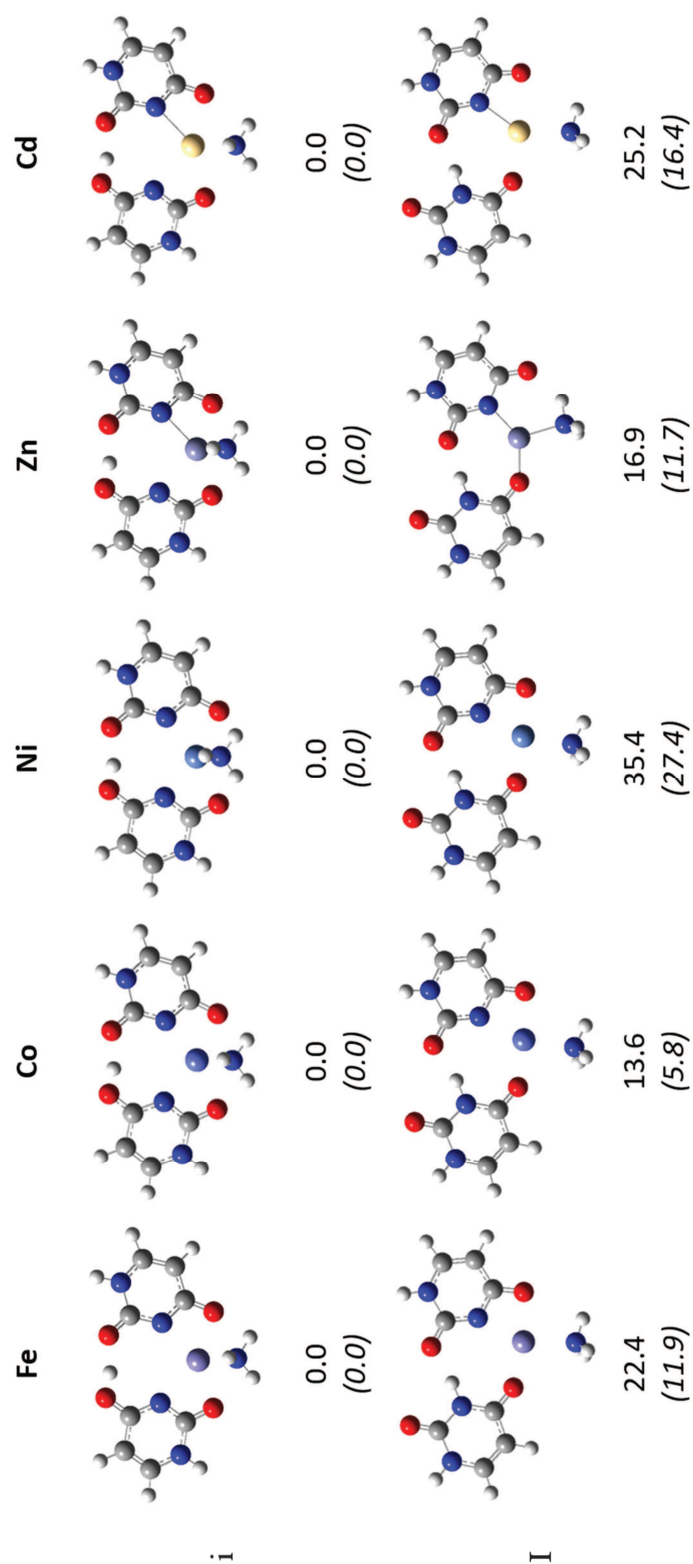
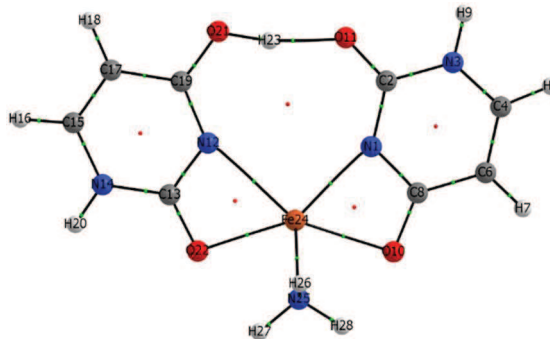


Figure D13. Comparison of the lowest energy structure **i** with structure **I** for $[M(\text{Ura-H})(\text{Ura})(\text{NH}_3)]^+$, $M = \text{Fe}, \text{Co}, \text{Ni}, \text{Zn}$ and Cd . The calculated relative enthalpies and Gibbs energies (parentheses) using calculation method 2 are shown in kJ mol^{-1} at 298 K.

FIGURE D14.**Structure i with Fe**

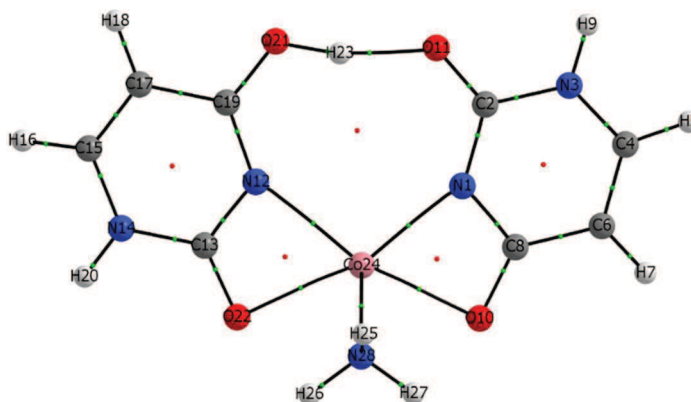
Electron densities ρ ($\text{e } \text{\AA}^{-3}$), Laplacian of the charge density $\nabla^2\rho$ ($\text{e } \text{\AA}^{-5}$) and ellipticity ε at the bond critical points, computed for geometries optimized at the B3LYP/6-31+G(d,p) level.



Bond	ρ	$\nabla^2\rho$	ε
N1 - C2	0.343	-1.229	0.162
C2 - N3	0.312	-1.037	0.143
N3 - C4	0.316	-0.805	0.034
N3 - H9	0.345	-1.881	0.040
C4 - H5	0.295	-1.149	0.021
N1 - Fe24	0.073	0.257	0.113
N1 - C8	0.330	-1.139	0.085
C4 - C6	0.337	-0.990	0.325
C6 - C8	0.299	-0.816	0.169
C6 - H7	0.289	-1.082	0.031
C8 - O10	0.372	-0.297	0.053
C2 - O11	0.394	-0.227	0.122
N12 - Fe24	0.046	0.131	0.087
N12 - C13	0.348	-1.262	0.152
C13 - N14	0.326	-1.053	0.147
N14 - C15	0.311	-0.766	0.028
N14 - H20	0.344	-1.881	0.037
C15 - H16	0.296	-1.163	0.023
N12 - C19	0.350	-1.203	0.116
C15 - C17	0.339	-1.003	0.324
C17 - C19	0.299	-0.820	0.169
C17 - H18	0.290	-1.100	0.027
O11 - H23	0.070	0.158	0.020
O21 - H23	0.286	-1.511	0.010
C19 - O21	0.349	-0.294	0.041
C13 - O22	0.383	-0.365	0.113
O10 - Fe24	0.060	0.230	0.147
O22 - Fe24	0.062	0.255	0.025
Fe24 - N25	0.065	0.233	0.171
N25 - H26	0.340	-1.807	0.026
N25 - H27	0.339	-1.802	0.026
N25 - H28	0.338	-1.805	0.025

Structure i with Co

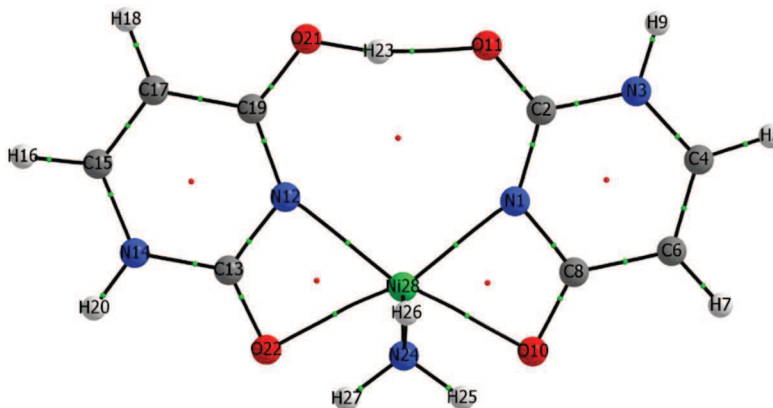
Electron densities ρ ($\text{e } \text{\AA}^{-3}$), Laplacian of the charge density $\nabla^2\rho$ ($\text{e } \text{\AA}^{-5}$) and ellipticity ε at the bond critical points, computed for geometries optimized at the B3LYP/6-31+G(d,p) level.



Bond	ρ	$\nabla^2\rho$	ε
N1 - Co24	0.084	0.343	0.238
N1 - C2	0.344	-1.231	0.161
C2 - N3	0.314	-1.042	0.145
N3 - C4	0.314	-0.804	0.035
N3 - H9	0.345	-1.880	0.040
C4 - H5	0.295	-1.149	0.022
N1 - C8	0.330	-1.129	0.081
C4 - C6	0.337	-0.986	0.326
C6 - C8	0.298	-0.811	0.167
C6 - H7	0.289	-1.083	0.031
C8 - O10	0.375	-0.293	0.059
C2 - O11	0.394	-0.241	0.123
O10 - Co24	0.058	0.201	0.125
N12 - Co24	0.064	0.245	0.285
N12 - C13	0.339	-1.211	0.144
C13 - N14	0.323	-1.053	0.147
N14 - C15	0.312	-0.774	0.028
N14 - H20	0.343	-1.880	0.037
C15 - H16	0.296	-1.163	0.022
N12 - C19	0.348	-1.191	0.121
C15 - C17	0.339	-0.999	0.323
C17 - C19	0.299	-0.824	0.174
C17 - H18	0.290	-1.099	0.029
O11 - H23	0.068	0.154	0.023
O21 - H23	0.285	-1.507	0.010
C19 - O21	0.348	-0.291	0.040
O22 - Co24	0.048	0.166	0.090
C13 - O22	0.394	-0.299	0.127
Co24 - N28	0.071	0.271	0.241
H25 - N28	0.340	-1.805	0.025
H27 - N28	0.339	-1.814	0.024
H26 - N28	0.340	-1.814	0.024

Structure i with Ni

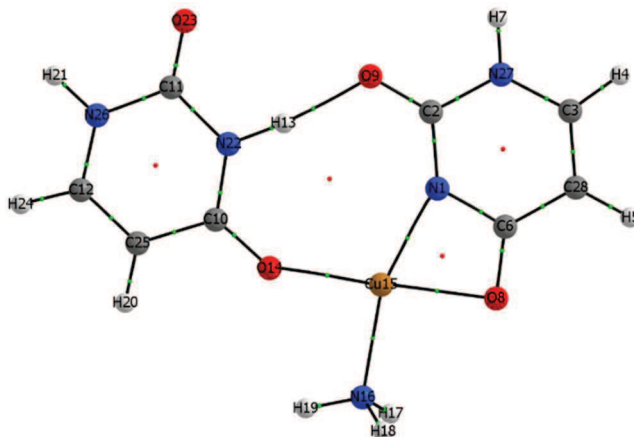
Electron densities ρ ($\text{e } \text{\AA}^{-3}$), Laplacian of the charge density $\nabla^2\rho$ ($\text{e } \text{\AA}^{-5}$) and ellipticity ε at the bond critical points, computed for geometries optimized at the B3LYP/6-31+G(d,p) level.



Bond	ρ	$\nabla^2\rho$	ε
N1 - C2	0.345	-1.227	0.164
C2 - N3	0.313	-1.041	0.145
N3 - C4	0.314	-0.805	0.035
N3 - H9	0.345	-1.880	0.040
N1 - Ni28	0.090	0.329	0.066
C4 - H5	0.295	-1.150	0.021
N1 - C8	0.331	-1.128	0.082
C4 - C6	0.336	-0.983	0.326
C6 - C8	0.298	-0.813	0.168
C6 - H7	0.289	-1.084	0.031
C8 - O10	0.374	-0.306	0.061
C2 - O11	0.395	-0.243	0.124
O10 - Ni28	0.062	0.217	0.141
N12 - Ni28	0.071	0.244	0.091
N12 - C13	0.339	-1.211	0.143
C13 - N14	0.324	-1.056	0.147
N14 - C15	0.312	-0.774	0.027
N14 - H20	0.343	-1.880	0.037
C15 - H16	0.296	-1.164	0.022
N12 - C19	0.349	-1.185	0.122
C15 - C17	0.338	-0.998	0.324
C17 - C19	0.299	-0.823	0.173
C17 - H18	0.290	-1.099	0.029
O11 - H23	0.066	0.152	0.022
O21 - H23	0.285	-1.516	0.010
C19 - O21	0.348	-0.294	0.040
O22 - Ni28	0.052	0.185	0.174
C13 - O22	0.393	-0.310	0.129
N24 - Ni28	0.078	0.300	0.029
N24 - H25	0.339	-1.816	0.024
N24 - H26	0.341	-1.816	0.024
N24 - H27	0.340	-1.815	0.024

Structure I with Cu

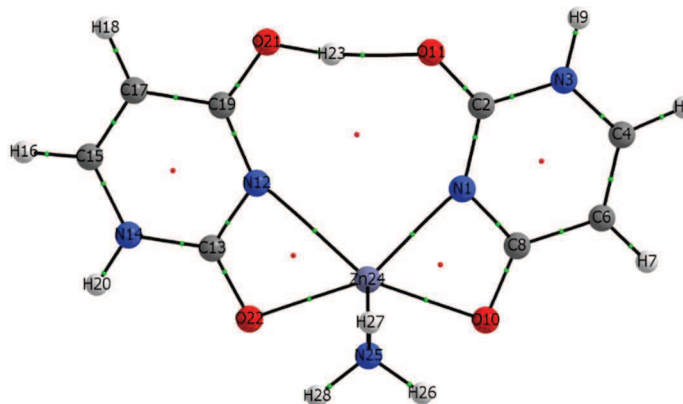
Electron densities ρ ($\text{e } \text{\AA}^{-3}$), Laplacian of the charge density $\nabla^2\rho$ ($\text{e } \text{\AA}^{-5}$) and ellipticity ε at the bond critical points, computed for geometries optimized at the B3LYP/6-31+G(d,p) level.



Bond	ρ	$\nabla^2\rho$	ε
N1 - C2	0.333	-1.162	0.149
C3 - N27	0.319	-0.814	0.035
C3 - C28	0.335	-0.976	0.317
C3 - H4	0.295	-1.156	0.019
N1 - Cu15	0.095	0.283	0.074
N1 - C6	0.340	-1.160	0.095
C6 - C28	0.303	-0.837	0.182
H5 - C28	0.289	-1.084	0.033
C2 - N27	0.307	-1.011	0.138
H7 - N27	0.344	-1.881	0.039
C6 - O8	0.361	-0.370	0.041
C2 - O9	0.410	-0.137	0.138
H13 - N22	0.313	-1.687	0.029
O9 - H13	0.041	0.119	0.035
C10 - N22	0.329	-1.081	0.124
C12 - N26	0.322	-0.812	0.032
C12 - C25	0.337	-0.990	0.323
C12 - H24	0.295	-1.154	0.018
C11 - O23	0.430	0.060	0.156
O8 - Cu15	0.081	0.270	0.027
Cu15 - N16	0.087	0.269	0.020
C10 - O14	0.364	-0.226	0.036
C10 - C25	0.299	-0.821	0.192
O14 - Cu15	0.081	0.369	0.063
N16 - H17	0.339	-1.815	0.023
N16 - H18	0.339	-1.815	0.023
N16 - H19	0.341	-1.829	0.022
H20 - C25	0.289	-1.076	0.038
C11 - N26	0.307	-1.010	0.142
C11 - N22	0.304	-1.003	0.140
H21 - N26	0.344	-1.882	0.039

Structure i with Zn

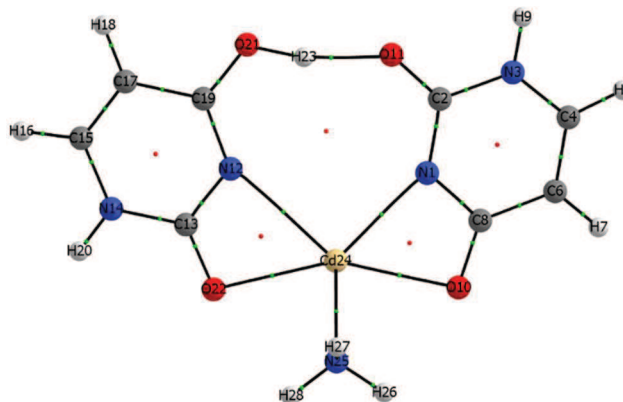
Electron densities ρ ($\text{e } \text{\AA}^{-3}$), Laplacian of the charge density $\nabla^2\rho$ ($\text{e } \text{\AA}^{-5}$) and ellipticity ε at the bond critical points, computed for geometries optimized at the B3LYP/6-31+G(d,p) level.



Bond	ρ	$\nabla^2\rho$	ε
N1 - C2	0.344	-1.230	0.164
C2 - N3	0.312	-1.035	0.143
N3 - C4	0.315	-0.805	0.036
C4 - H5	0.295	-1.147	0.021
N1 - Zn24	0.081	0.240	0.080
N1 - C8	0.330	-1.132	0.085
C4 - C6	0.337	-0.988	0.328
C6 - C8	0.297	-0.809	0.165
C6 - H7	0.289	-1.083	0.032
N3 - H9	0.345	-1.880	0.040
C8 - O10	0.374	-0.292	0.054
C2 - O11	0.394	-0.238	0.120
O11 - H23	0.062	0.155	0.026
N12 - Zn24	0.045	0.168	0.002
N12 - C13	0.348	-1.261	0.150
N14 - C15	0.311	-0.771	0.030
C13 - N14	0.325	-1.050	0.143
C15 - C17	0.338	-0.998	0.322
C15 - H16	0.296	-1.163	0.023
N12 - C19	0.352	-1.213	0.117
C17 - C19	0.299	-0.823	0.171
C17 - H18	0.290	-1.098	0.027
O21 - H23	0.292	-1.591	0.011
N14 - H20	0.344	-1.881	0.037
C19 - O21	0.347	-0.311	0.038
O22 - Zn24	0.064	0.241	0.040
C13 - O22	0.385	-0.357	0.117
O10 - Zn24	0.060	0.220	0.020
Zn24 - N25	0.076	0.229	0.002
N25 - H26	0.339	-1.810	0.025
N25 - H27	0.340	-1.811	0.025
N25 - H28	0.339	-1.812	0.025

Structure i with Cd

Electron densities ρ ($\text{e } \text{\AA}^{-3}$), Laplacian of the charge density $\nabla^2\rho$ ($\text{e } \text{\AA}^{-5}$) and ellipticity ε at the bond critical points, computed for geometries optimized at the B3LYP/6-31+G(d,p) level.



Bond	ρ	$\nabla^2\rho$	ε
N1 - Cd24	0.069	0.277	0.099
N1 - C2	0.343	-1.206	0.157
C2 - N3	0.312	-1.015	0.130
N3 - H9	0.345	-1.877	0.039
N3 - C4	0.314	-0.736	0.022
C4 - H5	0.295	-1.146	0.020
N1 - C8	0.326	-1.096	0.071
C4 - C6	0.338	-1.010	0.330
C6 - C8	0.295	-0.807	0.158
C6 - H7	0.289	-1.084	0.030
C8 - O10	0.376	-0.150	0.050
C2 - O11	0.391	-0.113	0.114
O21 - H23	0.292	-1.595	0.010
N12 - Cd24	0.041	0.154	0.047
N12 - C13	0.344	-1.241	0.143
C13 - N14	0.321	-0.996	0.127
N14 - H20	0.344	-1.880	0.037
C15 - H16	0.296	-1.162	0.021
N14 - C15	0.312	-0.708	0.017
C15 - C17	0.339	-1.018	0.321
N12 - C19	0.350	-1.145	0.107
C17 - C19	0.300	-0.834	0.168
C17 - H18	0.290	-1.098	0.026
O11 - H23	0.063	0.160	0.022
C19 - O21	0.344	-0.223	0.030
C13 - O22	0.385	-0.216	0.112
O10 - Cd24	0.048	0.186	0.019
O22 - Cd24	0.050	0.212	0.033
Cd24 - N25	0.059	0.231	0.006
N25 - H26	0.339	-1.810	0.026
N25 - H27	0.340	-1.809	0.026
N25 - H28	0.340	-1.811	0.026